

NASA Contractor Report 187091

The Flowfield Around a STOVL Aircraft Model in Ground Effect

Roderick J. MacLean
Purdue University
West Lafayette, Indiana

(NASA-CR-187091) THE FLOWFIELD
AROUND A STOVL AIRCRAFT MODEL IN
GROUND EFFECT M.S. Thesis - 1990
Final Report (Purdue Univ.) 270 p

N94-71797

Unclass

May 1991

Z9/07 0002855

Prepared for
Lewis Research Center
Under Grant NAG3-943

NASA
National Aeronautics and
Space Administration

THE FLOWFIELD AROUND A STOVL AIRCRAFT MODEL IN GROUND EFFECT

Roderick J. MacLean
Purdue University
West Lafayette, Indiana 47907

ABSTRACT

An experimental investigation was conducted to determine the causes of hot gas ingestion of engine inlets in STOVL and V/STOL aircraft in ground effect. Marker nephelometry was used to establish the interactions between the jets, forward velocity, and ground for a typical aircraft model configuration. The aircraft test model consisted of a two inlet configuration with four low subsonic velocity jets impacting vertically on a flat plate. The vertical distance between the plate and model under-surface was adjustable, and a wind tunnel provided forward air velocities from 0 to 0.1 times the jet velocity to simulate landing into a wind. Single frame pictures of the smoke concentration distribution in the flowfield revealed several vortical features in the interaction region, which were affected variously by the distance between the ground plane and model, the forward wind velocity, and the inlet suction. Some of these vortical features, such as the ground vortex, have been seen before in experiments using single jets. Other vortical features in the flowfield, such as the forward vortex pair, have not been seen before. Frame-averaged experimental smoke concentration profiles compared favorably with numerical time-averaged predictions of temperature distribution carried out at the University of Illinois. However, such predictions did not seem to reveal some aspects of the vortical flow features which should affect instantaneous distortion into the engine inlet.

ACKNOWLEDGMENTS

The author would like to thank his major professor, Dr. John P. Sullivan. His technical guidance, criticism, and support of this thesis are greatly appreciated.

The author would also like to thank Dr. S. N. B. Murthy and Dr. W. A. Gustafson for their participation on his committee.

This research was sponsored by the NASA-Lewis Research Center, and monitored by P. Batterton and J. Holdeman. Numerical data were provided by D. Tafti and S. Vanka at the University of Illinois.

Special thanks to all the support staff and other graduate students at the lab, especially Robert T. Johnston, for his help and support of the work in this thesis.

TABLE OF CONTENTS

	Page
LIST OF TABLES	v
LIST OF FIGURES	vi
 1. INTRODUCTION	 1
1.1 Vortical Structures in the Flowfield	4
1.1.1 The Ground Vortex	4
1.1.2 The Forward Vortex Pair	4
1.1.3 Vortices Produced by Jet-Fountain Interactions	5
1.1.4 Second Ground Vortex	5
 2. LITERATURE REVIEW	 8
 3. EXPERIMENTAL APPARATUS AND METHOD	 13
3.1 Experimental Method	13
3.2 Experimental Apparatus	14
3.3 Data Acquisition Method	17
 4. EXPERIMENTAL RESULTS	 32
4.1 Vortical Structures in the Flowfield	32
4.1.1 Illustration of Vortex Structures	33
4.1.2 Mean and RMS Concentration Measurements	35
4.1.2.1 Mean and RMS Concentration at the Ground Plane	36
4.1.2.2 Mean and RMS Concentration at the Mid Plane	38
4.1.2.3 Mean and RMS Concentration at the Model	40
4.2 Effects of Forward Velocity on Vortex Structures	42
4.2.1 Illustration of Vortex Structures	42
4.2.2 Mean and RMS Concentration Measurements	44
4.3 Effect of Model Height Variation on the Flowfield	45
4.3.1 Effect of Height Variation on Vortex Structures	46
4.3.2 Mean and RMS Concentration Profiles	48
4.4 Effect of Suction on Flowfield Vortex Structures	51

	Page
5. COMPARISON OF NUMERICAL AND EXPERIMENTAL RESULTS	130
5.1 Numerical and Experimental Comparisons at $U/V_1 = 0.09$	131
5.1.1 Ground Plane Comparisons	131
5.1.2 Comparisons at Mid Plane	133
5.1.3 Model Body Plane Comparisons	134
5.2 Numerical and Experimental Comparisons at $U/V_1 = 0.03$	136
5.2.1 Ground Plane Comparisons	136
5.2.2 Mid Plane Comparisons	138
5.2.3 Model Body Plane Comparisons	140
5.3 Vertical Plane Numerical and Experimental Comparisons	142
5.3.1 Numerical and Experimental Comparisons for $U/V_1 = 0.09$	142
5.3.2 Numerical and Experimental Comparisons at $U/V_1 = 0.03$	143
5.3.3 Numerical and Experimental Comparisons Along Z-Axis	145
6. CONCLUSIONS	234
LIST OF REFERENCES	237
APPENDIX	242

LIST OF TABLES

Table	Page
5.1 Extent of Recirculating Hot Gas Zone Upstream of Forward Lift Jets	147

LIST OF FIGURES

Figure	Page
1.1 Flowfield Features Visible in x-z Plane	6
1.2 Flowfield Features Visible in x-y Plane	7
3.1 Test Model	23
3.2 Jet Velocity Profile	24
3.3 Smoke Concentration Through Side Jet Centerlines at Jet Exit Plane	25
3.4 Smoke Concentration Variation With Time at Jet Exit	26
3.5 Experimental Setup	27
3.6 Wind Tunnel Velocity Distribution	28
3.7 Laser and Laser Sheet Optics	29
3.8 Data Acquisition Flowchart	30
3.9 Data Processing Software Flowchart	31
4.1 Single Frame Image of Smoke Concentration at Mid Plane $y/D_j = 2, H/D_j = 4, U/V_j = 0.09$	53
4.2 Single Frame Image of Smoke Concentration at Far Plane $z/D_j = 5.5, H/D_j = 4, U/V_j = 0.09$	54
4.3 Single Frame Image of Smoke Concentration at Edge Plane $z/D_j = 2.5, H/D_j = 4, U/V_j = 0.09$	55
4.4 Single Frame Image of Smoke Concentration at Side Jet Pair Centerline $z/D_j = 1.625, H/D_j = 4, U/V_j = 0.09$	56
4.5 Single Frame Image of Smoke Concentration at Model Centerline $z/D_j = 0.0, H/D_j = 4, U/V_j = 0.09$	57
4.6 Single Frame Image of Smoke Concentration at Ground Plane $y/D_j = 0, H/D_j = 4, U/V_j = 0.09$	58

4.7	Single Frame Image of Smoke Concentration at Body Plane $y/D_j = 3.6, H/D_j = 4, U/V_j = 0.09$	59
4.8	127 Frame Average of Smoke Concentration at Ground Plane $y/D_j = 0.0, H/D_j = 4, U/V_j = 0.09$	60
4.9	127 Frame Average of Smoke Concentration at Mid Plane $y/D_j = 2.0, H/D_j = 4, U/V_j = 0.09$	61
4.10	127 Frame Average of Smoke Concentration at Model Body Plane $y/D_j = 3.6, H/D_j = 4, U/V_j = 0.09$	62
4.11	Mean and RMS Concentration Profiles at Model Centerline: $z/D_j = 0.0$ Laser Sheet at Ground Plane: $y/D_j = 0, H/D_j = 4, U/V_j = 0.09$	63
4.12	Mean and RMS Concentration Profiles at Side Jet Centerlines: $z/D_j = 1.625$ Laser Sheet at Ground Plane: $y/D_j = 0, H/D_j = 4, U/V_j = 0.09$	64
4.13	Mean and RMS Concentration Profiles at Model Edge: $z/D_j = 2.5$ Laser Sheet at Ground Plane: $y/D_j = 0.0, H/D_j = 4, U/V_j = 0.09$	65
4.14	Mean and RMS Concentration Profiles at Far Plane: $z/D_j = 5.5$ Laser Sheet at Ground Plane: $y/D_j = 0.0, H/D_j = 4, U/V_j = 0.09$	66
4.15	Mean and RMS Concentration Profiles at Forward Jet Centerlines: $x/D_j = 0$ Laser Sheet at Ground Plane: $y/D_j = 0.0, H/D_j = 4, U/V_j = 0.09$	67
4.16	Mean and RMS Concentration Profiles at Rear Jet Centerlines: $x/D_j = 6$ Laser Sheet at Ground Plane: $y/D_j = 0.0, H/D_j = 4, U/V_j = 0.09$	68
4.17	Mean and RMS Concentration Profiles at Model Centerline: $z/D_j = 0.0$ Laser Sheet at Mid Plane: $y/D_j = 2.0, H/D_j = 4, U/V_j = 0.09$	69
4.18	Mean and RMS Concentration Profiles at Side Jet Centerlines: $z/D_j = 1.625$ Laser Sheet at Mid Plane: $y/D_j = 2.0, H/D_j = 4, U/V_j = 0.09$	70
4.19	Mean and RMS Concentration Profiles at Model Edge: $z/D_j = 2.5$ Laser Sheet at Mid Plane: $y/D_j = 2.0, H/D_j = 4, U/V_j = 0.09$	71
4.20	Mean and RMS Concentration Profiles at Far Plane: $z/D_j = 5.5$ Laser Sheet at Mid Plane: $y/D_j = 2.0, H/D_j = 4, U/V_j = 0.09$	72
4.21	Mean and RMS Concentration Profiles at Forward Jet Centerlines: $x/D_j = 0$ Laser Sheet at Mid Plane: $y/D_j = 2.0, H/D_j = 4, U/V_j = 0.09$	73
4.22	Mean and RMS Concentration Profiles at Rear Jet Centerlines: $x/D_j = 6$ Laser Sheet at Mid Plane: $y/D_j = 2.0, H/D_j = 4, U/V_j = 0.09$	74
4.23	Mean and RMS Concentration Profiles at Model Centerline: $z/D_j = 0.0$ Laser Sheet at Model Body Plane: $y/D_j = 3.6, H/D_j = 4, U/V_j = 0.09$	75

Figure	Page
4.24 Mean and RMS Concentration Profiles at Side Jet Centerlines: $z/D_j = 1.625$ Laser Sheet at Model Body Plane: $y/D_j = 3.6$, $H/D_j = 4$, $U/V_j = 0.09$	76
4.25 Mean and RMS Concentration Profiles at Model Edge: $z/D_j = 2.5$ Laser Sheet at Model Body Plane: $y/D_j = 3.6$, $H/D_j = 4$, $U/V_j = 0.09$	77
4.26 Mean and RMS Concentration Profiles at Far Plane: $z/D_j = 5.5$ Laser Sheet at Model Body Plane: $y/D_j = 3.6$, $H/D_j = 4$, $U/V_j = 0.09$	78
4.27 Mean and RMS Concentration Profiles at Forward Jet Centerlines: $x/D_j = 0$ Laser Sheet at Model Body Plane: $y/D_j = 3.6$, $H/D_j = 4$, $U/V_j = 0.09$	79
4.28 Mean and RMS Concentration Profiles at Rear Jet Centerlines: $x/D_j = 6$ Laser Sheet at Model Body Plane: $y/D_j = 3.6$, $H/D_j = 4$, $U/V_j = 0.09$	80
4.29 Single Frame Image of Smoke Concentration at Mid Plane $y/D_j = 2$, $H/D_j = 4$, $U/V_j = 0.03$	81
4.30 Single Frame Image of Smoke Concentration at Far Plane $z/D_j = 5.5$, $H/D_j = 4$, $U/V_j = 0.03$	82
4.31 Ground Vortex Location Versus Velocity Ratio: $H/D_j = 4$	83
4.32 Forward Vortex Pair Location Versus Velocity Ratio: $H/D_j = 4$	84
4.33 Single Frame Image of Smoke Concentration at Edge Plane $z/D_j = 2.5$, $H/D_j = 4$, $U/V_j = 0.03$	85
4.34 Single Frame Image of Smoke Concentration at Side Jet Pair Centerline $z/D_j = 1.625$, $H/D_j = 4$, $U/V_j = 0.03$	86
4.35 Single Frame Image of Smoke Concentration at Ground Plane $y/D_j = 0$, $H/D_j = 4$, $U/V_j = 0.03$	87
4.36 127 Frame Average of Smoke Concentration at Ground Plane $y/D_j = 0.0$, $H/D_j = 4$, $U/V_j = 0.03$	88
4.37 127 Frame Average of Smoke Concentration at Mid Plane $y/D_j = 2.0$, $H/D_j = 4$, $U/V_j = 0.03$	89
4.38 127 Frame Average of Smoke Concentration at Model Body Plane $y/D_j = 3.6$, $H/D_j = 4$, $U/V_j = 0.03$	90
4.39 Mean and RMS Concentration Profiles at Model Centerline: $z/D_j = 0.0$ Laser Sheet at Ground Plane: $y/D_j = 0$, $H/D_j = 4$, $U/V_j = 0.03$	91
4.40 Mean and RMS Concentration Profiles at Side Jet Centerlines: $z/D_j = 1.625$ Laser Sheet at Ground Plane: $y/D_j = 0$, $H/D_j = 4$, $U/V_j = 0.03$	92

Figure	Page
4.41 Mean and RMS Concentration Profiles at Model Edge: $z/D_j = 2.5$ Laser Sheet at Ground Plane: $y/D_j = 0.0$, $H/D_j = 4$, $U/V_j = 0.03$	93
4.42 Mean and RMS Concentration Profiles at Far Plane: $z/D_j = 5.5$ Laser Sheet at Ground Plane: $y/D_j = 0.0$, $H/D_j = 4$, $U/V_j = 0.03$	94
4.43 Single Frame Image of Smoke Concentration at Ground Plane $y/D_j = 0$, $H/D_j = 2$, $U/V_j = 0.03$	95
4.44 Single Frame Image of Smoke Concentration at Ground Plane $y/D_j = 0$, $H/D_j = 4$, $U/V_j = 0.03$	96
4.45 Single Frame Image of Smoke Concentration at Ground Plane $y/D_j = 0$, $H/D_j = 6$, $U/V_j = 0.03$	97
4.46 Ground Vortex Location Versus Velocity Ratio (U/V_j)	98
4.47 Forward Vortex Pair Location Versus Velocity Ratio (U/V_j)	99
4.48 Single Frame Image of Smoke Concentration at Ground Plane $y/D_j = 0$, $H/D_j = 2$, $U/V_j = 0.09$	100
4.49 Single Frame Image of Smoke Concentration at Ground Plane $y/D_j = 0$, $H/D_j = 4$, $U/V_j = 0.09$	101
4.50 Single Frame Image of Smoke Concentration at Ground Plane $y/D_j = 0$, $H/D_j = 6$, $U/V_j = 0.09$	102
4.51 Mean Concentration Profiles at Model Centerline: $z/D_j = 0.0$ Laser Sheet at Ground Plane: $y/D_j = 0.0$, $U/V_j = 0.09$	103
4.52 Single Frame Image of Smoke Concentration at Side Jet Pair Centerline $z/D_j = 1.625$, $H/D_j = 2$, $U/V_j = 0.09$	104
4.53 Single Frame Image of Smoke Concentration at Side Jet Pair Centerline $z/D_j = 1.625$, $H/D_j = 4$, $U/V_j = 0.09$	105
4.54 Single Frame Image of Smoke Concentration at Side Jet Pair Centerline $z/D_j = 1.625$, $H/D_j = 6$, $U/V_j = 0.09$	106
4.55 Single Frame Image of Smoke Concentration at Mid Plane $y/D_j = 1.0$, $H/D_j = 2$, $U/V_j = 0.03$	107
4.56 Single Frame Image of Smoke Concentration at Mid Plane $y/D_j = 2.0$, $H/D_j = 4$, $U/V_j = 0.03$	108
4.57 Single Frame Image of Smoke Concentration at Mid Plane $y/D_j = 3.0$, $H/D_j = 6$, $U/V_j = 0.03$	109

Figure	Page
4.58 Mean and RMS Concentration Profiles at Model Centerline: $z/D_j = 0.0$ Laser Sheet at Ground Plane: $y/D_j = 0, H/D_j = 2, U/V_j = 0.09$	110
4.59 Mean and RMS Concentration Profiles at Side Jet Centerlines: $z/D_j = 1.625$ Laser Sheet at Ground Plane: $y/D_j = 0, H/D_j = 2, U/V_j = 0.09$	111
4.60 Mean and RMS Concentration Profiles at Model Edge: $z/D_j = 2.5$ Laser Sheet at Ground Plane: $y/D_j = 0.0, H/D_j = 2, U/V_j = 0.09$	112
4.61 Mean and RMS Concentration Profiles at Far Plane: $z/D_j = 5.5$ Laser Sheet at Ground Plane: $y/D_j = 0.0, H/D_j = 2, U/V_j = 0.09$	113
4.62 Mean and RMS Concentration Profiles at Model Centerline: $z/D_j = 0.0$ Laser Sheet at Ground Plane: $y/D_j = 0, H/D_j = 6, U/V_j = 0.09$	114
4.63 Mean and RMS Concentration Profiles at Side Jet Centerlines: $z/D_j = 1.625$ Laser Sheet at Ground Plane: $y/D_j = 0, H/D_j = 6, U/V_j = 0.09$	115
4.64 Mean and RMS Concentration Profiles at Model Edge: $z/D_j = 2.5$ Laser Sheet at Ground Plane: $y/D_j = 0.0, H/D_j = 6, U/V_j = 0.09$	116
4.65 Mean and RMS Concentration Profiles at Far Plane: $z/D_j = 5.5$ Laser Sheet at Ground Plane: $y/D_j = 0.0, H/D_j = 6, U/V_j = 0.09$	117
4.66 Mean and RMS Concentration Profiles at Model Centerline: $z/D_j = 0.0$ Laser Sheet at Mid Plane: $y/D_j = 2.0, H/D_j = 2, U/V_j = 0.09$	118
4.67 Mean and RMS Concentration Profiles at Model Centerline: $z/D_j = 0.0$ Laser Sheet at Mid Plane: $y/D_j = 2.0, H/D_j = 6, U/V_j = 0.09$	119
4.68 Mean and RMS Concentration Profiles at Side Jet Centerlines: $z/D_j = 1.625$ Laser Sheet at Mid Plane: $y/D_j = 2.0, H/D_j = 2, U/V_j = 0.09$	120
4.69 Mean and RMS Concentration Profiles at Side Jet Centerlines: $z/D_j = 1.625$ Laser Sheet at Mid Plane: $y/D_j = 2.0, H/D_j = 6, U/V_j = 0.09$	121
4.70 Mean and RMS Concentration Profiles at Model Edge: $z/D_j = 2.5$ Laser Sheet at Mid Plane: $y/D_j = 2.0, H/D_j = 2, U/V_j = 0.09$	122
4.71 Mean and RMS Concentration Profiles at Model Edge: $z/D_j = 2.5$ Laser Sheet at Mid Plane: $y/D_j = 2.0, H/D_j = 6, U/V_j = 0.09$	123
4.72 Mean and RMS Concentration Profiles at Far Plane: $z/D_j = 5.5$ Laser Sheet at Mid Plane: $y/D_j = 2.0, H/D_j = 2, U/V_j = 0.09$	124
4.73 Mean and RMS Concentration Profiles at Far Plane: $z/D_j = 5.5$ Laser Sheet at Mid Plane: $y/D_j = 2.0, H/D_j = 6, U/V_j = 0.09$	125
4.74 Single Frame Image of Smoke Concentration with suction $y/D_j = 0.6, H/D_j = 2, U/V_j = 0.04$	126

Figure	Page
4.75 Single Frame Image of Smoke Concentration without suction $y/D_j = 0.6$, $H/D_j = 2$, $U/V_j = 0.04$	127
4.76 Ground Vortex Location Versus Velocity Ratio (U/V_j) With and Without Suction	128
4.77 Forward Vortex Pair Location Versus Velocity Ratio (U/V_j) With and Without Suction	129
5.1 Numerical Temperature Profile at Ground Plane: $y/D_j = 0.0$ $H/D_j = 4$, $U/V_j = 0.09$	148
5.2 Experimental Smoke Concentration Profile at Ground Plane: $y/D_j = 0.0$ $H/D_j = 4$, $U/V_j = 0.09$	149
5.3 Numerical and Experimental Results Along Model Centerline: $z/D_j = 0$ $y/D_j = 0.0$, $H/D_j = 4$, $U/V_j = 0.09$	150
5.4 Numerical and Experimental Results At Side Jet Centerline: $z/D_j = 1.625$ $y/D_j = 0.0$, $H/D_j = 4$, $U/V_j = 0.09$	151
5.5 Numerical and Experimental Results Along Model Edge: $z/D_j = 2.5$ $y/D_j = 0.0$, $H/D_j = 4$, $U/V_j = 0.09$	152
5.6 Numerical and Experimental Results at $z/D_j = 5.5$ $y/D_j = 0.0$, $H/D_j = 4$, $U/V_j = 0.09$	153
5.7 Numerical and Experimental Results Across Front Jet Pair: $x/D_j = 0$ $y/D_j = 0.0$, $H/D_j = 4$, $U/V_j = 0.09$	154
5.8 Numerical and Experimental Results Across Rear Jet Pair: $x/D_j = 6$ $y/D_j = 0.0$, $H/D_j = 4$, $U/V_j = 0.09$	155
5.9 Numerical and Experimental Results Between Inlets and Front Jets $z/D_j = -5$, $y/D_j = 0.0$, $H/D_j = 4$, $U/V_j = 0.09$	156
5.10 Numerical Temperature Profile at Mid Plane: $y/D_j = 2.0$ $H/D_j = 4$, $U/V_j = 0.09$	157
5.11 Experimental Smoke Concentration Profile at Mid Plane: $y/D_j = 2.0$ $H/D_j = 4$, $U/V_j = 0.09$	158
5.12 Numerical and Experimental Results Along Model Centerline: $z/D_j = 0$ $y/D_j = 2.0$, $H/D_j = 4$, $U/V_j = 0.09$	159
5.13 Numerical and Experimental Results At Side Jet Centerline: $z/D_j = 1.625$ $y/D_j = 2.0$, $H/D_j = 4$, $U/V_j = 0.09$	160
5.14 Numerical and Experimental Results Along Model Edge: $z/D_j = 2.5$ $y/D_j = 2.0$, $H/D_j = 4$, $U/V_j = 0.09$	161

Figure	Page
5.15 Numerical and Experimental Results at $z/D_j = 5.5$ $y/D_j = 2.0$, $H/D_j = 4$, $U/V_j = 0.09$	162
5.16 Numerical and Experimental Results Across Front Jet Pair: $x/D_j = 0$ $y/D_j = 2.0$, $H/D_j = 4$, $U/V_j = 0.09$	163
5.17 Numerical and Experimental Results Across Rear Jet Pair: $x/D_j = 6$ $y/D_j = 2.0$, $H/D_j = 4$, $U/V_j = 0.09$	164
5.18 Numerical and Experimental Results Between Inlets and Front Jets $z/D_j = -5$, $y/D_j = 2.0$, $H/D_j = 4$, $U/V_j = 0.09$	165
5.19 Numerical Temperature Profile at Model Body Plane: $y/D_j = 3.6$ $H/D_j = 4$, $U/V_j = 0.09$	166
5.20 Experimental Smoke Concentration Profile at Model Body Plane: $y/D_j = 3.6$ $H/D_j = 4$, $U/V_j = 0.09$	167
5.21 Numerical and Experimental Results Along Model Centerline: $z/D_j = 0$ $y/D_j = 3.6$, $H/D_j = 4$, $U/V_j = 0.09$	168
5.22 Numerical and Experimental Results At Side Jet Centerline: $z/D_j = 1.625$ $y/D_j = 3.6$, $H/D_j = 4$, $U/V_j = 0.09$	169
5.23 Numerical and Experimental Results Along Model Edge: $z/D_j = 2.5$ $y/D_j = 3.6$, $H/D_j = 4$, $U/V_j = 0.09$	170
5.24 Numerical and Experimental Results at $z/D_j = 5.5$ $y/D_j = 3.6$, $H/D_j = 4$, $U/V_j = 0.09$	171
5.25 Numerical and Experimental Results Across Front Jet Pair: $x/D_j = 0$ $y/D_j = 3.6$, $H/D_j = 4$, $U/V_j = 0.09$	172
5.26 Numerical and Experimental Results Across Rear Jet Pair: $x/D_j = 6$ $y/D_j = 3.6$, $H/D_j = 4$, $U/V_j = 0.09$	173
5.27 Numerical and Experimental Results Between Inlets and Front Jets $z/D_j = -5$, $y/D_j = 3.6$, $H/D_j = 4$, $U/V_j = 0.09$	174
5.28 Numerical Temperature Profile at Ground Plane: $y/D_j = 0.0$ $H/D_j = 4$, $U/V_j = 0.03$	175
5.29 Experimental Smoke Concentration Profile at Ground Plane: $y/D_j = 0.0$ $H/D_j = 4$, $U/V_j = 0.03$	176
5.30 Numerical and Experimental Results Along Model Centerline: $z/D_j = 0$ $y/D_j = 0.0$, $H/D_j = 4$, $U/V_j = 0.03$	177
5.31 Numerical and Experimental Results At Side Jet Centerline $z/D_j = 1.625$, $y/D_j = 0.0$, $H/D_j = 4$, $U/V_j = 0.03$	178

Figure	Page
5.32 Numerical and Experimental Results Along Model Edge: $z/D_j = 2.5$ $y/D_j = 0.0$, $H/D_j = 4$, $U/V_j = 0.03$	179
5.33 Numerical and Experimental Results at $z/D_j = 5.5$ $y/D_j = 0.0$, $H/D_j = 4$, $U/V_j = 0.03$	180
5.34 Numerical and Experimental Results Across Front Jet Pair: $x/D_j = 0$ $y/D_j = 0.0$, $H/D_j = 4$, $U/V_j = 0.03$	181
5.35 Numerical and Experimental Results Across Rear Jet Pair: $x/D_j = 6$ $y/D_j = 0.0$, $H/D_j = 4$, $U/V_j = 0.03$	182
5.36 Numerical and Experimental Results Between Inlets and Front Jets $z/D_j = -5$, $y/D_j = 0.0$, $H/D_j = 4$, $U/V_j = 0.03$	183
5.37 Numerical Temperature Profile at Mid Plane: $y/D_j = 2.0$ $H/D_j = 4$, $U/V_j = 0.03$	184
5.38 Experimental Smoke Concentration Profile at Mid Plane: $y/D_j = 2.0$ $H/D_j = 4$, $U/V_j = 0.03$	185
5.39 Numerical and Experimental Results Along Model Centerline: $z/D_j = 0$ $y/D_j = 2.0$, $H/D_j = 4$, $U/V_j = 0.03$	186
5.40 Numerical and Experimental Results At Side Jet Centerline $z/D_j = 1.625$, $y/D_j = 2.0$, $H/D_j = 4$, $U/V_j = 0.03$	187
5.41 Numerical and Experimental Results Along Model Edge: $z/D_j = 2.5$ $y/D_j = 2.0$, $H/D_j = 4$, $U/V_j = 0.03$	188
5.42 Numerical and Experimental Results at $z/D_j = 5.5$ $y/D_j = 2.0$, $H/D_j = 4$, $U/V_j = 0.03$	189
5.43 Numerical and Experimental Results Across Front Jet Pair: $x/D_j = 0$ $y/D_j = 2.0$, $H/D_j = 4$, $U/V_j = 0.03$	190
5.44 Numerical and Experimental Results Across Rear Jet Pair: $x/D_j = 6$ $y/D_j = 2.0$, $H/D_j = 4$, $U/V_j = 0.03$	191
5.45 Numerical and Experimental Results Between Inlets and Front Jets $z/D_j = -5$, $y/D_j = 2.0$, $H/D_j = 4$, $U/V_j = 0.03$	192
5.46 Numerical Temperature Profile at Model Body Plane: $y/D_j = 3.6$ $H/D_j = 4$, $U/V_j = 0.03$	193
5.47 Experimental Smoke Concentration Profile at Model Body Plane $y/D_j = 3.6$, $H/D_j = 4$, $U/V_j = 0.03$	194
5.48 Numerical and Experimental Results Along Model Centerline: $z/D_j = 0$ $y/D_j = 3.6$, $H/D_j = 4$, $U/V_j = 0.03$	195

Figure	Page
5.49 Numerical and Experimental Results At Side Jet Centerline $z/D_j = 1.625$, $y/D_j = 3.6$, $H/D_j = 4$, $U/V_j = 0.03$	196
5.50 Numerical and Experimental Results Along Model Edge: $z/D_j = 2.5$ $y/D_j = 3.6$, $H/D_j = 4$, $U/V_j = 0.03$	197
5.51 Numerical and Experimental Results at $z/D_j = 5.5$ $y/D_j = 3.6$, $H/D_j = 4$, $U/V_j = 0.03$	198
5.52 Numerical and Experimental Results Across Front Jet Pair: $x/D_j = 0$ $y/D_j = 3.6$, $H/D_j = 4$, $U/V_j = 0.03$	199
5.53 Numerical and Experimental Results Across Rear Jet Pair $x/D_j = 6$, $y/D_j = 3.6$, $H/D_j = 4$, $U/V_j = 0.03$	200
5.54 Numerical and Experimental Results Between Inlets and Front Jets $z/D_j = -5$, $y/D_j = 3.6$, $H/D_j = 4$, $U/V_j = 0.03$	201
5.55 Numerical Temperature Distribution Along Model Centerline $z/D_j = 0.0$, $H/D_j = 4$, $U/V_j = 0.09$	202
5.56 Experimental Smoke Concentration Along Model Centerline $z/D_j = 0.0$, $H/D_j = 4$, $U/V_j = 0.09$	203
5.57 Numerical Temperature Distribution Along Side Jet Centerline $z/D_j = 1.625$, $H/D_j = 4$, $U/V_j = 0.09$	204
5.58 Experimental Smoke Concentration Along Side Jet Centerlines $z/D_j = 1.625$, $H/D_j = 4$, $U/V_j = 0.09$	205
5.59 Numerical Temperature Distribution Along Model Edge $z/D_j = 2.5$, $H/D_j = 4$, $U/V_j = 0.09$	206
5.60 Experimental Smoke Concentration Along Model Edge $z/D_j = 2.5$, $H/D_j = 4$, $U/V_j = 0.09$	207
5.61 Numerical Temperature Distribution Along $z/D_j = 5.5$ $H/D_j = 4$, $U/V_j = 0.09$	208
5.62 Experimental Smoke Concentration Along $z/D_j = 5.5$ $H/D_j = 4$, $U/V_j = 0.09$	209
5.63 Numerical Temperature Distribution Along Model Centerline $z/D_j = 0.0$, $H/D_j = 4$, $U/V_j = 0.03$	210
5.64 Experimental Smoke Concentration Along Model Centerline $z/D_j = 0.0$, $H/D_j = 4$, $U/V_j = 0.03$	211
5.65 Numerical Temperature Distribution Along Side Jet Centerline $z/D_j = 1.625$, $H/D_j = 4$, $U/V_j = 0.03$	212

Figure	Page
5.66 Experimental Smoke Concentration Along Side Jet Centerlines $z/D_j = 1.625$, $H/D_j = 4$, $U/V_j = 0.03$	213
5.67 Numerical Temperature Distribution Along Model Edge $z/D_j = 2.5$, $H/D_j = 4$, $U/V_j = 0.03$	214
5.68 Experimental Smoke Concentration Along Model Edge $z/D_j = 2.5$, $H/D_j = 4$, $U/V_j = 0.03$	215
5.69 Numerical Temperature Distribution Along $z/D_j = 5.5$ $H/D_j = 4$, $U/V_j = 0.03$	216
5.70 Experimental Smoke Concentration Along $z/D_j = 5.5$ $H/D_j = 4$, $U/V_j = 0.03$	217
5.71 Numerical Temperature Distribution Across Front Jets $x/D_j = 0.0$, $H/D_j = 4$, $U/V_j = 0.09$	218
5.72 Experimental Smoke Concentration Across Front Jets $x/D_j = 0.0$, $H/D_j = 4$, $U/V_j = 0.09$	219
5.73 Numerical Temperature Distribution Across Rear Jets $x/D_j = 6.0$, $H/D_j = 4$, $U/V_j = 0.09$	220
5.74 Experimental Smoke Concentration Across Rear Jets $x/D_j = 6.0$, $H/D_j = 4$, $U/V_j = 0.09$	221
5.75 Numerical Temperature Distribution Between Front and Rear Jets $x/D_j = 3.0$, $H/D_j = 4$, $U/V_j = 0.09$	222
5.76 Experimental Smoke Concentration Between Front and Rear Jets $x/D_j = 3.0$, $H/D_j = 4$, $U/V_j = 0.09$	223
5.77 Numerical Temperature Distribution Between Inlets and Front Jets $x/D_j = -5.0$, $H/D_j = 4$, $U/V_j = 0.09$	224
5.78 Experimental Smoke Concentration Between Inlets and Front Jets $x/D_j = -5.0$, $H/D_j = 4$, $U/V_j = 0.09$	225
5.79 Numerical Temperature Distribution Across Front Jets $x/D_j = 0.0$, $H/D_j = 4$, $U/V_j = 0.03$	226
5.80 Experimental Smoke Concentration Across Front Jets $x/D_j = 0.0$, $H/D_j = 4$, $U/V_j = 0.03$	227
5.81 Numerical Temperature Distribution Across Rear Jets $x/D_j = 6.0$, $H/D_j = 4$, $U/V_j = 0.03$	228
5.82 Experimental Smoke Concentration Across Rear Jets $x/D_j = 6.0$, $H/D_j = 4$, $U/V_j = 0.03$	229

Figure	Page
5.83 Numerical Temperature Distribution Between Front and Rear Jets $x/D_j = 3.0$, $H/D_j = 4$, $U/V_j = 0.03$	230
5.84 Experimental Smoke Concentration Between Front and Rear Jets $x/D_j = 3.0$, $H/D_j = 4$, $U/V_j = 0.03$	231
5.85 Numerical Temperature Distribution Between Inlets and Front Jets $x/D_j = -5.0$, $H/D_j = 4$, $U/V_j = 0.03$	232
5.86 Experimental Smoke Concentration Between Inlets and Front Jets $x/D_j = -5.0$, $H/D_j = 4$, $U/V_j = 0.03$	233
Appendix	
Figure	
A.1 Left, Central, and Merged Image Profiles Across Front Jet Centerline Laser Sheet at Ground Plane, $H/D_j = 4$, $U/V_j = 0.09$	245
A.2 Merged, Corrected, and Uncorrected Image Profiles at Front Jet Centerline Laser Sheet at Ground Plane, $H/D_j = 4$, $U/V_j = 0.09$	246
A.3 Merged, Best Fit, and Uncorrected Image Profiles at Front Jet Centerline Laser Sheet at Ground Plane, $H/D_j = 4$, $U/V_j = 0.09$	247
A.4 Narrow Laser Sheet Intensity Curves	248
A.5 Decrease in Laser Sheet Intensity Along X-Axis	249
A.6 Light Intensity Across Wide Laser Sheet	250

1. INTRODUCTION

Research investigating V/STOL and STOVL concepts has been undertaken since 1954, with the first experimental VTOL aircraft, the Lockheed XFV-1. While this aircraft was unsuccessful, numerous experimental aircraft concepts have been studied and tested since then. Only a few aircraft, such as the Harrier, have been actually produced.

V/STOL and STOVL aircraft offer several advantages over both helicopters and conventional aircraft. Unlike conventional aircraft, VTOL and STOVL aircraft take off and land vertically or in very short distances, allowing shorter runways to be used. VTOL and STOVL aircraft also are able to fly much faster than conventional helicopters.

While simple in concept, most V/STOL and STOVL aircraft configurations are extremely difficult to design. A large number of concepts have been tested, but only a few have been successful. The Harrier uses vectored thrust, which allows the aircraft to take off and land vertically by rotating the jet nozzles from horizontal to vertical. The Soviet YAK-38 uses a hybrid vectored thrust/liftjet to take off and land vertically by using a liftjet located behind the cockpit to provide some of the vertical thrust necessary. The V-22 Osprey uses a tilt-rotor to convert from a helicopter-like hover to horizontal flight. The C-17, a STOL aircraft, uses deflected thrust to land on short runways.

One of the more important considerations in the design and operation of V/STOL and STOVL aircraft in ground effect is the ingestion of hot exhaust gasses into the engine inlets. Such ingestion leads to a time varying rise in inlet temperature in addition to velocity and stagnation pressure distortion in the inlet flow. This temperature rise decreases engine efficiency and performance, and may cause compressor stall in the

engine. Ingestion is an extremely complex process affected by (a) the aircraft configuration, including the inlet and nozzle design and location, (b) the engine performance characteristics, (c) the altitude of the aircraft from the ground, (d) the attitude of the aircraft, (e) the velocity of the aircraft, and (f) the wind direction and velocity relative to the aircraft. The engine exhaust jet is turbulent, hot, and often at high Mach numbers due to choking and underexpansion within the nozzle. Coherent vortical structures can be expected in the jet due to turbulence. The temperature gives rise to buoyancy effects. When the jet is supersonic, Mach waves appear in the jet and at ground interaction. The jet interaction with the ground causes the jet to spread, which can become further complicated when more than one jet is employed. The formation of a fountain between multiple jets is well known. During forward flight of such an aircraft in ground effect, a relative wind becomes established. Both inviscid and viscous interactions between the jet spread and the forward wind velocity are of great importance. Inlet suction is in the nature of a complicated sink in the flow and the flowfield is therefore affected by the suction.

One of the principal questions in hot gas ingestion concerns the time varying distortion in the flow and thermal fields at the inlet face. It is of considerable interest to establish the manner in which instantaneous distortion varies during approach of a V/STOL aircraft to a landing ground. One approach to addressing the problem is to examine if there are any discernable characteristic features in the flow interaction region beneath the aircraft and further, if there is a pattern to changes in such characteristic features as the aircraft descends as a function of time. This has been one of the main motivations in the current investigation.

A second motivation for the current experiment at Purdue University has been to provide experimental data for comparison with numerical predictions. In a concurrent investigation done by Tafti and Vanka [52] at the University of Illinois, an investigation

has been carried out on predicting the interactive flowfield for the same model configuration used in this experiment. It was therefore possible to compare numerical predictions with experimental results. The calculations are based on time-averaged and Reynolds-averaged equations of motion.

It was felt that a four-poster configuration with two symmetrically located inlets provided an opportunity for examining a number of flow features in the interaction region that would be of interest from the point of view of practical V/STOL or STOVL aircraft. It also provided a reasonably complicated configuration to examine prediction capability.

The three main geometric parameters in this experiment were H , the model height above the ground plane, D_j , the jet diameter, and H_i , the inlet height above the ground. The main velocity parameters are U , the free stream velocity, and V_j , the jet velocity. The scaling parameters, although given in terms of D_j and V_j , are essentially unknown.

In the experiments, a non-intrusive technique, marker nephelometry, was chosen to determine the flowfield, qualitatively and also quantitatively, in the interaction region. Based on the visualization of the smoke concentration field, one could obtain the flow interactions. At the same time, the concentration field is analogous to the temperature field provided the concentration and the temperature are both in the nature of a marker, neither introducing density nor transport differences in the flowfield. On this basis, the concentration field determined in the experiments became available for comparison with numerical predictions of the temperature field done by the University of Illinois.

The flow velocities, both of the jets and of the forward wind, have small subsonic values in the current experiments. Compressibility effects are therefore entirely eliminated. At the same time, it may be worth pointing out that, although the ratio of jet to forward wind velocities is typical of ground effect situations, the absolute velocity of the jet is too small for direct comparison of observed flowfield interactions with those found in practice. Nevertheless, it is hoped that the nature of flow interactions may be

adequately representative of those occurring in actual aircraft operations.

In the following, details of the experiments and the data obtained are presented along with (a) various observations on the structure of the flow interaction region and (b) some typical comparisons between experimental data and predictions.

1.1 Vortical Structures in the Flowfield

The formation of various vortical structures in the flowfield is one of the most noticeable features. In particular, three types of vortex structures may be identified: (i) the horseshoe ground vortex, (ii) the forward vortex pair, (iii) the vortices associated with the interaction between the fountain and the jets, and (iv) the ground vortex associated with the downstream pair of jets. Further remarks will be made on the inlet interaction; meanwhile, the three types of vortex structures may be discussed as follows.

1.1.1 The Ground Vortex

The horseshoe ground vortex is shown in figure 1.1. It forms in the ground plane, and occurs in the region where boundary layer flow produced by the jets impacting on the ground plane meets the free stream flow. It has the features of a horse-shoe vortex, although it will be split by the forward motion of the flow emanating from the inner flow region between the pair of forward jets.

1.1.2 The Forward Vortex Pair

The forward vortex pair is also shown in figure 1.1. Each of the two counter-rotating vortices in the forward vortex pair are anchored to the ground plane, generally with their axes oriented normal to the ground plane. The forward vortex pair is located in the stagnation region where the flow moving outward from between the two forward jets and the free stream flow meet. The unsteady nature of the forward vortex pair makes it difficult to determine the various factors contributing to its formation.

1.1.3 Vortices Produced by Jet-Fountain Interactions

The third major feature visible in the flowfield is a pair of counter-rotating vortices between a side pair of jets and the fountain, as shown in figure 1.2. At high velocity ratios, only the downstream vortex seems to be formed. This feature propagates outward from the region between the jets crosswise into the free stream flow. In this region, only the downstream vortex is visible and acts similar to a ground vortex associated with the downstream (rear) pair of jets.

1.1.4 Second Ground Vortex

The second ground vortex is associated with the downstream pair of jets, and appears to arise due to the fountain upwash in the inner flow region, as stated above. At low velocity ratios and low model heights, the second ground vortex does not appear in the inner flow region. Instead, the vortex structures described in section 1.1.3 appear. At high velocity ratios and model heights, the second ground vortex does appear in the inner flow region, since the forward wind velocity can now affect the inner flowfield region. The second ground vortex nearly always appears in the outer flow region, and is seen in numerical as well as experimental results. The second ground vortex is shown in figure 1.1.

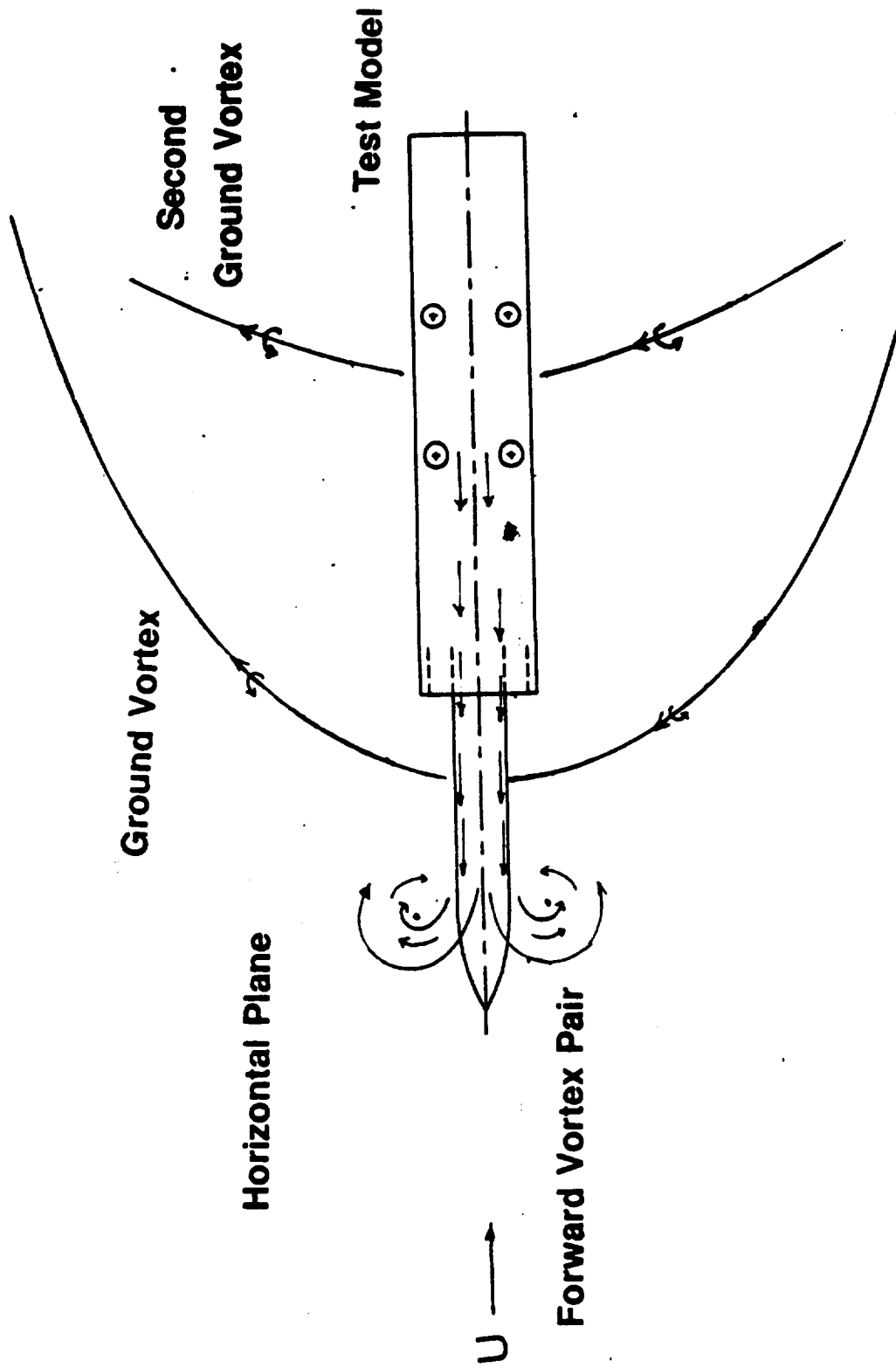


Figure 1.1: Flowfield Features Visible in x-z Plane

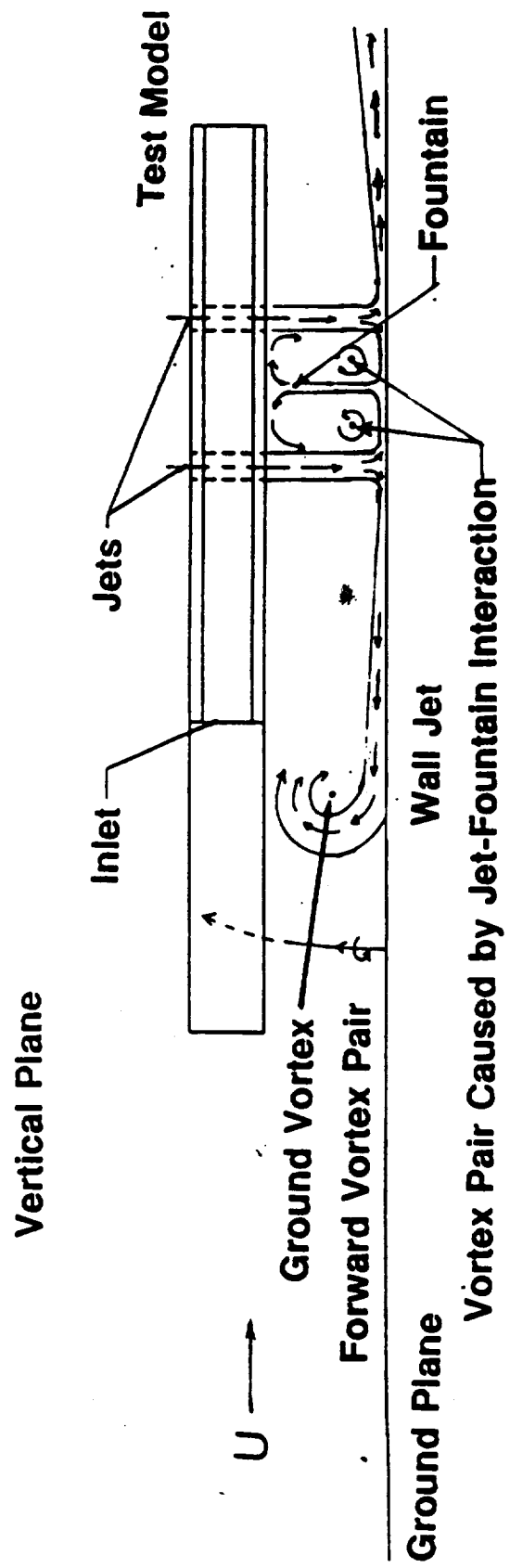


Figure 1.2: Flowfield Features Visible in x-y Plane

2. LITERATURE REVIEW

A large amount of research has been done in the past to investigate the flowfield around V/STOL and STOVL aircraft in ground effect. This area of the flight regime is by far the most complex and difficult part to operate in and design for, since the V/STOL aircraft is generally hovering or in transition. This in itself generates complex aerodynamic forces, which make the aircraft difficult to control. Stewart and Kuhn [51] have investigated several different configurations to determine some of the aerodynamic forces involved in V/STOL aircraft operations in ground effect. Kuhn [33] has also developed empirical models for predicting the aerodynamic forces and moments felt by V/STOL aircraft. They have found that aircraft lift is lost in ground effect due to entrainment by the jets and wall jet, and ground vortex suction. In addition, lift in ground effect may be increased by flow from the fountain impinging on the aircraft undersurface. The aerodynamic pitching moment is also affected by these flow features. All these flow features are highly dependent on the aircraft geometry, including the number, size, and placement of the jets, wings, and fuselage. As such, it is difficult to get more than an approximation of aerodynamic forces on the aircraft using empirical models. They have also documented, in multiple-jet configurations, the existence of stagnation lines at the ground plane, where wall jets from opposing jets meet, and are turned upwards to form part of the fountain. Kotansky [29] has also documented these features, and has developed some empirical equations for calculating fountain strength, and the location of stagnation lines, for multiple-jet configurations. Hall and Rogers [25] have documented recirculating flows for two jet experiments. Two recirculation regions between the

fountain and jets were observed. These two recirculation regions were caused by fountain flow being entrained by the two jets.

An important factor in STOVL and V/STOL aircraft design, and the main focus of this thesis, is the reingestion of hot engine exhaust back into the inlets, which can lead to a large loss in thrust, and possibly compressor stall. Schwantex [45] has documented a one percent loss in thrust for every two degree rise in inlet temperature for some aircraft configurations. Kuhn and Eshlemann [34] also mention this problem, along with the other flow features mentioned above. Hammond and McLemore [26] have investigated hot gas ingestion for a number of configurations using large-scale models.

Since the flow structure around the aircraft is configuration dependent, a large amount of research has been conducted in order to understand the flow of hot exhaust gasses around experimental V/STOL aircraft and small scale V/STOL aircraft models in ground effect. Aulehla and Kissel [5] have documented some of the aerodynamic forces and problems with the VJ-101C, a tilt-jet supersonic V/STOL fighter concept. Weber [56] has investigated a lift plus lift cruise concept, by measuring the unsteady inlet temperature at various forward wind speeds. Barrack [7] has examined the effects of hot gas ingestion on the performance of lift jets in ground effect at low forward speeds for three large-scale models using different lift jet configurations in the 40- by 80-foot wind tunnel at Ames Research Center. Sherreib [48] has investigated a civil V/STOL transport using two, three, and four jets.

Another approach used in investigating the flowfield around V/STOL aircraft is to look at the characteristics of a simple jet system, since the flowfield of complex geometries is very difficult to investigate, due to its inherent complexity and unsteadiness. Detailed experimental investigations have been conducted on single jets in a crossflow impinging on flat plates by Shayesteh et. al. [47]. Both Nosseir [41] and Donaldson and Snedecker [18],[19] have conducted experiments on single jets impacting on flat plates

without crossflows. Kotansky and Glaze [32] have investigated rectangular jet impingement on a ground plane. Stewart and Kemmerly [50] have investigated single jet impingement for a moving jet. Experiments done by Aoyagi and Schnyder [4] have measured velocities using laser doppler velocimetry for a free jet issuing from a flat plate into a free stream. They also have conducted velocity measurements for a twin jet configuration. Saripalli [44] has also conducted detailed velocity measurements using laser doppler velocimetry for a twin jet configuration as well. Hall and Rogers [25], and Bower et. al. [11] have conducted research investigating the recirculation of a twin jet configuration. Wohlbee et. al. [58] has investigated two and three jet model configurations near the ground plane.

Most experimental techniques are limited in the amount and location of measured data. Numerical methods used to model the flowfield around a V/STOL aircraft allow the examination of a number of different physical quantities in most of the flowfield. This allows a number of different configurations to be investigated quickly, as well as giving a large number of points at which different parameters can be examined. Chawla et. al [14] has done numerical calculations on the flowfield around a delta wing with multiple impinging jets. VanOverbeke and Holdeman [53] have investigated the hot gas environment and flowfield around the four jet, two inlet configuration used in this experiment, for several forward speeds and model heights. Agarwal [1] has reviewed a number of numerical methods for jet-induced aerodynamic effects on V/STOL aircraft. The difficulty with using numerical techniques is that there are very few experiments which are able to verify the results of these numerical calculations.

Since large amounts of data are available from single and dual jet experiments, most numerical comparisons are done using single jets in a crossflow, or dual jets without crossflow in order to verify the numerical code. Barata et. al. [6] have done this for single jets in a crossflow, using a k-epsilon turbulence model. Agarwal [2],[3] has

investigated numerical techniques to model two dimensional jets issuing from a wing using both Euler and Navier-Stokes solutions. Both Childs and Nixon [15], and Childs and Patel [16] have conducted numerical investigations with a numerical code using the Navier-Stokes equations, and have calculated the flow around both an impinging jet in a crossflow, and a twin jet configuration. Both these models were compared to experimental data from Saripalli [44].

Marker nephelometry, using a laser sheet to illuminate smoke particles in a flowfield, and a camera to record the flowfield, has the potential to provide detailed experimental measurements of smoke concentration easily. These data can be quantified using analog-to-digital conversion, providing large amounts of data for comparison with numerical results. In addition to being able to provide steady, time averaged smoke concentration measurements in a flowfield, marker nephelometry also allows time-varying flowfields to be recorded. Calculations of root-mean-squared concentration in the flowfield can then give a quantitative measurement of the amount of unsteadiness and turbulence in the flowfield. Becker [9] has given a detailed theoretical description of the methods and problems of using this technique, as well as having conducted experiments investigating single jets, both with and without swirl. Balint et. al. [8], Borleteau [10], and Brandt [12] have all investigated free jets. Seal [46] has also investigated single free jets, both with and without swirl. Morgan [39] and Dwenger [19] have also used this technique to look at unsteady flows in an annular combustor. Mueller [40] and Veret [54] have also use this technique to look at flows over stalled wings and blunt bodies. Johns [28] has used this technique to investigate hot gas ingestion for an advanced STOVL fighter aircraft.

Marker nephelometry provides a great deal of information on smoke concentration measurements in a flowfield. This information can be used for comparison with numerical models of the same model configuration in order to verify the numerical code.

The relative ease with which this technique can be used allows a number of configurations to be quickly tested. Flowfield structures are also visible, allowing the investigator to see what features may be causing certain aerodynamic effects on the test model. This is in contrast to most other experimental techniques, which are difficult, such as laser doppler velocimetry, or only give limited amounts of information, such as force balance measurements or thermocouple readings at the inlet, for instance. This thesis provides comparisons between numerical and experimental results for a four jet, two inlet V/STOL aircraft model, and documents the effects of free stream velocity and model height on various flowfield features.

3. EXPERIMENTAL APPARATUS AND METHOD

The experimental apparatus was designed to investigate the flowfield around a generic V/STOL configuration in ground effect using a flow visualization technique known as marker nephelometry. A secondary goal was to generate a data base of smoke concentration profiles for comparison with numerically generated temperature profiles of the same basic model configuration. The test model used in this experiment was based on one used in a numerical study by VanOverbeke and Holdeman [53]. A direct comparison between experimental smoke concentration profiles and numerical temperature profiles done by Tafti and Vanka [52] on the same basic configuration was then possible. A number of data sets at different forward velocities and model heights above the ground were generated.

3.1 Experimental Method

A method of flow visualization known as marker nephelometry was used to view the flowfield. Marker nephelometry is a technique used to detect concentrations of small particles (markers) in a fluid using reflected or refracted light. The technique used in this experiment is similar to one used by Borleteau [10], who used a laser sheet generated by a cylindrical lens to view a freon jet. In the present experiment, a planar laser sheet generated by a five watt argon-ion laser and a cylindrical lens was used to illuminate smoke particles of propylene glycol in the flowfield. The light scattered off the particles was viewed by a CCD (Charge-Coupled Device) video camera mounted normal to the laser sheet. Becker [9] has proven that in a flow containing marker particles that the intensity of reflected light in any small part of the flow is proportional to the number of

particles in that part of the flow. Since CCD cameras generally have a linear response to light intensity, the quantified intensity recorded by the camera was proportional to the smoke particle density. Details and theory of this technique can be found in Becker [9].

3.2 Experimental Apparatus

The experimental apparatus was designed around a four jet, two inlet model, shown in figure 3.1. It has the same dimensions, relative to the jet diameter, as that used in the example of predictions carried out by VanOverbeke and Holdeman [53]. The jet diameter (D_j) of the test model is 0.5 inch, while that employed in VanOverbeke and Holdeman [53] is roughly 1.5 inches; accordingly, all of the other dimensions of the test configuration have been scaled by the factor 0.333 relative to that of [53]. The jet velocity of the model was nominally set at 75 feet/second, yielding a Reynolds Number of about 20000 based on the jet diameter. Larger mass flow rates and thus jet velocities decreased the smoke concentration in the flow field to unusable amounts. Each of the four half-inch jets was preceded by a contraction section with an area ratio of 5 to 1. A set of screens and honeycomb just before the contraction removed large scale unsteady features in the flow. A velocity profile across the jet exit plane for a single half-inch jet is shown in figure 3.2. Jet velocities were measured at a static pressure port located just upstream of the contraction section in the nozzle of each jet. A Validyne pressure transducer was used to measure the static pressure at each jet in inches of water. The jet velocity could be calculated using Bernoulli's Equation and the continuity equation:

$$V_j = \sqrt{2 \frac{\Delta p}{\rho \left(1 - \left(\frac{A_j}{A_s} \right)^2 \right)}}$$

where A_j is the area of the jet, A_s is the cross sectional area at the static pressure port, and Δp the pressure change between the static pressure port and the jet exit. The quantity $(1-(A_j/A_s)^2)$ was theoretically 0.961 for each of the jets. To obtain an effective value, each of the jets was calibrated by measuring the dynamic pressure at the jet exit plane with a pitot probe and comparing this value to the static pressure at the port. This constant, the ratio of the static pressure over the dynamic pressure, was 1.05, due to pressure losses across the screens and honeycomb. So for this experiment,

$$V_j = \sqrt{2 \frac{\Delta p}{1.05 \rho}}$$

A direct measurement of smoke concentration was not possible using this method of marker nephelometry. All smoke concentration measurements were therefore normalized to the smoke concentration in the vicinity of the model jets, which was generally found to be the maximum smoke concentration in the flowfield as well. Accurate results required the smoke concentration at each of the jets had to be uniform with time. The smoke concentration for all four jets was also required to be nearly the same. This ensured that any unsteadiness in smoke concentration measurements did not result from unsteadiness in the jet smoke concentration. The smoke concentration in all four jets was nearly the same, as shown in figure 3.3, which shows smoke concentration profiles through both side jet pairs. The smoke concentration at the jets is generally constant with time, as seen in figure 3.4. The standard deviation of the smoke concentration for this case was only 4.7 counts with a mean of about 208. The variations in smoke concentration in the jets with time, and between jets, was small enough to provide accurate results for both analysis of unsteady flow features, and comparisons with numerical results.

The inlet was located 5 inches, or 10 jet diameters, forward from the front pair of jets, measured from the jet centerlines. The inlet measured 0.5 inches horizontally by 1.0 inches vertically, with the bottom of the inlet 0.25 inches from the base of the model from which the jets emanated. The distance between the ground and inlet, denoted H_i , was then 0.25 inches greater than the distance between the model and ground plane.

Figure 3.5 shows the complete experimental setup. The model was mounted in a small two-dimensional wind tunnel with an open section. A fan upstream of the model provided an airflow to simulate wind past the model in forward motion. A set of two screens and a honeycomb and a two-to-one contraction were utilized in this flow to remove most of the swirl and non-uniformity. The tunnel section measured 22 inches horizontally and 12 inches vertically. Velocities were measured using a Kanomax Anemometer constant temperature hot wire probe mounted just before the open test section. The hot wire was covered by a wire mesh screen to prevent damage. This also damped out small scale fluctuations in the velocity measurement. Velocity was measured every .125 seconds and a running average was displayed every second. The maximum velocity of airflow that could be generated was about 7.5 feet/second. This gave free stream-to-jet velocity ratios of up to 0.10. The mean velocity of the wind tunnel varied by about +/- 5 percent across the test section, as shown in figure 3.6.

The model was mounted in the test section with the jets pointing up towards a 30 inch by 30 inch glass ground plate serving as the ground plane in the test section. This resulted in a less complicated mounting and support structure for the model, and also allowed the flowfield to be viewed through the ground plane. The distance between the model and the ground plane could be adjusted over a distance between 0 and 14 jet diameters.

A single blower was utilized to supply air to the jet nozzles. The inlet to the blower was connected to the model inlets, which merged into a single duct. In this

manner, the inlet and the jet mass flows were essentially balanced. The velocity of each of the jets was controlled by means of a ball valve. An oil mister was used to generate smoke particles of propylene glycol. The smoke was injected between the blower and ball valves. Four feet of 1.25 inch diameter tubing were incorporated between the crossflow smoke injector location and the jets in order to provide adequate mixing distance. Except for a small proportion of the larger particles that tended to condense on the tubing walls, the low velocity in the tubing assured that the smoke was reasonably well mixed with air at entry to the jet.

A laser sheet was used to illuminate the smoke particles in the flow field. The laser sheet was generated using a five watt argon-ion laser and an optics train, shown in figure 3.7. The cylindrical lens could be rotated to create a horizontal (xz plane) or vertical (xy plane) laser sheet. The focusing lens allowed the laser sheet thickness to be minimized in the test section. The optics train and laser were mounted on a movable table, allowing the laser sheet to illuminate different planes. Three dimensional pictures and vertical smoke concentration images of the flow field could then be generated by combining several different planes of data.

3.3 Data Acquisition Method

Data were acquired using a Panasonic CCD video camera and recorded on video tape. Each 120 minute video tape contained data for one model height. The data stored on video tape was then played back and digitized by a Data Translation frame grabber. Software allowed single frames or multiple frame averages to be stored.

Figure 3.8 shows the data acquisition flowchart. A Panasonic CCD video camera was mounted to take pictures of the illuminated smoke particles in the flow field. The camera could be moved to view either a horizontal or vertical laser sheet illuminated flow field. Shutter speed was 1/30th of a second, with 574 horizontal by 499 vertical pixel resolution.

The images were sent to a Super VHS video recorder and stored on video tape. With 512 horizontal by 400 vertical pixel resolution, the Super VHS video recorder allowed data to be stored with less resolution loss than conventional video recorders, which only have 200 vertical pixel lines. Three video tapes were recorded for model heights of two, four, and six jet diameters above the ground plane. Each video tape contained data for one height. Ten forward speeds were tested, varying between 0 and .10 times the jet velocity. At each forward speed, 20 different horizontal laser sheet heights between the ground plane and model were recorded. Thirty seconds of data were recorded for each laser sheet height, allowing 127 frame averages to be taken of the data. A grid of one inch squares was recorded at the end of each set of 20 laser sheet heights, to be used in determining the scale of the recorded flow field.

A three dimensional picture of the time averaged flow field between the model and ground plane could then be generated for each forward speed. This time averaged flow field could then be compared to numerical data of the same flow field.

At the end of each video tape, smoke concentrations using a vertical laser sheet were recorded. Four different laser sheet locations were used: at the centerline of the model, the centerline of one pair of jets, the edge of the model, and 1.5 inches from the edge of the model. Only two forward speeds were used: $U/V_j = 0.03$, and $U/V_j = 0.09$. Images using a horizontal laser sheet 0.60 jet diameters from the ground plane with the inlet suction off at ten forward speeds were recorded as well. This particular height allowed the determination of the location of the ground vortex and forward vortex at all three model heights.

Video recorder playback of the video tapes was then sent to a Data Translation DT2851 high speed frame grabber. The frame grabber was capable of capturing an image at a sampling frequency of 10 MHz, giving the image a screen resolution of 512 horizontal by 480 vertical pixels. Eight bit analog to digital conversion at a sampling

frequency of 10 MHz allowed up to 256 different concentration values. Data Translation's IRIS data acquisition and processing program controlled the frame grabber and could average and store images to an IBM AT computer for later processing. Both single frames and 127 frame averages of the flow field were stored on the computer. The frame grabber could also be used to redisplay false color images in real time to an RGB display. A Data Translation DT2869 video board allowed false color data to be displayed on a standard television or stored to a video recorder.

Data Translation's IRIS program was also used to determine the location of the ground vortex and forward vortex pair. Individual pixel locations could be determined by moving a cross hair on the RGB monitor with the cursor keys. Using this cross hair, ground vortex and forward vortex pair locations were measured from the forward extent of these features in the 127 frame averaged images .6 jet diameters from the ground plane. Single frame images were used to determine these locations at low velocity ratios, since frame averaged data smeared the forward vortex pair and ground vortex into the background. Data was recorded for all three heights and ten forward speeds, with inlet suction both on and off.

Two other programs, RMSV and RMSH, were used to calculate mean and root-mean-squared smoke concentration from the video taped data at several locations in the flow. Mean and root-mean-squared (rms) smoke concentration were digitized using the frame grabber for certain columns and rows. Data was recorded for rows in the x-axis direction at the model centerline, side jet pair centerline ($z/D_j = 1.625$), model edge ($z/D_j = 2.5$), and 5.5 jet diameters from the model centerline. Data was recorded for columns in the z-axis direction at the upstream (forward) jet pair centerline ($x/D_j = 0$) and downstream (rear) jet pair centerline ($x/D_j = 6$). This data was then plotted using SIGMAPLOT, a commercial software plotting package.

The root-mean-squared measurements of the smoke concentration at several locations allowed at least some measure of the unsteadiness in the flowfield. Calculations of mean concentration were also used for comparison purposes with numerical data.

The mean concentration in the flowfield was defined as:

$$\bar{C} = \frac{\sum_{i=1}^N C_i}{N}$$

The rms (root-mean-squared) concentration was defined as:

$$c' = \left[\frac{\sum_{i=1}^N C_i^2 - \frac{1}{N} \left[\sum_{i=1}^N C_i \right]^2}{N-1} \right]^{1/2}$$

where:

\bar{C} = mean concentration

c' = rms concentration

N = number of frames

C_i = i^{th} instantaneous concentration

Some small scale fluctuations in the flowfield may not be seen in the flowfield due to the limitations of the measurement system. Fluctuations in smoke concentration smaller than the probe volume (0.04 inches) will be averaged out. Frequency fluctuations of greater than 15 Hz will also averaged out, since the camera exposure time was about 1/30th of a second for two interleaved frames. Therefore, the rms values may not represent the unsteadiness and turbulence in the flowfield in areas with small, high frequency fluctuations. These rms values do, however, give a good indication of the large scale unsteadiness associated with the ground vortex and forward vortex pairs.

Images stored on the IBM AT computer were processed a number of different ways. Figure 3.9 shows a generalized processing flowchart for most of the software used.

The programs HFSIGNS and VFSIGNS displayed smoke concentration versus horizontal (x-axis) or vertical (z-axis) pixel location respectively. Several different smoke concentration profiles could be displayed at once. Comparisons between smoke concentration profiles at the left and right jet pairs using HFSIGNS, for instance, were possible. Smoke concentration profiles of different files, along either x- (HFSIGNS) or z-axes, could also be compared. This allowed direct comparison between numerical and experimental results at several locations in the flowfield. Individual data sets could also be shifted in order to line up the origins of different files. The final results of the output on the screen could then be written to a file. This file was then plotted using SIGMAPLOT.

Data could also be uploaded to an Ardent computer. IRIS files of 20 different heights were converted, using the program CVTG, into a three dimensional picture of the flow field for use with NASA's PLOT3D program. PLOT3D files containing numerically generated flow fields could also be converted into IRIS files using the program RMCVT. This program scaled the numerical temperature profiles in amplitude and location, so that numerical temperature profiles and experimental smoke concentrations had the same scale and maximum amplitude. The resulting IRIS files were then downloaded for data processing on the IBM AT.

IRIS files could also be viewed in color on an EGA or VGA monitor using PAINTVGQ and PAINTRVP. Both programs had a 640 horizontal by 480 vertical pixel resolution in sixteen grey scales, allowing a full IRIS image file to be viewed. The resulting grey scale image could then be printed to a printer. PAINTRVP allowed the image files to be rotated 180 degrees, and was used on files containing images which

were generated using a vertical laser sheet. Since the experimental test model was mounted upside-down in the test section, this program was used to "right" the image.

HFTEC and VFTEC displayed smoke concentration versus horizontal or vertical pixel location, similar to HFSIGNS and VFSIGNS, except the output file was configured to operate using TECPLOT, another commercial plotting software package.

The program TECCVT converted IRIS files into TECPLOT files to generate two dimensional smoke concentration profiles. Data could be scaled to reflect actual dimensions rather than screen pixel location. TECPLOT allowed both grey scales and contour plots of individual files.

Using this experimental apparatus and technique, it was possible to obtain smoke concentration data that was directly comparable to numerically generated temperature profiles. This experimental apparatus could also be used to test a number of different model configurations, making the determination of the temperature environment around a STOVL configuration relatively easily.

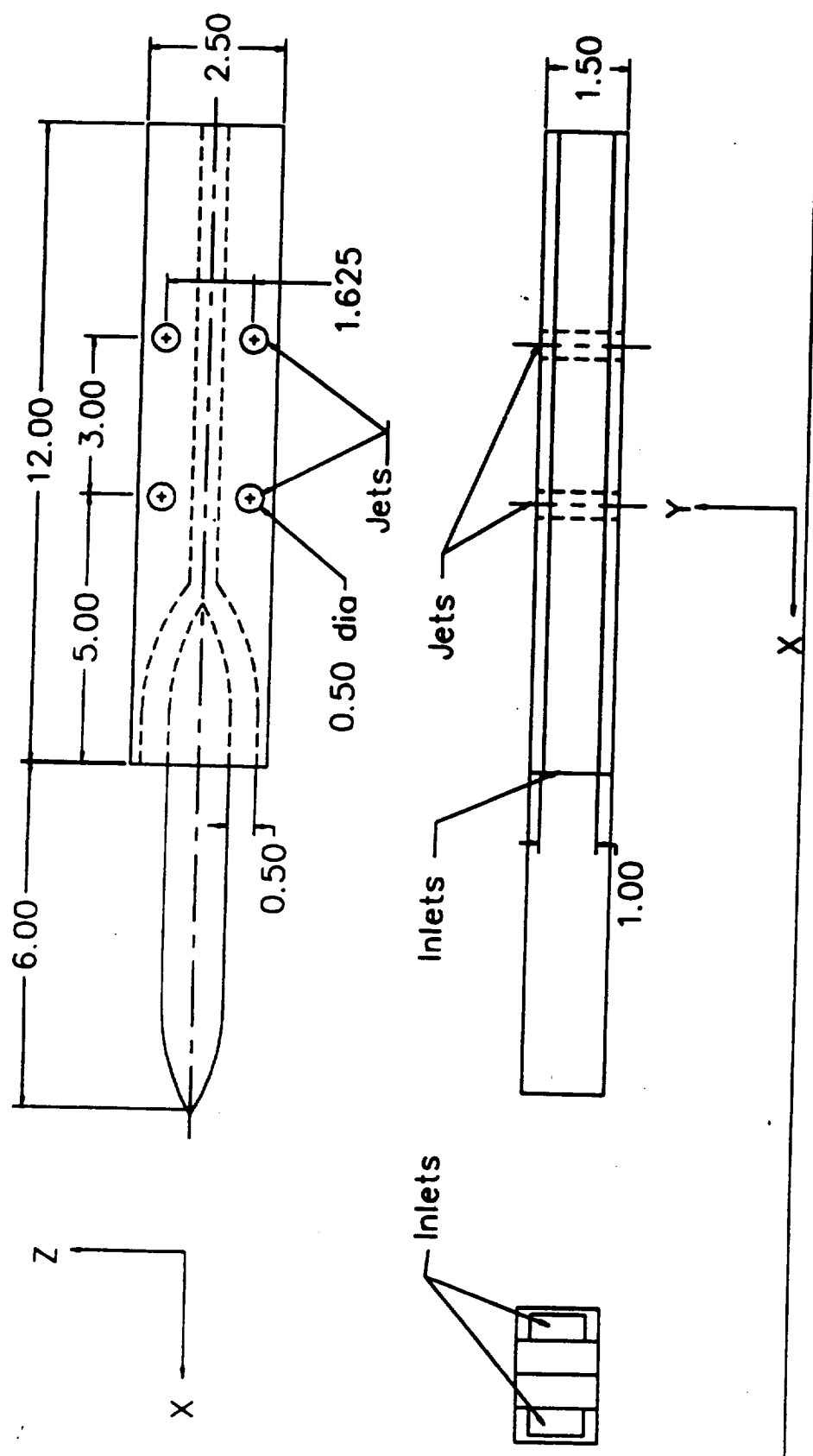


Figure 3.1: Test Model

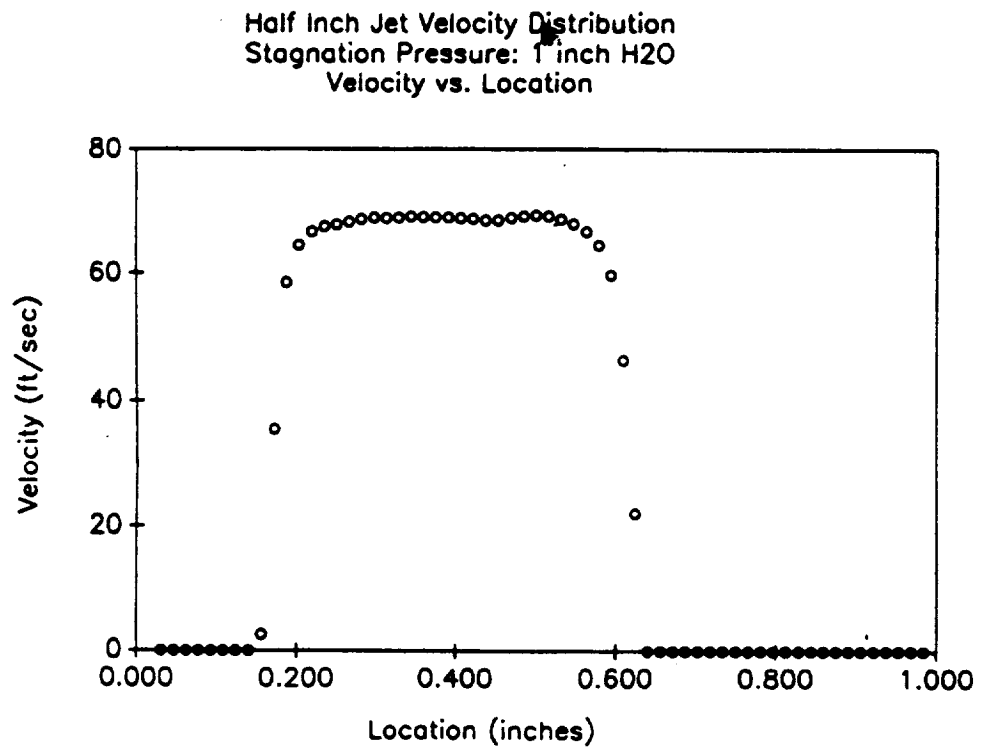


Figure 3.2: Jet Velocity Profile

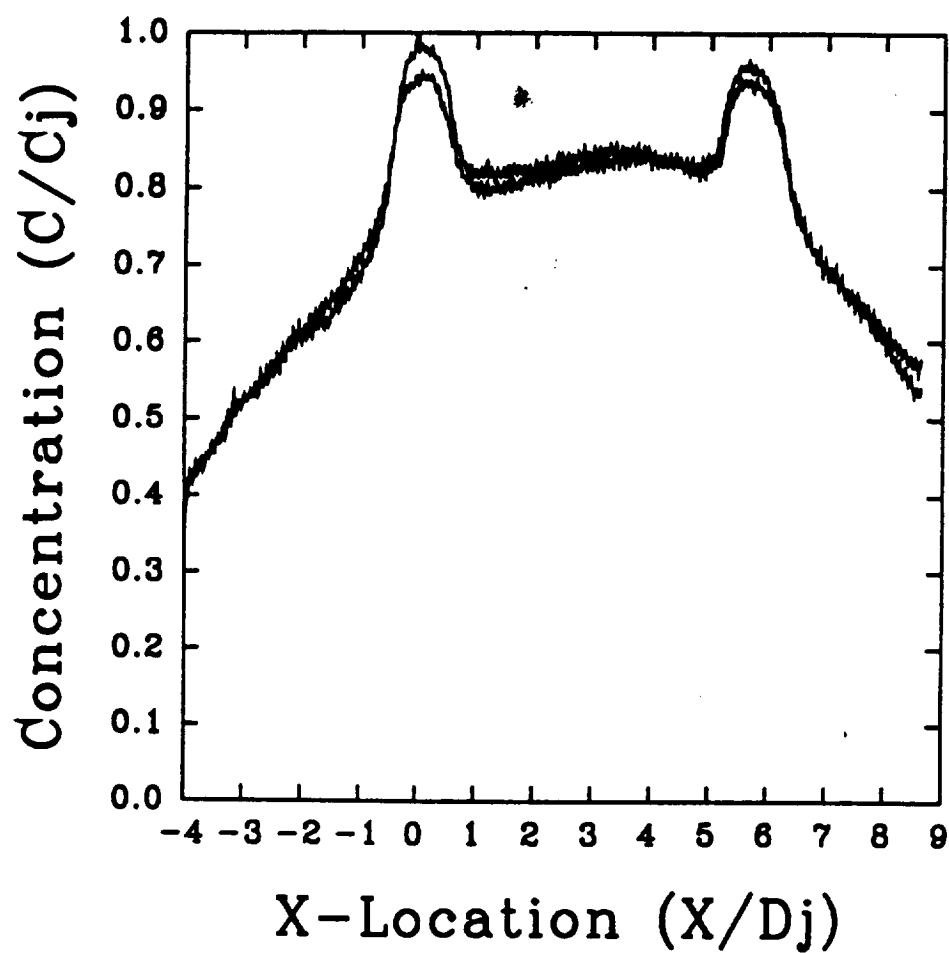


Figure 3.3: Smoke Concentration Profiles Through Side Jet Centerlines at Jet Exit Plane

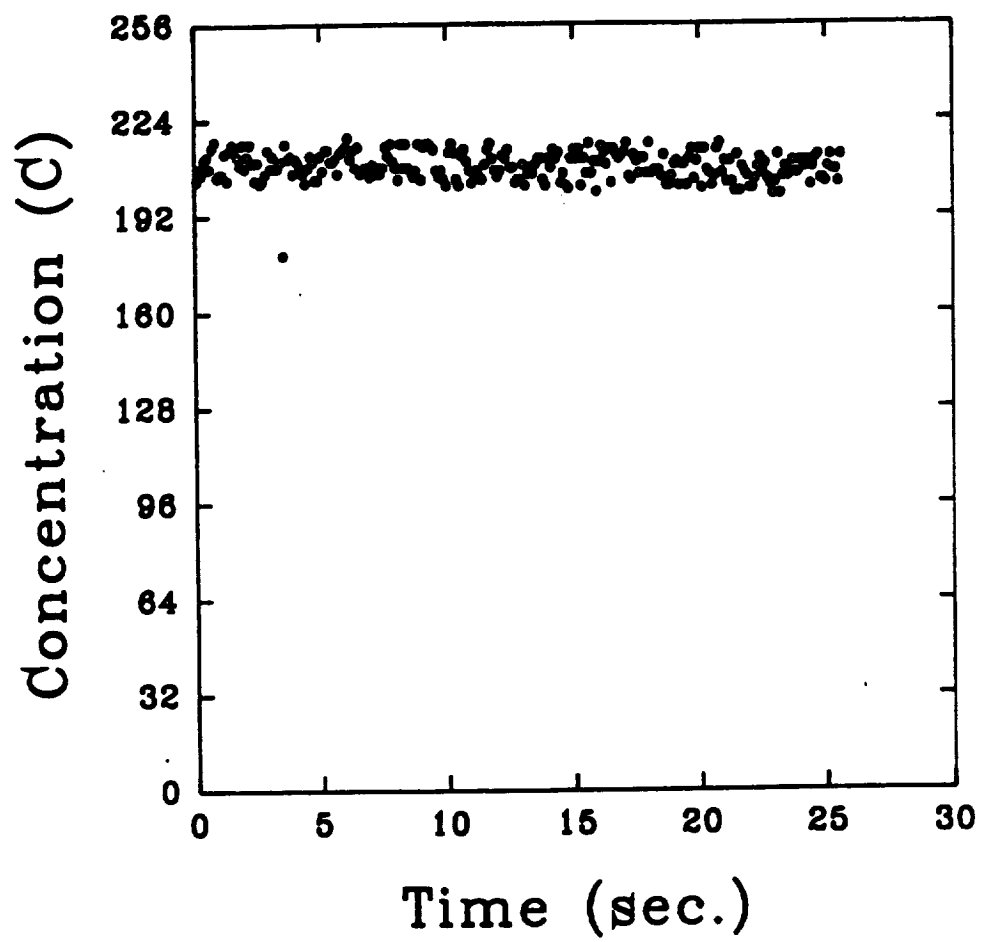


Figure 3.4: Smoke Concentration Variation With Time at Jet Exit

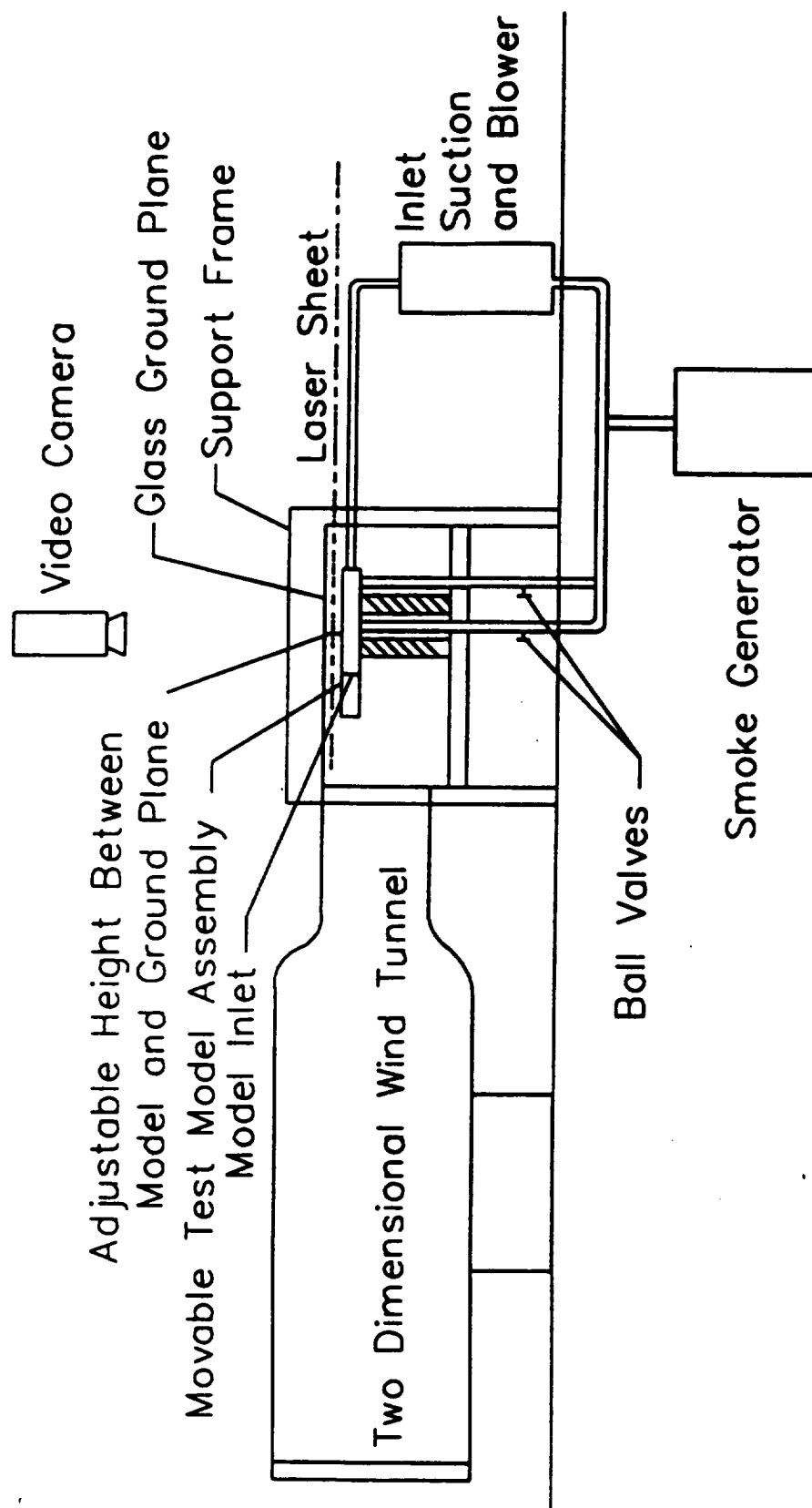


Figure 3.5: Experimental Setup

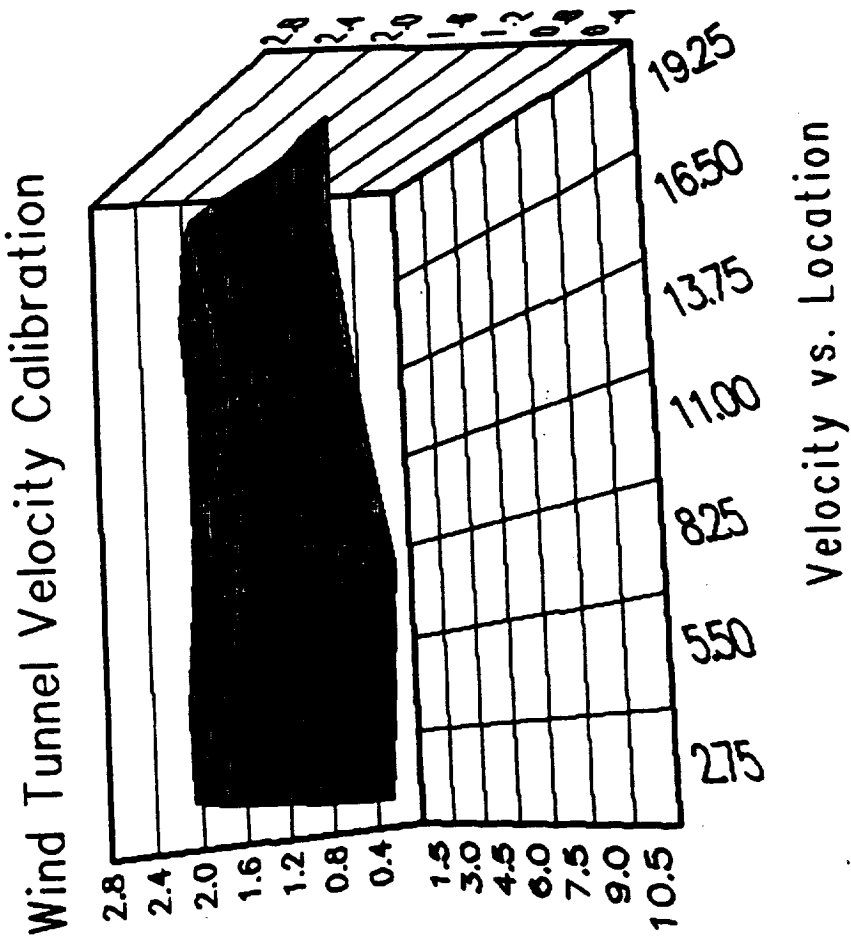


Figure 3.6: Wind Tunnel Velocity Distribution

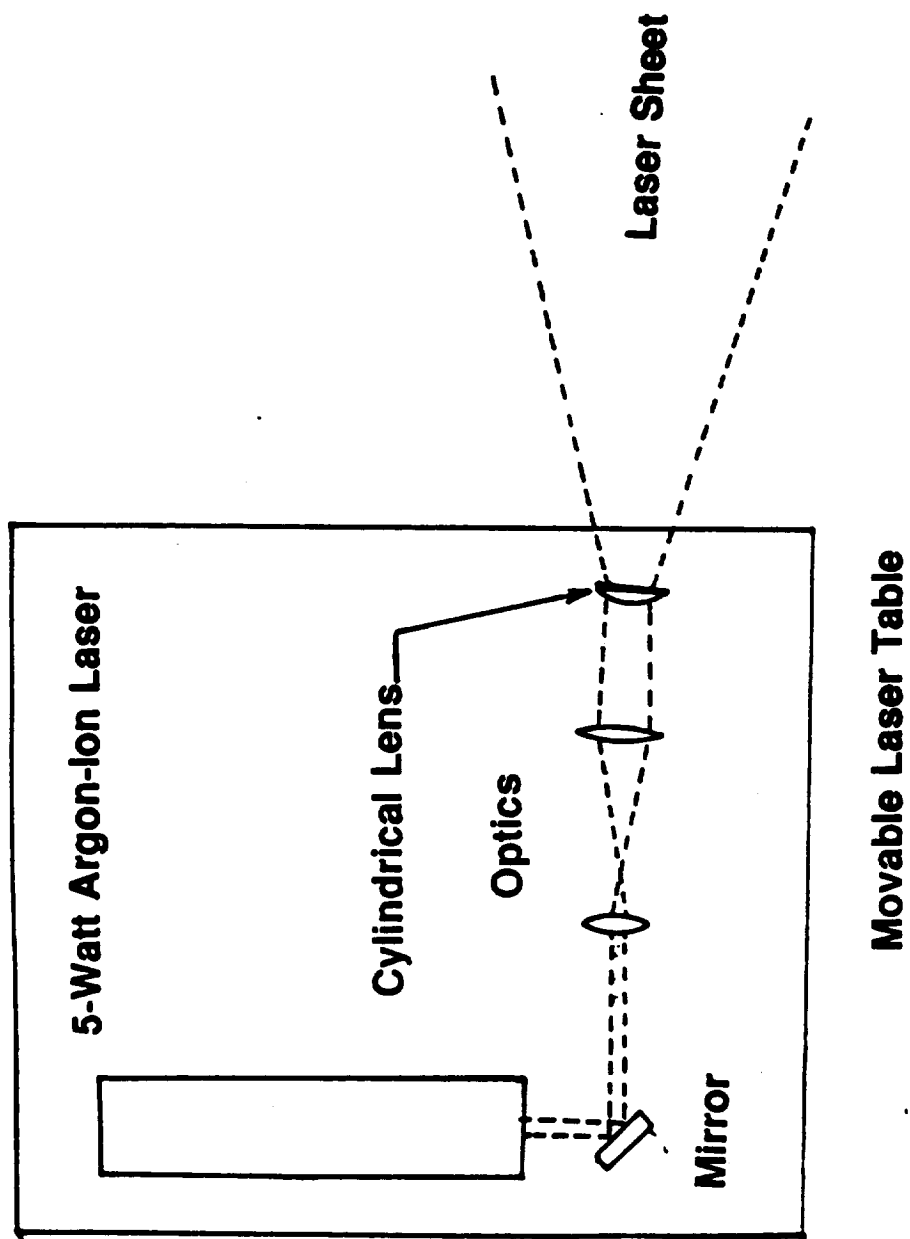


Figure 3.7: Laser and Laser Sheet Optics

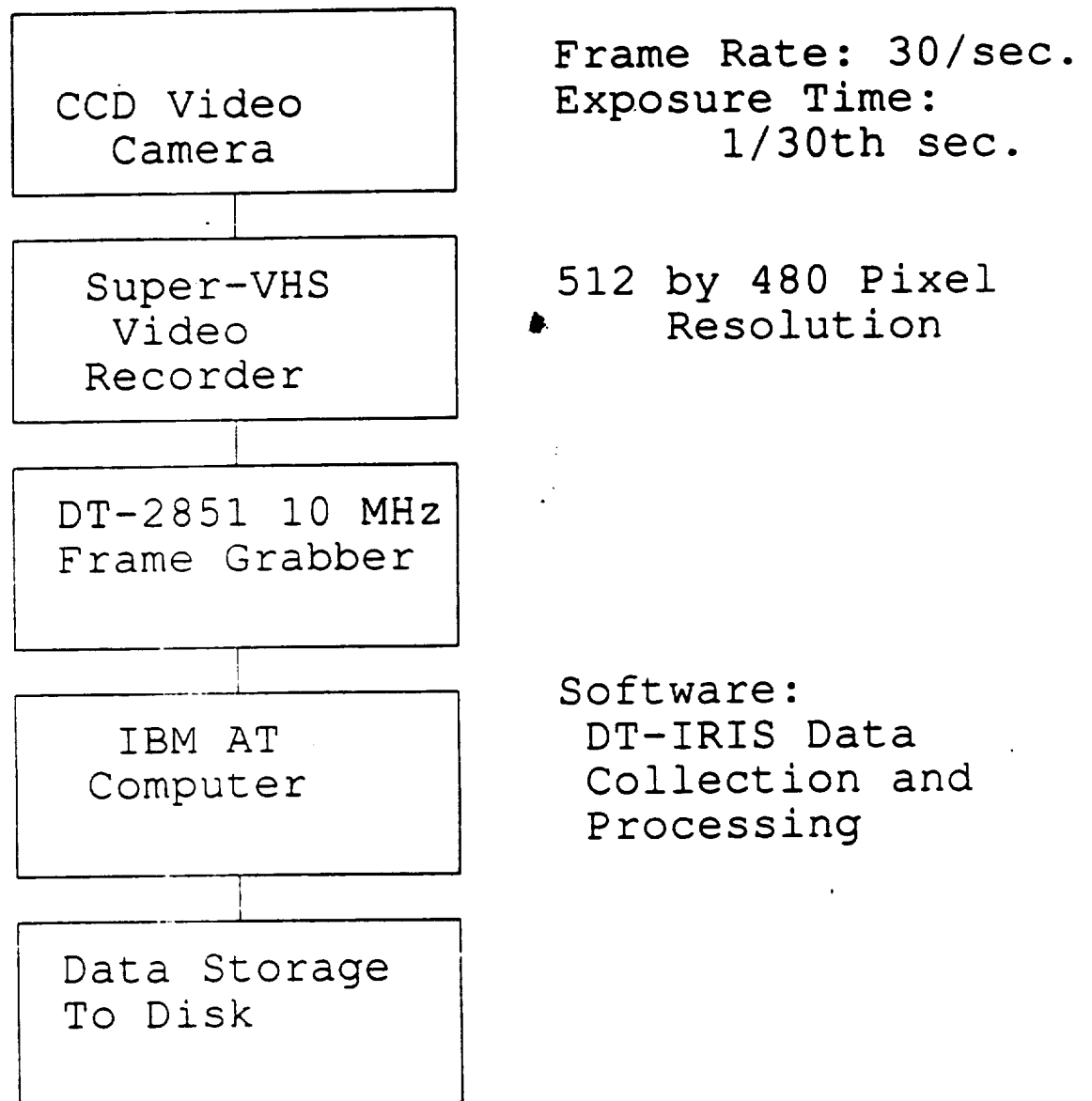


Figure 3.8: Data Acquisition Flowchart

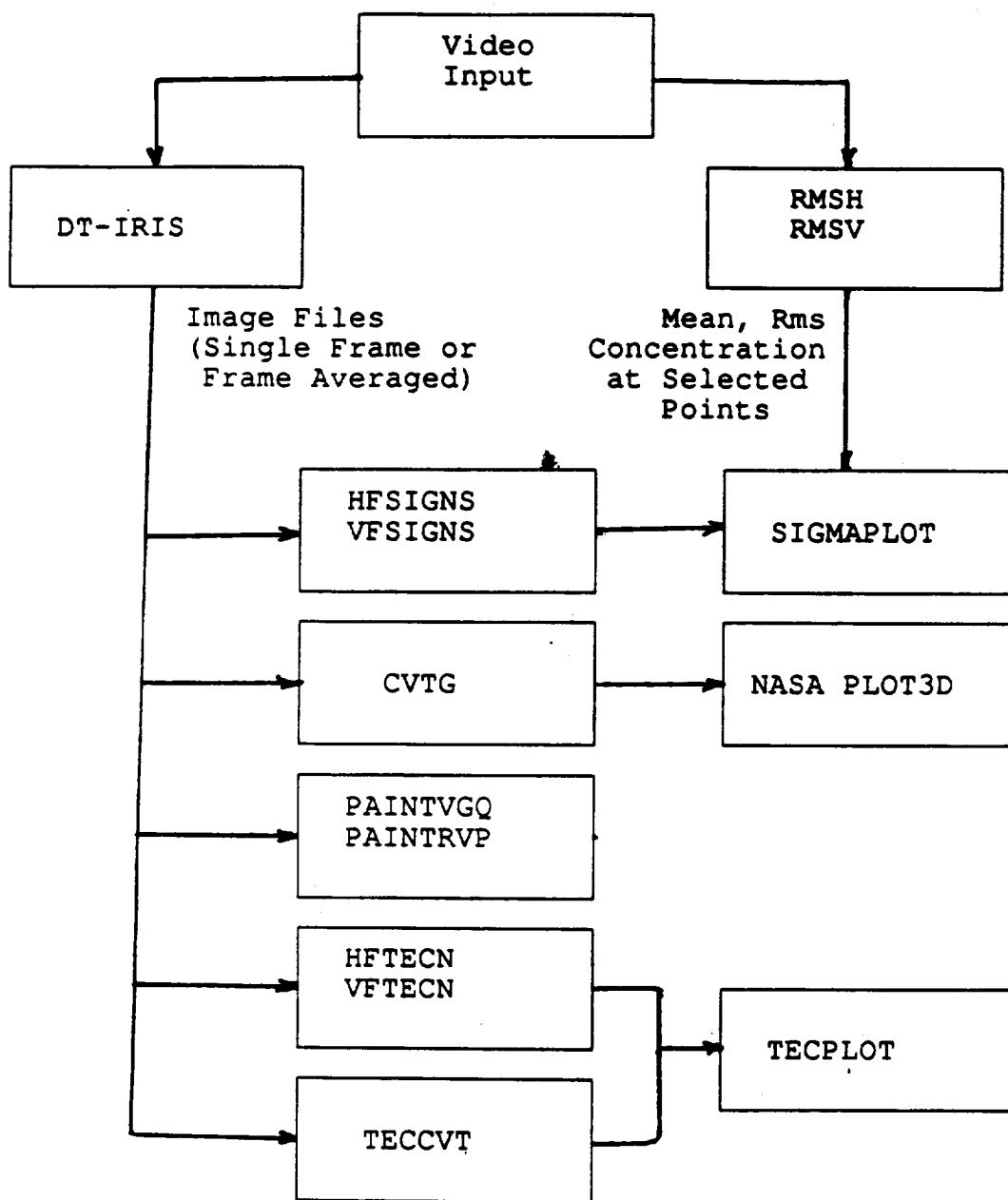


Figure 3.9: Data Analysis Software Flowchart

4. EXPERIMENTAL RESULTS

The flowfield around the model has a number of interesting features. Most of these features are associated with vortex flows, and show some unsteadiness.

In the following, we first illustrate the formation of four types of vortical structures: the ground vortex, located where the wall jet meets the free stream flow; the forward vortex pair, located at the stagnation point between the free stream flow and fountain flow; the vortex pair located between the fountain and jets in the inner flow region; and the second ground vortex associated with the rear pair of jets, located where flow from the wall jet associated with the rear pair of jets meets the wall jet associated with the front pair of jets and the free stream flow. Unsteadiness in the flow causes the presence of such structures to be somewhat blurred in frame-averaging. Measurements of root-mean-squared (rms) concentration show some of the large scale unsteadiness in the flow in the region near the ground vortex and forward vortex pair. Other unsteadiness exists in the flow, but due to limitations in the measurement system, is not seen in rms concentration measurements.

The vortex features in the flow are also influenced by the velocity ratio. This is seen in single frame, time averaged, and rms plots of concentration. The ground to model height and inlet suction also appear to be major factors in influencing the flow structure for this particular configuration.

4.1 Vortical Structures in the Flowfield

Presented first are examples of the basic flow features seen in the flowfield, for a velocity ratio of 0.09 and a model height of 4 jet diameters. In section 4.1.2, mean

concentration profiles and rms concentration profiles at selected areas in the flowfield will be presented.

4.1.1 Illustration of Vortex Structures

The four types of vortex structures described in section 1.1 are shown in figures 4.1 through 4.5. Figure 4.1 shows two of the features in an image of the smoke concentration in the flowfield using a horizontal laser sheet located midway between the ground plane and the model. Figures 4.2 through 4.5 show the other flow features in vertical planes 5.5 jet diameters from the model centerline, at the model edge (2.5 jet diameters from the model centerline), through the side jet pair centerline, and through the model centerline, all at a velocity ratio of .09 and a model height of 4 jet diameters. Figures 4.6 and 4.7 show images of the flowfield illuminated by a laser sheet located at the ground plane and model undersurface respectively. Figures 4.8 through 4.10 show frame-averaged images of the ground, mid, and body planes respectively.

One of the two features visible in figure 4.1 is the formation of the horseshoe ground vortex in the ground plane. A cross-section of the vortex can be seen in profile in figure 4.2 at a plane located 5.5 jet diameters from the model centerline. It has been seen in experiments by Colin and Olivari [17] investigating single jets in cross flows. This feature has also been seen in operations with the Harrier. Unlike the single jet case, where one obtains a continuous horseshoe vortex, the ground vortex is bisected in the four poster case by flow moving radially outward along the stagnation (or the center) line between the two forward jets. The behavior of the two branches of the ground vortex in relation to the outward flow between the jets is then determined by the ratio U/V_j .

The second major feature visible in figure 4.1 is the pair of vortices referred to as the forward vortex pair, formed where flow moving radially outward along the stagnation line between the two forward jets meets the free stream flow. This feature is located in the stagnation region of the two flows. The forward vortex pair is normal to

the ground plane and is found to be unsteady in the movie, with the size and location of each vortex changing rapidly.

A third feature visible in figure 4.2 is the second ground vortex associated with the downstream pair of jets. The second ground vortex eventually merges into the inner flowfield, and connects with the vortex pair between the fountain and jets. Also visible is the wall jet, which creates both ground vortices where it interacts with the free stream.

The fourth feature, caused by interactions between the fountain and jets, can be seen in figure 4.3, which is a vertical plane located at the edge of the model, 2.5 jet diameters from the centerline of the model. This feature is caused by the impingement of the fountain on the model and entrainment of the resulting flow field by the jets. This is evident as two counter rotating vortices between the jets and fountain. These two vortices propagate out of the inner flow region between the jets crosswise into the free stream flow, and connect with the ground vortex associated with the downstream pair of jets. This feature is similar to one seen by Hall [25] and Saripalli [44] in twin jet configurations. It is only seen at low model heights and low forward wind velocities.

Figure 4.4 is a vertical plane located through the centerline of the jets, 1.625 jet diameters from the centerline of the model. This shows the fountain, jets, and counter-rotating vortices caused by the jets and fountain interacting. Figure 4.5 is at the centerline of the model for the same model height and velocity ratio. The centerline plane is located right at the fountain, and does not show many features. This is expected, since the centerline plane lies on a plane of symmetry through the fountain. The lack of flowfield features may also be due to the camera averaging out portions of the unsteadiness in the flow.

Figure 4.6 shows the ground plane. The forward vortex pair is visible in profile, and is anchored to the ground plane. The four jets are clearly visible in the flowfield. The wall jet is responsible for the broad area of smoke concentration outside the jets, and

covers a large area in the flowfield. The fountain is also visible in between the jets, especially the high concentration regions where flow from adjacent jets meet.

Figure 4.7 shows a horizontal plane located close to the model. The forward vortex pair is much less visible, and in this case, appears to be sucked into the inlets. The four jets are much more distinct than at the ground plane, and the fountain is much less distinct.

Figures 4.8 through 4.10 show 127 frame averages of the flowfield. Figure 4.8 shows a horizontal plane located close to the ground plane. Comparing this figure to figure 4.6 shows that the forward vortex pair has become smeared. The four jets and fountain structure are still clearly visible. Figure 4.9 shows a horizontal plane midway between the ground plane and model. Again, frame averaging has smeared the structure in both the ground vortex and forward vortex pair. This is also seen in figure 4.10, at a horizontal plane closest to the model body.

4.1.2 Mean and RMS Concentration Measurements

Presented next are mean and rms concentration measurements at the ground plane, mid plane and body plane at selected locations. The x-axis in the plots are measured positive downstream, so the free stream is coming from the left. The x-axis origin for all rms and mean concentration plots is located through the centerline of the forward pair of jets. The inlet is located ten jet diameters upstream (at -10), and the centerline of the rear pair of jets is located six jet diameters downstream of the origin. The z-axis origin is located at the centerline of the model. Side jets are located at ± 1.625 jet diameters from the origin. Since the flowfield is generally symmetric, no distinction is generally made between left and right sides. Measurements of mean and rms concentration were made, for each plane, through the model centerline, through the left side jet centerline, at the edge of the model (2.5 jet diameters from the model centerline), and 5.5 jet

diameters from the model centerline. Plots across the forward and rear jet pair centerline are also presented.

Some small scale fluctuations in the flowfield may not be seen due to the limitations of the measurement system. Fluctuations smaller than the probe volume (0.04 inches) will be averaged out. Turbulent flow with frequencies of greater than 15 Hz will also be averaged out, since the camera exposure time is about 1/30th of a second for two interleaved frames. Therefore, the root-mean squared (rms) concentration values may not represent the unsteadiness and turbulence in the flowfield in areas with small, high frequency fluctuations. These rms concentration values do, however, give a good indication of the large scale unsteadiness associated with the ground vortex and forward vortex pairs.

Most of the peaks in root-mean-squared (rms) concentration can be associated with flowfield features such as the ground vortex, second ground vortex, forward vortex pair, and fountain. Some of the other large peaks in rms concentration can be associated with interactions between the free stream velocity and jets. These peaks are especially visible in plots of mean and rms concentration which are oriented across the forward and rear jet pairs.

4.1.2.1 Mean and RMS Concentration at the Ground Plane.

Figures 4.11 through 4.16 show profiles of mean and rms concentration at the ground plane. Mean and rms profiles are shown first oriented along the x-axis through the model centerline, side jet pair centerline, model edge, and 5.5 jet diameters from the model centerline. Next, mean and rms profiles are shown oriented along the z-axis at the forward and rear jet pair centerline. Figure 4.6 shows a single frame, and figure 4.8 a 127 frame average at the ground plane for the same conditions in figures 4.11 through 4.16.

Figure 4.11 shows a profile of the mean concentration and rms concentrations through the centerline of the model for a velocity ratio (U/V_j) of 0.09 with a model height of 4 jet diameters. The horizontal laser sheet is located at the ground plane. The mean concentration, represented by the solid line and scale on the left, has been normalized to the maximum concentration in the flowfield (C_j), assumed to be at the jets. The rms concentration, represented by the dashed line, has also been divided by the maximum concentration. The peak in mean concentration is located at the center of the fountain. The peak in rms concentration corresponds to the area of the flowfield near the stagnation region between the free stream and forward flow associated with the fountain. This area is also the location of the forward vortex pair.

Figure 4.12 shows both mean and rms concentration profiles through the jet centerline. The laser sheet is located near the ground plane. A peak in rms concentration occurs in the region where the free stream flow stagnates against the flow from the jets. This area again corresponds to the location of the ground vortex and forward vortex pairs. Another small peak in rms occurs just in front of the forward jet, located at the x axis origin. This may be caused by unsteady mixing between the free stream flow and jet flow. The two large peaks in the mean concentration plot (solid line) correspond to the two side jets. The smaller peak in mean concentration between the two jets is located in the fountain region, where wall jets from the two impinging jets meet.

Similar features are seen in figure 4.13, a concentration profile located at the edge of the model, 2.5 jet diameters from the centerline. The forward rms concentration peak associated with the forward vortex pair and ground vortex is visible, as well as a small peak in rms concentration in front of the forward jets, which is similar to that seen in figure 4.12. Also visible in figure 4.13 is a small peak in rms concentration just upstream of the rear pair of jets. This corresponds to the location of the ground vortex associated with the downstream pair of jets. This rms concentration peak is much more

visible in figure 4.14, a profile located 5.5 jet diameters from the model centerline. Peaks of mean and rms concentration associated with the ground vortex are visible, as well as rms and mean concentration peaks associated with the second downstream ground vortex. The rms concentration peak associated with the forward pair of jets, and seen in figures 4.12 and 4.13, is no longer visible.

Figure 4.15 shows a profile across the forward pair of jets at the ground plane. The two large peaks in the mean concentration are located where the jets impact the ground plane. The two small peaks in the rms concentration just outside the jets may be caused by mixing between the free stream flow and jet flow. Figure 4.16, a profile across the rear pair of jets, shows similar trends, except the two peaks in the rms concentration outside the jets are much broader. The broad areas of high rms show only some of the turbulence and unsteadiness in the wall jet.

4.1.2.2 Mean and RMS Concentration at the Mid Plane.

Figures 4.17 through 4.22 show profiles of mean and rms concentration at the mid plane. Mean and rms concentration profiles are shown first oriented along the x-axis through the model centerline, side jet pair centerline, model edge, and 5.5 jet diameters from the model centerline. Next, mean and rms profiles are shown oriented along the z-axis at the forward and rear jet pair centerline. Figure 4.1 shows a single frame of the flowfield associated with these plots, and figure 4.9 a 127 frame average at the mid plane.

Figure 4.17 shows mean and rms concentration plots along the centerline of the model, with the laser sheet located midway between the ground plane and model. This figure shows features similar to those seen at the ground plane. There is a central peak in mean concentration corresponding to the location of the fountain. Measurements of rms concentration show a peak similar to the one seen in figure 4.11, located at the stagnation area between the free stream and fountain, corresponding to the location of the

forward vortex pair. The amplitude of the rms concentration is greater than at the ground plane.

Figure 4.18 shows mean and rms concentration profiles through the jet centerline, with the laser sheet again located midway between the ground plane and model. The two peaks in concentration correspond to the jet locations. The peak in rms concentration located near $X/D_j = -15$ is similar to the one seen at the forward edge of the flow at the ground plane in figure 4.12. A second, sharp peak is located just forward of the front jet, and probably represents an area where entrainment occurs. This peak is much sharper than the one in front of the jet at the ground plane, in figure 4.13. The general level of rms concentration is much greater than at the ground plane in figure 4.12, especially outside of the inner flow region. This suggests that more large-scale unsteady flow is occurring at the mid plane.

Figure 4.19 shows mean and rms concentration profiles at the edge of the model, 2.5 jet diameters from the centerline. The laser sheet is again located at a plane located midway between the ground plane and the model. A broad region of high rms concentration is located in the region corresponding to the ground vortex and forward vortex pair. A peak in rms concentration just forward of the front jet location is similar to that seen in figure 4.18 at the jet plane. Unlike figure 4.18, a small peak in rms concentration occurs just forward of the rear jet, located at $X/D_j = -6$. A large rms concentration peak occurs in the region where the ground vortex interacts with the free stream, again similar to figure 4.18. The level of rms concentration is again much greater than in figure 4.13, located at the ground plane.

Figure 4.20 shows mean and rms concentration profiles located 5.5 jet diameters from the centerline of the model, with the laser sheet midway between the model and ground plane. This plot is much different than figure 4.14, located at the ground plane. The two peaks in mean concentration correspond to the ground vortex (forward peak), and

the second ground vortex associated with the rear pair of jets (rear peak). The peaks in rms concentration located forward of each ground vortex peak correspond to the area of interaction between the free stream and vortices.

Figure 4.21 shows mean and rms concentration plots across the forward pair of jets, again with the laser sheet located midway between the ground plane and model. The two large peaks in mean concentration correspond to the two forward jets. Peaks in rms concentration occur just outside the jets, where areas of entrainment and mixing occur between the jets and free stream. Turbulent flow around the jets also may cause these peaks. Figure 4.22 shows similar trends at the rear pair of jets, but with the rms peaks much broader and lower. Both these figures have different rms concentration distributions in comparison to figures 4.15 and 4.16, located at the ground plane, where the wall jet removes most of the interactions.

4.1.2.3 Mean and RMS Concentration at the Model.

Figures 4.23 through 4.29 are of mean and rms concentration plots with the laser sheet located at the plane closest to the model, for a model height of 4 jet diameters and a velocity ratio of 0.09. Figure 4.10 shows the mean concentration and figure 4.7 a single frame of the flowfield for the same conditions as figures 4.23 through 4.29.

Figure 4.23 shows mean and rms concentration profiles through the centerline of the model, with the laser sheet close to the model. There is a peak in rms concentration near the forward edge of the flow which corresponds to the stagnation region between the free stream flow and the fountain, similar to figure 4.11 at the ground plane. This again corresponds to the location of the forward vortex pair and ground vortex. The second peak in rms concentration just downstream of this peak may be due to interaction between the free stream flow and fountain flow which follows the model underside. This underside fountain flow is the mechanism which may cause near field hot gas ingestion.

Figure 4.24 shows mean and rms concentration plots through the model jet centerline. The two peaks in mean concentration correspond to the jets. Unlike the ground and midplane rms concentration profiles, the plane closest to the model shows no distinct central peak at the forward edge of the mean concentration rise. The absence of rms concentration peaks in this region suggests that the flow at the model body is not greatly influenced by the forward vortex pair or ground vortex. Flow along the model underside may be responsible for these flow conditions. The decrease in rms concentration values in between the jets may again be due to the inability of the measurement system to resolve small, high speed turbulent and unsteady flow structures. Large scale unsteadiness in the flow increases downstream of the jets. Comparison to figure 4.18 at the mid plane show some similarities between the two flows, with the exception of a distinct forward peak corresponding to the ground vortex and forward vortex pair positions.

The edge plane, 2.5 jet diameters from the centerline, is shown in figure 4.25. The broad peak in mean concentration represents flow moving out of the inner flow region between the jets. Measurements of rms concentration are nearly the same order of magnitude as the mean concentration measurements outside the inner region. This flow pattern is similar to that of figures 4.13 and 4.19, located at the ground and mid planes respectively. Like these two figures, figure 4.25 has a small peak in rms concentration just forward of the front jet. Some other peaks in rms concentration are missing, such as the peak associated with the forward edge of the ground vortex. Due to the distance from the ground plane, figure 4.25 may not show flow patterns due to the ground vortex or forward vortex pair. Instead, most flow mean and rms concentration measurements are probably due to flow movement along the model underside.

Figure 4.26 shows mean and rms concentration profiles located 5.5 jet diameters from the centerline. Like figures 4.14 and 4.20 at the ground and mid planes

respectively, the two peaks in mean concentration correspond to the ground vortex and second ground vortex. Peaks in rms concentration also occur in these regions. Due to the distance from the ground plane, only the tops of the two ground vortices are actually seen, and the peaks in rms concentration are centered over the peaks in concentration. The rms concentration measurements are also on the same order of magnitude as the mean concentration values.

Figures 4.27 and 4.28 show mean and rms concentration profiles across the front and rear pairs of jets respectively. The two peaks in mean concentration correspond to the jet locations. The peaks in rms concentration are similar to those seen at the mid plane in figures 4.21 and 4.22. Free stream flow is mixing with flow from the region between the jets, causing unsteady structures to form. Flow moving around the jets may also act similar to flow around circular cylinders. Where separation occurs around the cylinder edges, unsteady flow structures result.

4.2 Effects of Forward Velocity on Vortex Structures

Most of the flowfield structures are changed by changing the forward velocity. In the following, changes to the size and shape of the vortex structures in the flowfield are illustrated. Mean and rms concentration measurements are also shown at the ground plane, and are compared to results from the previous section. All plots are shown for a velocity ratio of 0.03 and a model height of 4 jet diameters.

4.2.1 Illustration of Vortex Structures

The characteristics of the vortex structures in the flowfield are changed by changing the forward velocity ratios. Illustrations of the ground vortex and forward vortex pair at a velocity ratio of 0.03 are shown in figures 4.29 and 4.30. The variation of ground vortex and forward vortex pair locations are then shown in figures 4.31 and

4.32. Next, results are shown of the other vortex structures. Finally, frame averaged images of the flowfield at the ground, mid and body planes are displayed.

The distance between the ground vortex and forward pair of jets increases as the velocity ratio decreases. Figure 4.29 shows a single frame with a velocity ratio (U/V_j) of 0.03. The model is four jet diameters above the ground plane, with the laser sheet two jet diameters from the ground plane. A comparison with figure 4.1 shows several differences if scale is taken into account. The ground vortex, in addition to being further from the forward pair of jets, has been visibly entrained by the radial flow from the fountain region between the two jets. In some cases, it has been observed to actually wrap around into the forward vortex pair at these low velocity ratios. Figure 4.30 shows the ground vortex in profile 5.5 jet diameters from the centerline of the model. Comparing this figure to figure 4.2, and accounting for differences in camera magnification, it can be seen that the ground vortex size is not greatly influenced by the velocity ratio.

At lower velocity ratios, the forward vortex pair merges almost completely with the background in the 127-frame averages of the flow field, although it is still visible in single frame pictures of the same flow field. Figure 4.29 shows the forward vortex pair for U/V_j of 0.03 with the laser sheet at the mid plane, two jet diameters above the ground plane. Comparing this figure to figure 4.1 shows that the forward vortex pair becomes much larger at lower forward velocity ratios. In addition, the location of the forward vortex pair seems to become much more variable as observed in videos of the flowfield. This may partially be due to variations in the free stream velocity at such low velocity ratios.

Figures 4.31 and 4.32 show the variation of the ground vortex and forward vortex pair locations relative to the forward pair of jets for various velocity ratios at a height of four jet diameters. These locations are measured from the forward edge of the

ground vortex and forward vortex pair in the frame averaged images. In some cases, the forward edge of the ground vortex and forward vortex pair was estimated using single frame pictures for low velocity ratios. In these cases, the ground vortex and forward vortex pair merged with the background in frame averaged images.

The ground vortex associated with the second pair of jets is also visible in figure 4.30. It is very similar to the one seen in figure 4.2. Figure 4.33, showing a vertical laser sheet at the edge of the model, or 2.5 jet diameters from the centerline of the model, does not show the second ground vortex at a velocity ratio of 0.03. Instead, the vortex pair between the fountain and jets has moved out of the inner flow region, and its structure is much more visible. Figure 4.34 shows a similar plot through the centerline of the jets, 1.625 jet diameters from the model centerline. The vortex pair between the fountain and jets is visible, and is much more evident than in figure 4.4.

The forward vortex pair and fountain structure are visible at the ground plane in figure 4.35. The velocity ratio is 0.03. Comparing this figure to figure 4.6 shows that the forward vortex pair has become much larger and more diffuse. In figure 4.36, a 127 frame average at the ground plane, the forward vortex pair and parts of the ground vortex have been smeared into the background due to the unsteadiness and low smoke concentration in these areas. Figure 4.37, a 127 frame average at the centerline plane at a velocity ratio of 0.03, shows the smoke concentration in the ground vortex much lower than in figure 4.9, which has a velocity ratio of 0.09. The second ground vortex, associated with the rear pair of jets, extends much further out than in figure 4.9 as well. Similar trends are seen in figure 4.38, with the laser sheet located close to the model.

4.2.2 Mean and RMS Concentration Measurements

Presented next are plots of the mean and rms concentration at the ground plane for a velocity ratio of 0.03 and a model height of four jet diameters. Results are

presented for profiles along the model centerline, side jet centerline, model edge, and 5.5 jet diameters from the model edge.

Figure 4.39 shows mean and rms concentration plots through the model centerline, normalized to the maximum concentration in the flowfield, and rms concentration, divided by the maximum concentration in the flowfield. The laser sheet in this case is located at the ground plane, with the model four jet diameters from the ground plane and a velocity ratio of 0.03. The sharp peak in mean concentration is in the fountain region, similar to figure 4.11. The peak in rms concentration, however, is much broader and shallower than in figure 4.11. Also, the mean concentration only gradually drops off. This may be due to the larger size of the forward vortex pair, which may have a larger variation in location, as well as a lower smoke concentration. Figure 4.40 shows similar comparisons with 4.12 at a plane through the jet centerline. The forward peak in rms is lower and much broader than at a velocity ratio of 0.09. There is still a peak in front of the forward jet, but it is not as prominent. Plots outside the inner flow show very little variation at all. Much of the unsteadiness in the flow may be missing, due to the limitations on the measurement system. Figures 4.41 and 4.42 show mean concentration and rms plots 2.5 and 5.5 jet diameters from the model centerline respectively. These two plots show almost no variation in rms concentration at a velocity ratio of 0.03.

4.3 Effect of Model Height Variation on the Flowfield

Changes in the model height with respect to the ground plane produce changes in the flowfield. Most of the vortex structures are affected by changes in model height. Mean and rms concentration profiles also show some changes in flow structure, although there are still large similarities between the structures seen at all three heights. General trends seen in the flowfield by increasing model height are also discussed.

4.3.1 Effect of Height Variation on Vortex Structures

At lower velocity ratios, it appears that the ground vortex and forward vortex pair locations depend on the height of the test model above the ground. Figures 4.43, 4.44, and 4.45 show the flowfield with a laser sheet located at the ground plane and a velocity ratio of 0.03 at heights of 2, 4, and 6 jet diameters respectively. Taking into account the variation in camera magnification, the ground vortex and forward vortex pair locations decrease with decreasing model height. The variation of ground vortex location relative to the forward pair of jets with model height for various velocity ratios is shown in figure 4.46. The ground vortex location increases with increasing model height for low velocity ratios. At high velocity ratios, the ground vortex location appears to be independent of model height. Another interesting thing to note is that at a model height of two jet diameters, the ground vortex is located very near the inlet for all the velocity ratios tested here. This suggests, that at low model heights, the ground vortex location is influenced by inlet suction.

A similar trend is noticed for the forward vortex pair. Figure 4.47 shows the forward vortex pair location relative to the forward pair of jets versus velocity ratio for the three model heights tested. The trends in forward vortex pair location are similar to the ground vortex, but the forward vortex pair does not appear as greatly influenced by suction at lower model heights.

For lower velocity ratios, some of the flowfield structures change, as well as the ground vortex and forward vortex pair locations. Figures 4.43, 4.44, and 4.45 also show some of the changes in size and shape of the flowfield structures. At a model height of two jet diameters, the forward vortex pair is much smaller, as well as being closer to the inlets, than at a model height of six jet diameters. In addition, the ground vortex shape is different. At a height of six jet diameters, the ground vortex appears to be deformed by flow moving outward from the fountain region between the two forward jets, while

at a height of two jet diameters, the ground vortex is nearly normal to the free stream flow. Most of these differences can be attributed to inlet suction.

The structure and location of the ground vortex associated with the downstream pair of jets, and the counter-rotating vortex pair between the jets, does not appear to change much with height variation, as seen in figures 4.43 through 4.45. This is expected, since flow from the forward pair of jets has much more influence on these structures than the free stream flow.

At higher velocity ratios, there is not much variation in forward vortex pair and ground vortex locations, and the structure of the flowfield is quite similar at all three heights. Figures 4.48, 4.49, and 4.50 show 127 frame averages at the ground plane for a velocity ratio of 0.09 and model heights of 2, 4, and 6 jet diameters respectively. All of the major structures in the flowfield are almost identical in the three cases. The main difference between these three cases is the amount of mixing which occurs. Figure 4.51 shows normalized concentration plots of the flowfield through the centerline of the model for model heights of 2, 4, and 6 jet diameters. The laser sheet is located near the ground plane. At a model height of six jet diameters, the concentration is lower than at two jet diameters in the region ahead of the fountain. The larger distance between the model and ground plane allows more entrainment and mixing to take place. At the lower model heights, the ground vortex may block a large portion of the mixing flow. Figures 4.52, 4.53, and 4.54 show vertical images of the flowfield through the jet centerline at a velocity ratio of 0.09 for model heights of 2, 4, and 6 jet diameters. At a model height of two jet diameters, the ground vortex completely blocks flow from entering the inner flow region, preventing mixing. At a model height of six jet diameters, the ground vortex does not span the distance between the ground plane and the model, allowing the inner flowfield to mix with the free stream,

decreasing smoke concentration. For all these model heights, the structure of the flowfield remains similar, but does not depend on the model height above the ground.

Figures 4.55, 4.56, and 4.57 show some of the flowfield structures at the mid plane for model heights of 2, 4, and 6 jet diameters respectively. While not directly comparable, since most of the flow structures do not scale with model height, there are still some interesting features to note. For the mid plane at a height of 2 jet diameters (figure 4.55), all the flowfield structures are quite prominent, and include the ground vortex, forward vortex pair, and second ground vortex associated with the rear pair of jets. At a height of 4 jet diameters (figure 4.56), all these features are still visible, but the ground vortex and second ground vortex appear more unsteady. Since both ground vortices are generally of fixed size, as the model height is increased, images along the mid plane progressively show sections of the ground vortex further from the ground plane. At a height of six jet diameters, the ground vortex is almost entirely below the mid plane.

The variation in forward vortex pair size and location is also evident in these three figures. Increasing the model height progressively increases the forward vortex pair size and distance from the forward pair of jets. Inlet suction appears to play a role in the size and location of this structure.

4.3.2 Mean and RMS Concentration Profiles

A comparison of both mean concentration and rms concentration show the same flow structures for all model heights of 2, 4, and 6 jet diameters with the laser sheet at the ground plane and a velocity ratio of 0.09. Figures 4.58 through 4.61 show mean and rms concentration profiles, for a model height of two jet diameters, through the model centerline, side jet pair centerline, model edge (2.5 jet diameters from the model centerline), and 5.5 jet diameters from the model centerline. Figures 4.62 through 4.65 show similar plots for a height of six jet diameters. These sets can be compared to the

corresponding plots for a height of four jet diameters in figures 4.11 through 4.14. Comparing these sets, some general trends can be seen. As the model height is increased, the rms concentration peak just in front of the forward jet, and rms concentration peak just in front of the fountain increase in amplitude relative to the background rms concentration. These peaks are prominent at a height of six jet diameters, but are not seen at a height of two jet diameters. This trend is seen in plots corresponding to the jet centerline, model edge, and 5.5 jet diameters from the model centerline. The larger model heights appear to allow more free stream flow to mix with the inner flow region, increasing the apparent large scale unsteadiness, which is seen in the increase in amplitude of these rms concentration peaks. At a height of two jet diameters, almost no mixing between the free stream flow and jets occurs, since the ground vortex almost completely blocks the distance between the model and ground plane. The rms concentration peak associated with the ground vortex and forward vortex pair does not appear to vary in amplitude between the three heights. However, in plots 5.5 jet diameters from the model centerline, a second peak that appears in the same region as the forward vortex pair and ground vortex is seen to decrease in amplitude as the height is increased. At a height of six jet diameters, this feature is no longer visible. This feature may be related to the forward vortex pair, since flow from the forward vortex pair forward of the ground vortex may be impacting the ground vortex, showing up as unsteadiness ahead of the ground vortex. At lower heights, this feature is more prominent, since flow from the forward vortex pair does not have room to flow back over the center area between the model and ground vortex, and must spread out towards the sides of the model.

Direct comparisons of the flowfield at the mid plane for different heights are not possible, since it appears that the flowfield features do not directly scale with height.

There are still some interesting flow features at the mid plane which are not seen at a height of four jet diameters, however.

Figure 4.66 shows a centerline plot for a model height of 2 jet diameters and a velocity ratio of 0.09. This plot is very similar to figure 4.17 at a model height of 4 jet diameters. A peak in rms concentration is located at the forward edge of the flow in the location corresponding to the forward vortex pair. At a model height of six jet diameters, with the laser sheet 3 jet diameters from the ground plane, the flowfield is much different, as shown in figure 4.67. The forward rms concentration peak corresponding to the forward vortex pair is much lower in amplitude. The fountain has also been pushed back between the rear pair of jets, and is evident in mean concentration measurements, as well as figure 4.50. The large peak in rms concentration is located just behind the forward pair of jets. This peak is not evident at a model height of 2 or 4 jet diameters. Most of the differences between these three figures can be attributed to the difference in the height of the laser sheet from the ground plane. For a laser sheet midway between the ground plane and model, the laser sheet is located 1, 2, and 3 jet diameters from the ground plane for model heights of 2, 4, and 6 jet diameters. The vertical size of most of the distinct features in the flow appear to be independent of model height. The ground vortex, for instance, appears to have a diameter of about 1.5 inches, or 3 jet diameters, for all model heights.

Figures 4.68 and 4.69 show mean and rms concentration plots through the side jet pair centerline at model heights of 2 and 6 jet diameters respectively, again with the laser sheet at the midplane. Figure 4.68 shows a prominent peak in rms concentration in the region where the forward vortex pair and ground vortex are located. Figure 4.68 also shows this peak, but it is much smaller. Instead, rms concentration peaks occur just forward of the forward jet, and in between the jets. This is not seen in figure 4.67.

Figures 4.70 and 4.71 show mean and rms concentration plots at the edge of the model, 2.5 jet diameters from the model centerline, for heights of 2 and 6 jet diameters respectively. Interestingly, both these graphs show peaks both in rms and mean concentration in the same locations as at a height of four jet diameters, shown in figure 4.19. The amplitudes of these peaks, however, are quite different from each other.

Figures 4.72 and 4.73 show mean and rms concentration plots at 5.5 jet diameters from the model centerline, for model heights of 2 and 6 jet diameters from the ground plane respectively. Figure 4.20, at a height of 4 jet diameters, shows similar features to both these figures. The decrease in amplitude of both rms and mean concentration is due to the laser sheet location. As the model height is increased, the mid plane is moved further from the ground plane. As previously stated, the ground vortex appears to have a nearly constant size, independent of model height. As the model height is increased, the distance from the laser sheet to the ground is also increased at the mid plane, and different sections of the ground vortex are illuminated. The further from the ground plane, the lower the amplitudes of both rms and mean concentration.

4.4 Effect of Suction on Flowfield Vortex Structures

In a real aircraft, inlet suction cannot be turned off. However, it is interesting to note the effects that inlet suction has on the structure of the flowfield. Figures 4.73 and 4.74 show 127 frame averages of the flowfield at a velocity ratio of 0.03 and a model height of two jet diameters. Figure 4.74 has the inlet suction on, and figure 4.75 has the inlet suction off. There is a dramatic difference between the location of the ground vortex and forward vortex pairs in these two flowfields.

Figure 4.76 shows the ground vortex location relative to the forward pair of jets as a function of the velocity ratio U/V_j with and without inlet suction, for three different test model heights. At the higher velocity ratios, the ground vortex location appears to be independent of inlet suction and test model height relative to the ground plane. At low

velocity ratios, it appears that the ground vortex location depends on the height of the test model above the ground. At greater heights, the inlets have less influence on the location of the ground vortex. The ground vortex location appears to be independent of height with the inlet suction off. Therefore, most of the changes in the ground vortex location versus height are due to inlet suction.

The forward vortex pair location also appears to be influenced by inlet suction. Figure 4.77 shows the forward vortex location relative to the forward pair of jets as a function of velocity ratio for three different heights. Again, at high velocity ratios the forward vortex location appears to be independent of test model height and inlet suction up to a height of six jet diameters. At low velocity ratios, the distance between the forward vortex pair location and the forward pair of jets appears to increase with increasing height. At lower heights, inlet suction influences considerably the forward vortex pair location. Also, the forward free stream flow contributes less to the overall flow field in comparison to the inlet suction at lower velocity ratios.

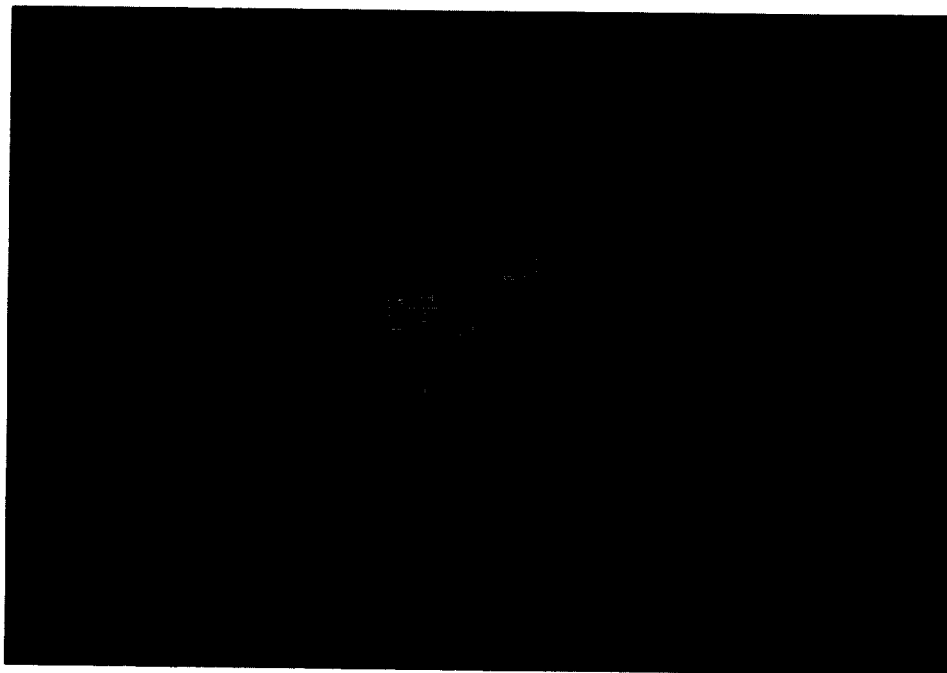
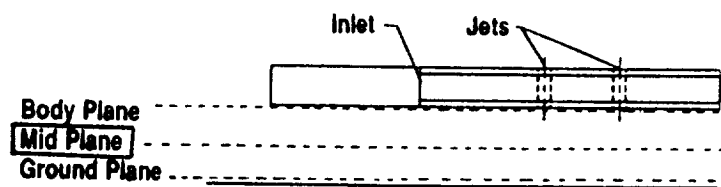


Figure 4.1: Single Frame Image of Smoke Concentration at Mid Plane
 $y/D_j = 2$, $H/D_j = 4$, $U/V_j = 0.09$

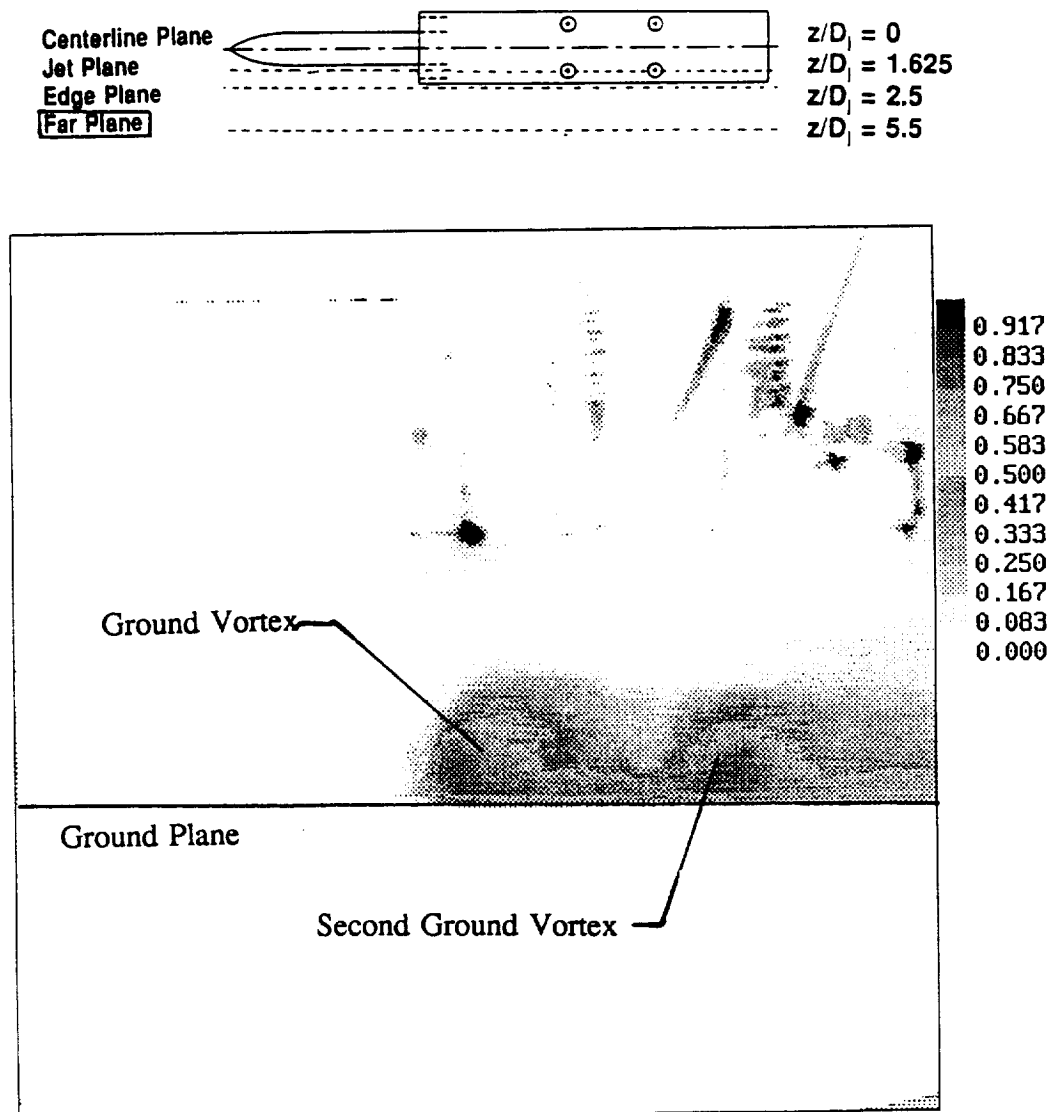


Figure 4.2: Single Frame Image of Smoke Concentration at Far Plane
 $z/D_j = 5.5$, $H/D_j = 4$, $U/V_j = 0.09$

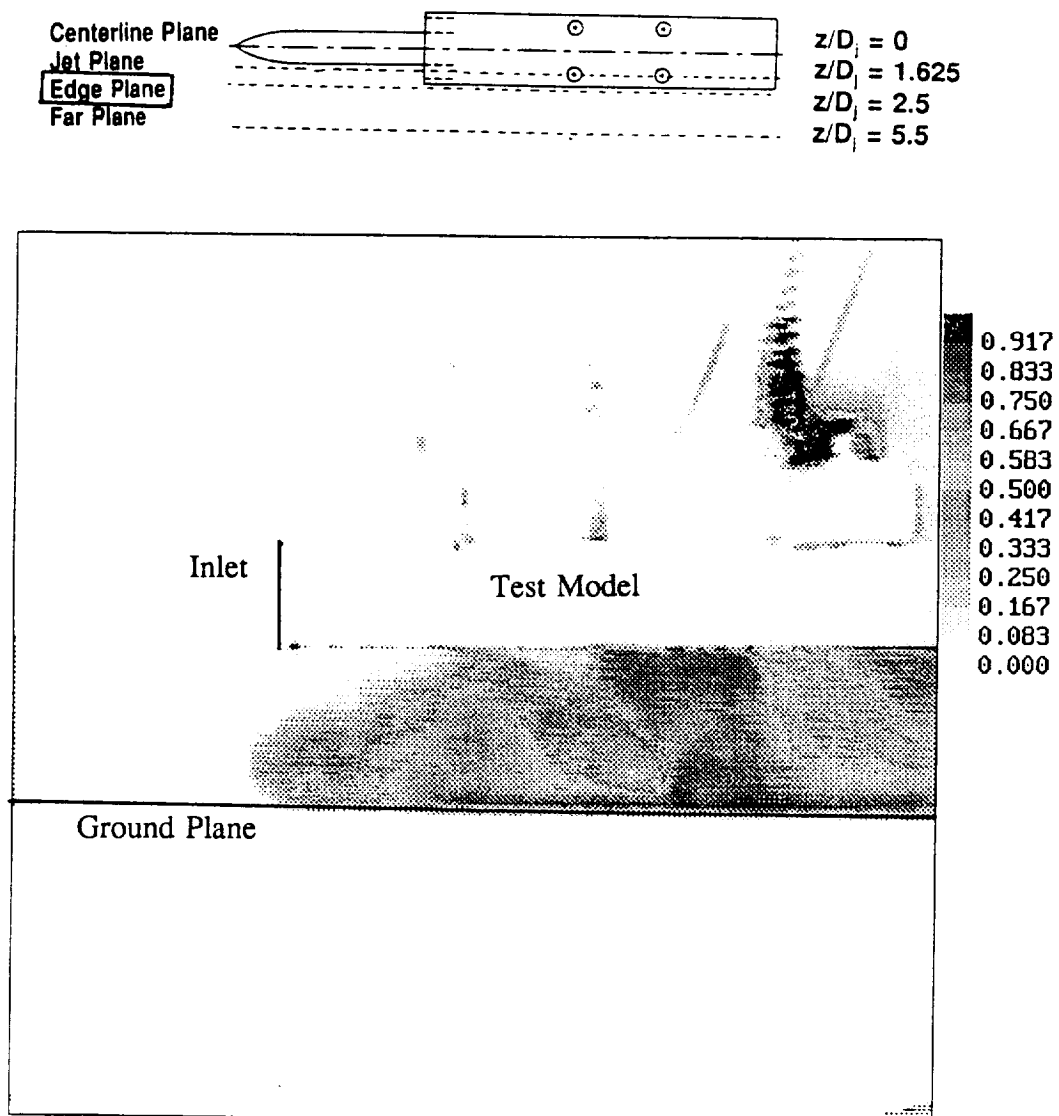


Figure 4.3: Single Frame Image of Smoke Concentration at Edge Plane
 $z/D_j = 2.5$, $H/D_j = 4$, $U/V_j = 0.09$

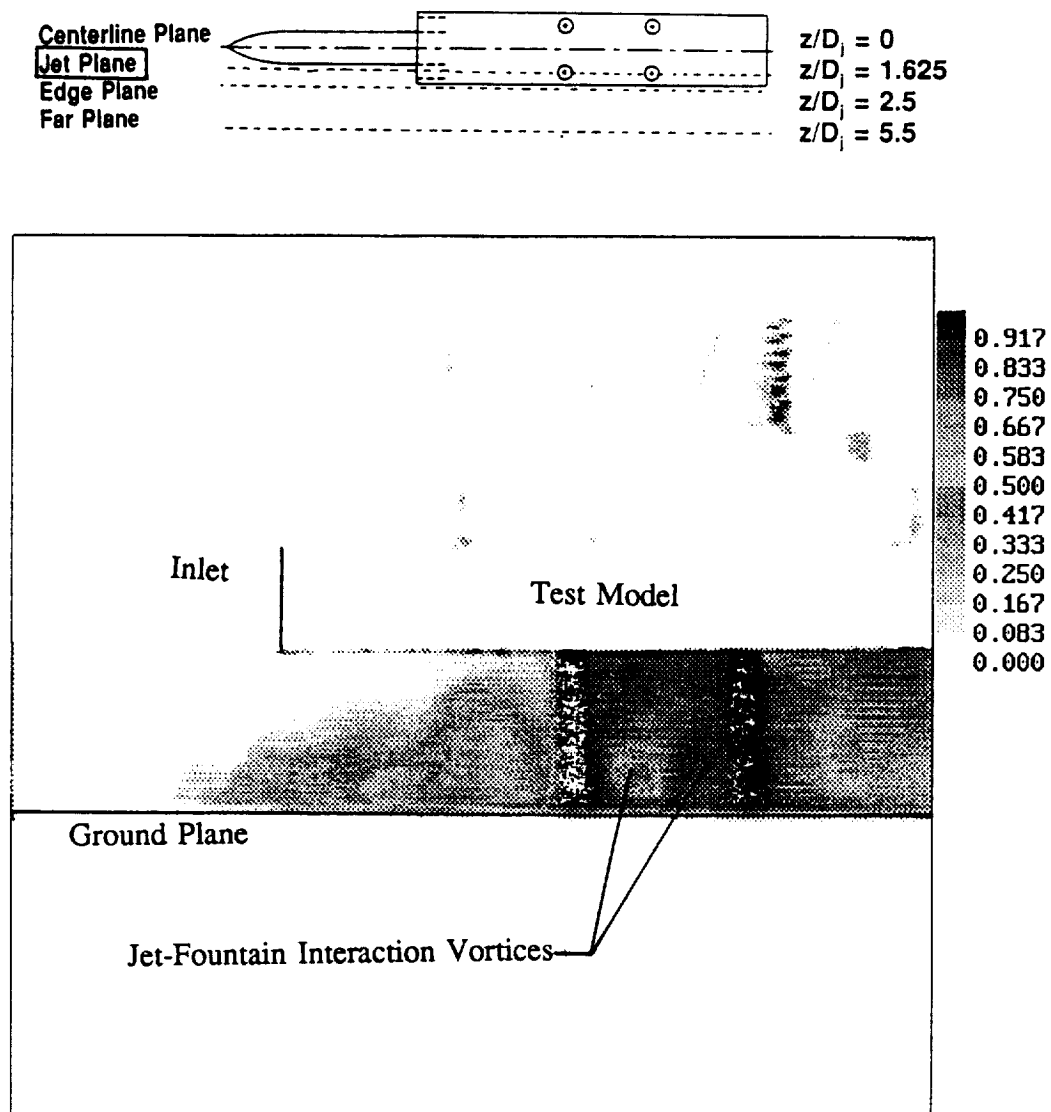


Figure 4.4: Single Frame Image of Smoke Concentration at Side Jet Pair Centerline
 $z/D_j = 1.625$, $H/D_j = 4$, $U/V_j = 0.09$

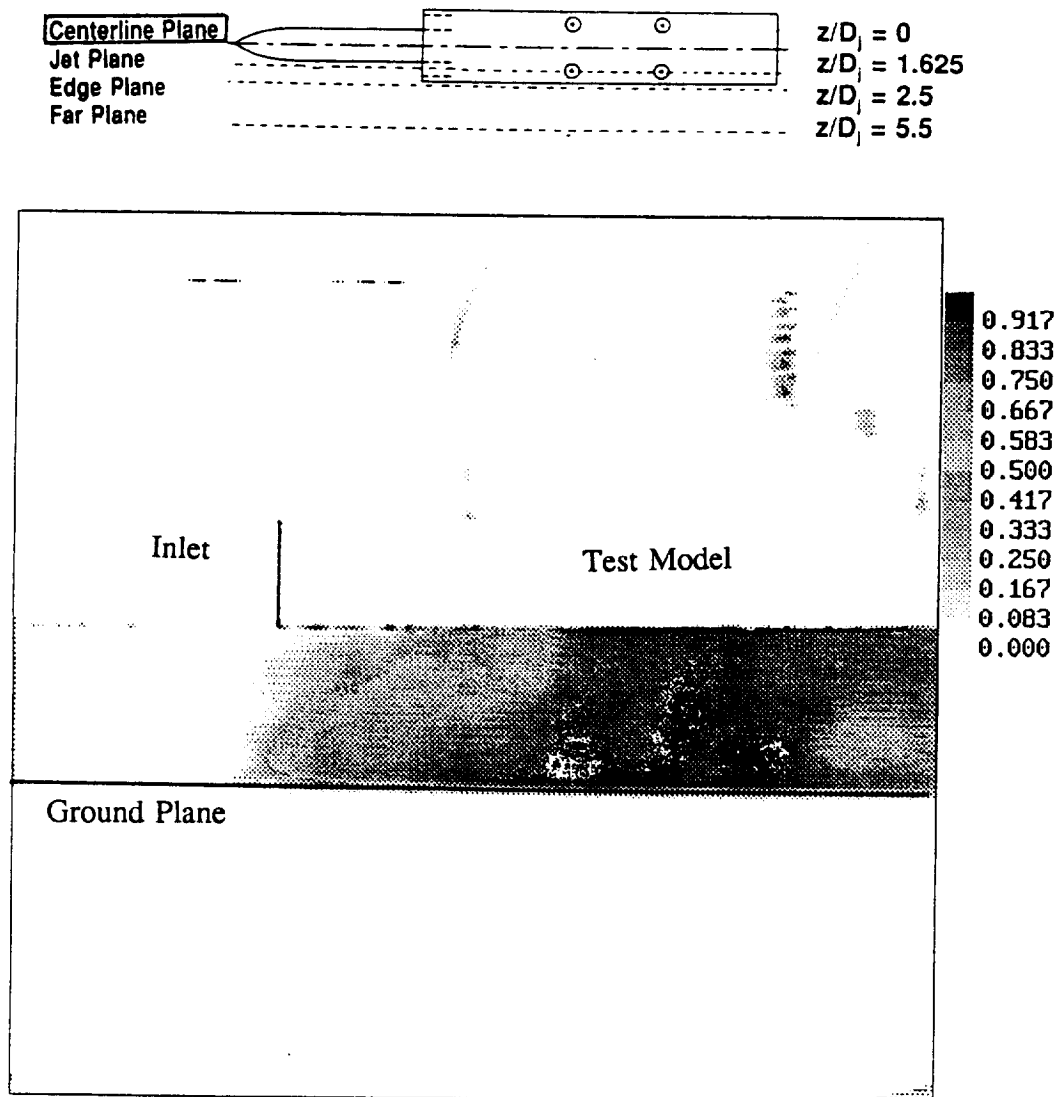


Figure 4.5: Single Frame Image of Smoke Concentration at Model Centerline
 $z/D_j = 0.0$, $H/D_j = 4$, $U/V_j = 0.09$

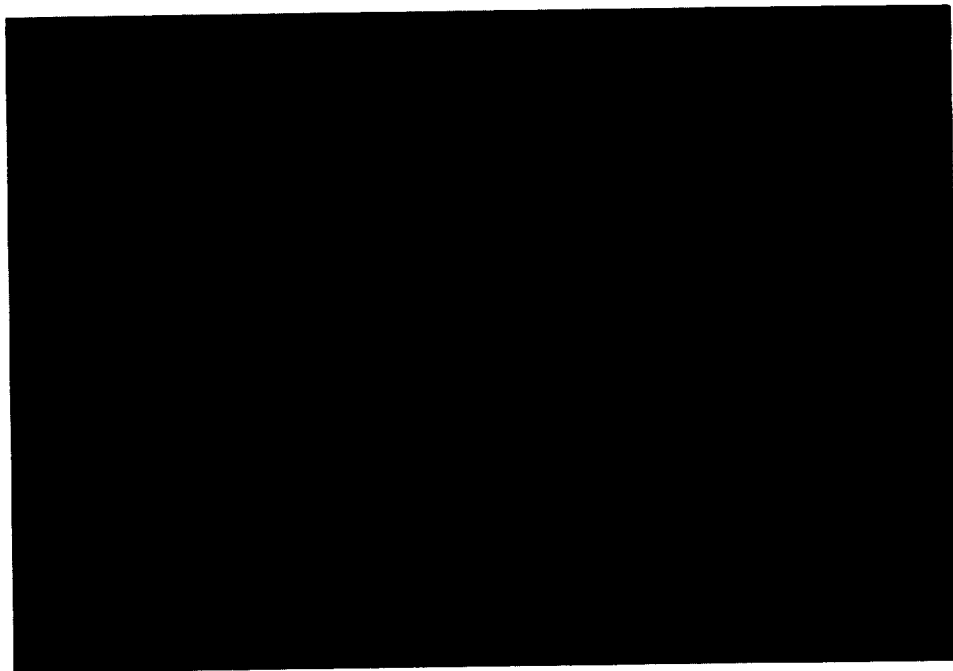
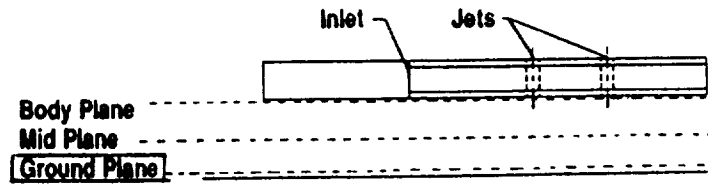


Figure 4.6: Single Frame Image of Smoke Concentration at Ground Plane
 $y/D_j = 0$, $H/D_j = 4$, $U/V_j = 0.09$

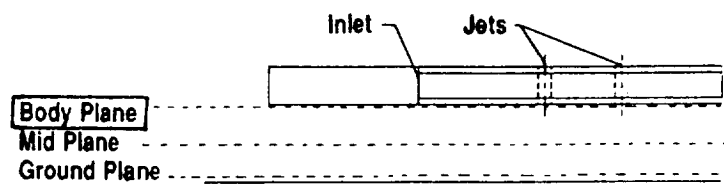


Figure 4.7: Single Frame Image of Smoke Concentration at Body Plane
 $y/D_j = 3.6$, $H/D_j = 4$, $U/V_j = 0.09$

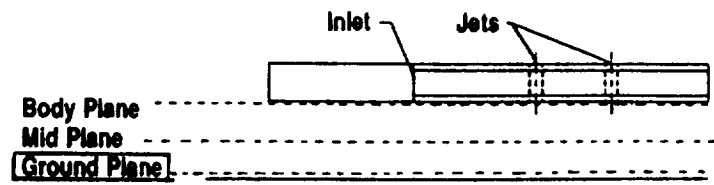


Figure 4.8: 127 Frame Average of Smoke Concentration at Ground Plane
 $y/D_j = 0.0$, $H/D_j = 4$, $U/V_j = 0.09$

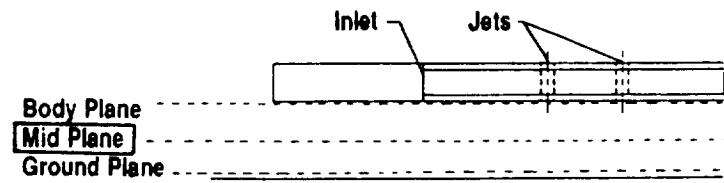


Figure 4.9: 127 Frame Average of Smoke Concentration at Mid Plane
 $y/D_j = 2.0$, $H/D_j = 4$, $U/V_j = 0.09$

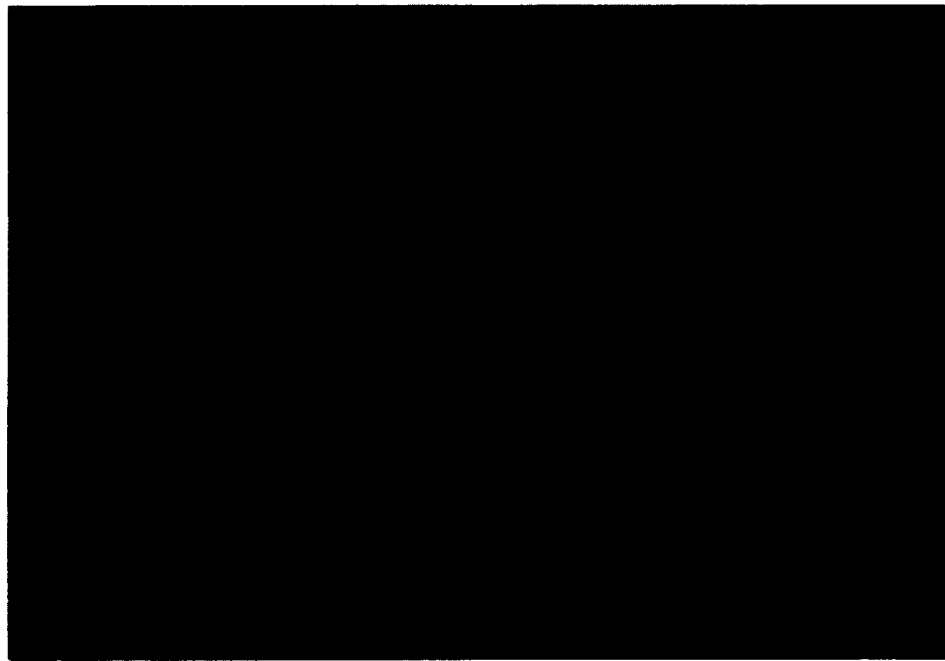
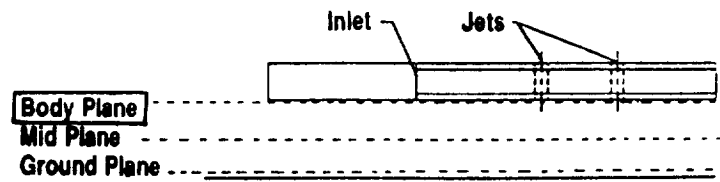


Figure 4.10: 127 Frame Average of Smoke Concentration at Model Body Plane
 $y/D_j = 3.6$, $H/D_j = 4$, $U/V_j = 0.09$

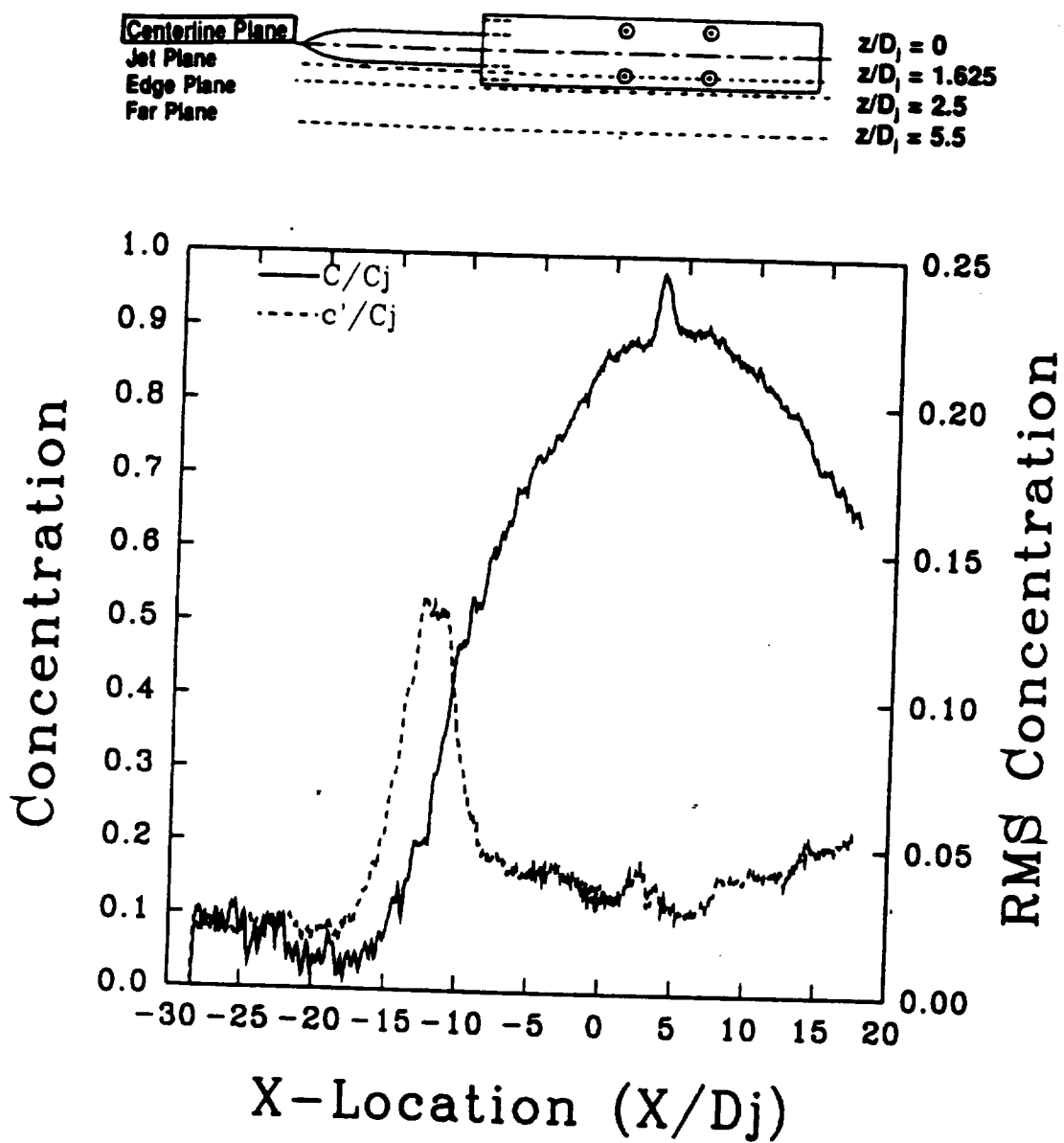


Figure 4.11: Mean and RMS Concentration Profiles at Model Centerline: $z/D_j = 0.0$
 Laser Sheet at Ground Plane: $y/D_j = 0$, $H/D_j = 4$, $U/V_j = 0.09$

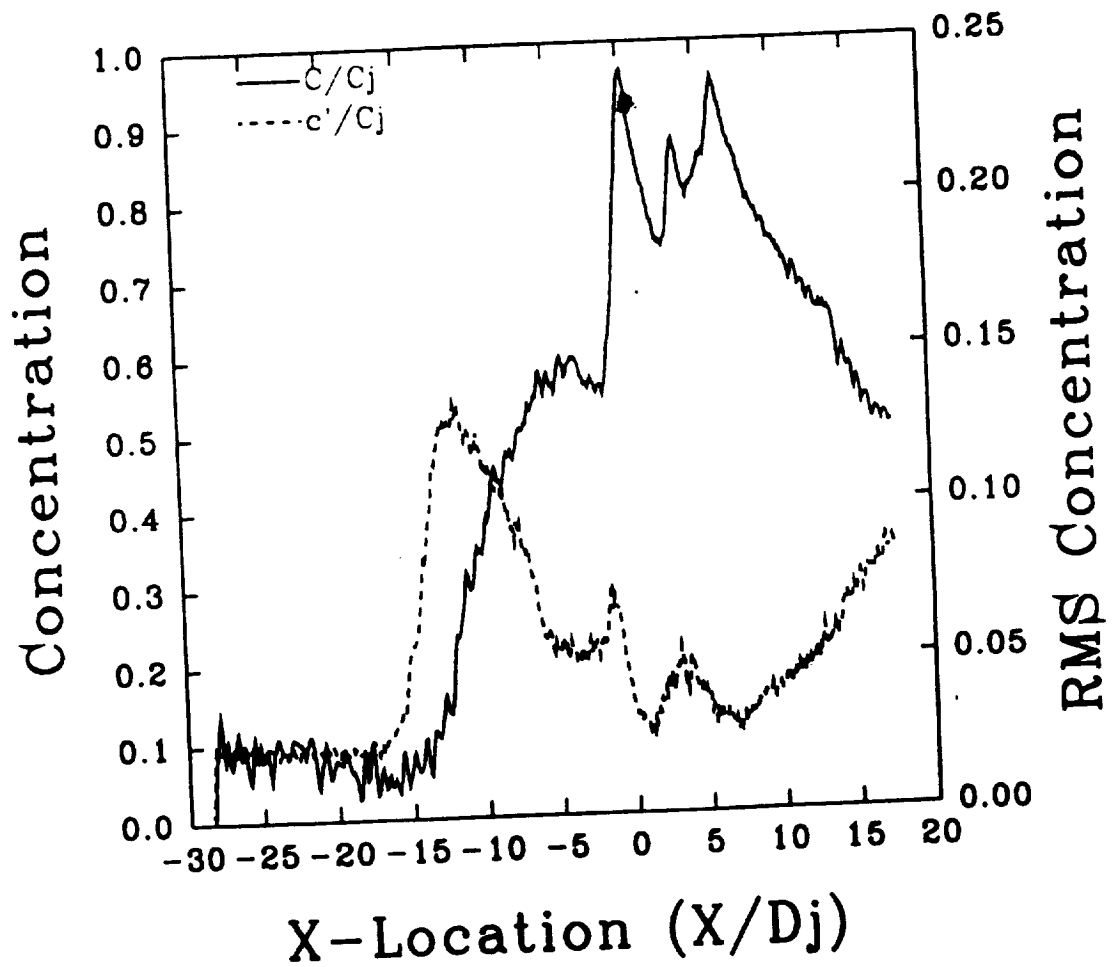
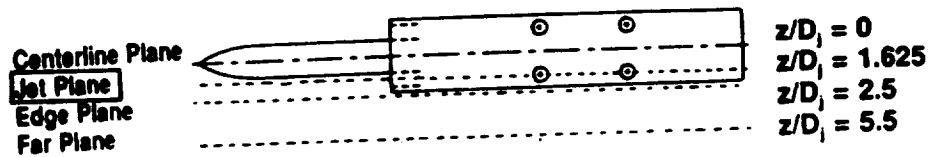


Figure 4.12: Mean and RMS Concentration Profiles at Side Jet Centerlines: $z/D_j = 1.625$
Laser Sheet at Ground Plane: $y/D_j = 0$, $H/D_j = 4$, $U/V_j = 0.09$

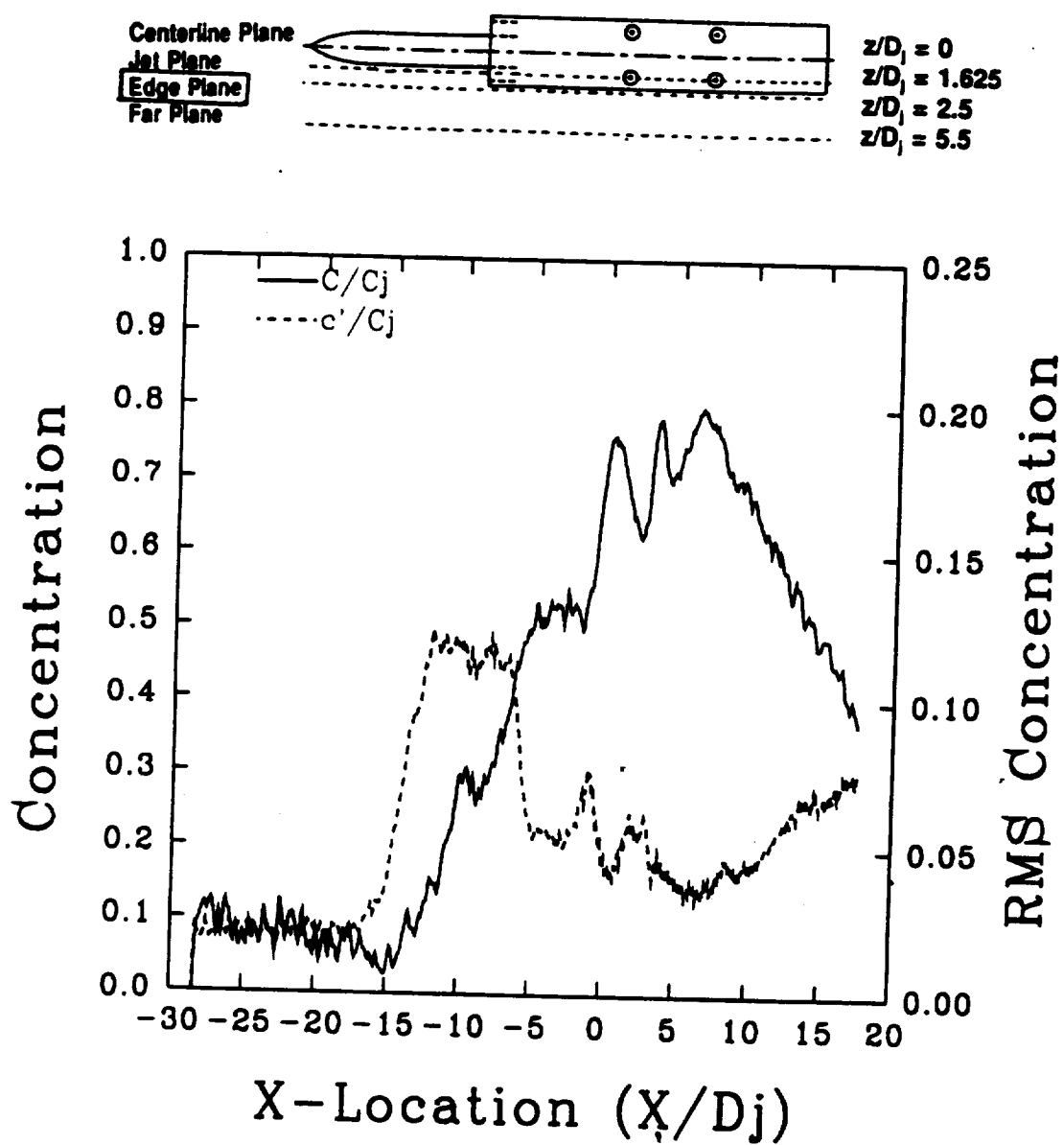


Figure 4.13: Mean and RMS Concentration Profiles at Model Edge: $z/D_j = 2.5$
 Laser Sheet at Ground Plane: $y/D_j = 0.0$, $H/D_j = 4$, $U/V_j = 0.09$

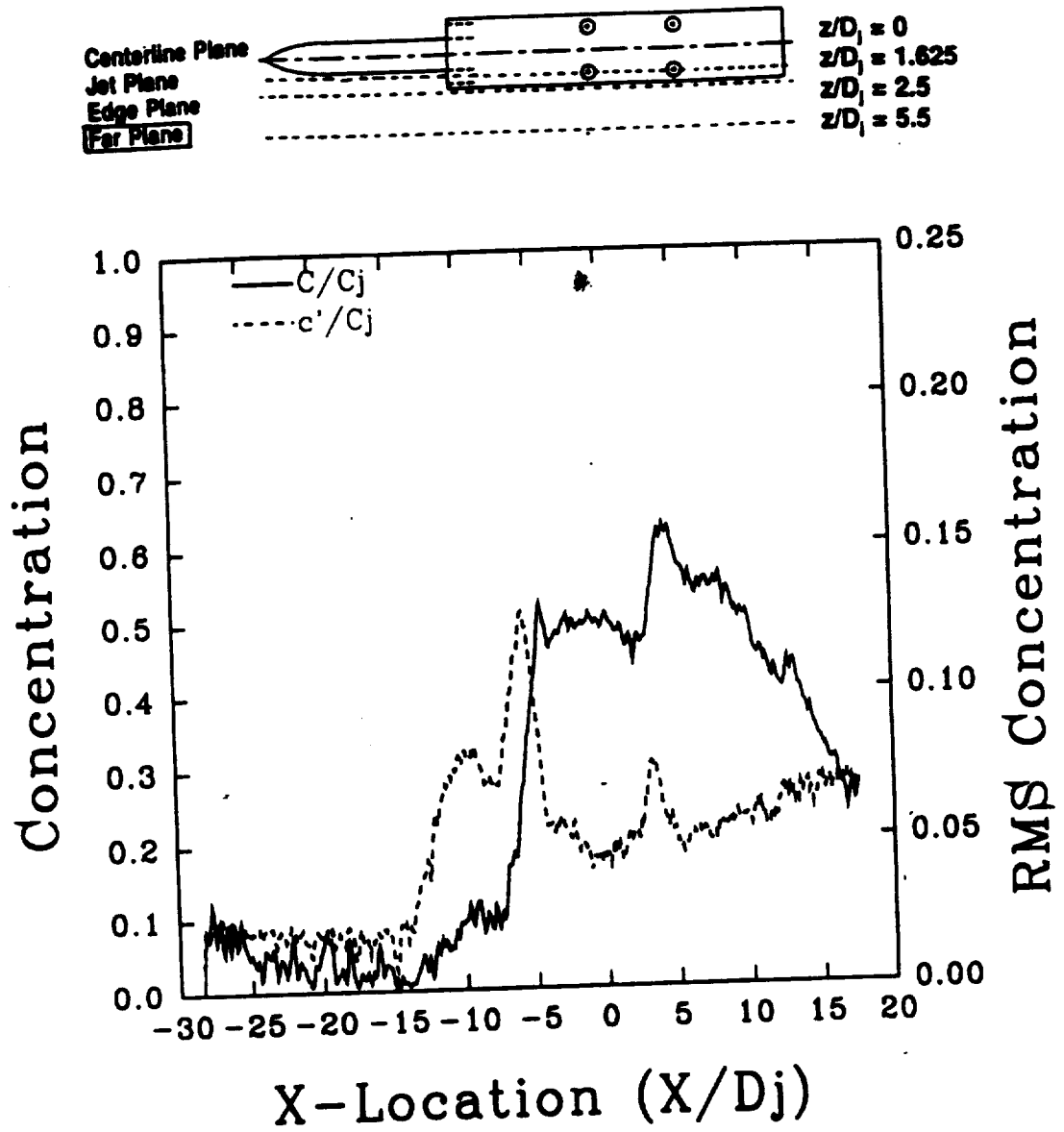


Figure 4.14: Mean and RMS Concentration Profiles at Far Plane: $z/D_j = 5.5$
 Laser Sheet at Ground Plane: $y/D_j = 0.0$, $H/D_j = 4$, $U/V_j = 0.09$

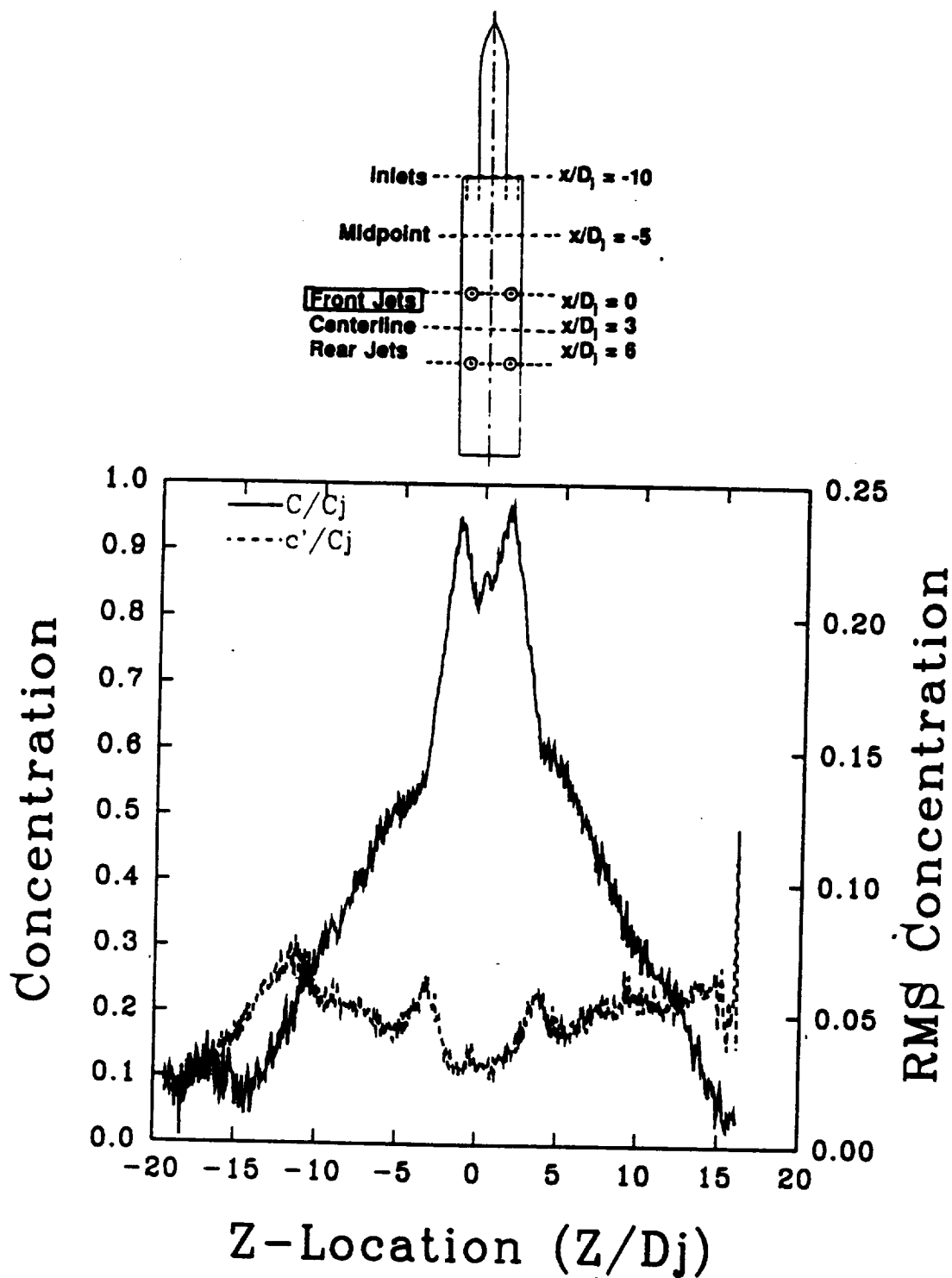


Figure 4.15: Mean and RMS Concentration Profiles at Forward Jet Centerlines: $x/D_j = 0$
 Laser Sheet at Ground Plane: $y/D_j = 0.0$, $H/D_j = 4$, $U/V_j = 0.09$

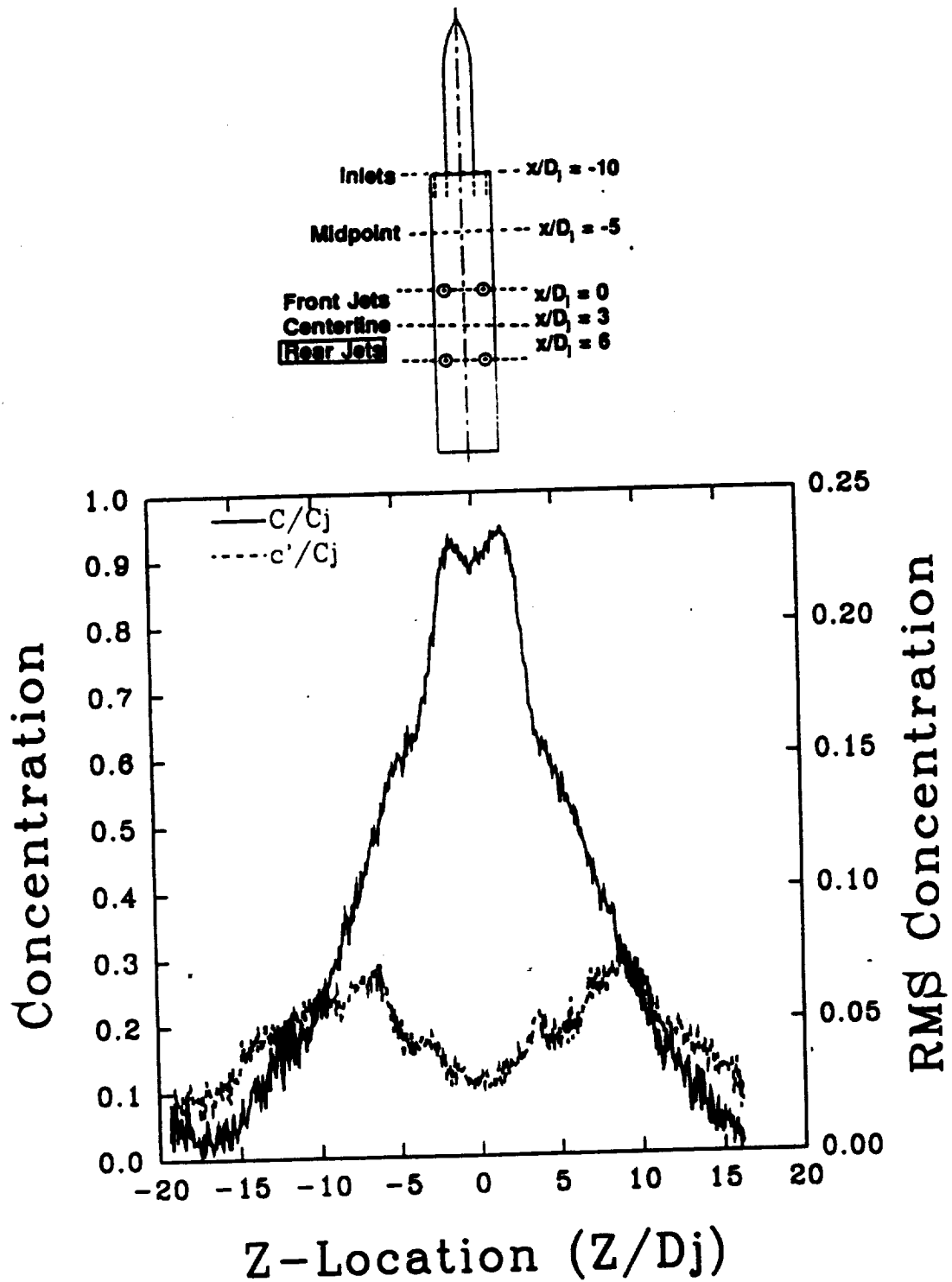


Figure 4.16: Mean and RMS Concentration Profiles at Rear Jet Centerlines: $x/D_j = 6$
 Laser Sheet at Ground Plane: $y/D_j = 0.0$, $H/D_j = 4$, $U/V_j = 0.09$

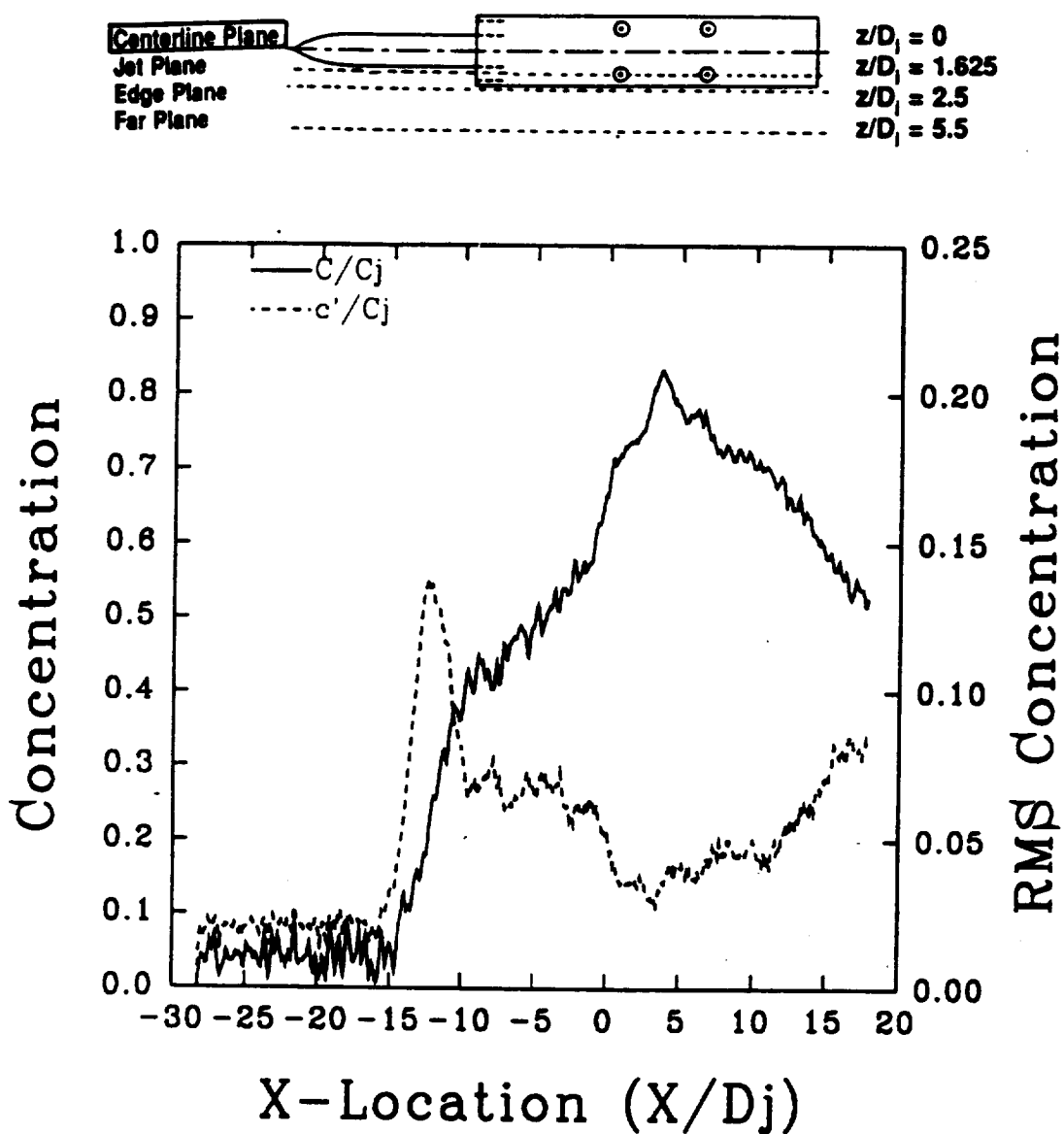


Figure 4.17: Mean and RMS Concentration Profiles at Model Centerline: $z/D_j = 0.0$
 Laser Sheet at Mid Plane: $y/D_j = 2.0$, $H/D_j = 4$, $U/V_j = 0.09$

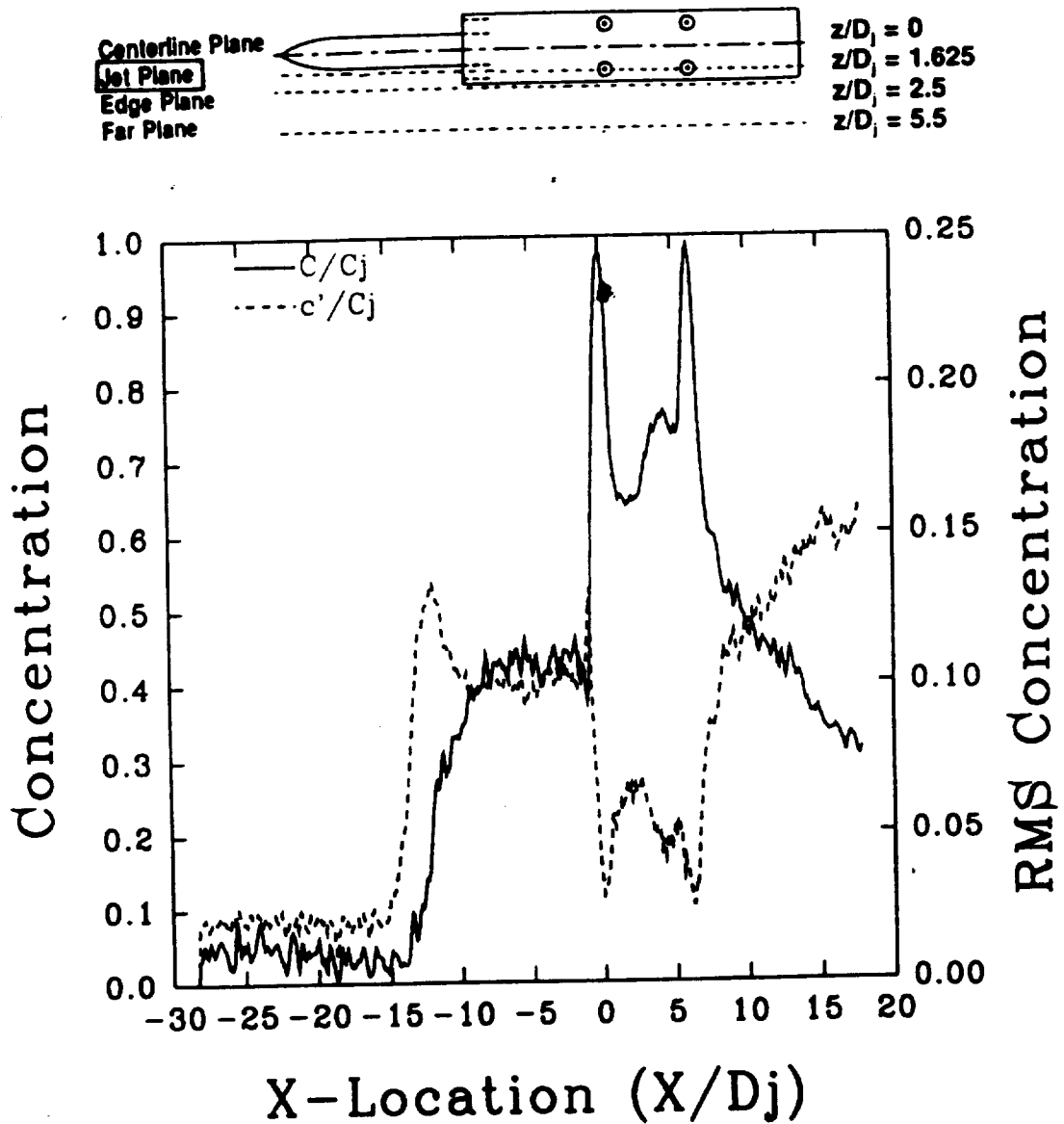


Figure 4.18: Mean and RMS Concentration Profiles at Side Jet Centerlines: $z/D_j = 1.625$
 Laser Sheet at Mid Plane: $y/D_j = 2.0$, $H/D_j = 4$, $U/V_j = 0.09$

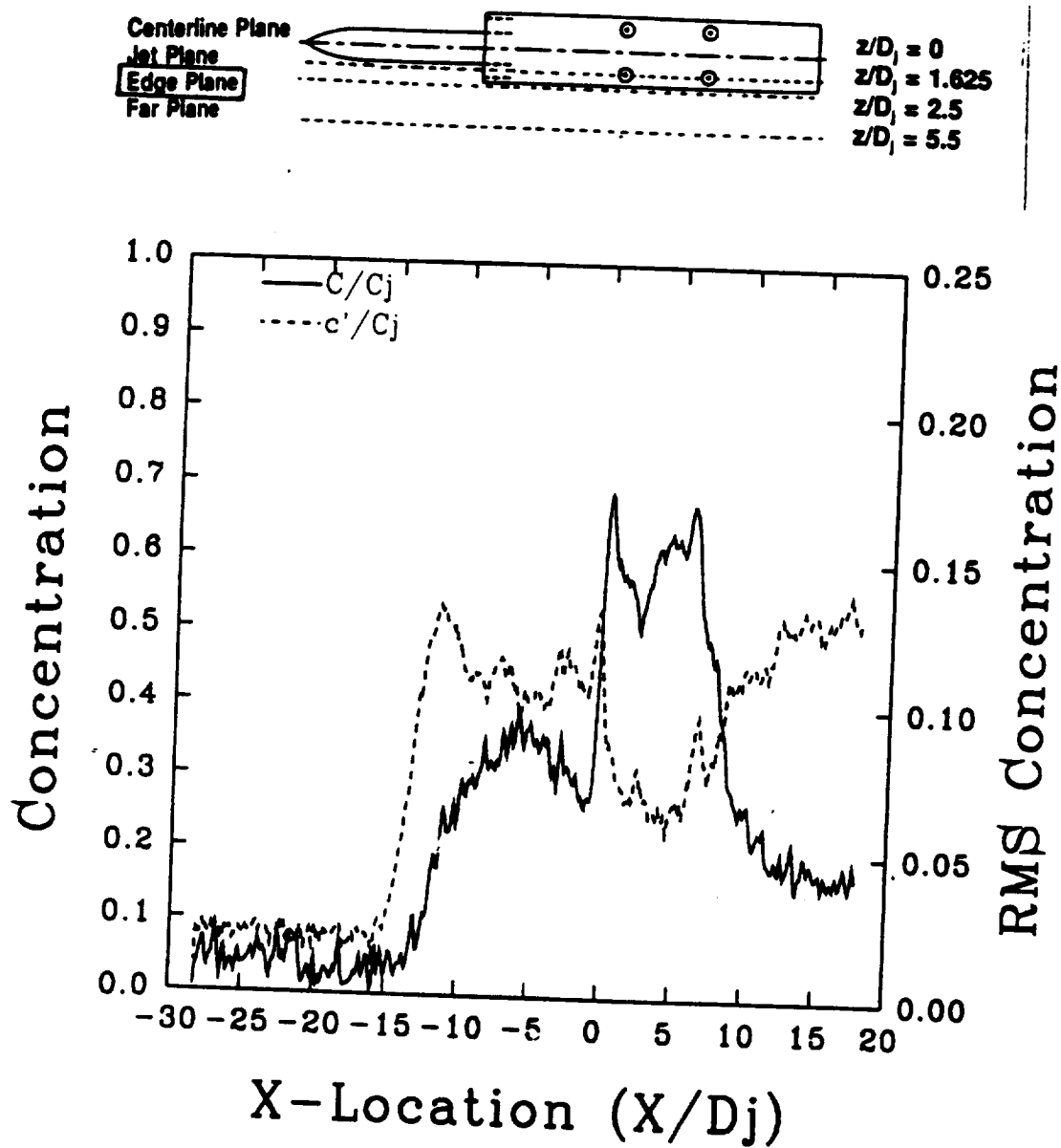


Figure 4.19: Mean and RMS Concentration Profiles at Model Edge: $z/D_j = 2.5$
 Laser Sheet at Mid Plane: $y/D_j = 2.0$, $H/D_j = 4$, $U/V_j = 0.09$

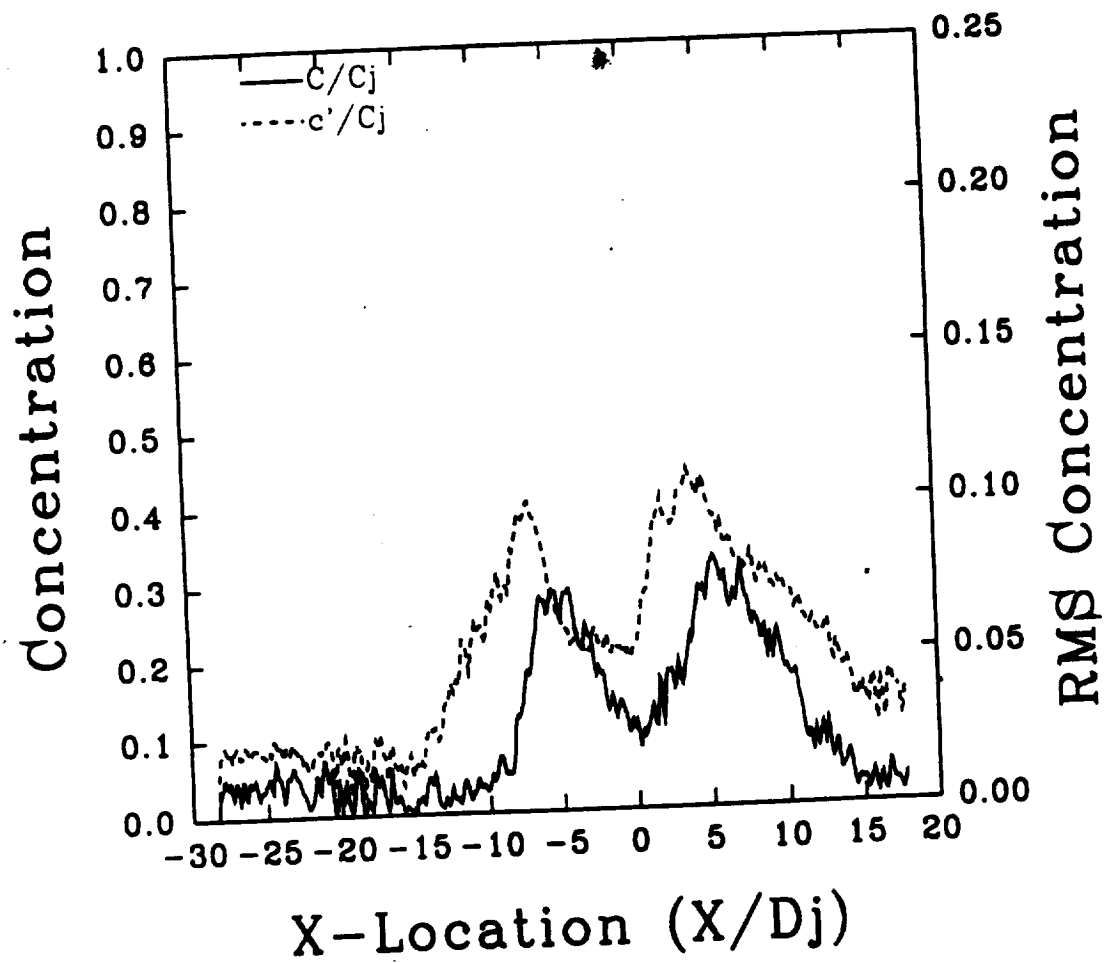
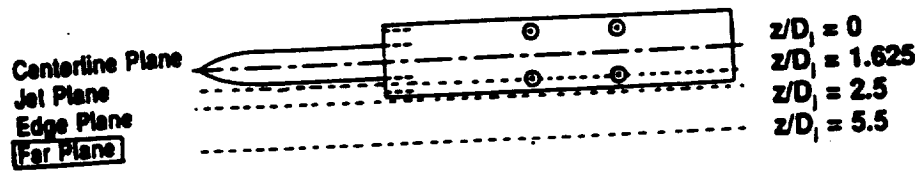


Figure 4.20: Mean and RMS Concentration Profiles at Far Plane: $z/D_j = 5.5$
Laser Sheet at Mid Plane: $y/D_j = 2.0$, $H/D_j = 4$, $U/V_j = 0.09$

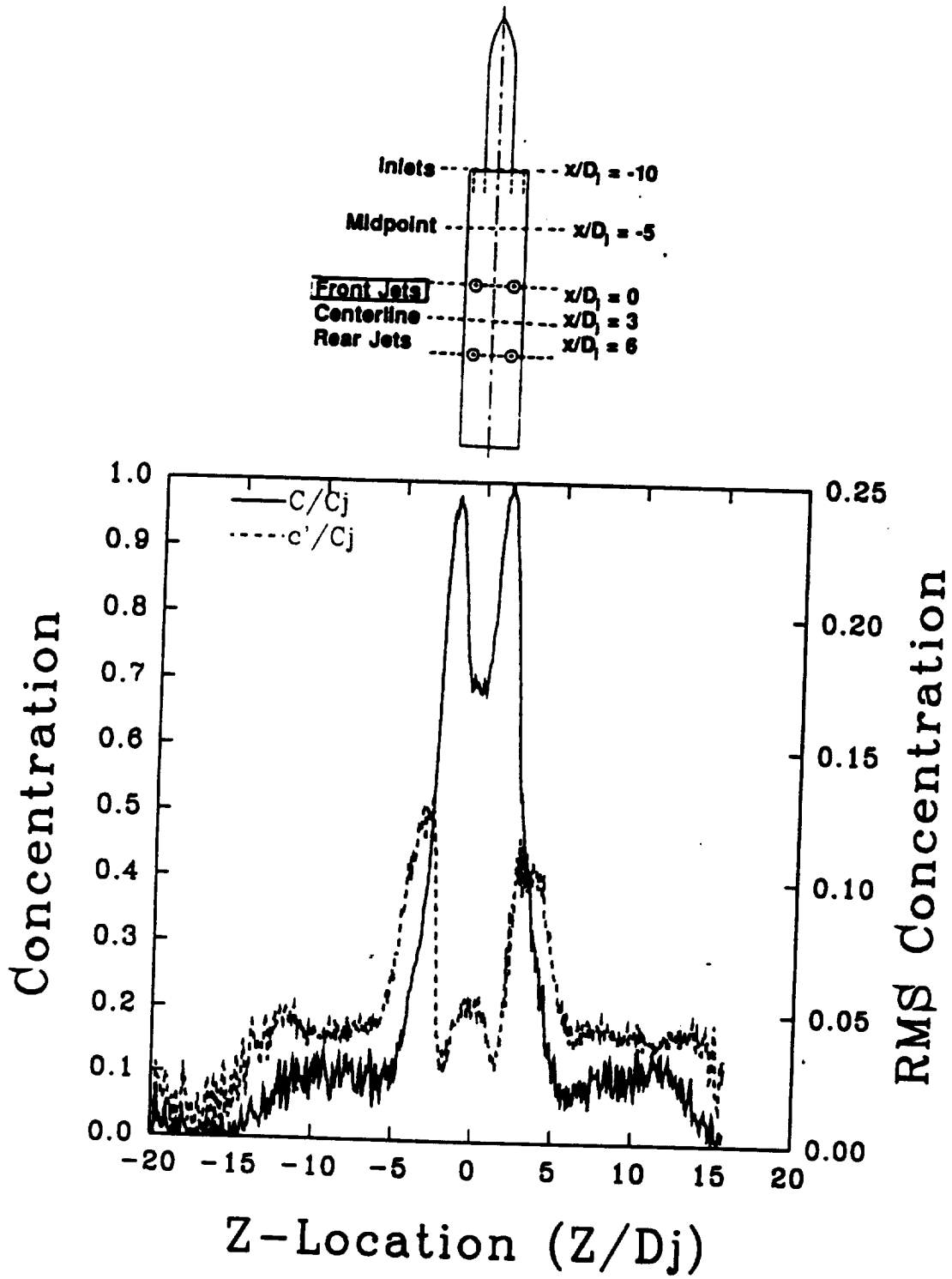


Figure 4.21: Mean and RMS Concentration Profiles at Forward Jet Centerlines: $x/D_j=0$
 Laser Sheet at Mid Plane: $y/D_j = 2.0$, $H/D_j = 4$, $U/V_j = 0.09$

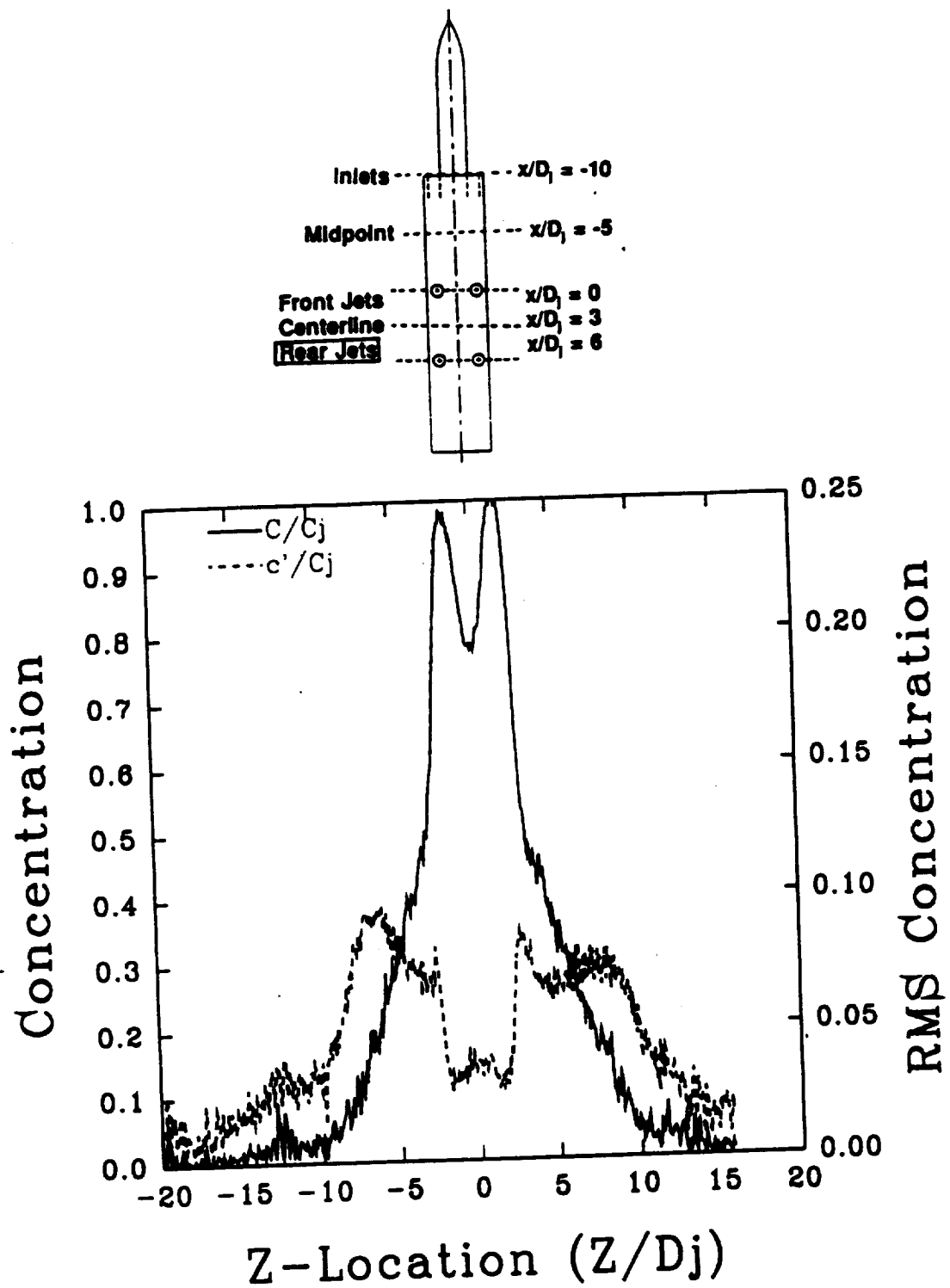


Figure 4.22: Mean and RMS Concentration Profiles at Rear Jet Centerlines: $x/D_j = 6$
 Laser Sheet at Mid Plane: $y/D_j = 2.0$, $H/D_j = 4$, $U/V_j = 0.09$

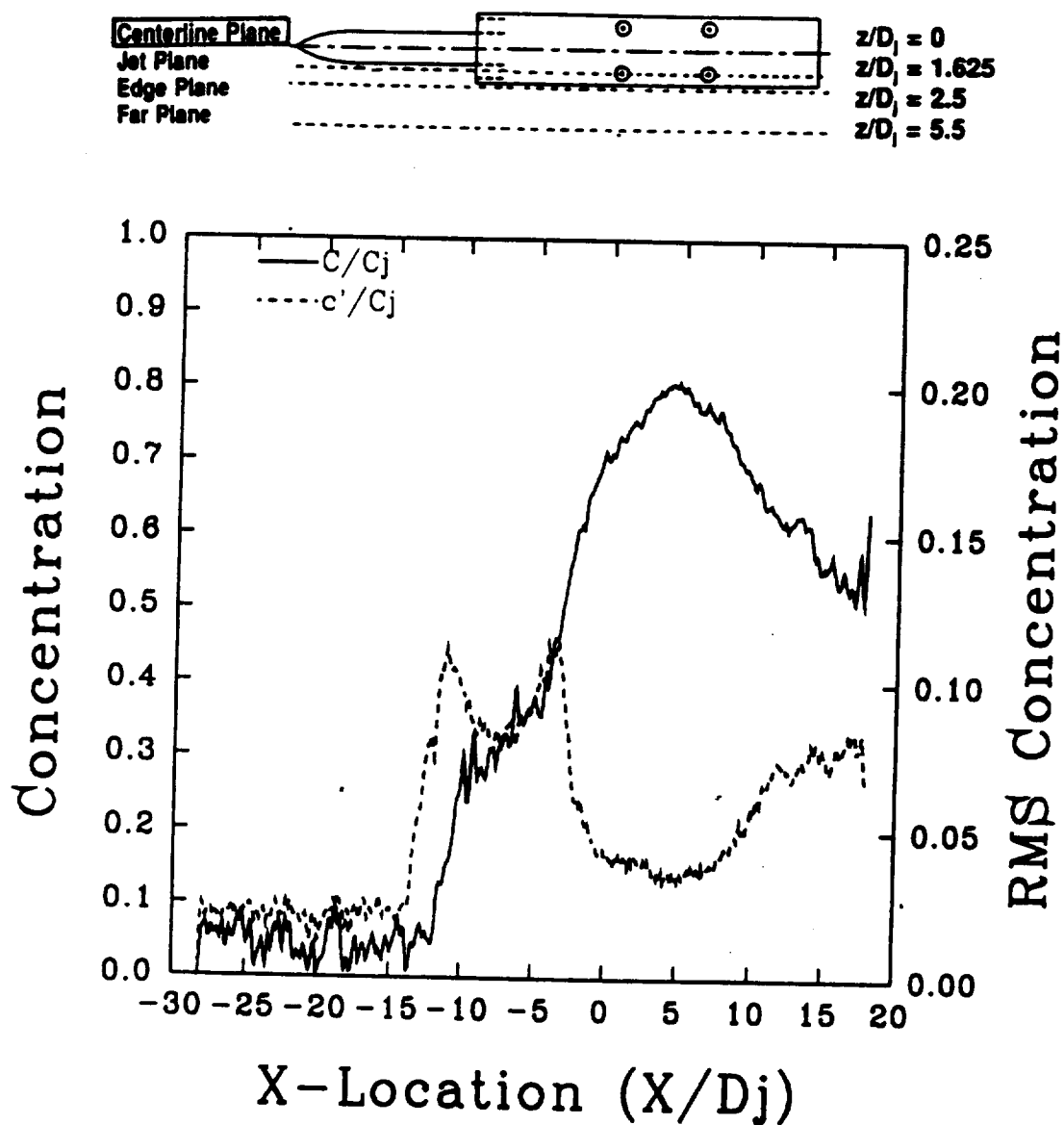


Figure 4.23: Mean and RMS Concentration Profiles at Model Centerline: $z/D_j = 0.0$
 Laser Sheet at Model Body Plane: $y/D_j = 3.6$, $H/D_j = 4$, $U/V_j = 0.09$

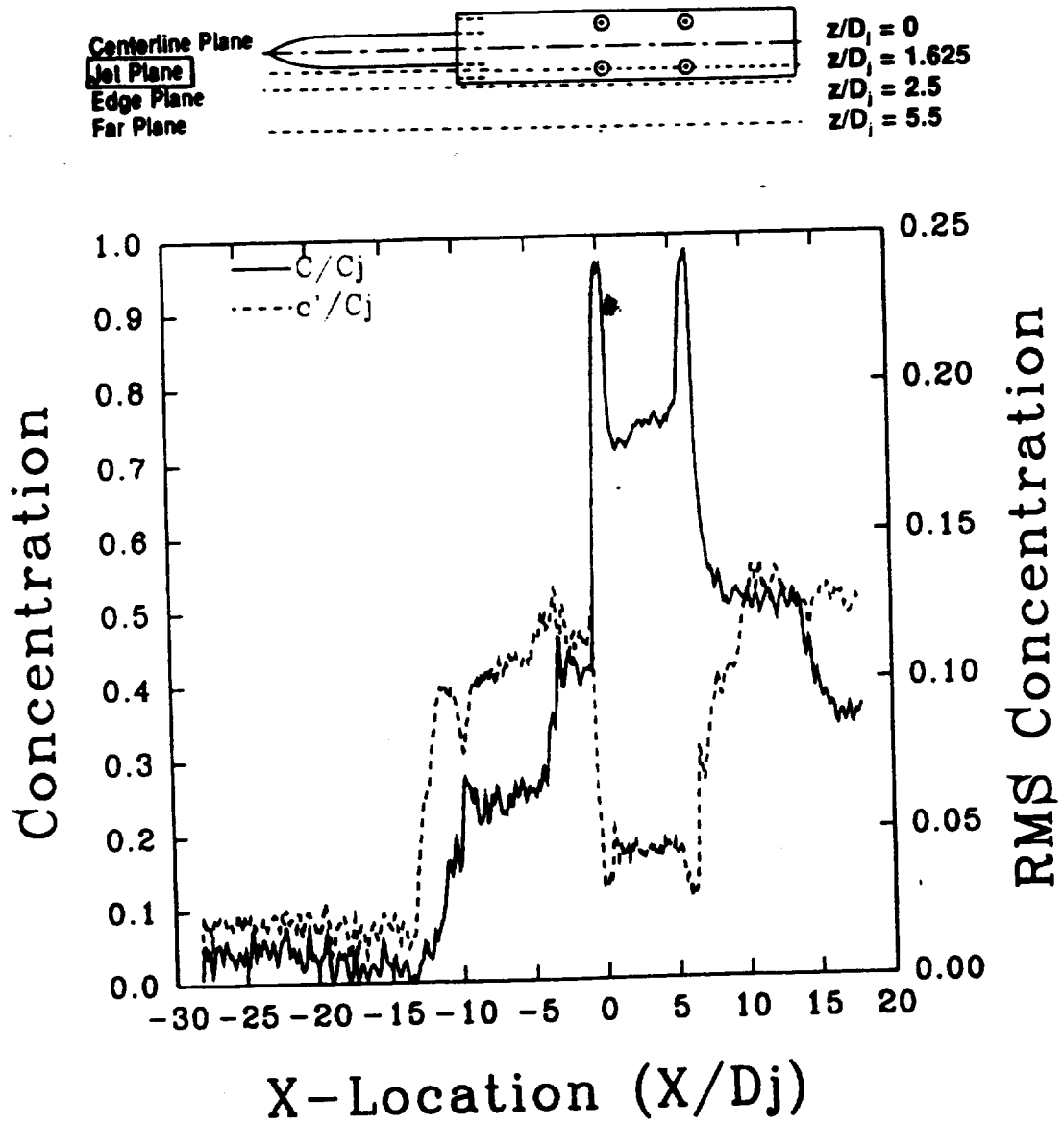


Figure 4.24: Mean and RMS Concentration Profiles at Side Jet Centerlines: $z/D_j = 1.625$
 Laser Sheet at Model Body Plane: $y/D_j = 3.6$, $H/D_j = 4$, $U/V_j = 0.09$

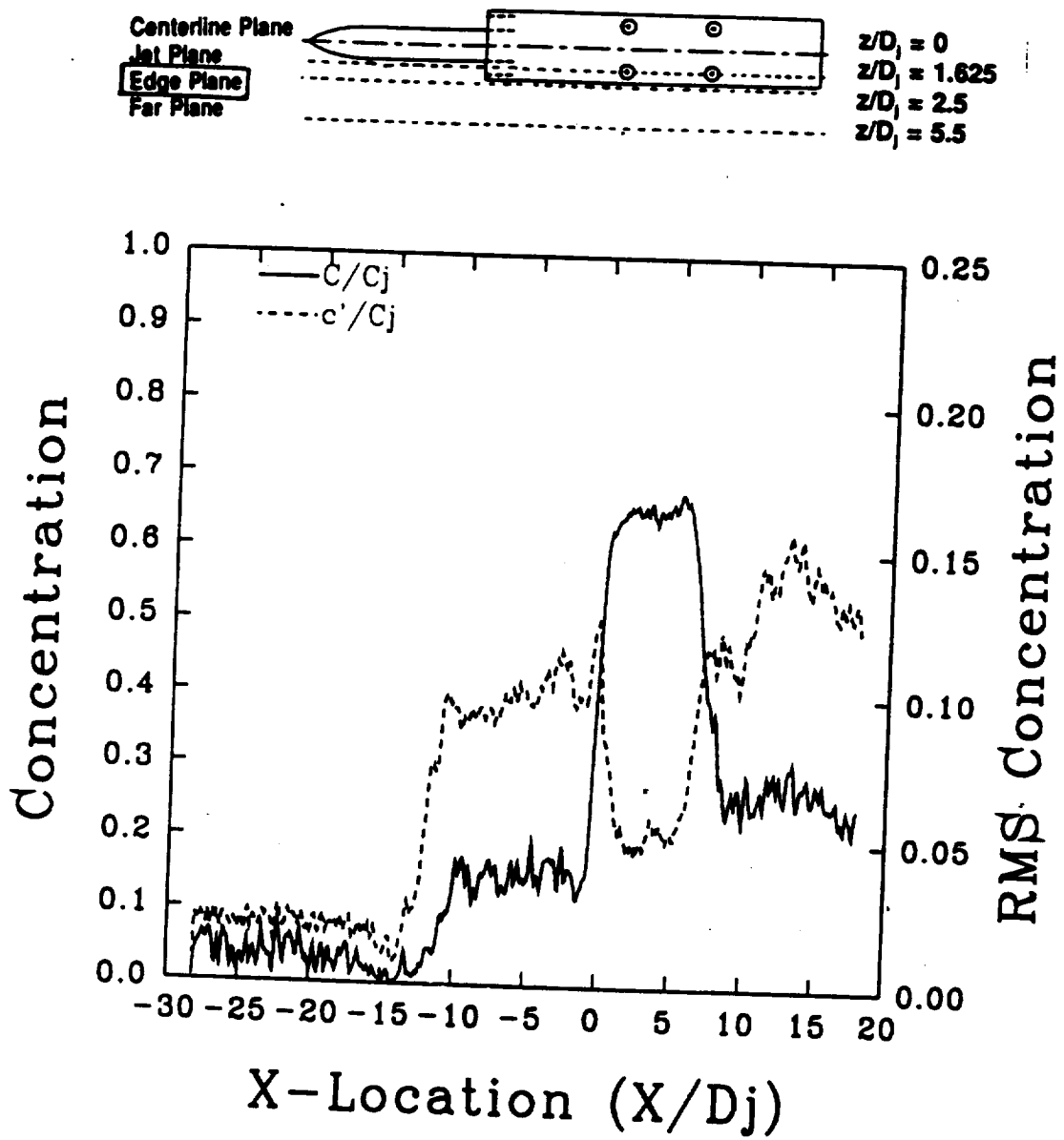


Figure 4.25: Mean and RMS Concentration Profiles at Model Edge: $z/D_j = 2.5$
 Laser Sheet at Model Body Plane: $y/D_j = 3.6$, $H/D_j = 4$, $U/V_j = 0.09$

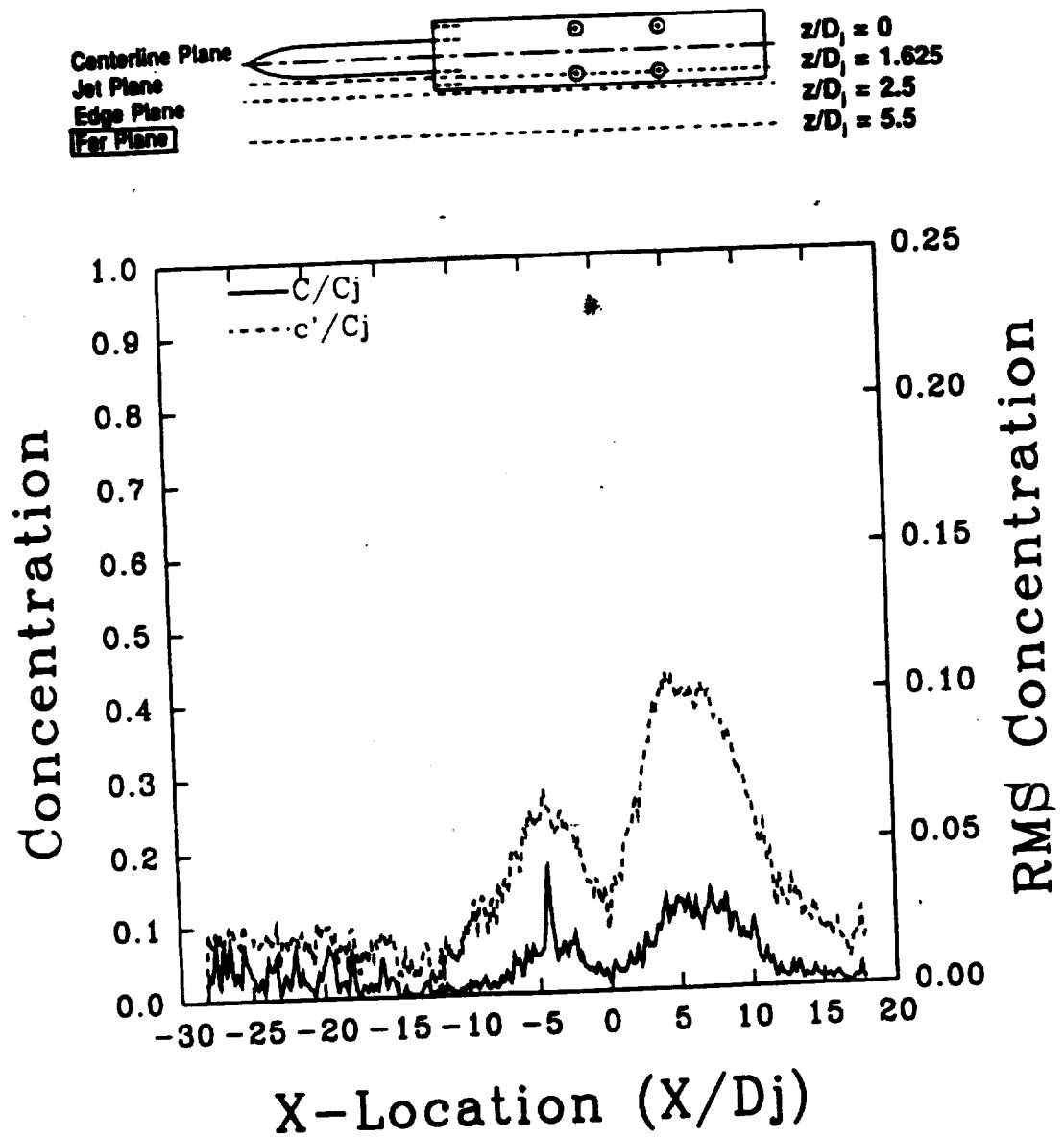


Figure 4.26: Mean and RMS Concentration Profiles at Far Plane: $z/D_j = 5.5$
 Laser Sheet at Model Body Plane: $y/D_j = 3.6$, $H/D_j = 4$, $U/V_j = 0.09$

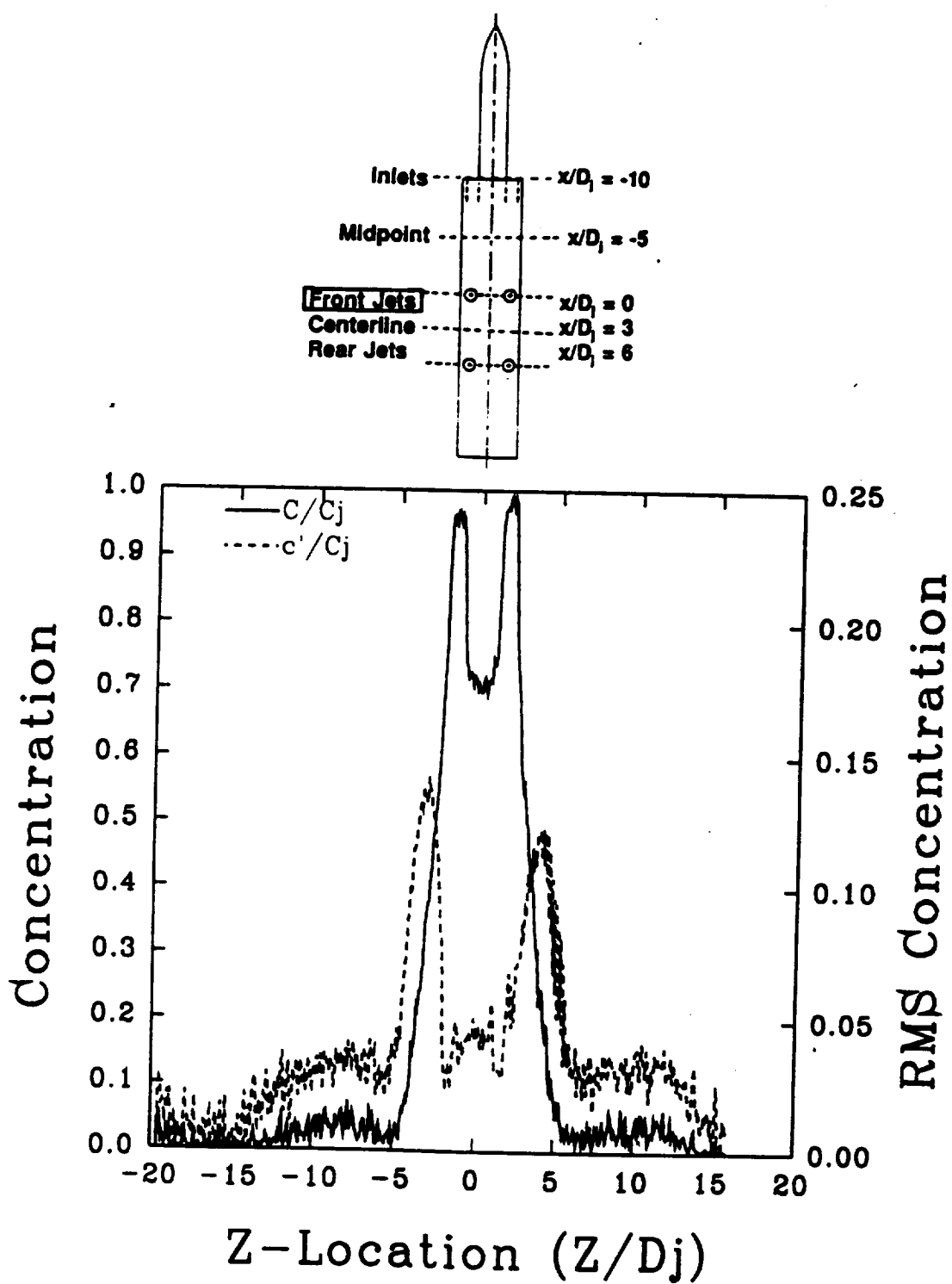


Figure 4.27: Mean and RMS Concentration Profiles at Forward Jet Centerlines: $x/D_j=0$
 Laser Sheet at Model Body Plane: $y/D_j = 3.6$, $H/D_j = 4$, $U/V_j = 0.09$

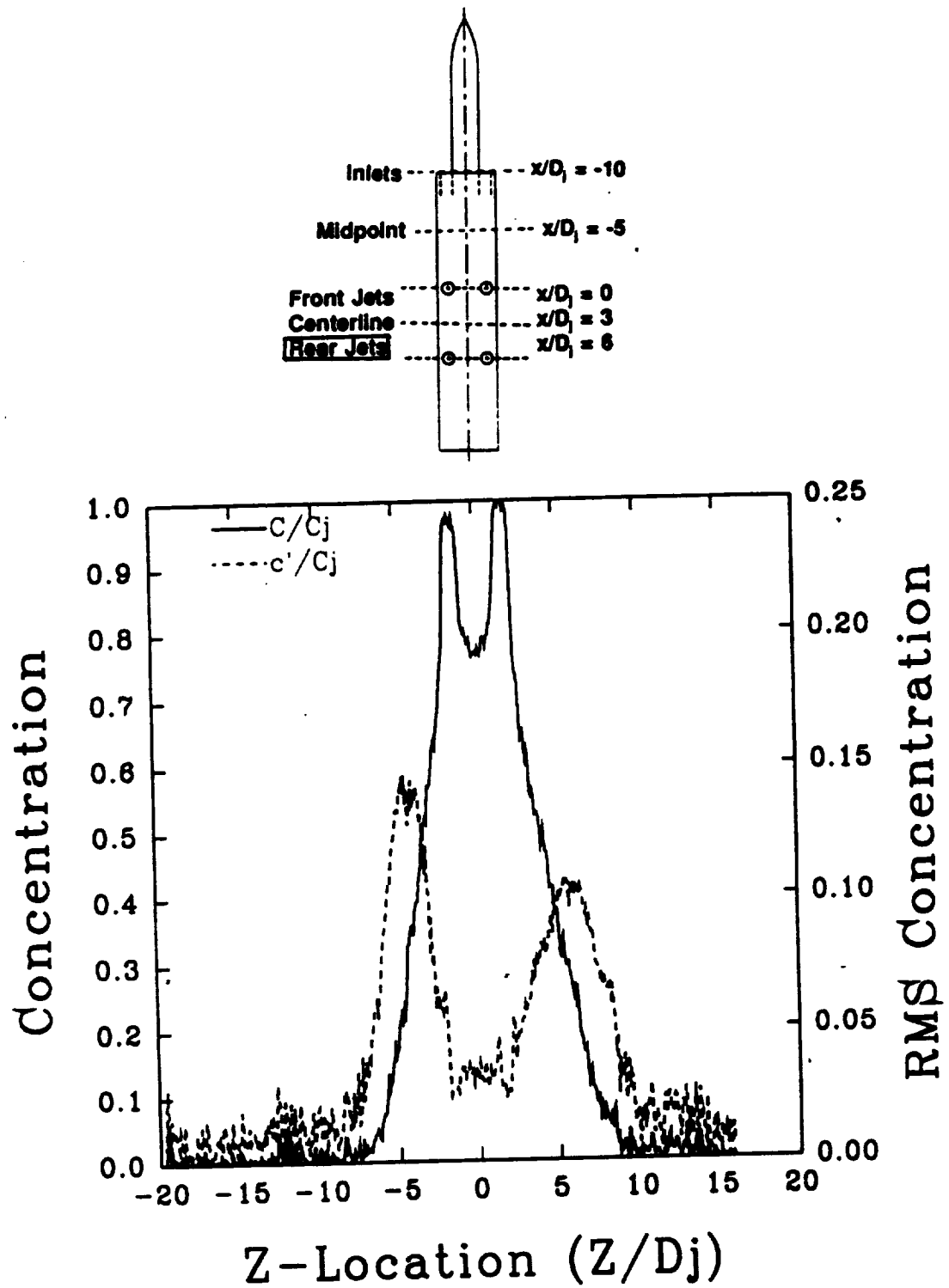


Figure 4.28: Mean and RMS Concentration Profiles at Rear Jet Centerlines: $x/D_j = 6$
 Laser Sheet at Model Body Plane: $y/D_j = 3.6$, $H/D_j = 4$, $U/V_j = 0.09$

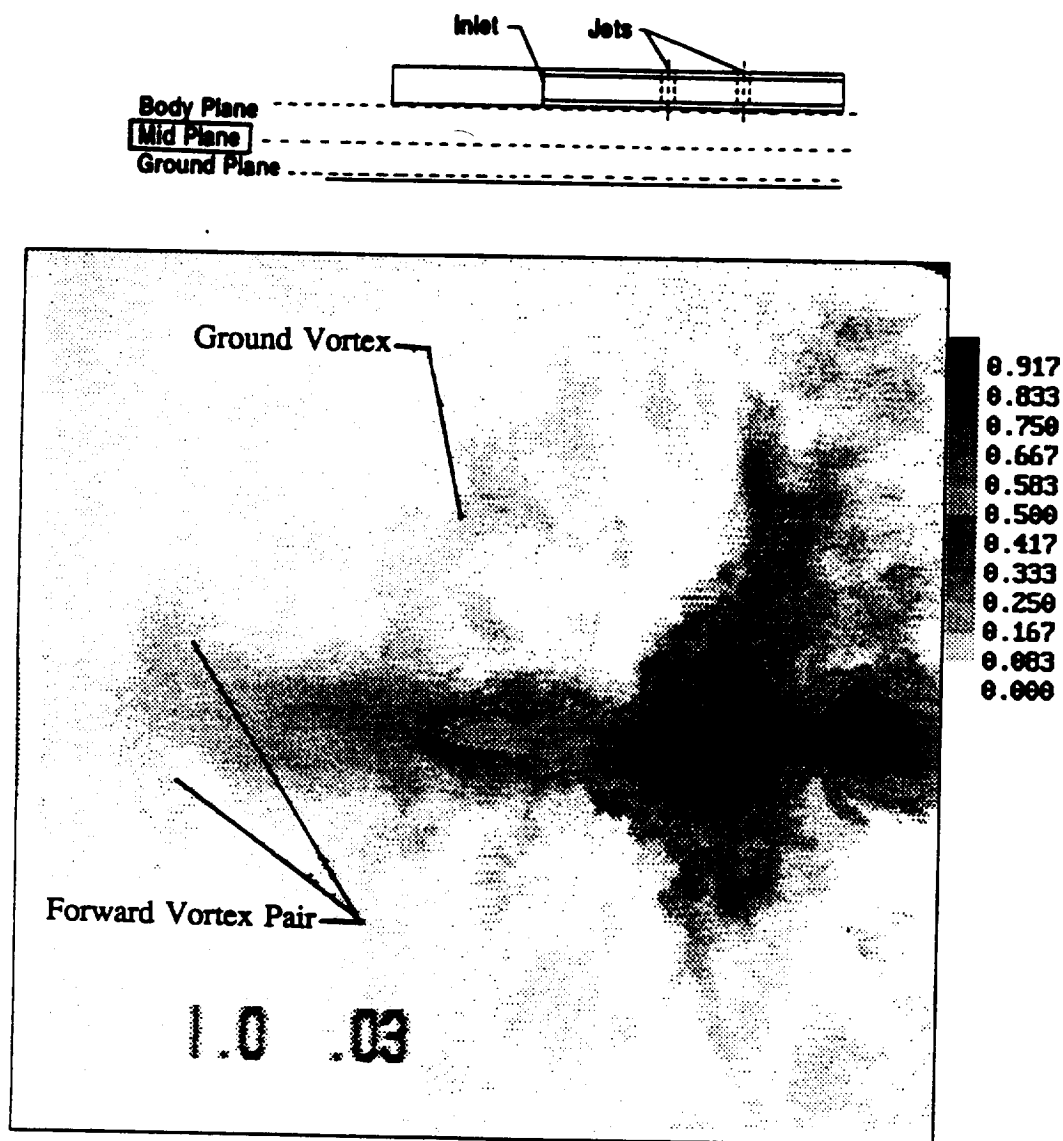


Figure 4.29: Single Frame Image of Smoke Concentration at Mid Plane
 $y/D_j = 2$, $H/D_j = 4$, $U/V_j = 0.03$

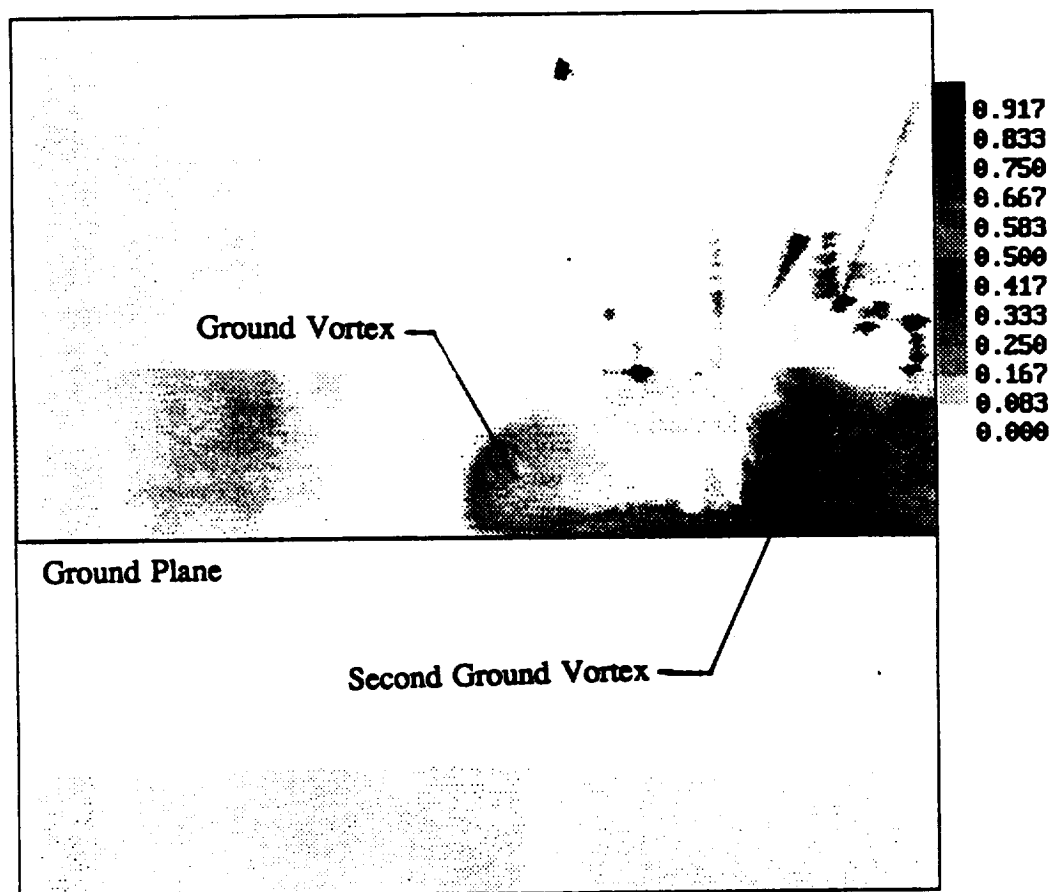
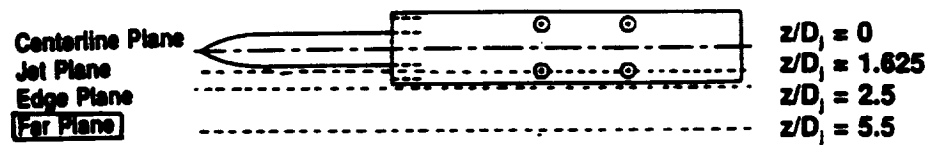


Figure 4.30: Single Frame Image of Smoke Concentration at Far Plane
 $z/D_j = 5.5$, $H/D_j = 4$, $U/V_j = 0.03$

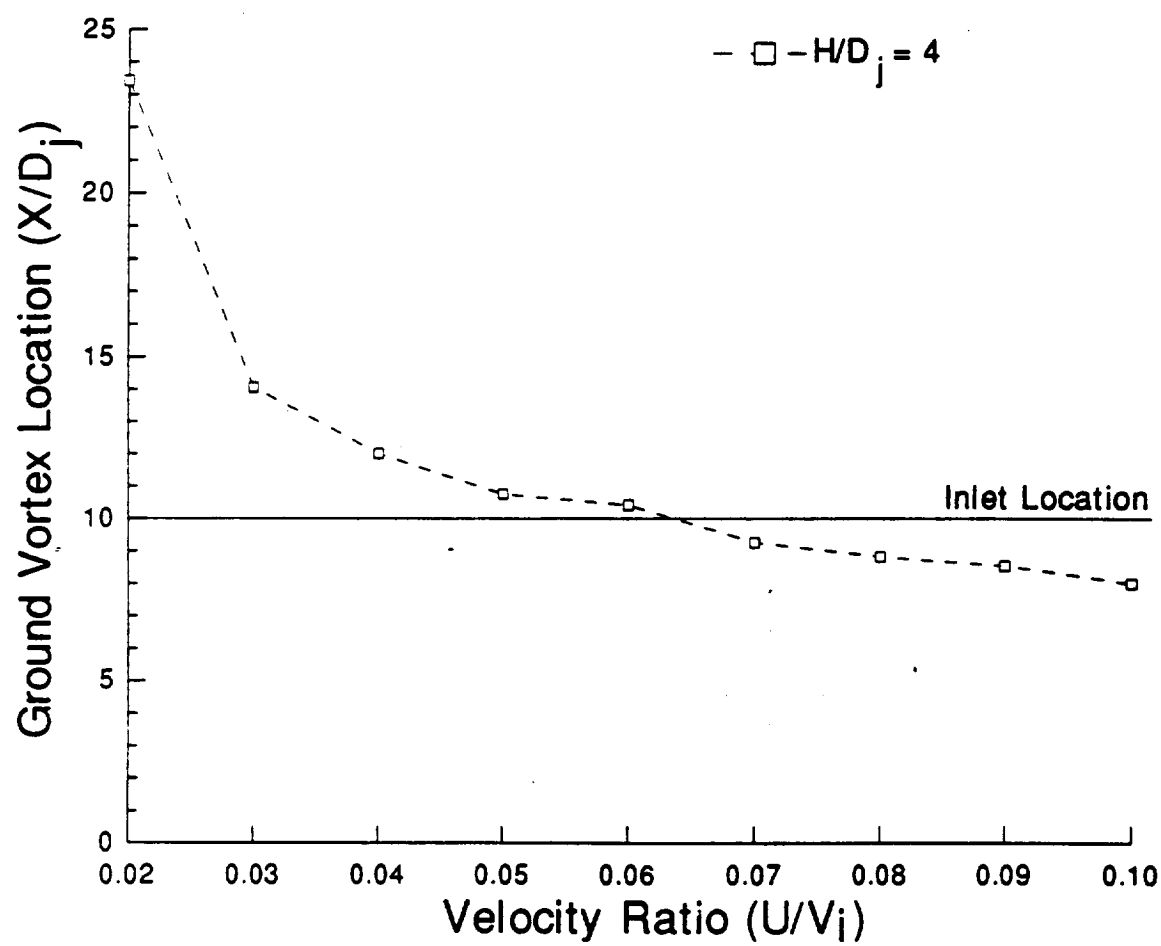


Figure 4.31: Ground Vortex Location Versus Velocity Ratio: $H/D_j = 4$

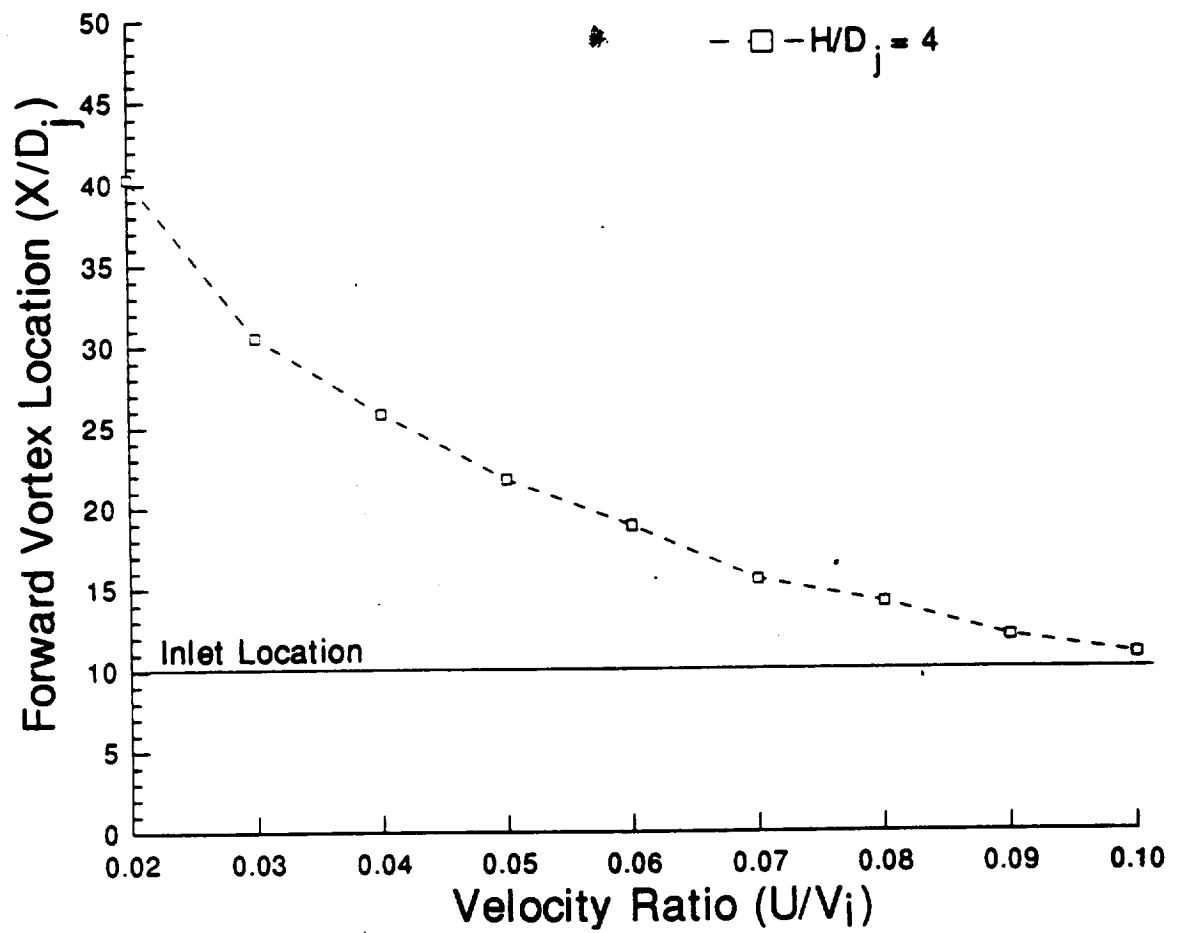


Figure 4.32: Forward Vortex Pair Location Versus Velocity Ratio: $H/D_j = 4$

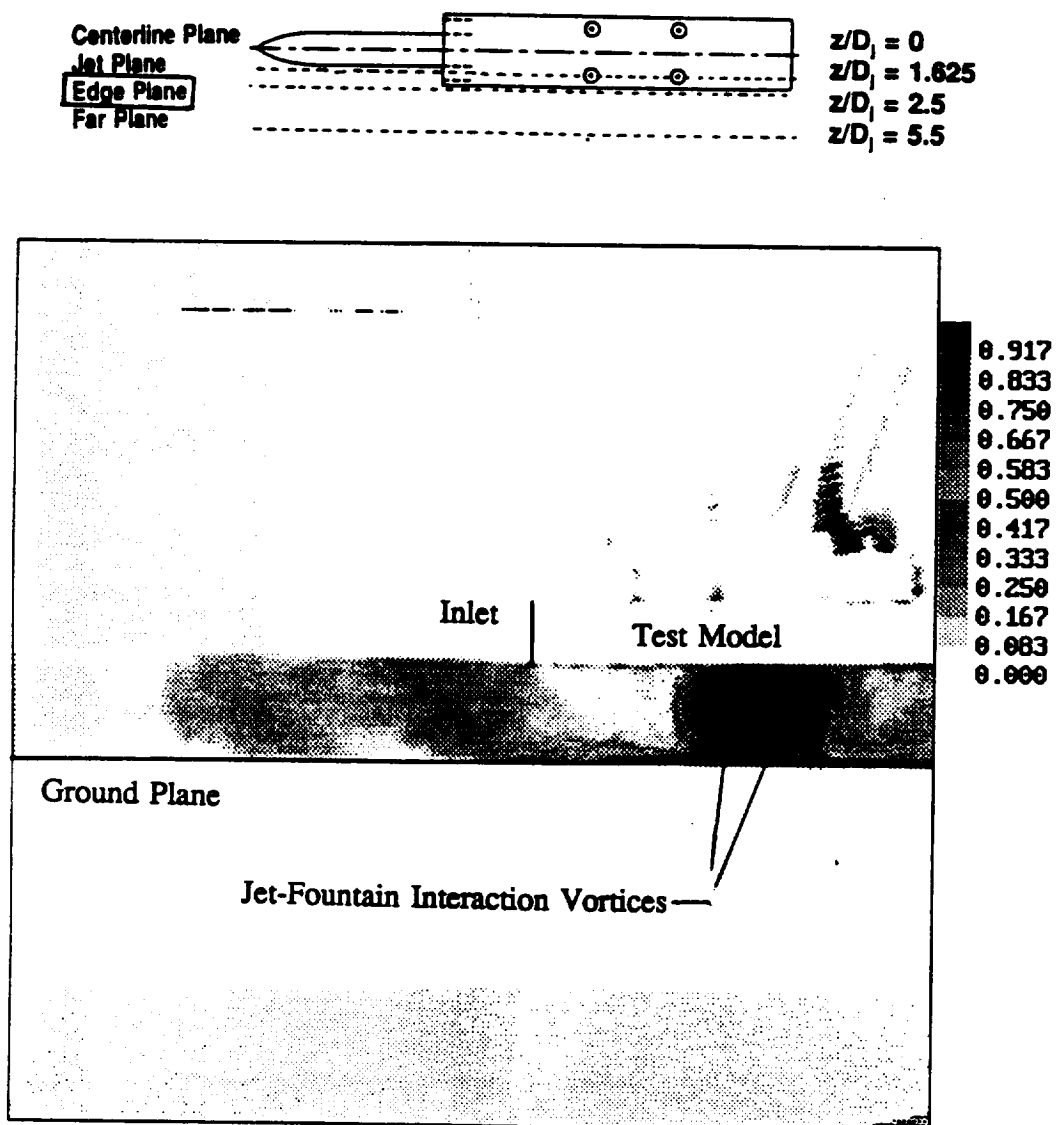


Figure 4.33: Single Frame Image of Smoke Concentration at Edge Plane
 $z/D_j = 2.5$, $H/D_j = 4$, $U/V_j = 0.03$

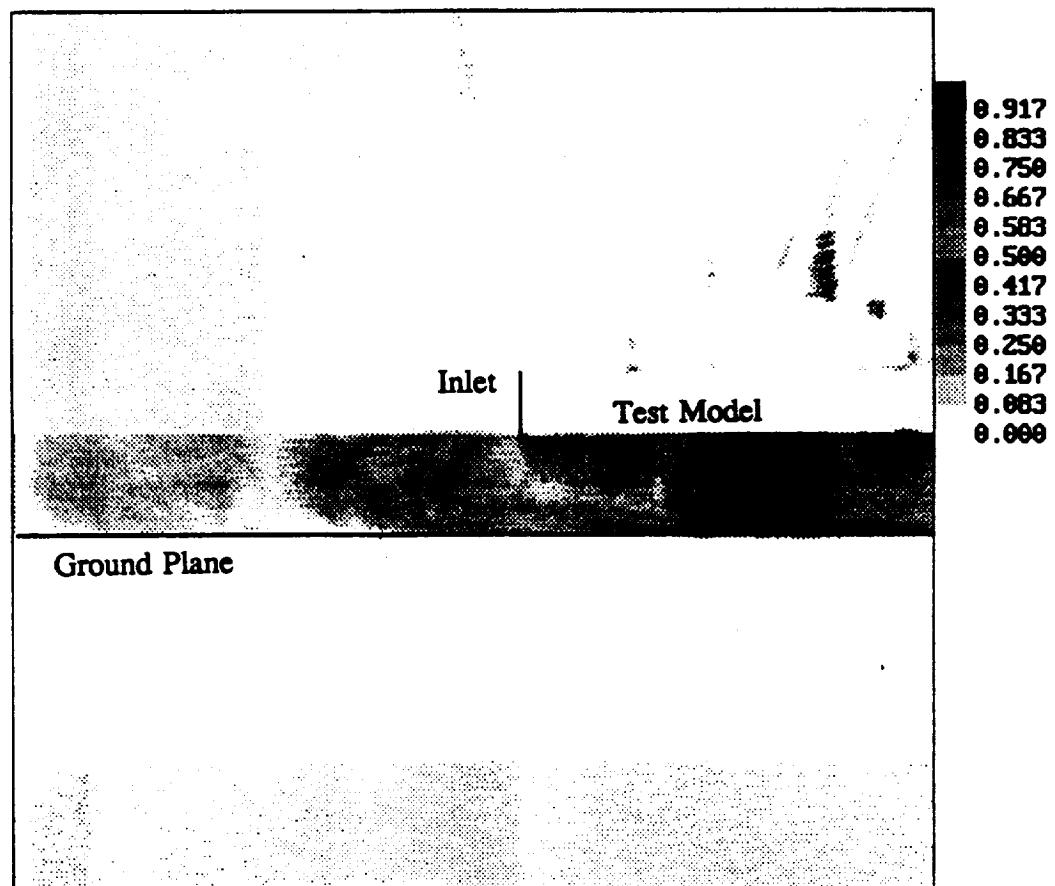
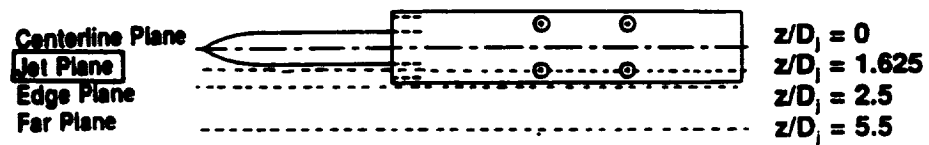


Figure 4.34: Single Frame Image of Smoke Concentration at Side Jet Pair Centerline
 $z/D_j = 1.625$, $H/D_j = 4$, $U/V_j = 0.03$

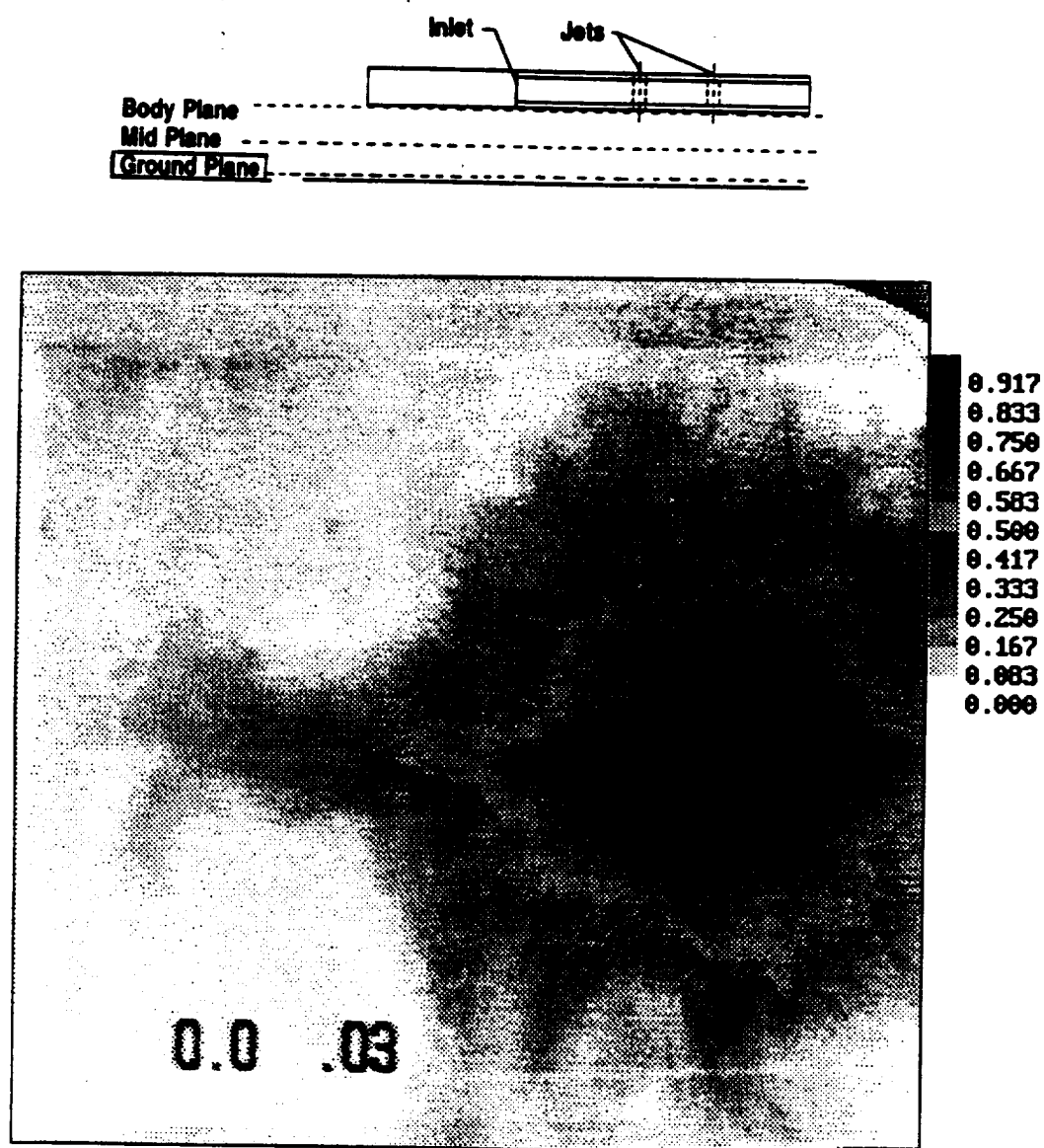


Figure 4.35: Single Frame Image of Smoke Concentration at Ground Plane
 $y/D_j = 0$, $H/D_j = 4$, $U/V_j = 0.03$

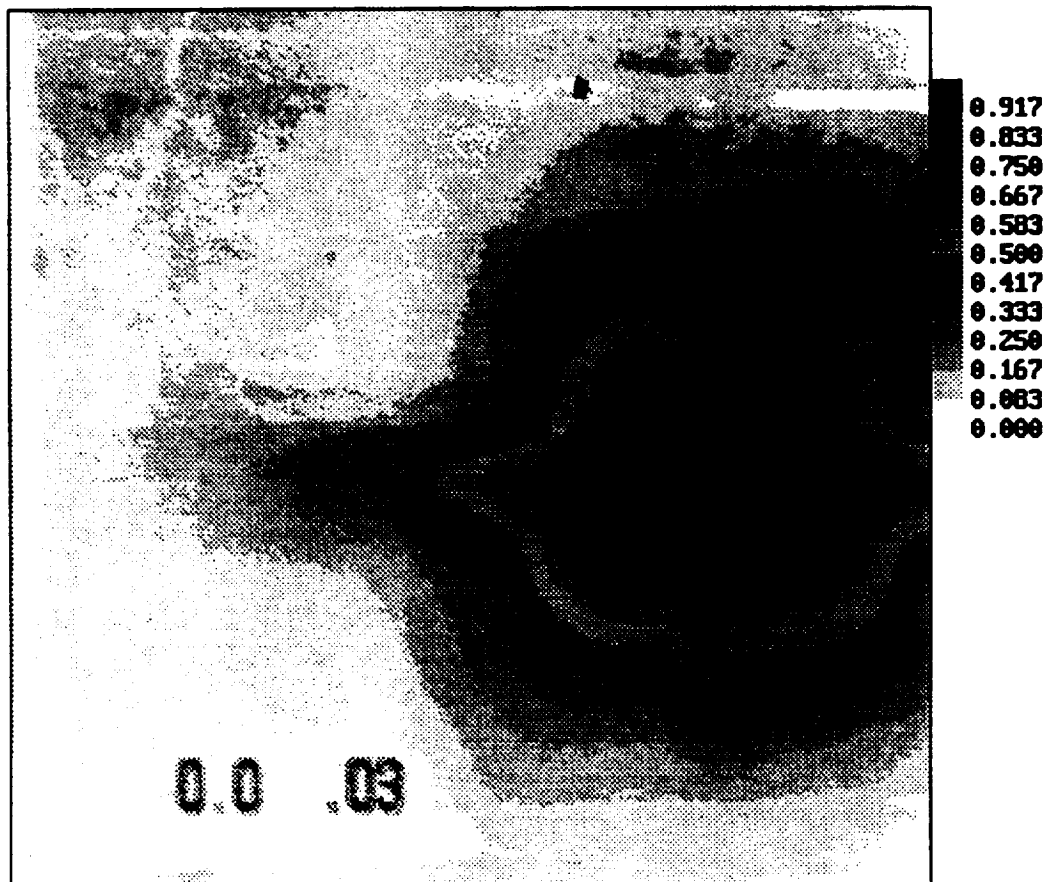
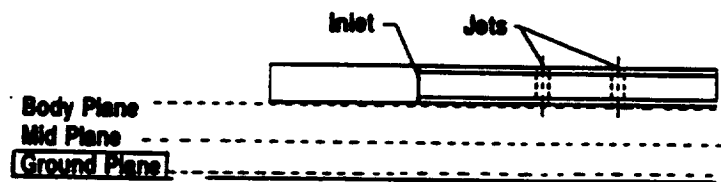


Figure 4.36: 127 Frame Average of Smoke Concentration at Ground Plane
 $y/D_j = 0.0$, $H/D_j = 4$, $U/V_j = 0.03$

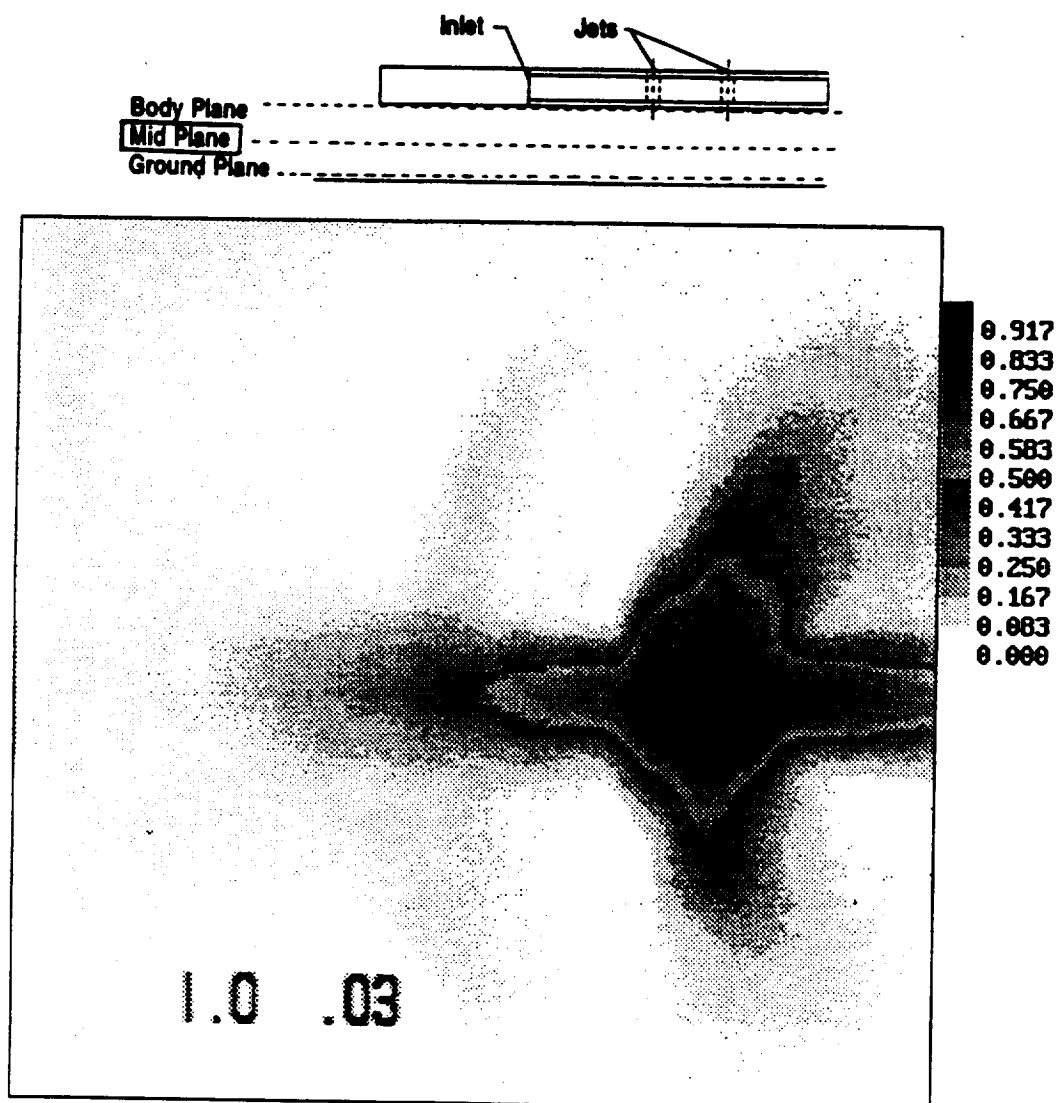


Figure 4.37: 127 Frame Average of Smoke Concentration at Mid Plane
 $y/D_j = 2.0$, $H/D_j = 4$, $U/V_j = 0.03$

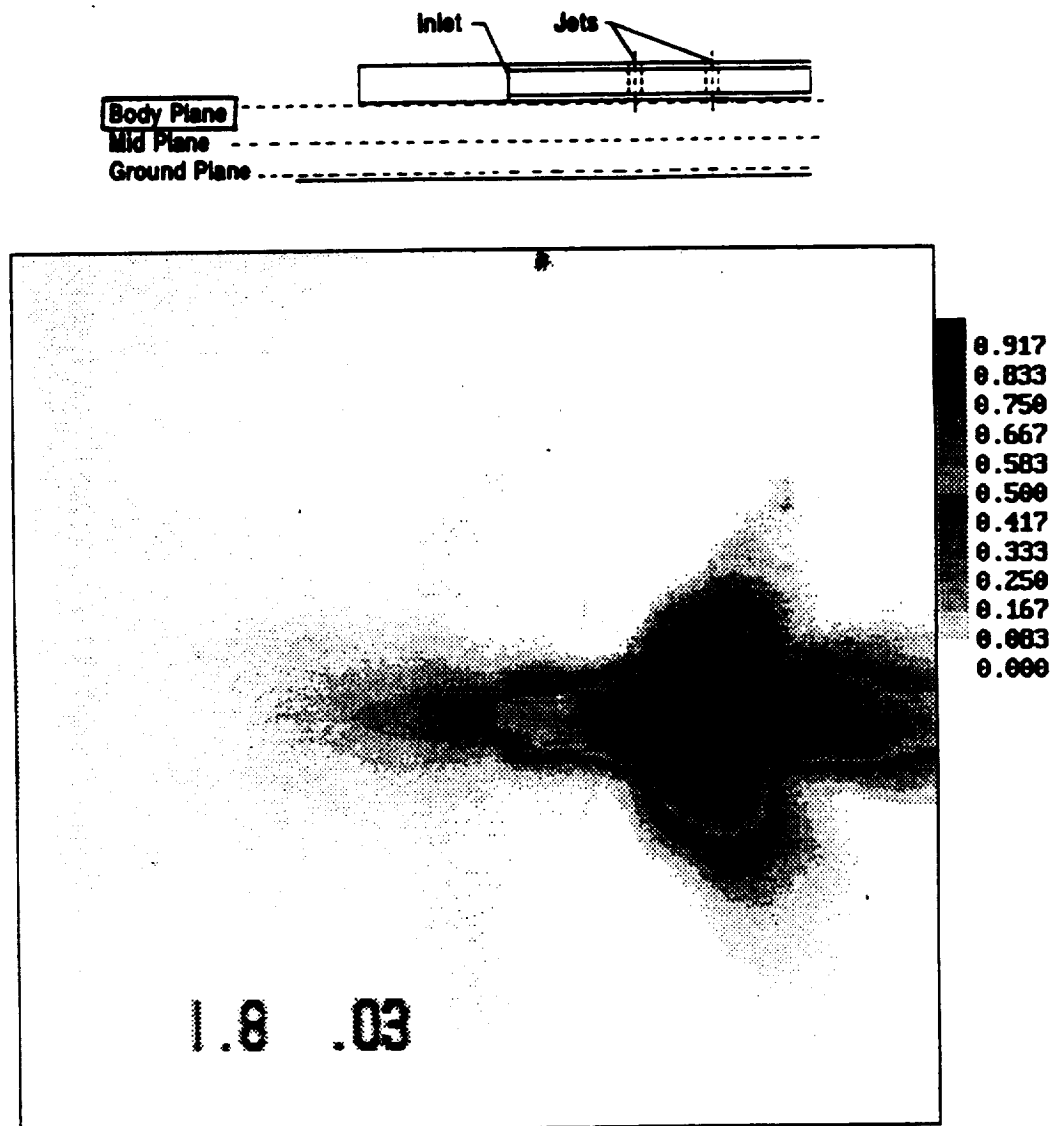


Figure 4.38: 127 Frame Average of Smoke Concentration at Model Body Plane
 $y/D_j = 3.6$, $H/D_j = 4$, $U/V_j = 0.03$

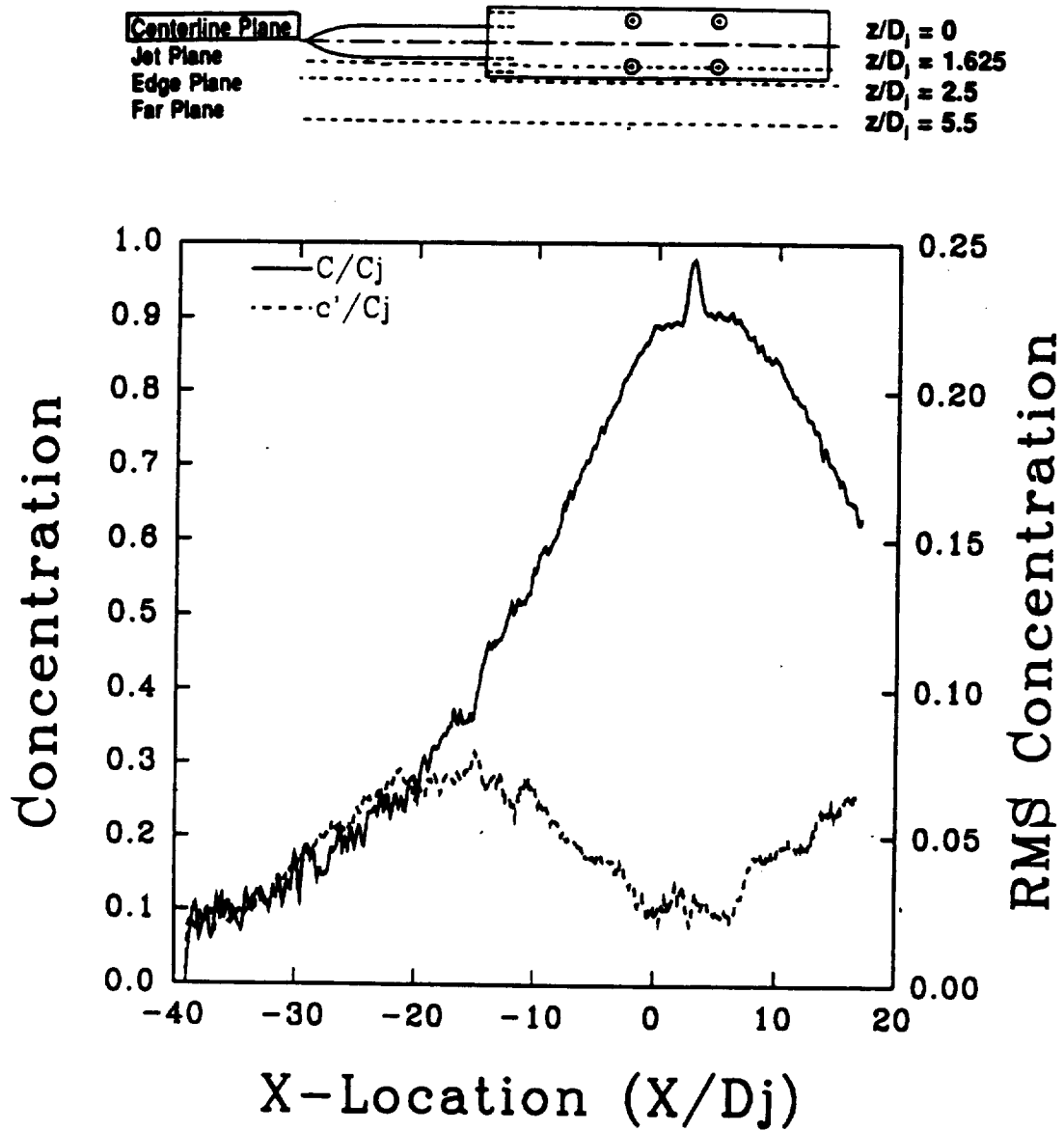


Figure 4.39: Mean and RMS Concentration Profiles at Model Centerline: $z/D_j = 0.0$
 Laser Sheet at Ground Plane: $y/D_j = 0$, $H/D_j = 4$, $U/V_j = 0.03$

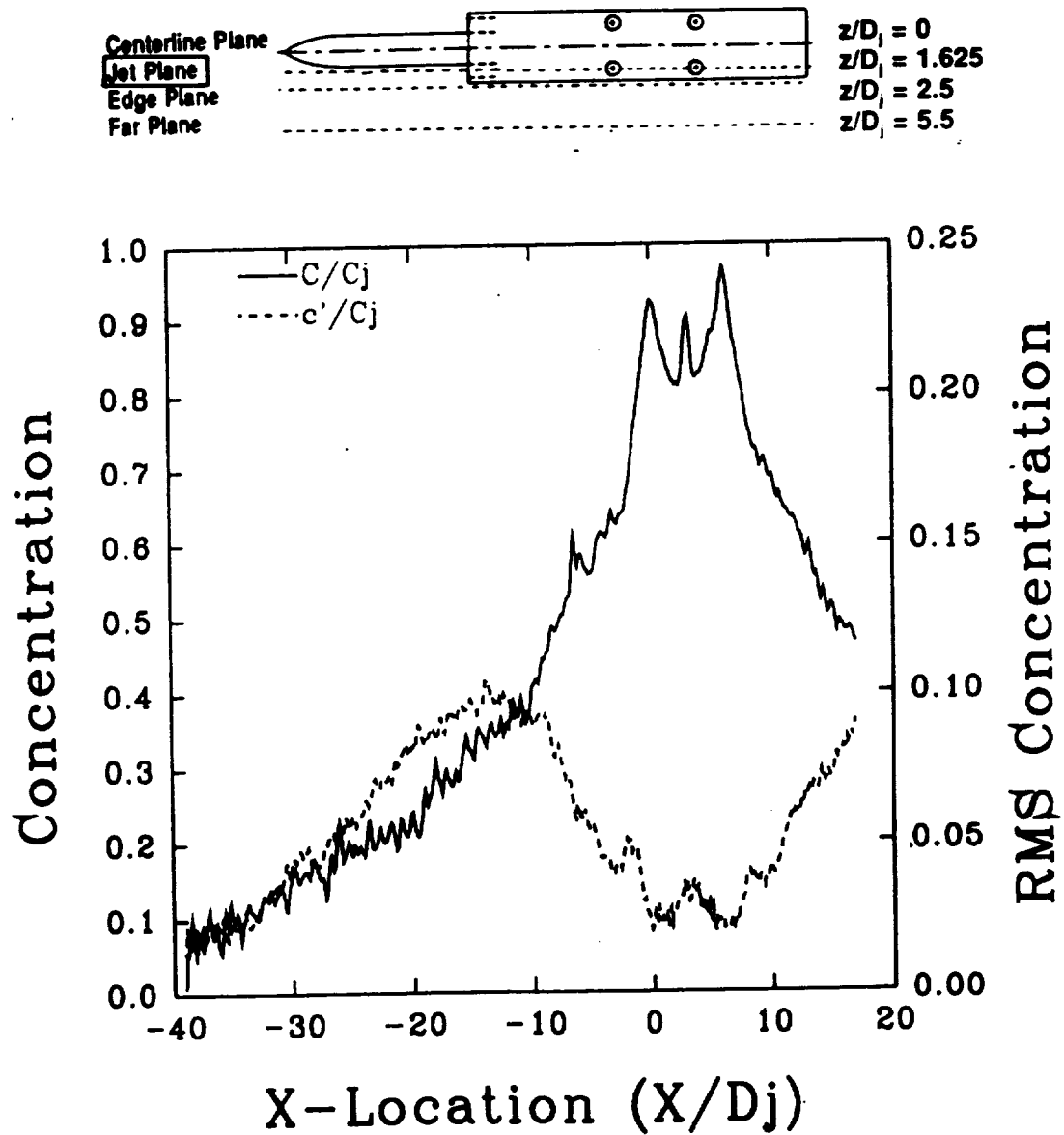


Figure 4.40: Mean and RMS Concentration Profiles at Side Jet Centerlines: $z/D_j = 1.625$
 Laser Sheet at Ground Plane: $y/D_j = 0$, $H/D_j = 4$, $U/V_j = 0.03$

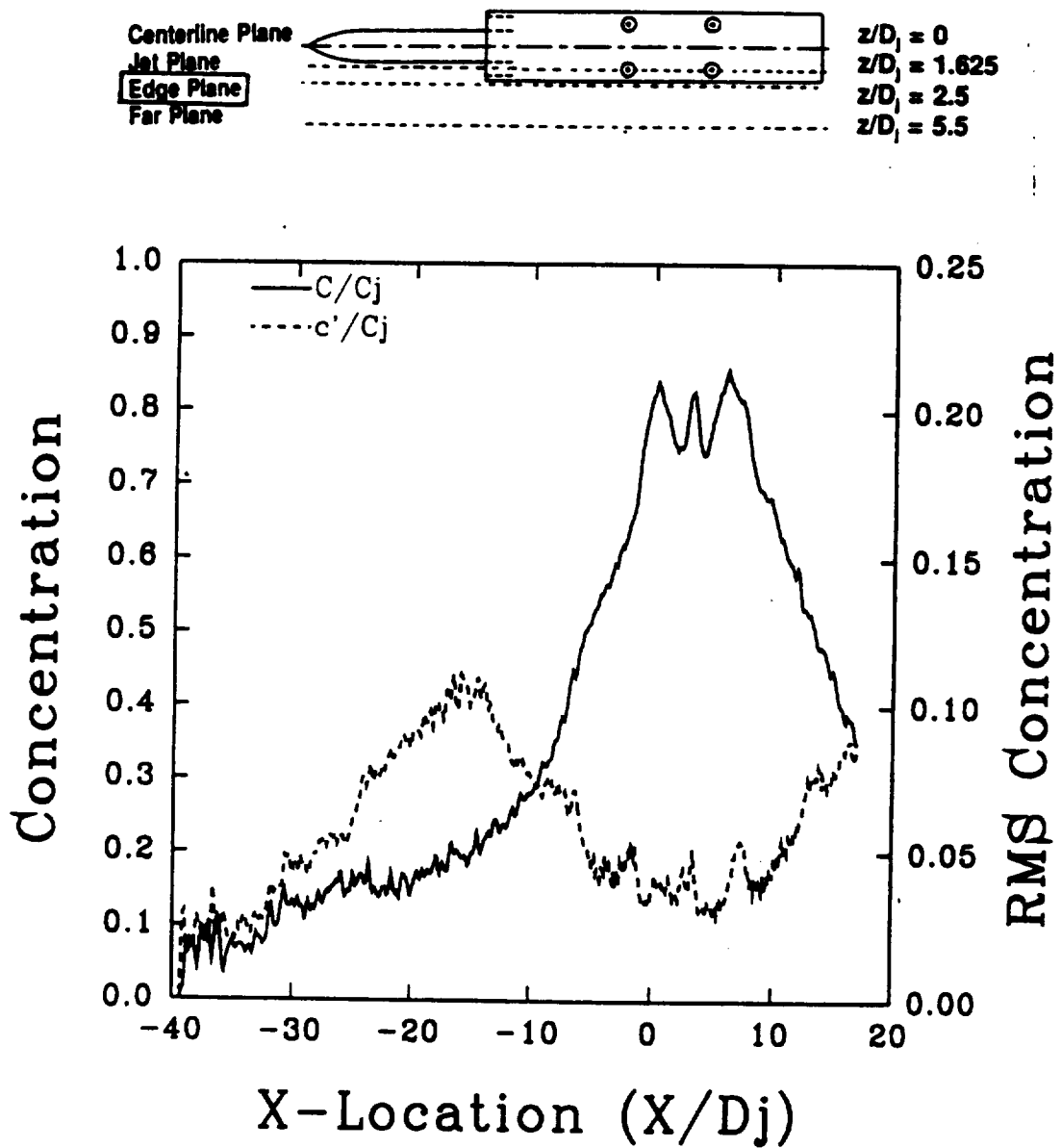


Figure 4.41: Mean and RMS Concentration Profiles at Model Edge: $z/D_j = 2.5$
 Laser Sheet at Ground Plane: $y/D_j = 0.0$, $H/D_j = 4$, $U/V_j = 0.03$

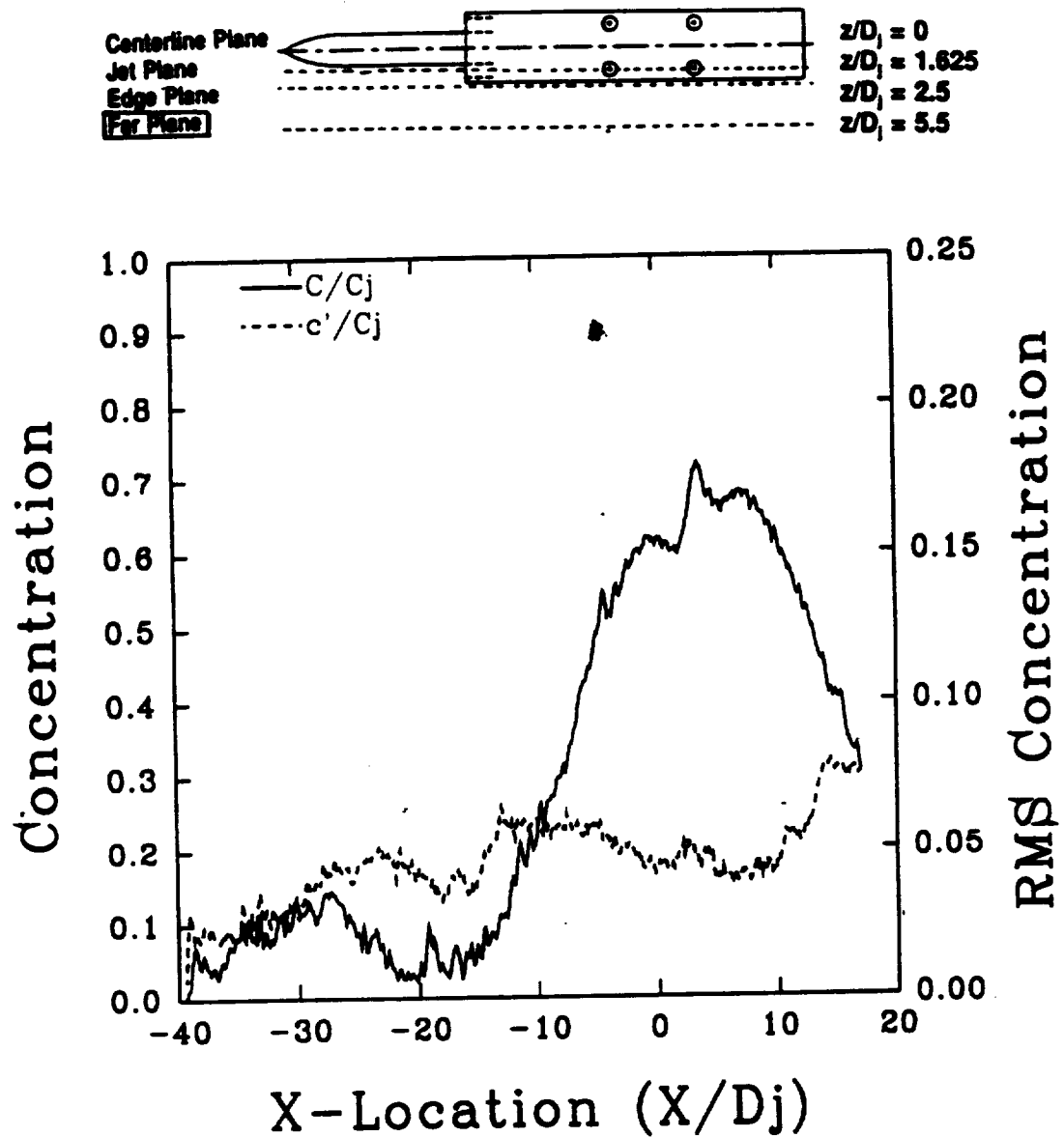


Figure 4.42: Mean and RMS Concentration Profiles at Far Plane: $z/D_j = 5.5$
 Laser Sheet at Ground Plane: $y/D_j = 0.0$, $H/D_j = 4$, $U/V_j = 0.03$

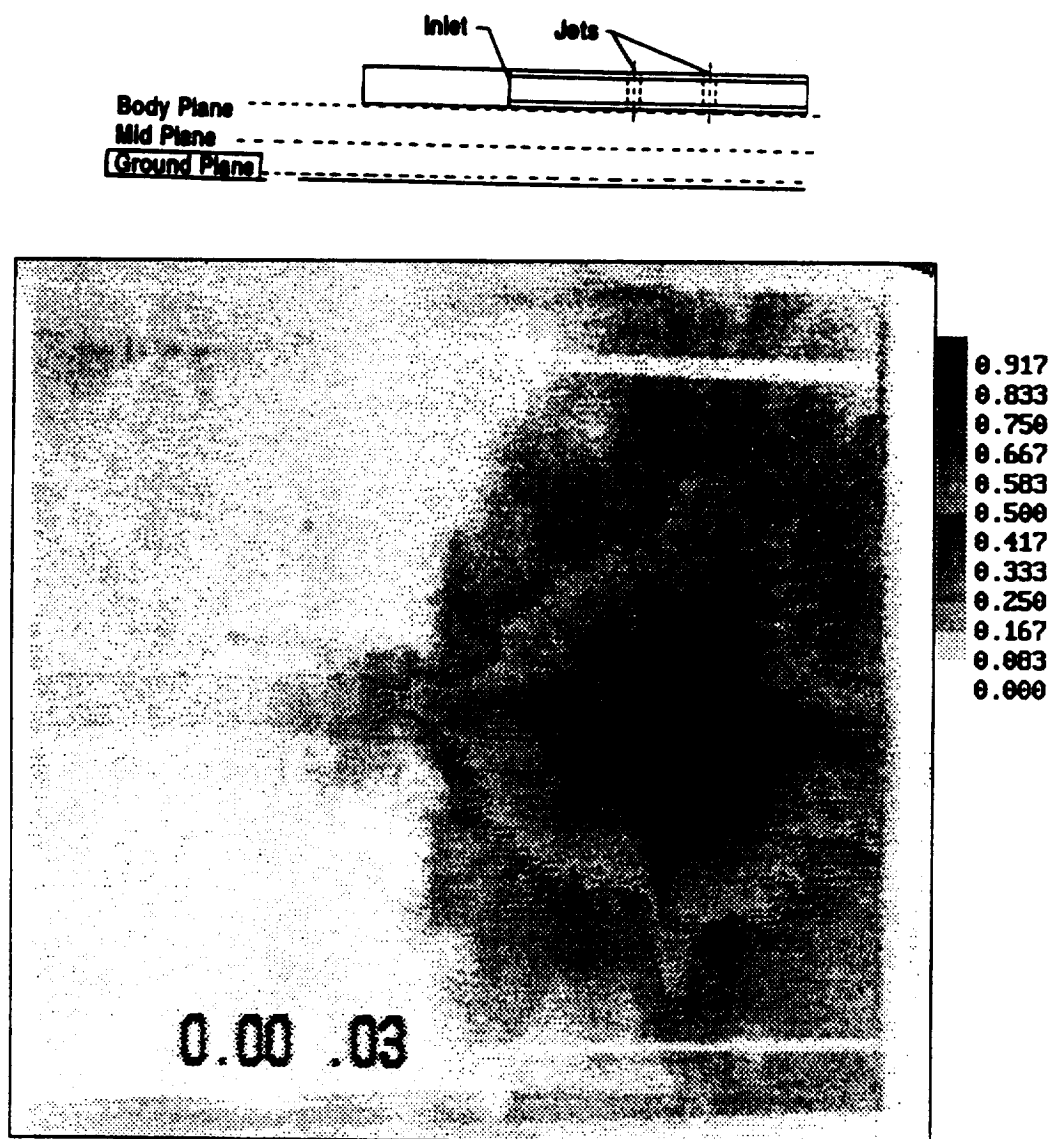


Figure 4.43: Single Frame Image of Smoke Concentration at Ground Plane
 $y/D_j = 0$, $H/D_j = 2$, $U/V_j = 0.03$

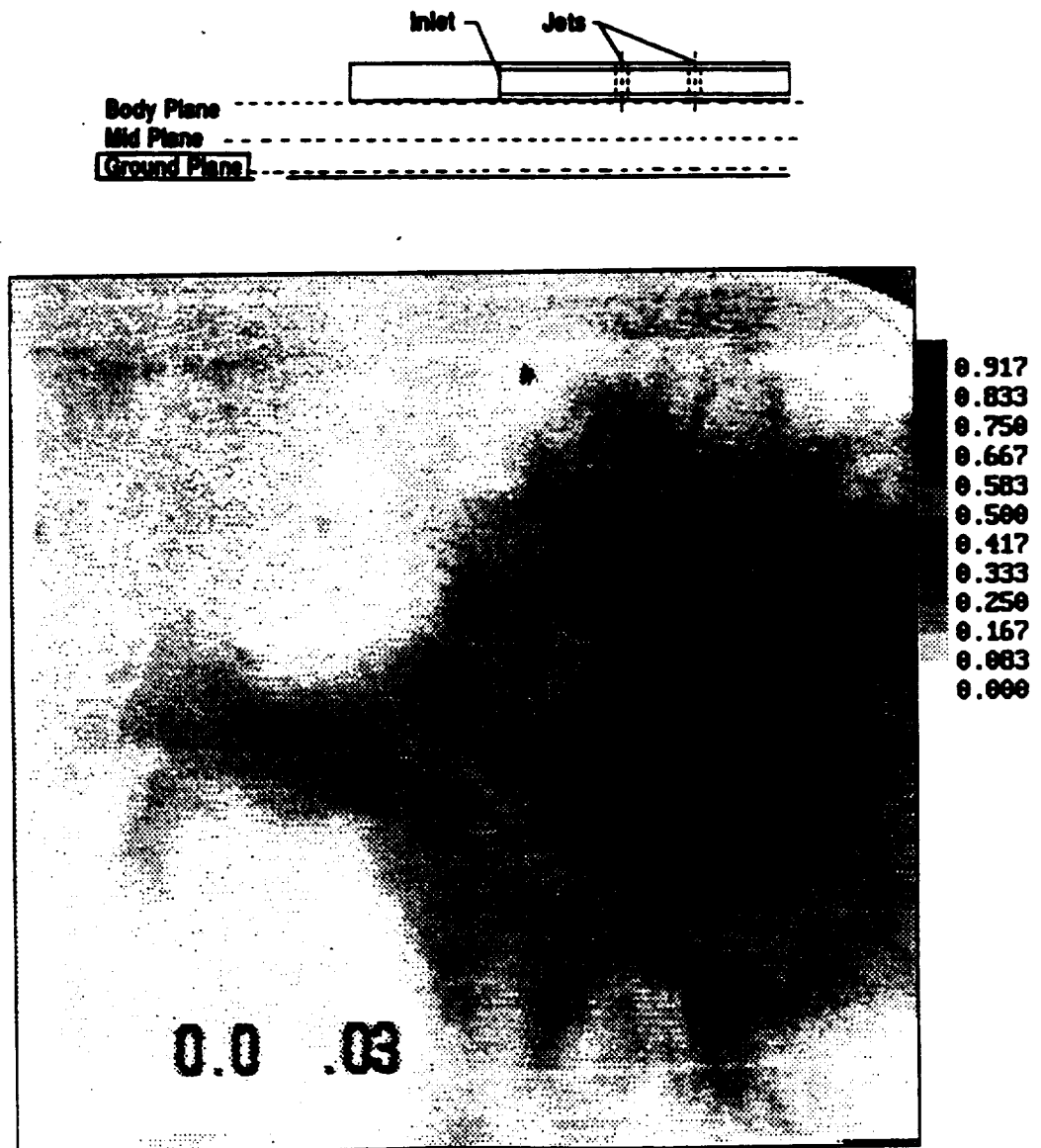


Figure 4.44: Single Frame Image of Smoke Concentration at Ground Plane
 $y/D_j = 0$, $H/D_j = 4$, $U/V_j = 0.03$

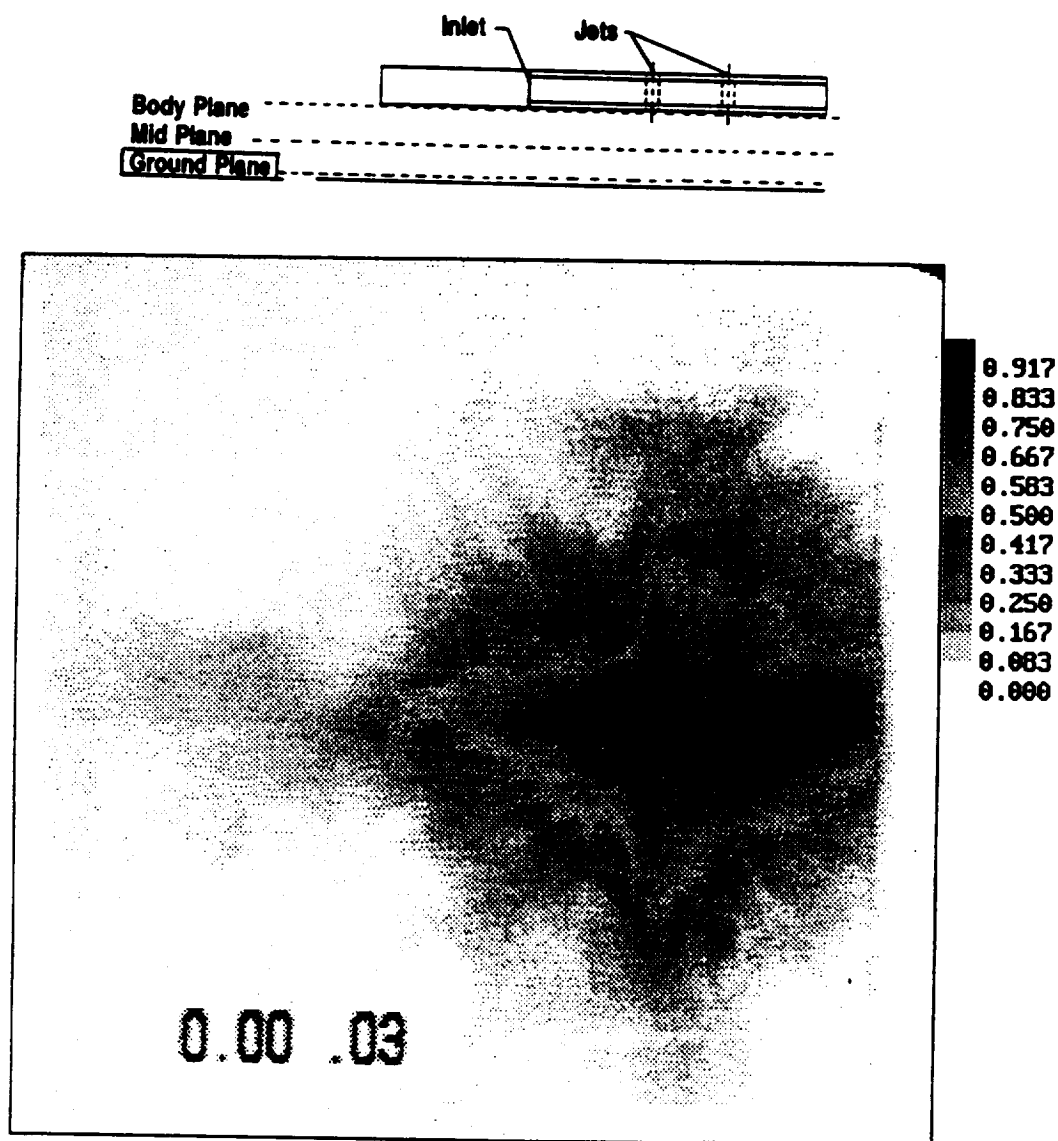


Figure 4.45: Single Frame Image of Smoke Concentration at Ground Plane
 $y/D_j = 0$, $H/D_j = 6$, $U/V_j = 0.03$

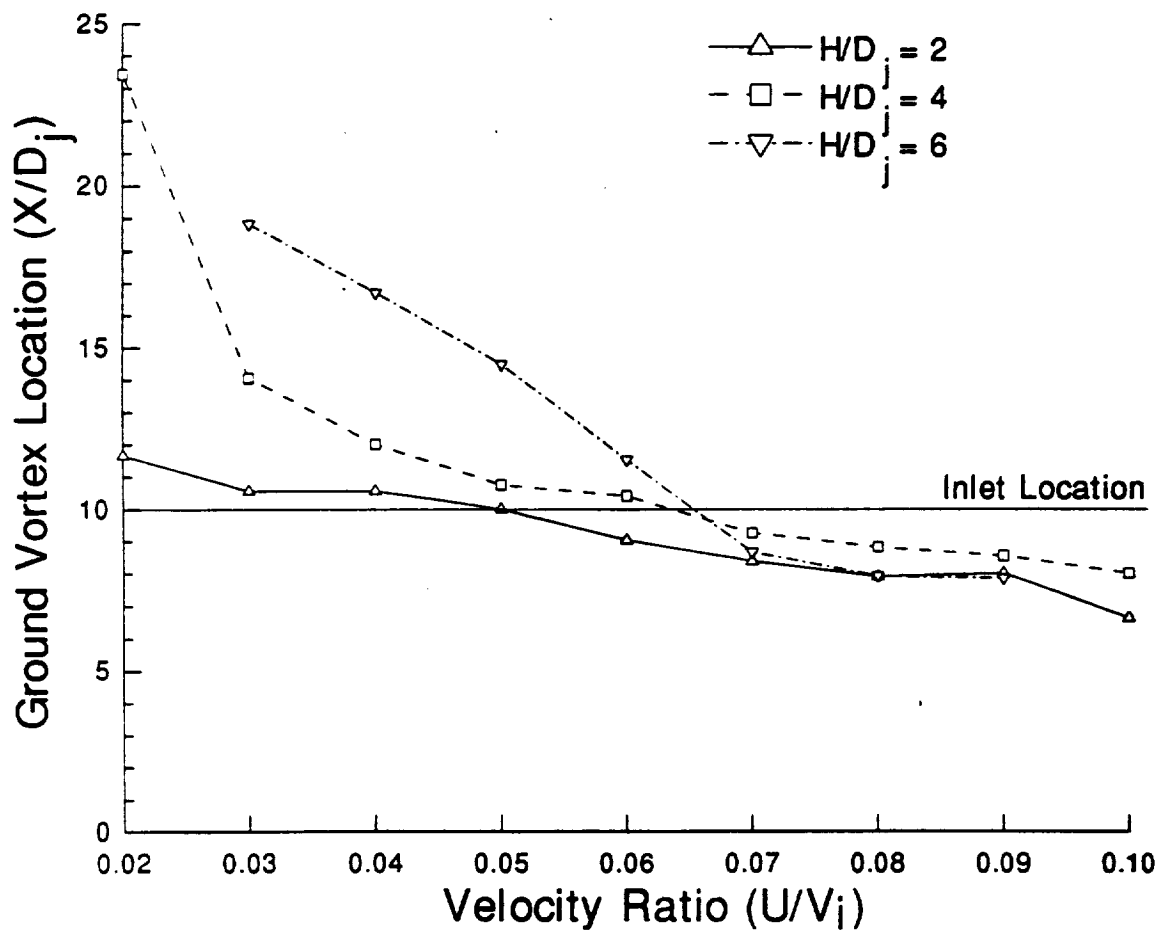


Figure 4.46: Ground Vortex Location Versus Velocity Ratio (U/V_j)

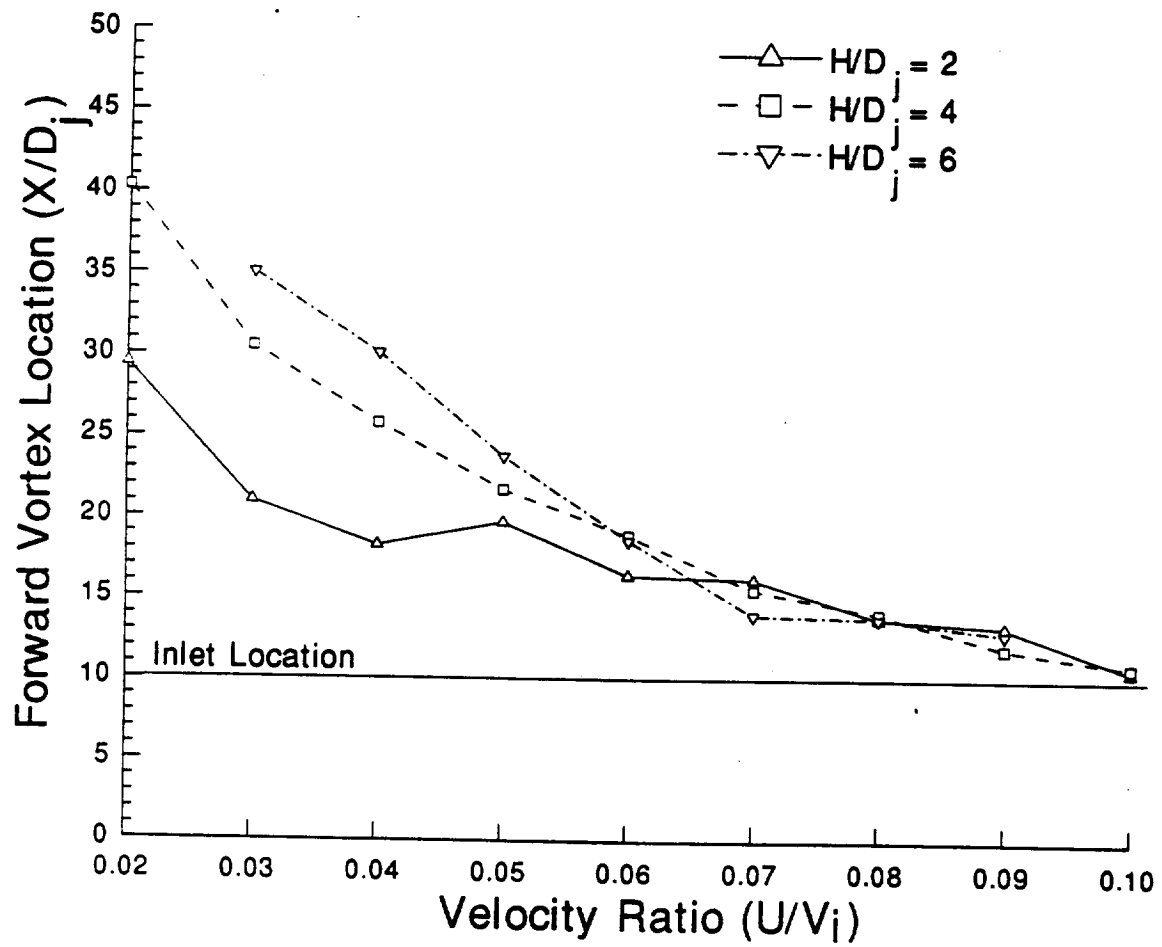


Figure 4.47: Forward Vortex Pair Location Versus Velocity Ratio (U/V_i)

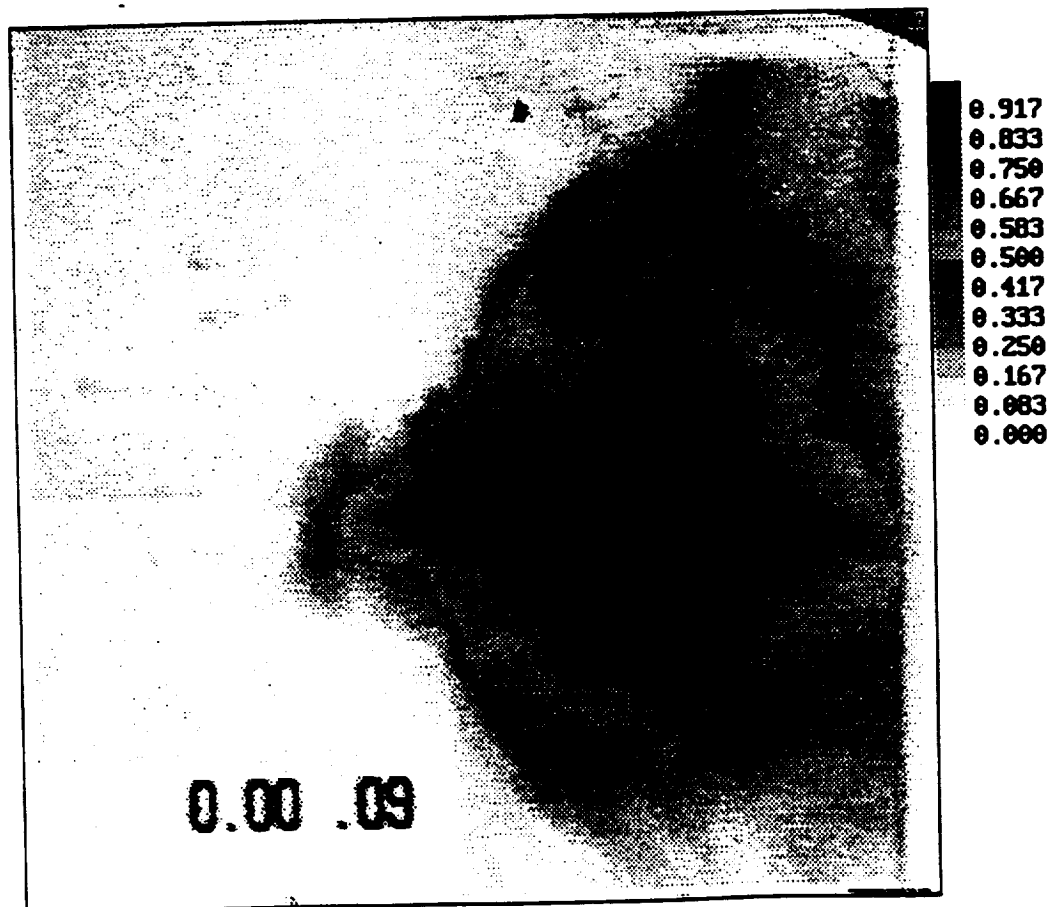
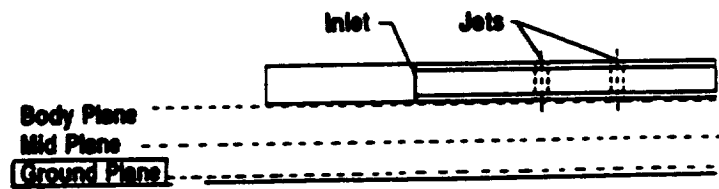


Figure 4.48: Single Frame Image of Smoke Concentration at Ground Plane
 $y/D_j = 0$, $H/D_j = 2$, $U/V_j = 0.09$

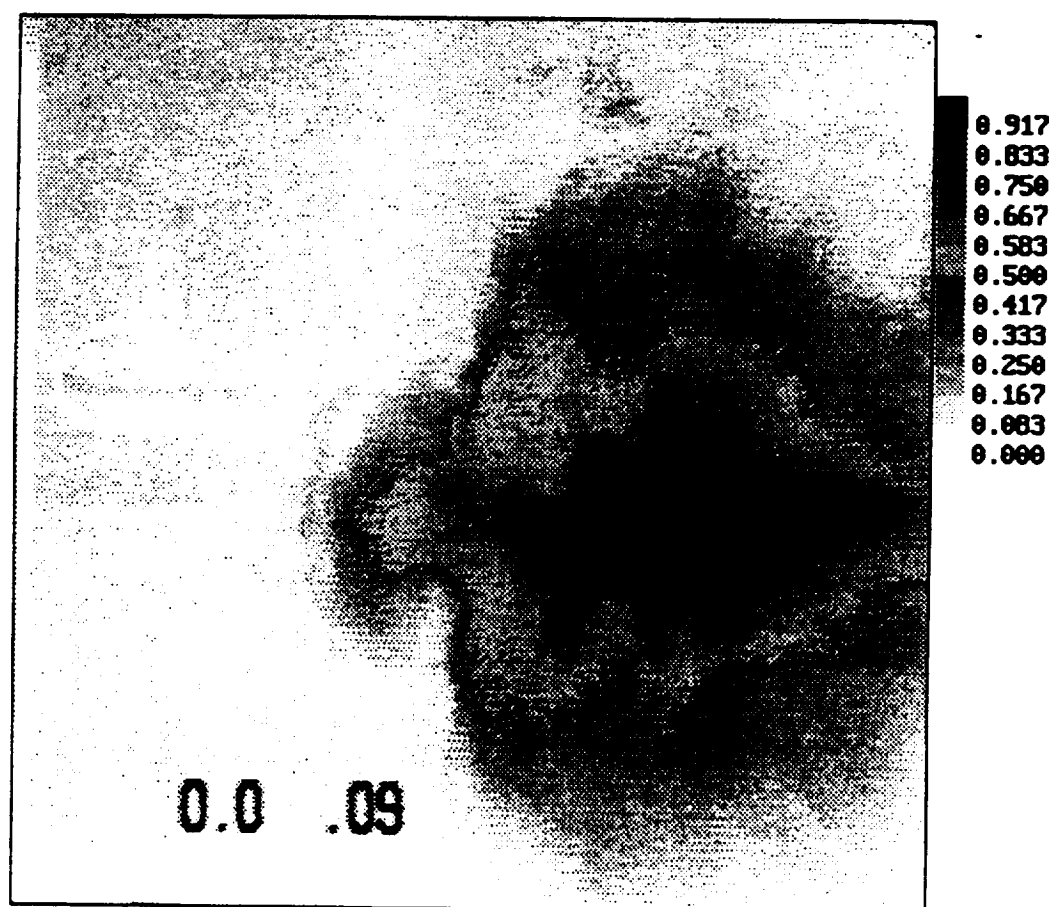
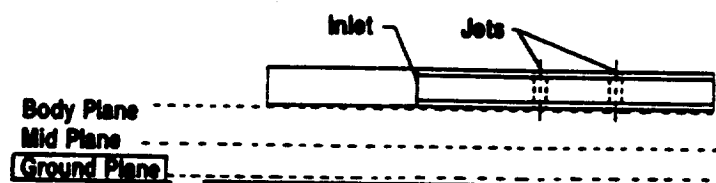


Figure 4.49: Single Frame Image of Smoke Concentration at Ground Plane
 $y/D_j = 0$, $H/D_j = 4$, $U/V_j = 0.09$

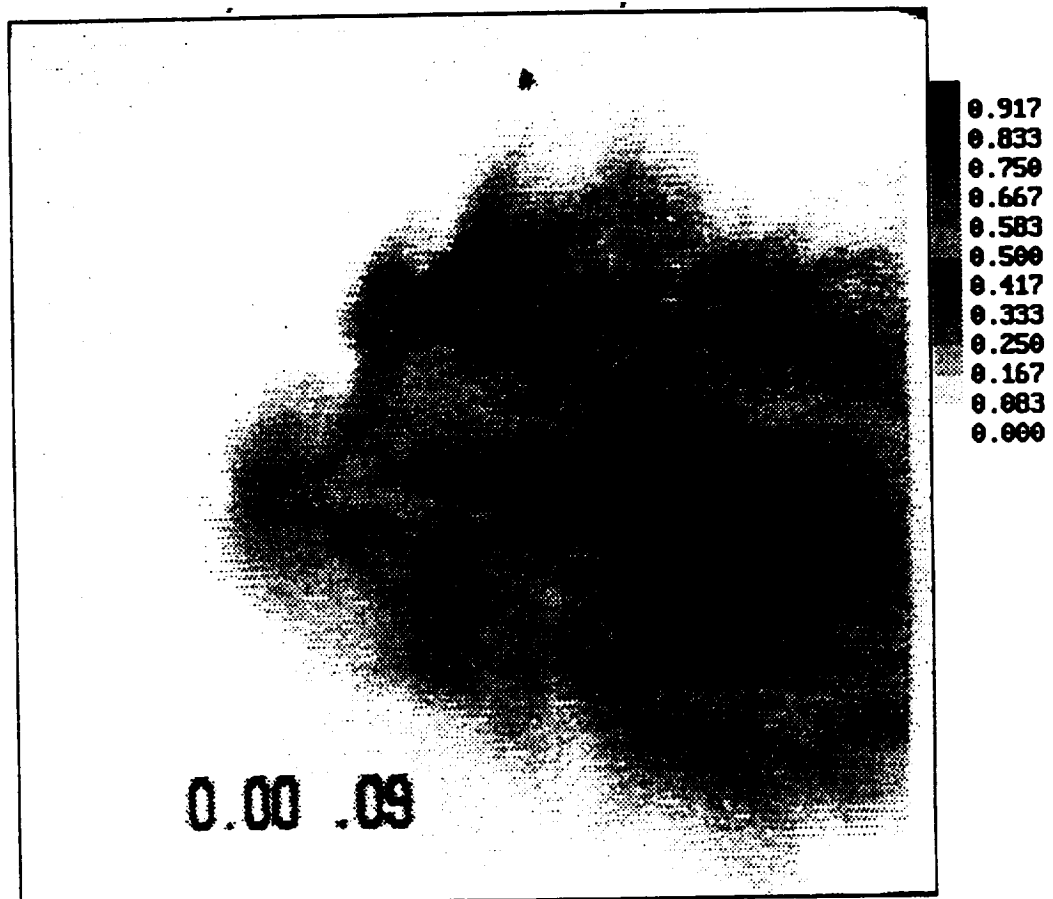
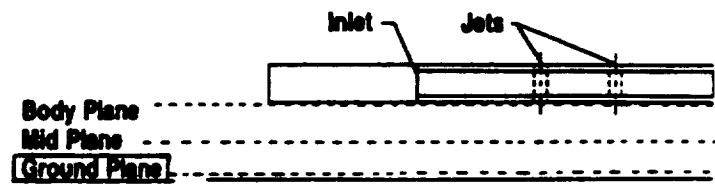


Figure 4.50: Single Frame Image of Smoke Concentration at Ground Plane
 $y/D_j = 0$, $H/D_j = 6$, $U/V_j = 0.09$

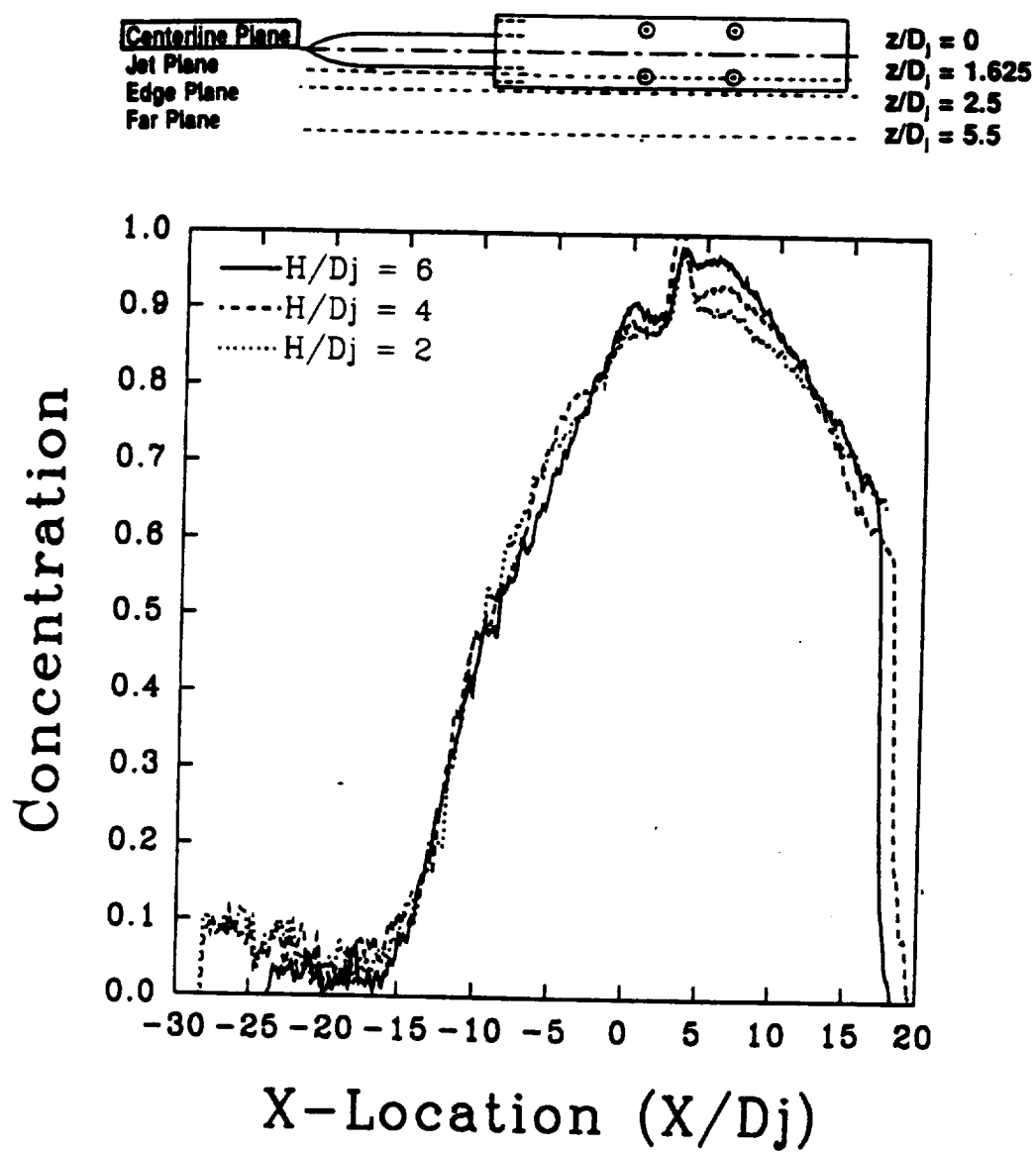


Figure 4.51: Mean Concentration Profiles at Model Centerline: $z/D_j = 0.0$
 Laser Sheet at Ground Plane: $y/D_j = 0.0$, $U/V_j = 0.09$

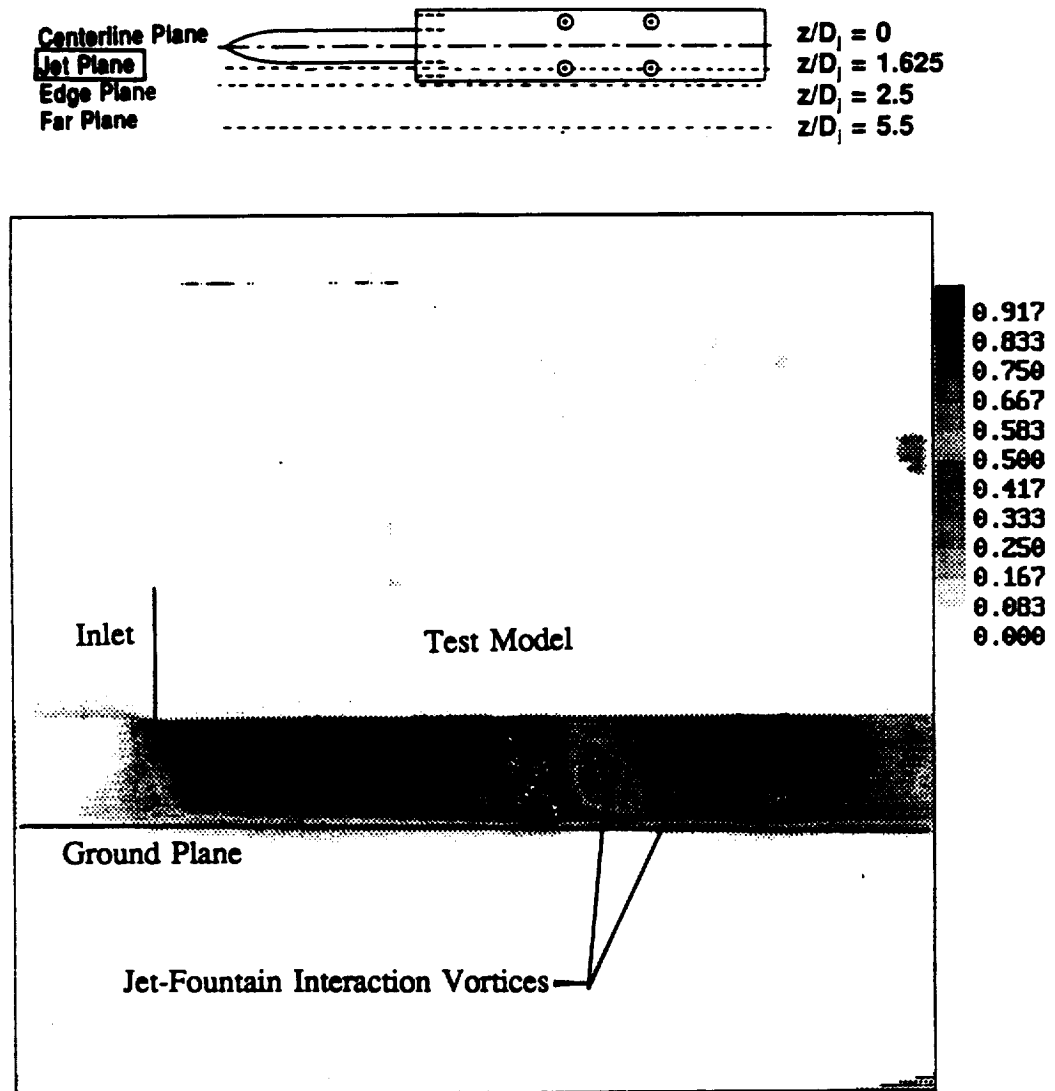


Figure 4.52: Single Frame Image of Smoke Concentration at Side Jet Pair Centerline
 $z/D_j = 1.625$, $H/D_j = 2$, $U/V_j = 0.09$

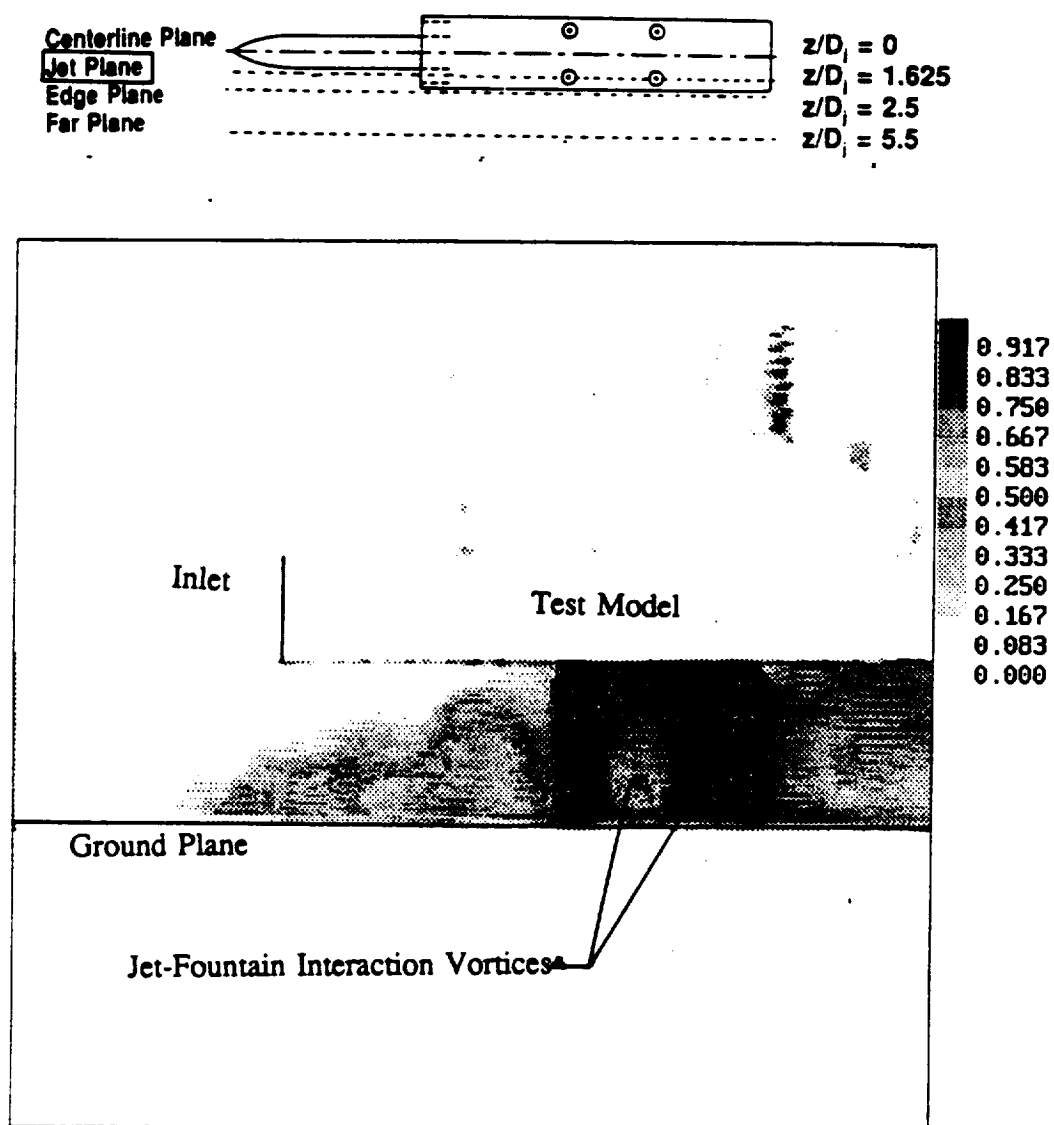


Figure 4.53: Single Frame Image of Smoke Concentration at Side Jet Pair Centerline
 $z/D_j = 1.625$, $H/D_j = 4$, $U/V_j = 0.09$

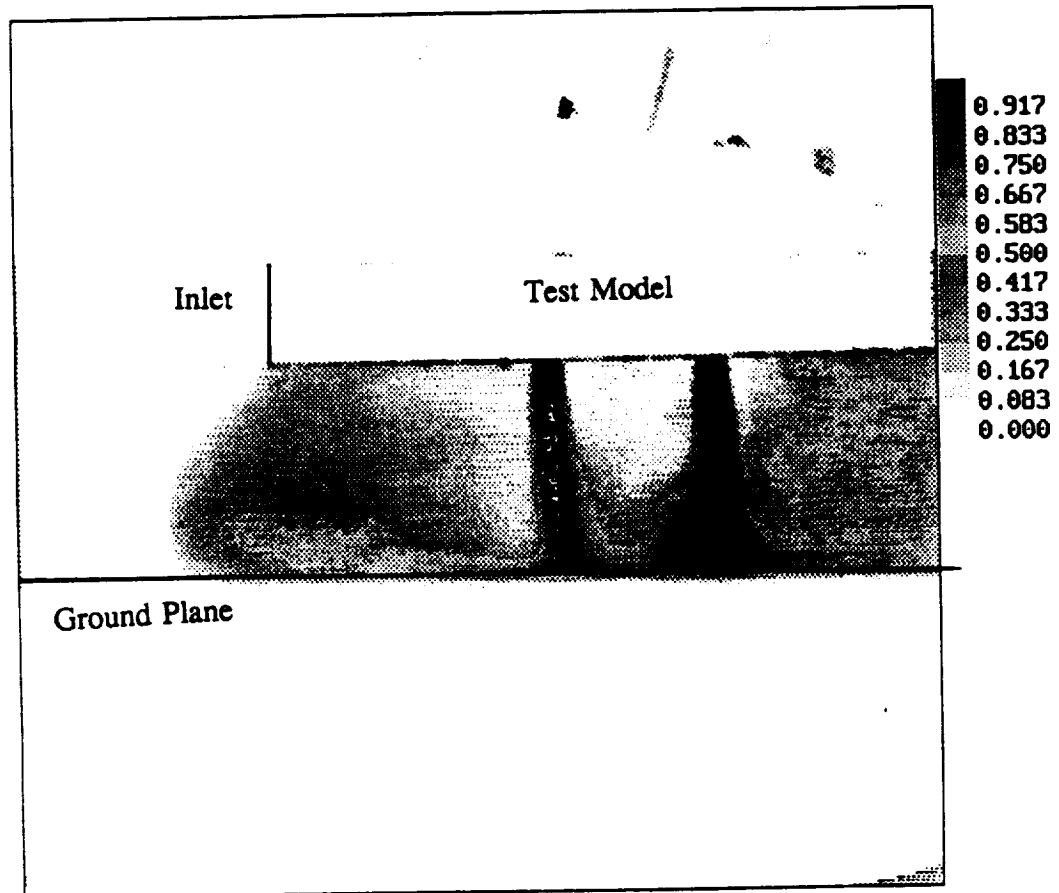
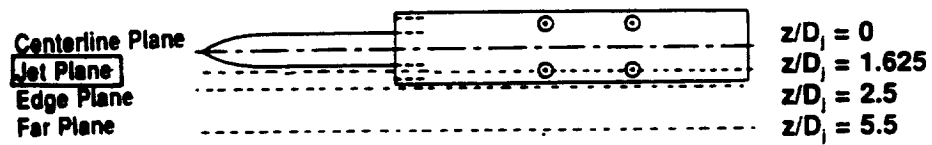


Figure 4.54: Single Frame Image of Smoke Concentration at Side Jet Pair Centerline
 $z/D_j = 1.625$, $H/D_j = 6$, $U/V_j = 0.09$

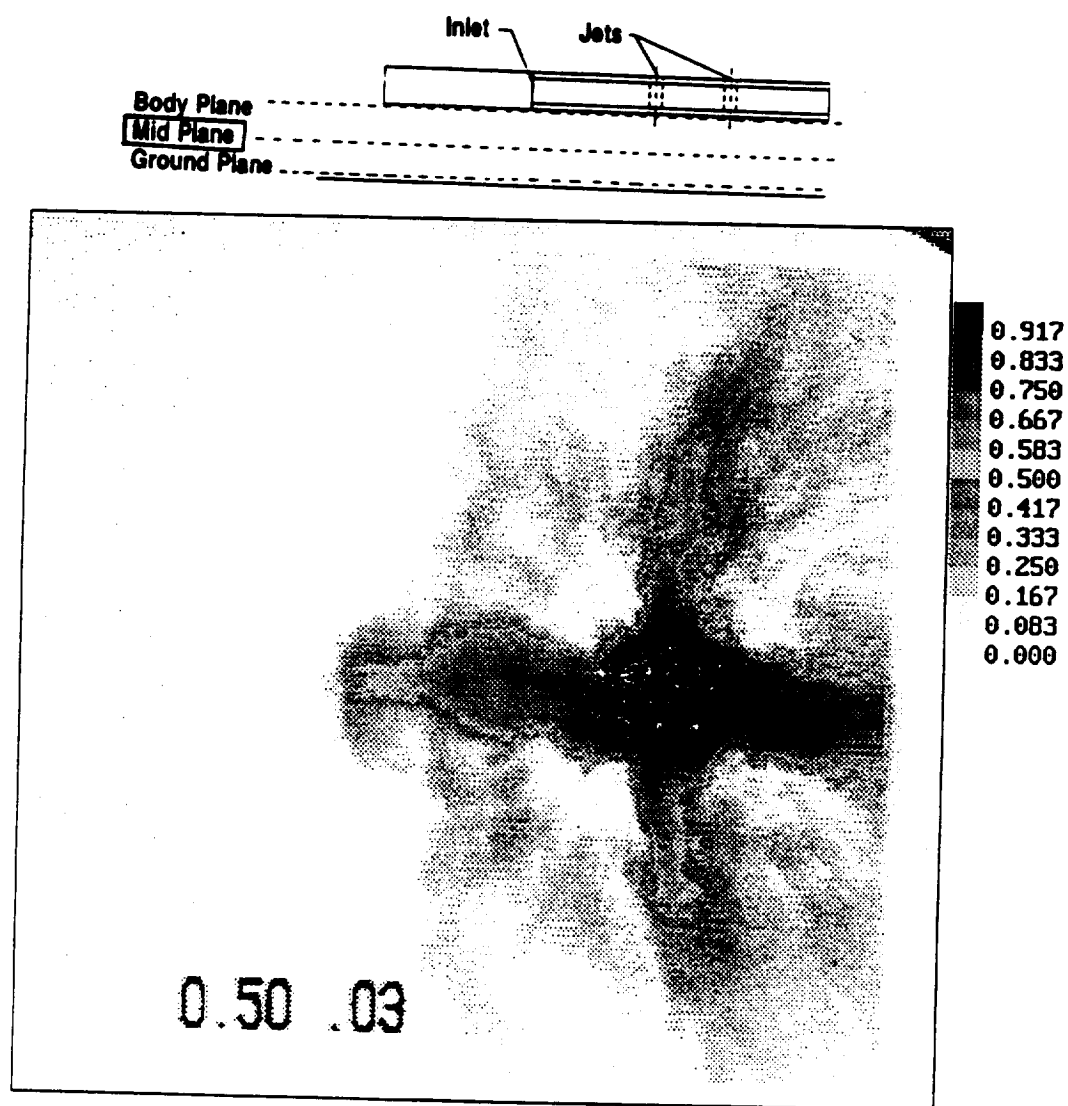


Figure 4.55: Single Frame Image of Smoke Concentration at Mid Plane
 $y/D_j = 1.0$, $H/D_j = 2$, $U/V_j = 0.03$

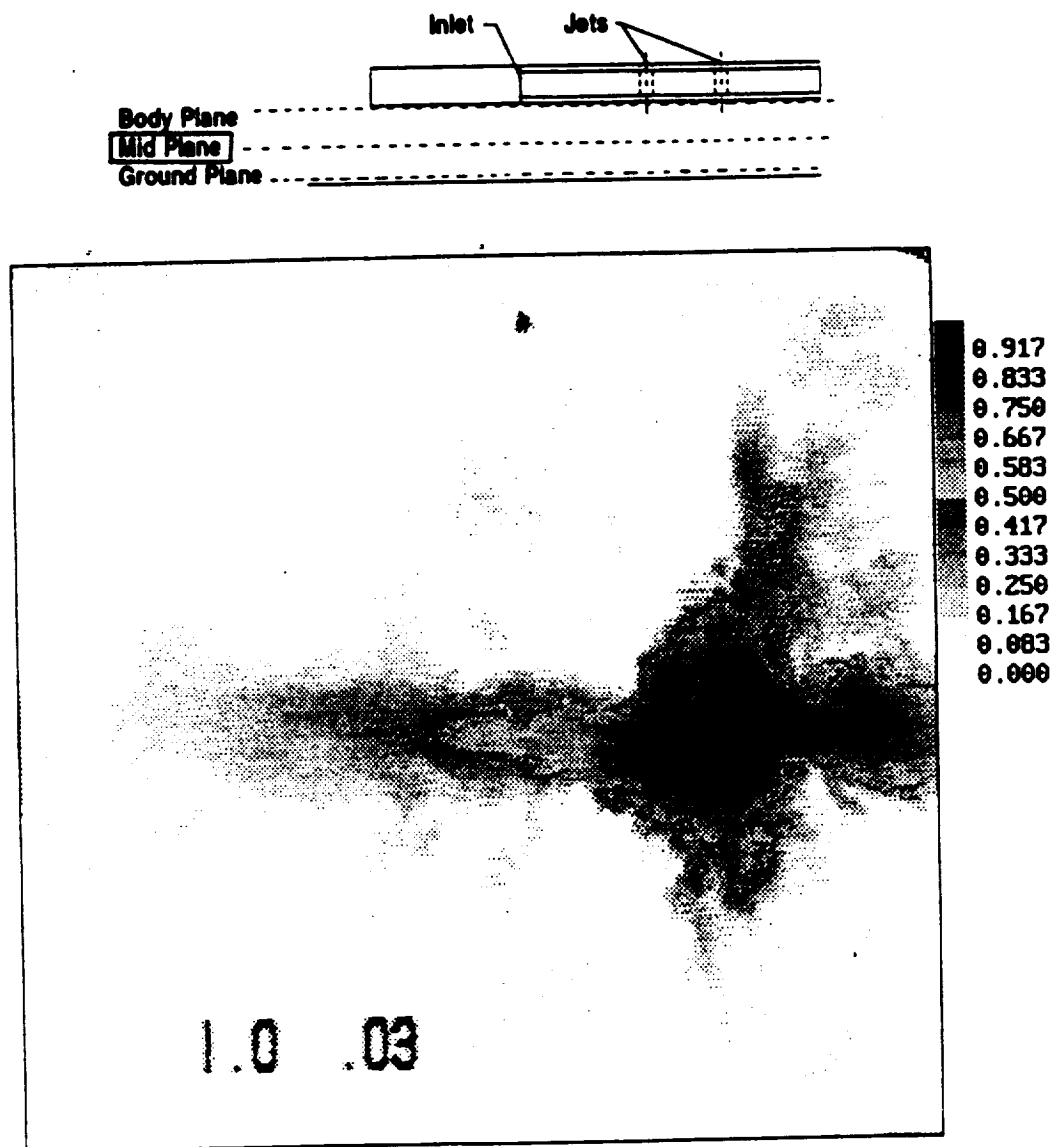


Figure 4.56: Single Frame Image of Smoke Concentration at Mid Plane
 $y/D_j = 2.0$, $H/D_j = 4$, $U/V_j = 0.03$

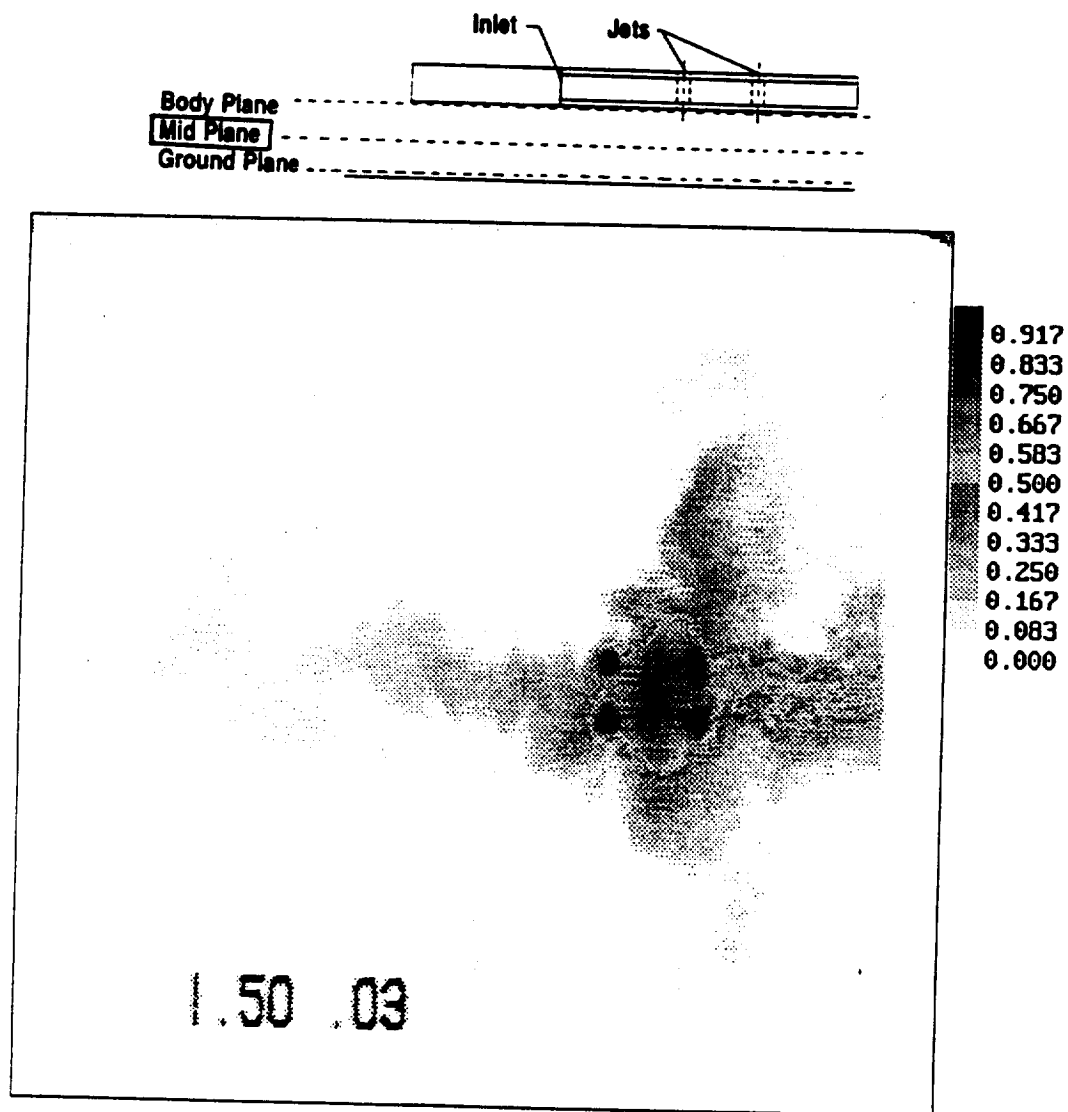


Figure 4.57: Single Frame Image of Smoke Concentration at Mid Plane
 $y/D_j = 3.0$, $H/D_j = 6$, $U/V_j = 0.03$

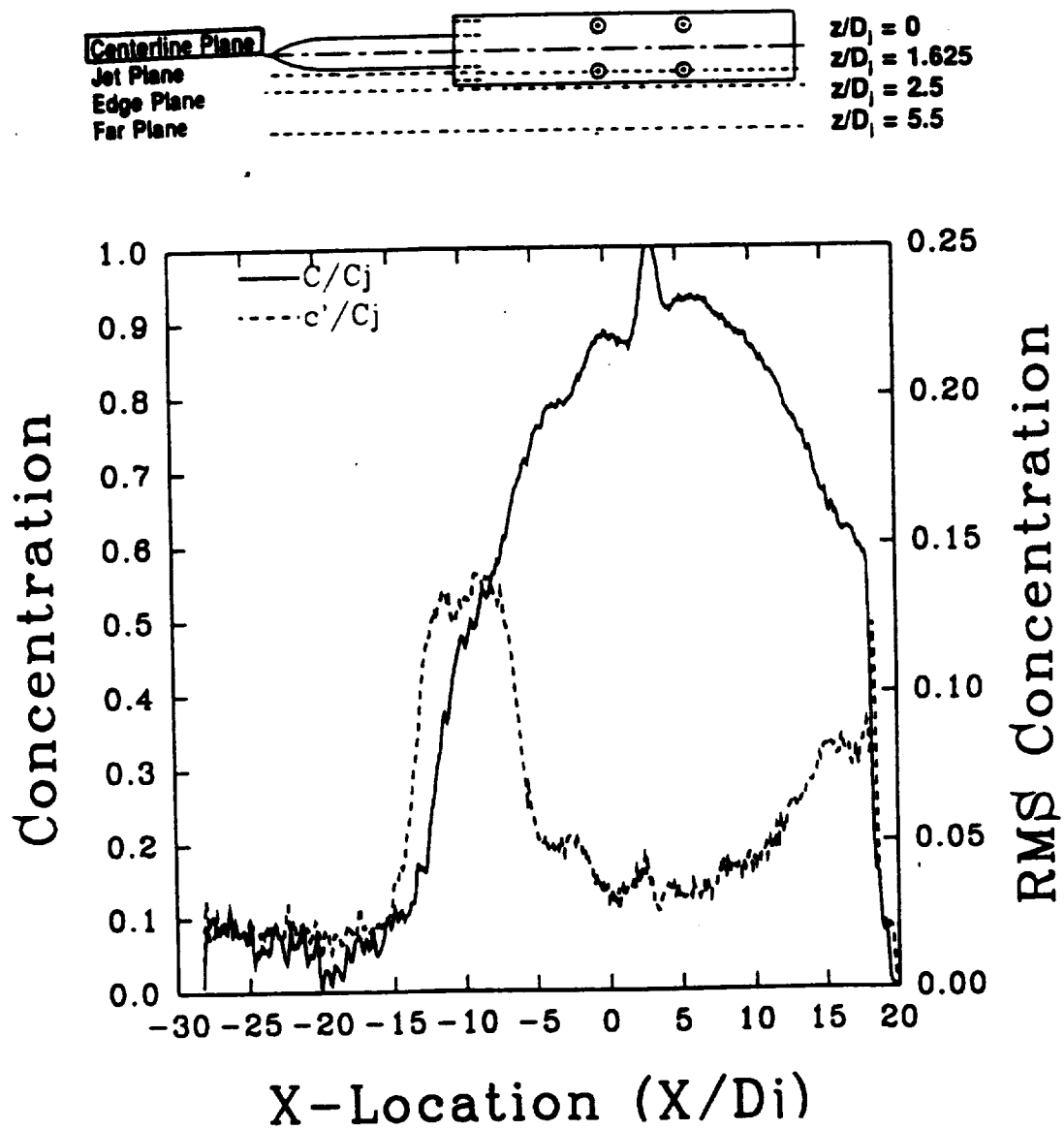


Figure 4.58: Mean and RMS Concentration Profiles at Model Centerline: $z/D_j = 0.0$
 Laser Sheet at Ground Plane: $y/D_j = 0$, $H/D_j = 2$, $U/V_j = 0.09$

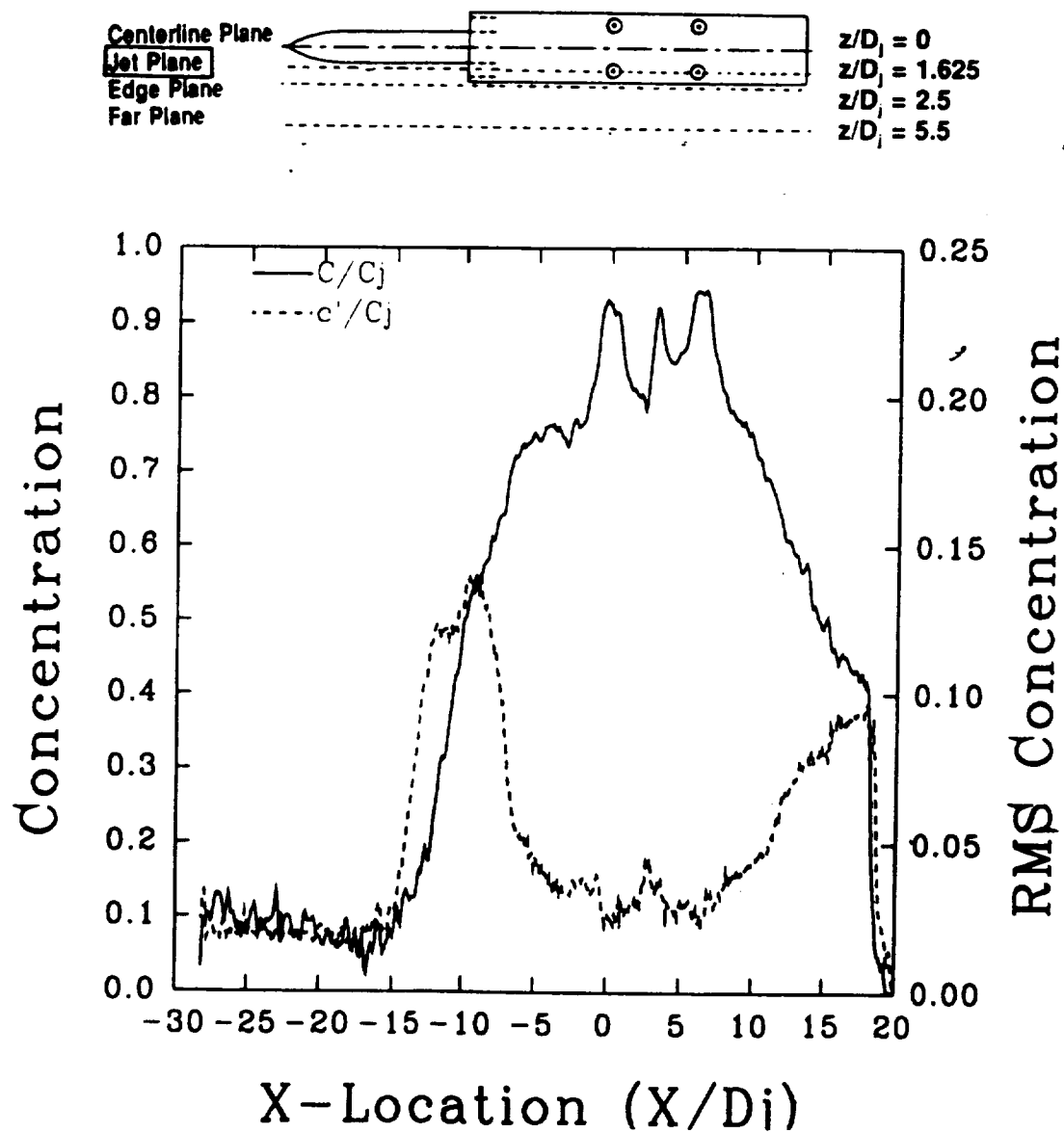


Figure 4.59: Mean and RMS Concentration Profiles at Side Jet Centerlines: $z/D_j = 1.625$
 Laser Sheet at Ground Plane: $y/D_j = 0$, $H/D_j = 2$, $U/V_j = 0.09$

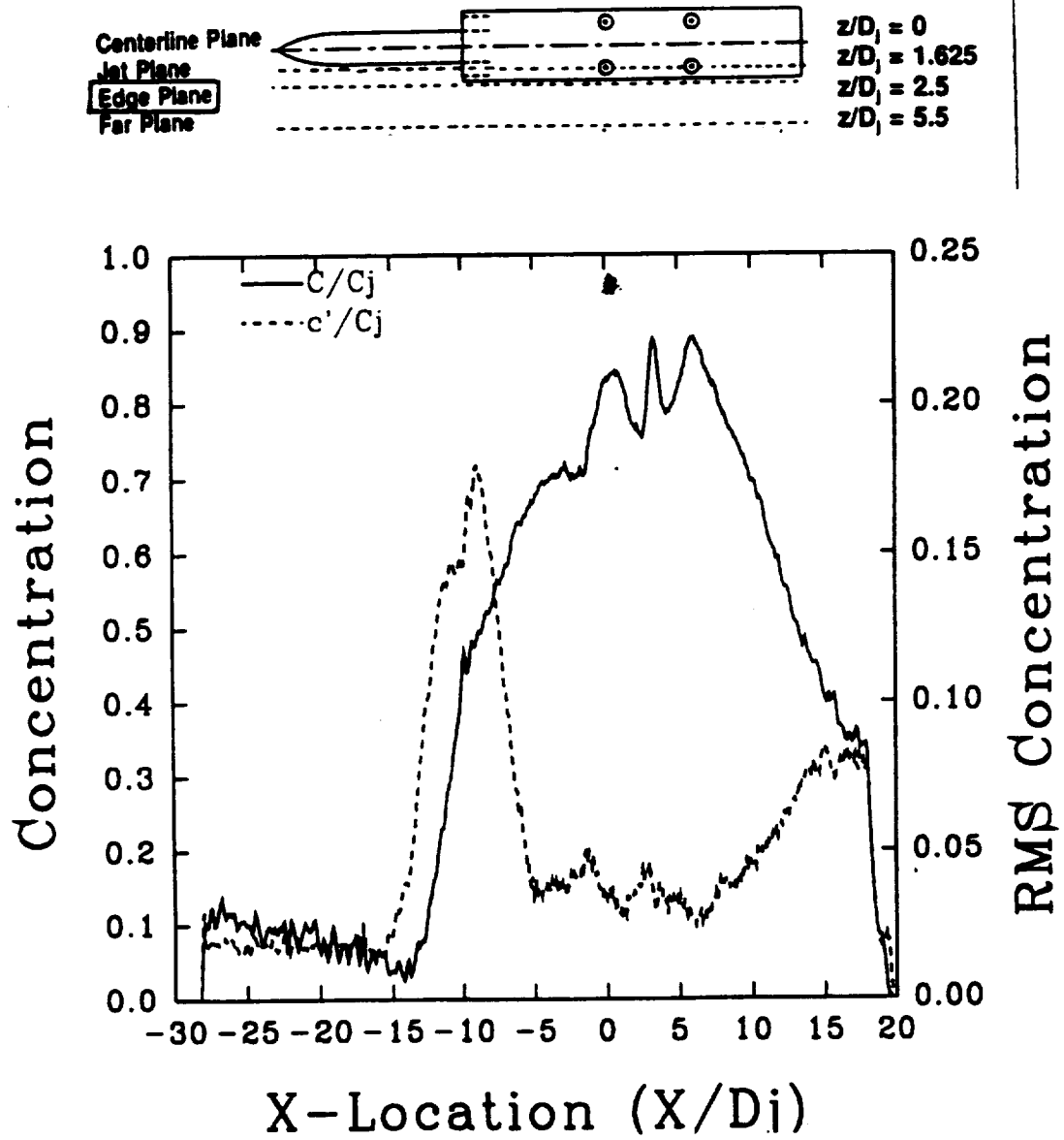


Figure 4.60: Mean and RMS Concentration Profiles at Model Edge: $z/D_j = 2.5$
 Laser Sheet at Ground Plane: $y/D_j = 0.0$, $H/D_j = 2$, $U/V_j = 0.09$

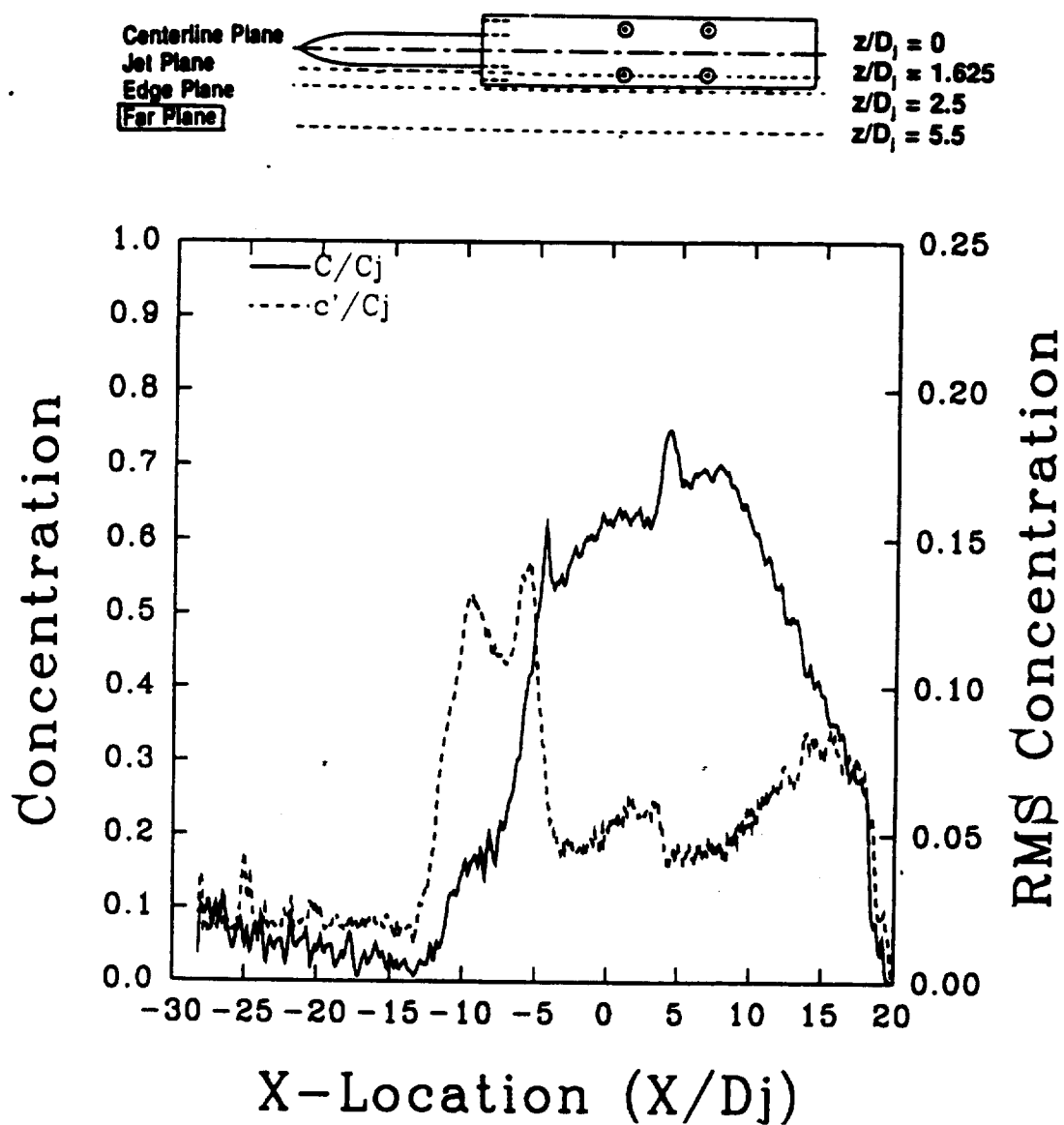


Figure 4.61: Mean and RMS Concentration Profiles at Far Plane: $z/D_j = 5.5$
 Laser Sheet at Ground Plane: $y/D_j = 0.0$, $H/D_j = 2$, $U/V_j = 0.09$

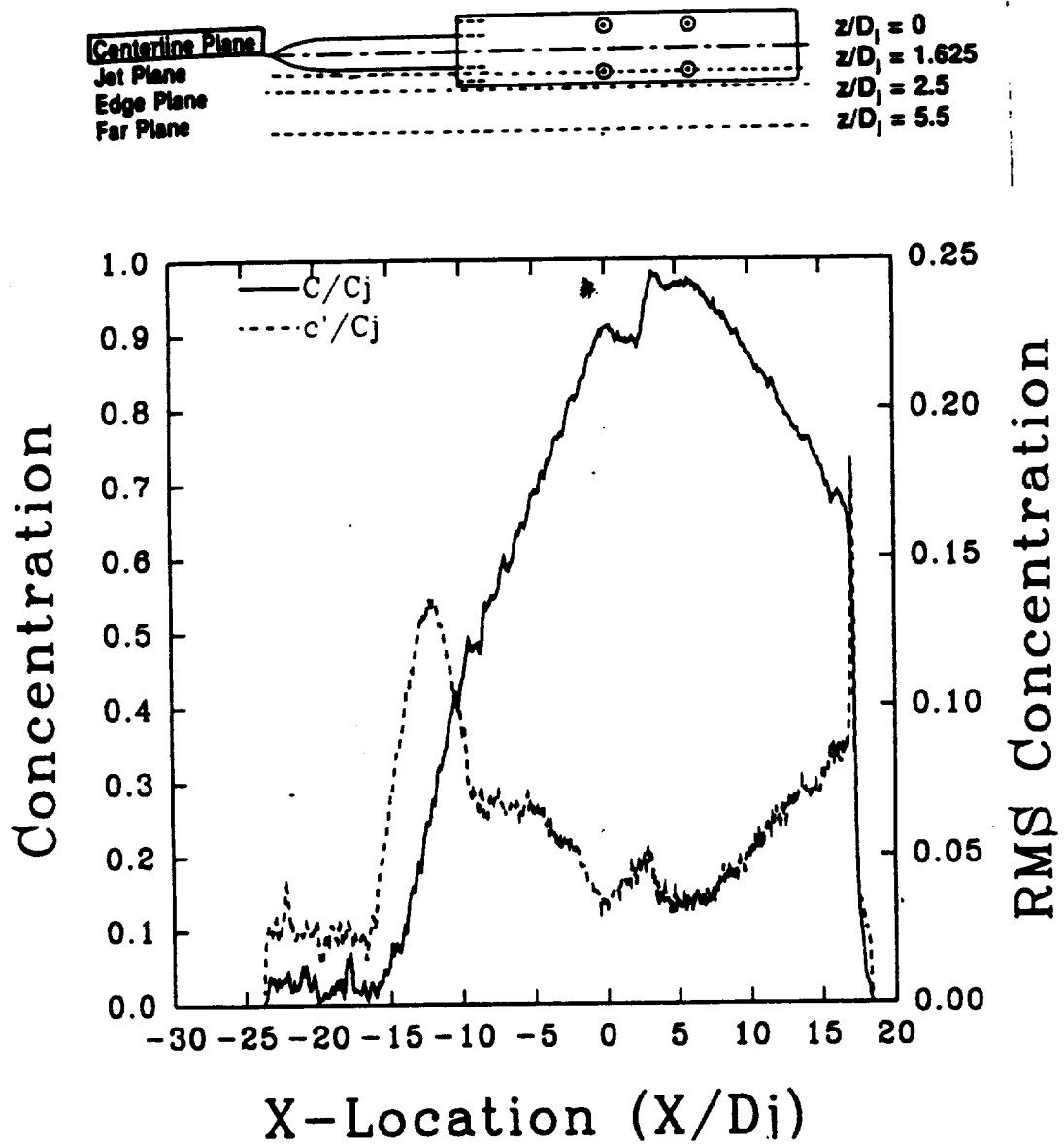


Figure 4.62: Mean and RMS Concentration Profiles at Model Centerline: $z/D_j = 0.0$
 Laser Sheet at Ground Plane: $y/D_j = 0$, $H/D_j = 6$, $U/V_j = 0.09$

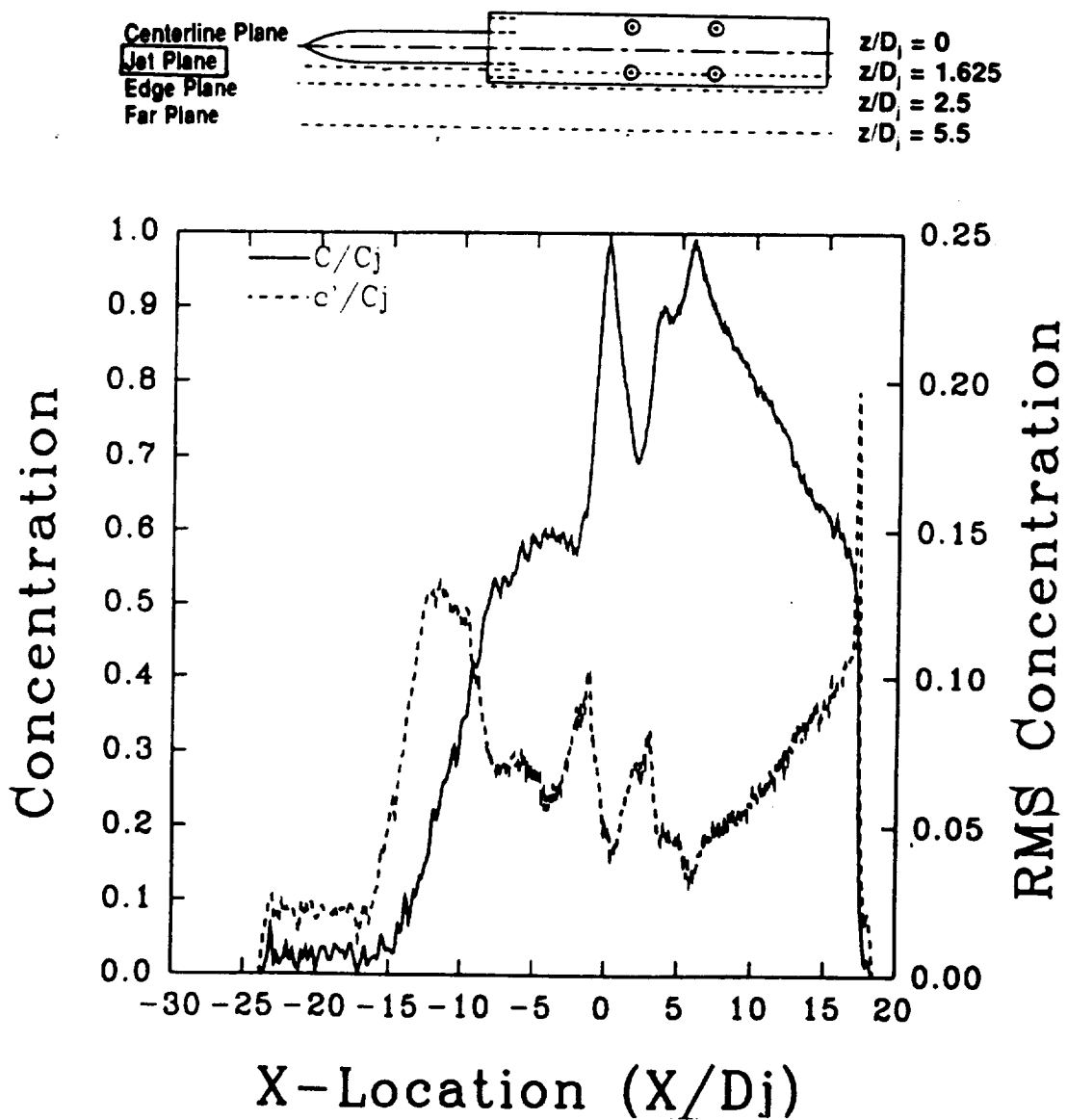


Figure 4.63: Mean and RMS Concentration Profiles at Side Jet Centerlines: $z/D_j=1.625$
 Laser Sheet at Ground Plane: $y/D_j = 0$, $H/D_j = 6$, $U/V_j = 0.09$

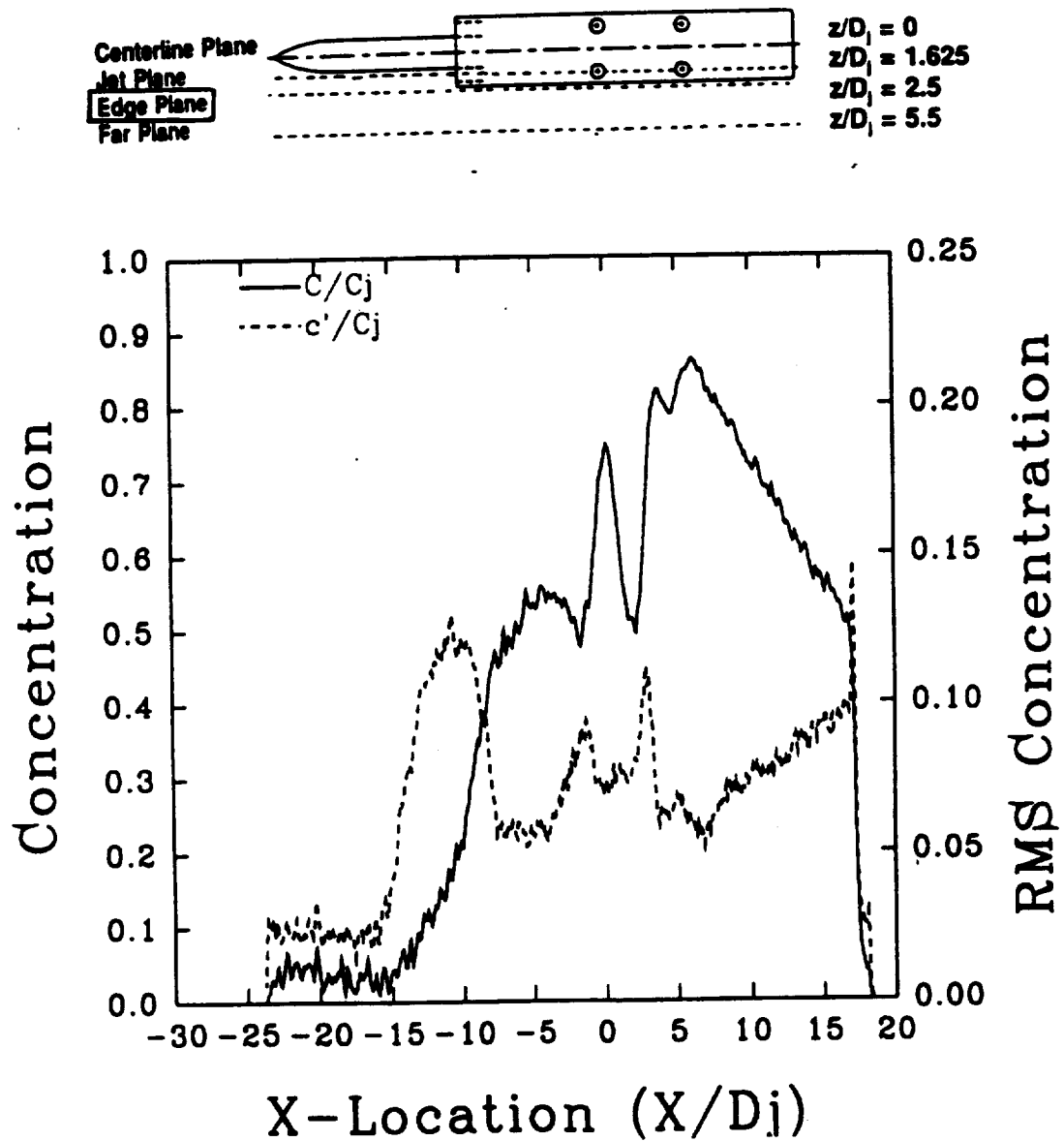


Figure 4.64: Mean and RMS Concentration Profiles at Model Edge: $z/D_j = 2.5$
 Laser Sheet at Ground Plane: $y/D_j = 0.0$, $H/D_j = 6$, $U/V_j = 0.09$

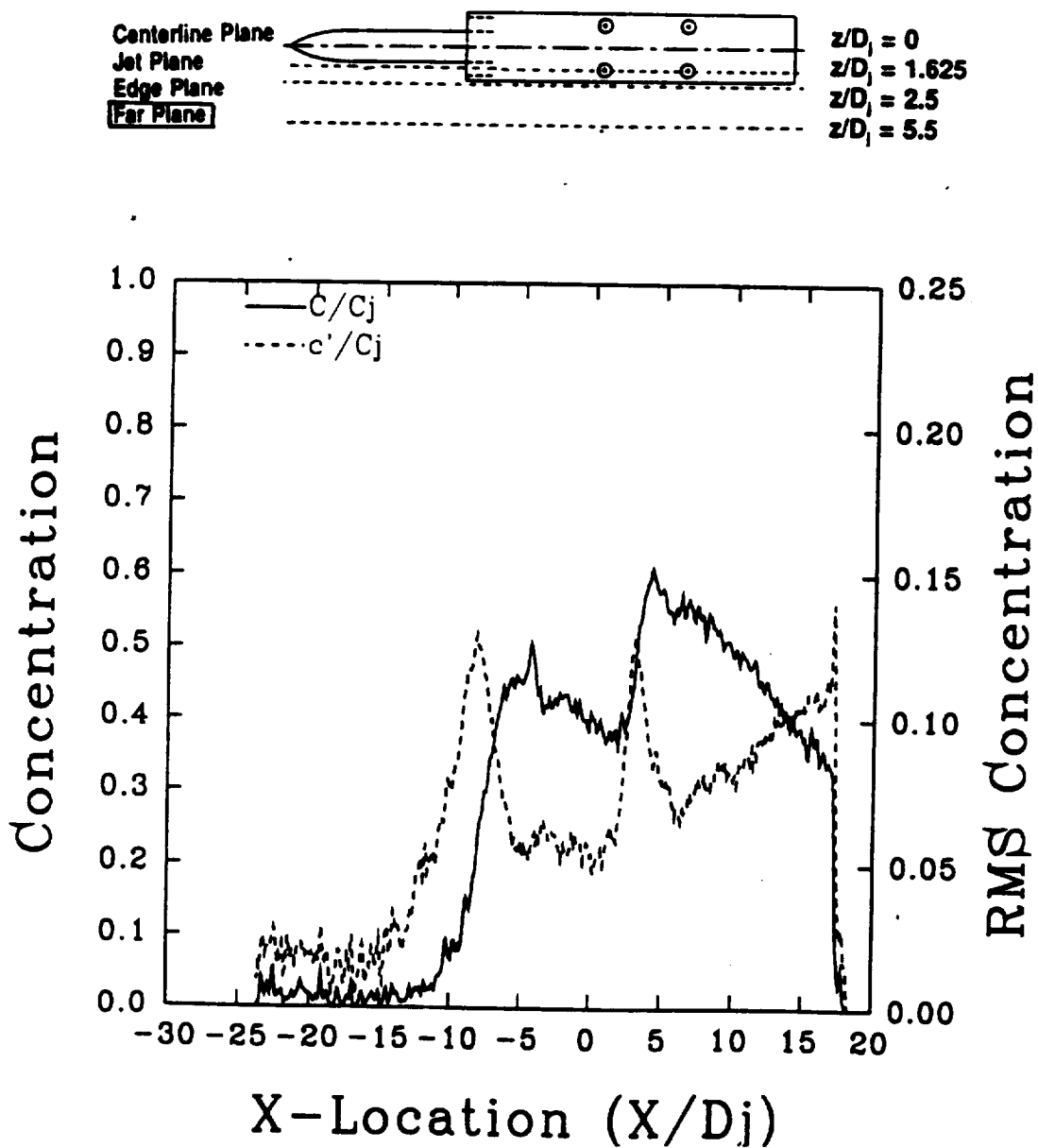


Figure 4.65: Mean and RMS Concentration Profiles at Far Plane: $z/D_j = 5.5$
 Laser Sheet at Ground Plane: $y/D_j = 0.0$, $H/D_j = 6$, $U/V_j = 0.09$

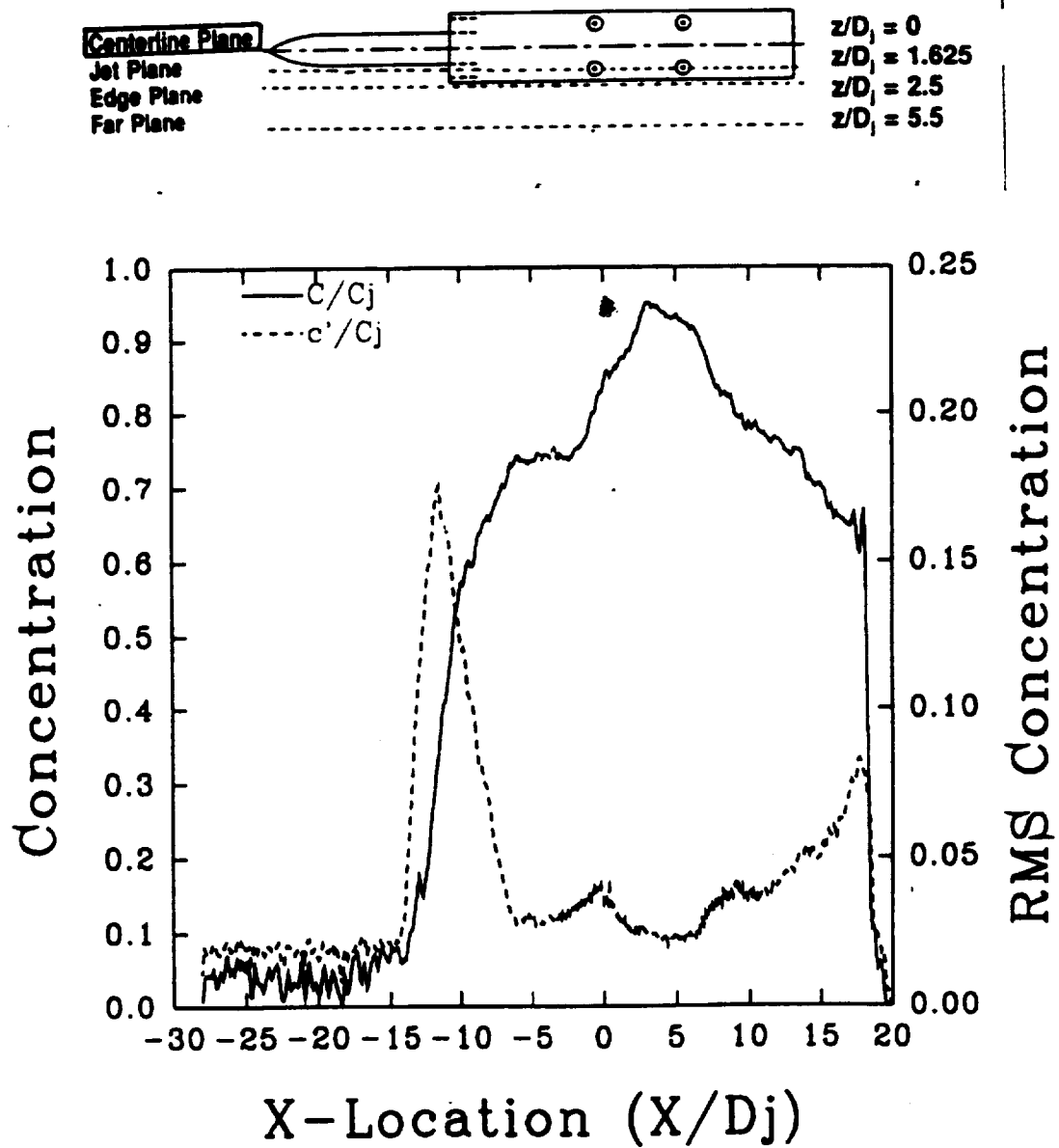


Figure 4.66: Mean and RMS Concentration Profiles at Model Centerline: $z/D_j = 0.0$
 Laser Sheet at Mid Plane: $y/D_j = 2.0$, $H/D_j = 2$, $U/V_j = 0.09$

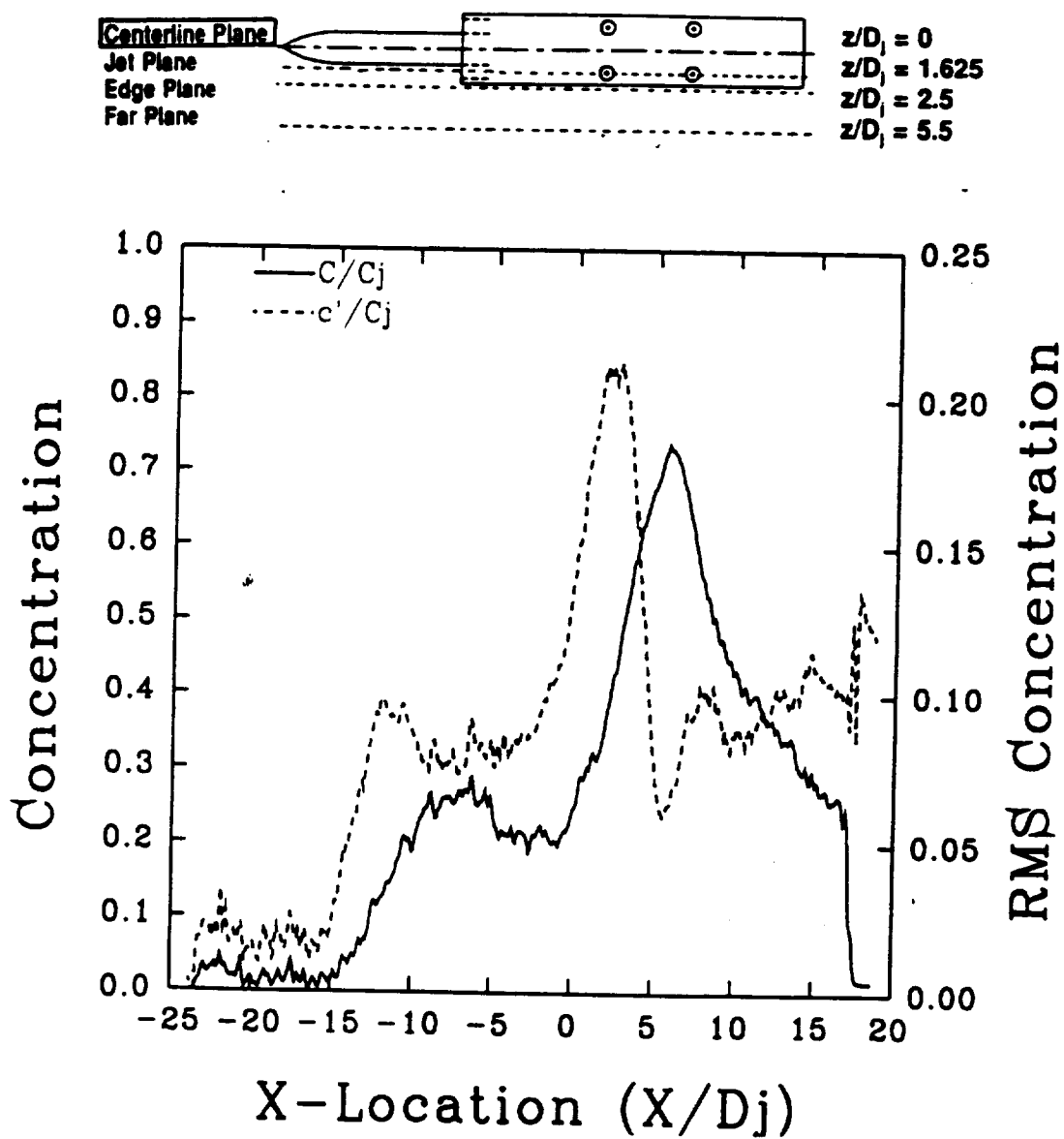


Figure 4.67: Mean and RMS Concentration Profiles at Model Centerline: $z/D_j = 0.0$
 Laser Sheet at Mid Plane: $y/D_j = 2.0$, $H/D_j = 6$, $U/V_j = 0.09$

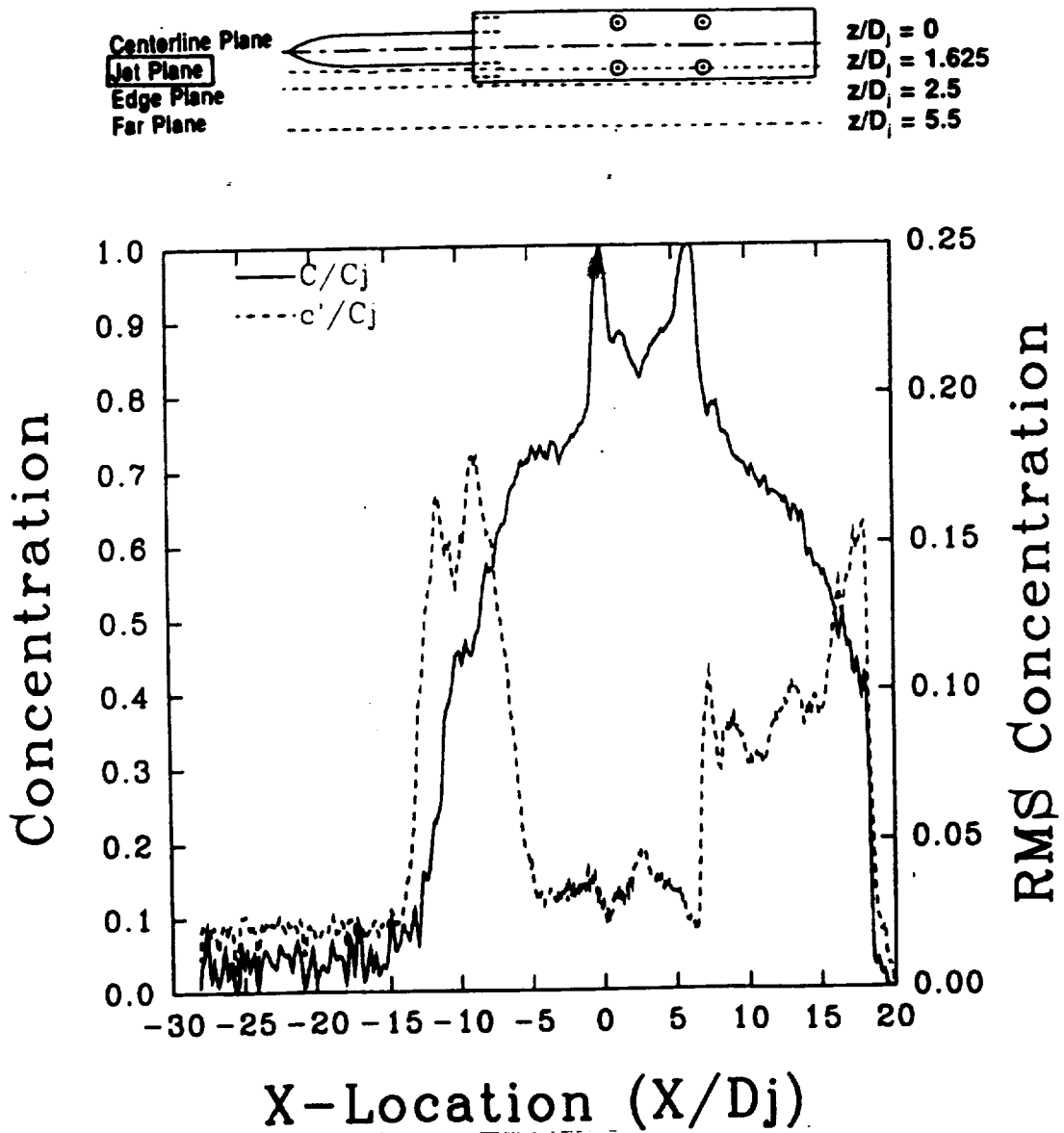


Figure 4.68: Mean and RMS Concentration Profiles at Side Jet Centerlines: $z/D_j=1.625$
 Laser Sheet at Mid Plane: $y/D_j = 2.0$, $H/D_j = 2$, $U/V_j = 0.09$

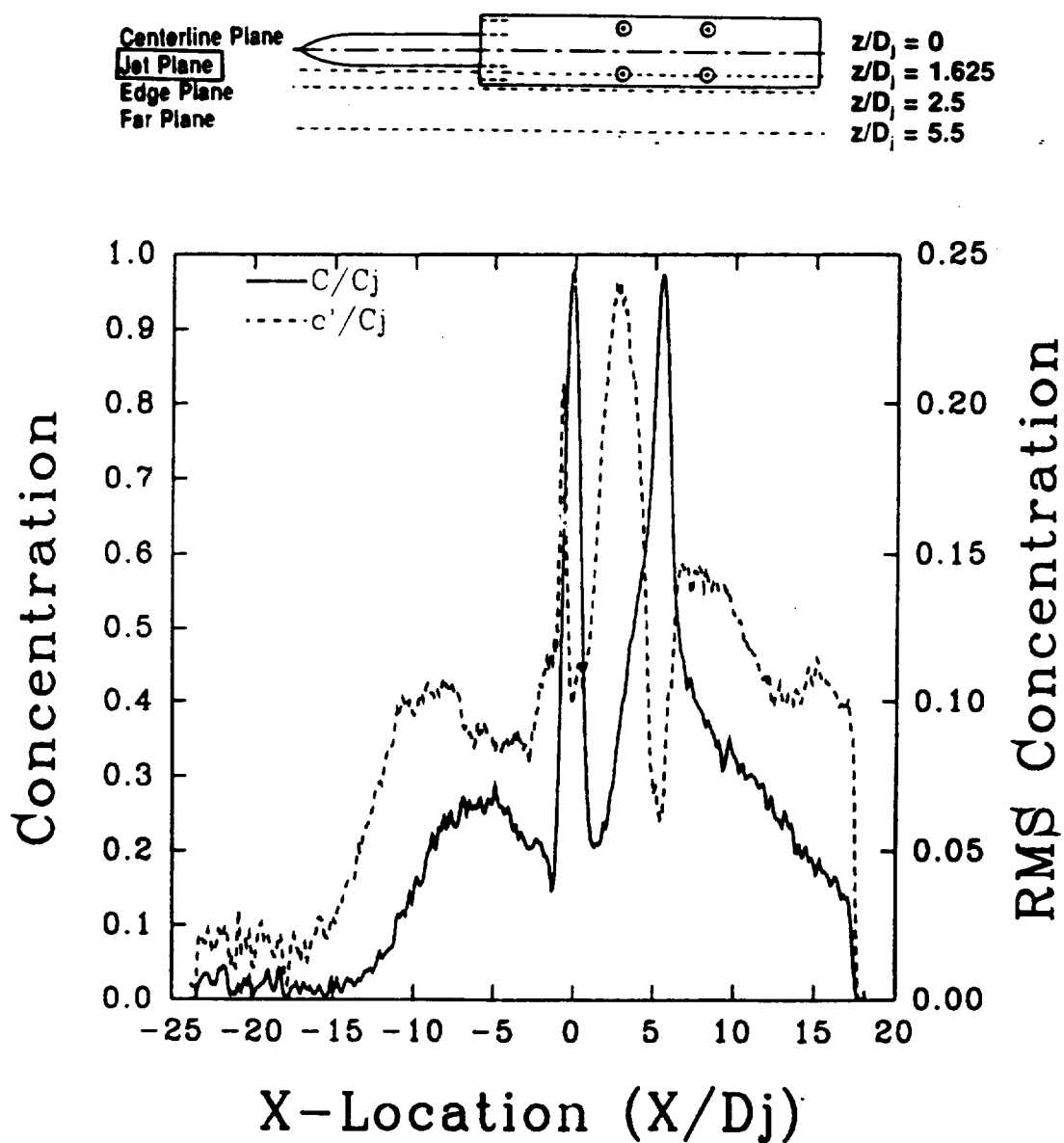


Figure 4.69: Mean and RMS Concentration Profiles at Side Jet Centerlines: $z/D_j = 1.625$
 Laser Sheet at Mid Plane: $y/D_j = 2.0$, $H/D_j = 6$, $U/V_j = 0.09$

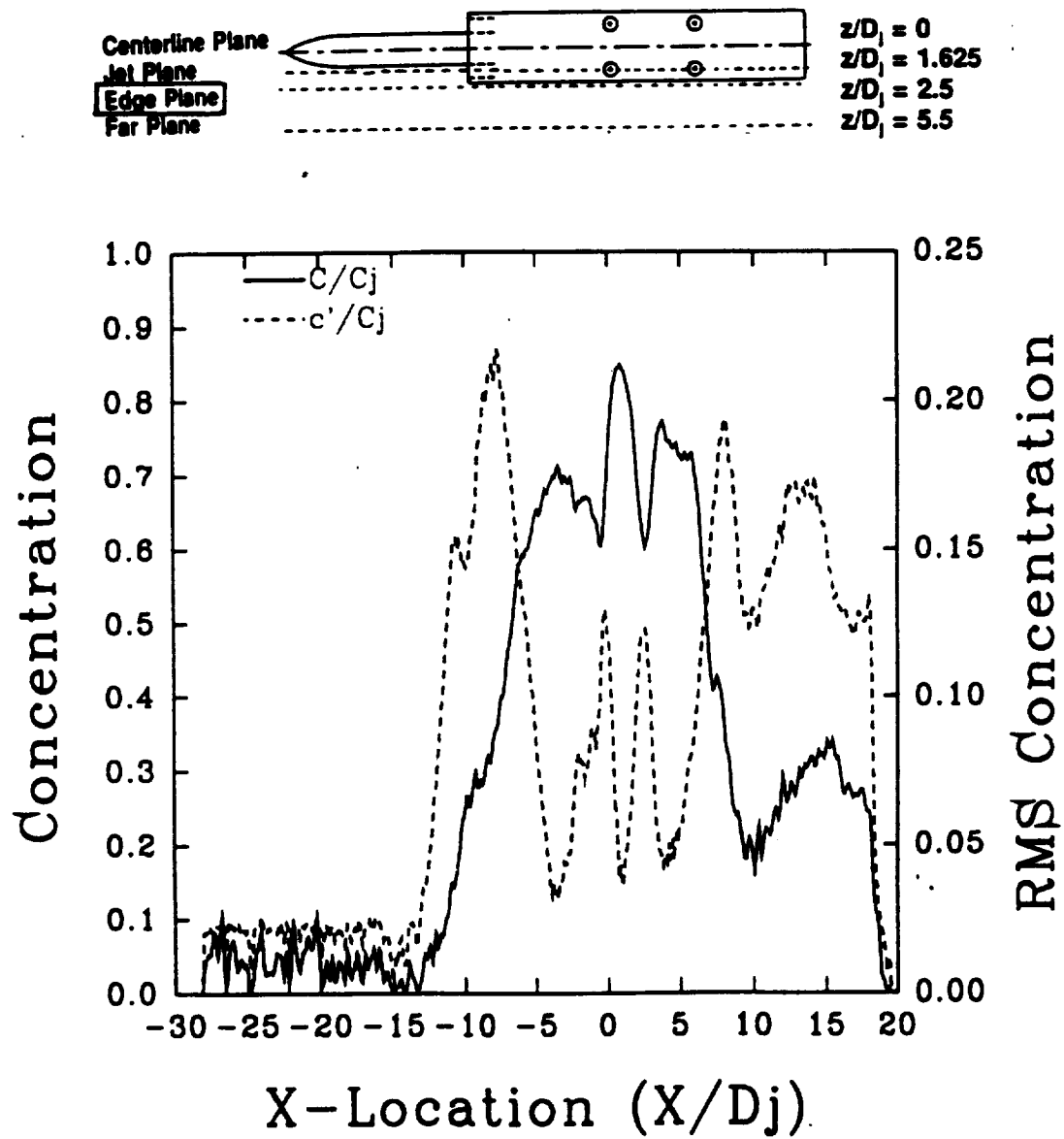


Figure 4.70: Mean and RMS Concentration Profiles at Model Edge: $z/D_j = 2.5$
 Laser Sheet at Mid Plane: $y/D_j = 2.0$, $H/D_j = 2$, $U/V_j = 0.09$

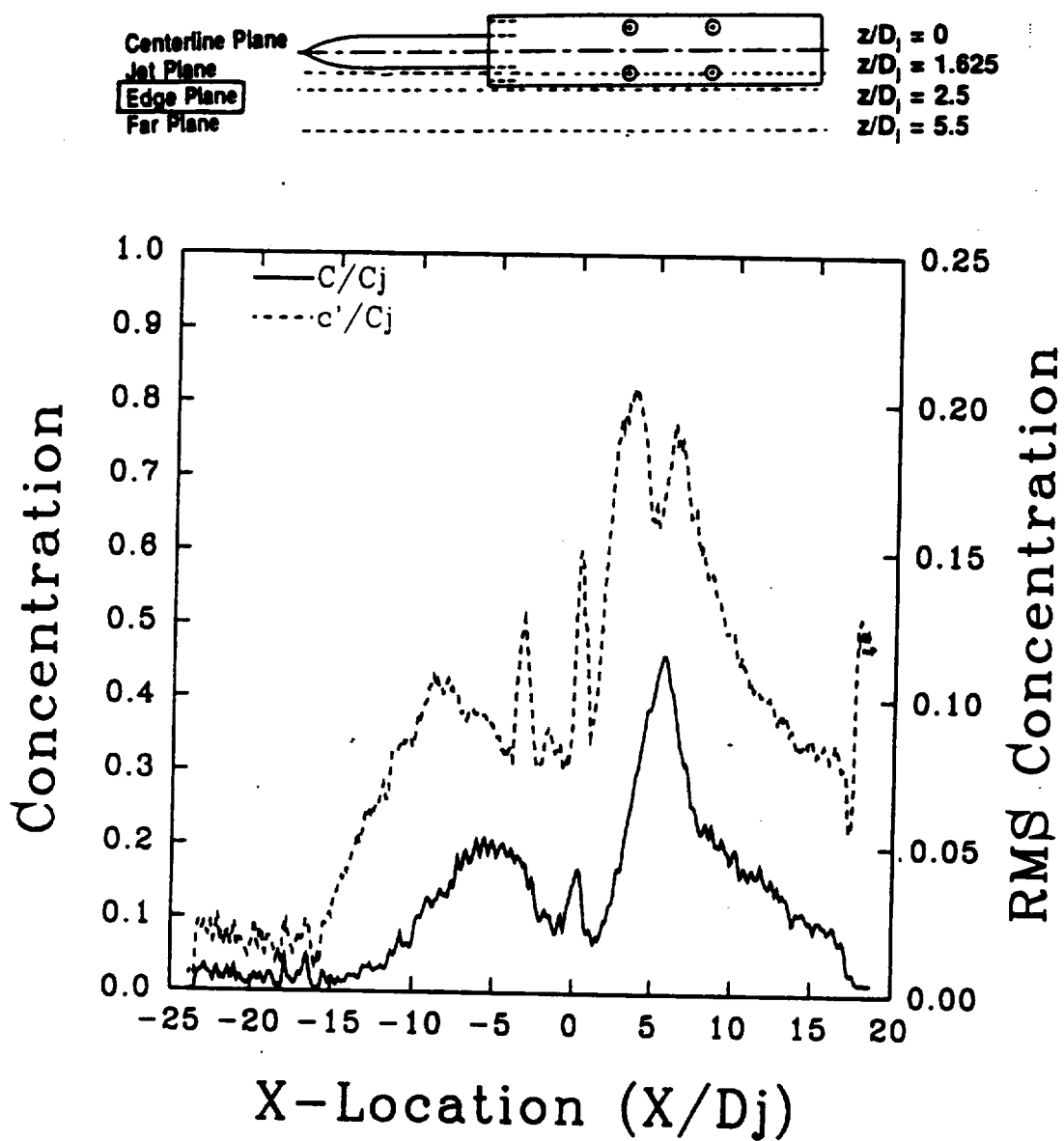


Figure 4.71: Mean and RMS Concentration Profiles at Model Edge: $z/D_j = 2.5$
 Laser Sheet at Mid Plane: $y/D_j = 2.0$, $H/D_j = 6$, $U/V_j = 0.09$

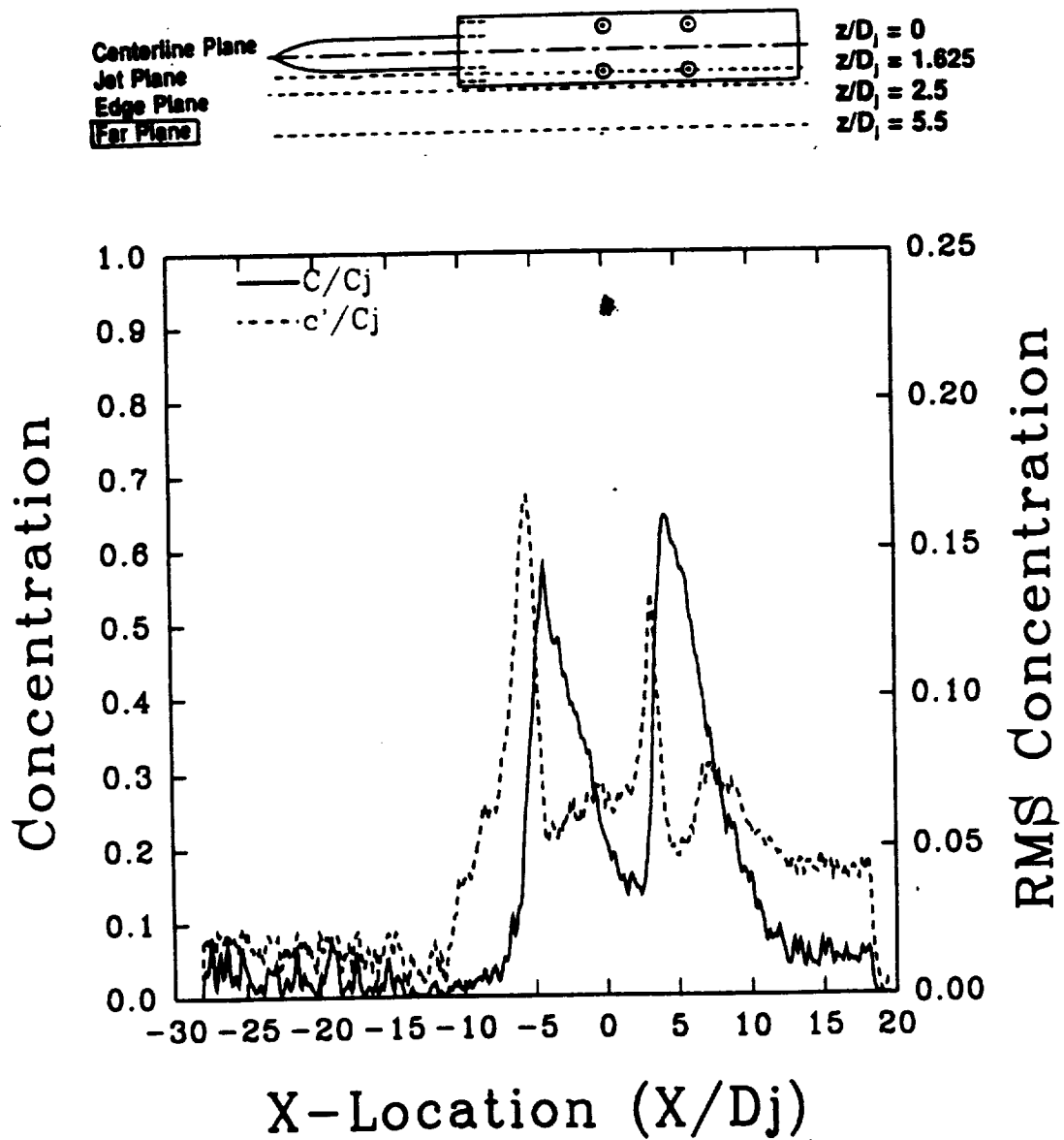


Figure 4.72: Mean and RMS Concentration Profiles at Far Plane: $z/D_j = 5.5$
 Laser Sheet at Mid Plane: $y/D_j = 2.0$, $H/D_j = 2$, $U/V_j = 0.09$

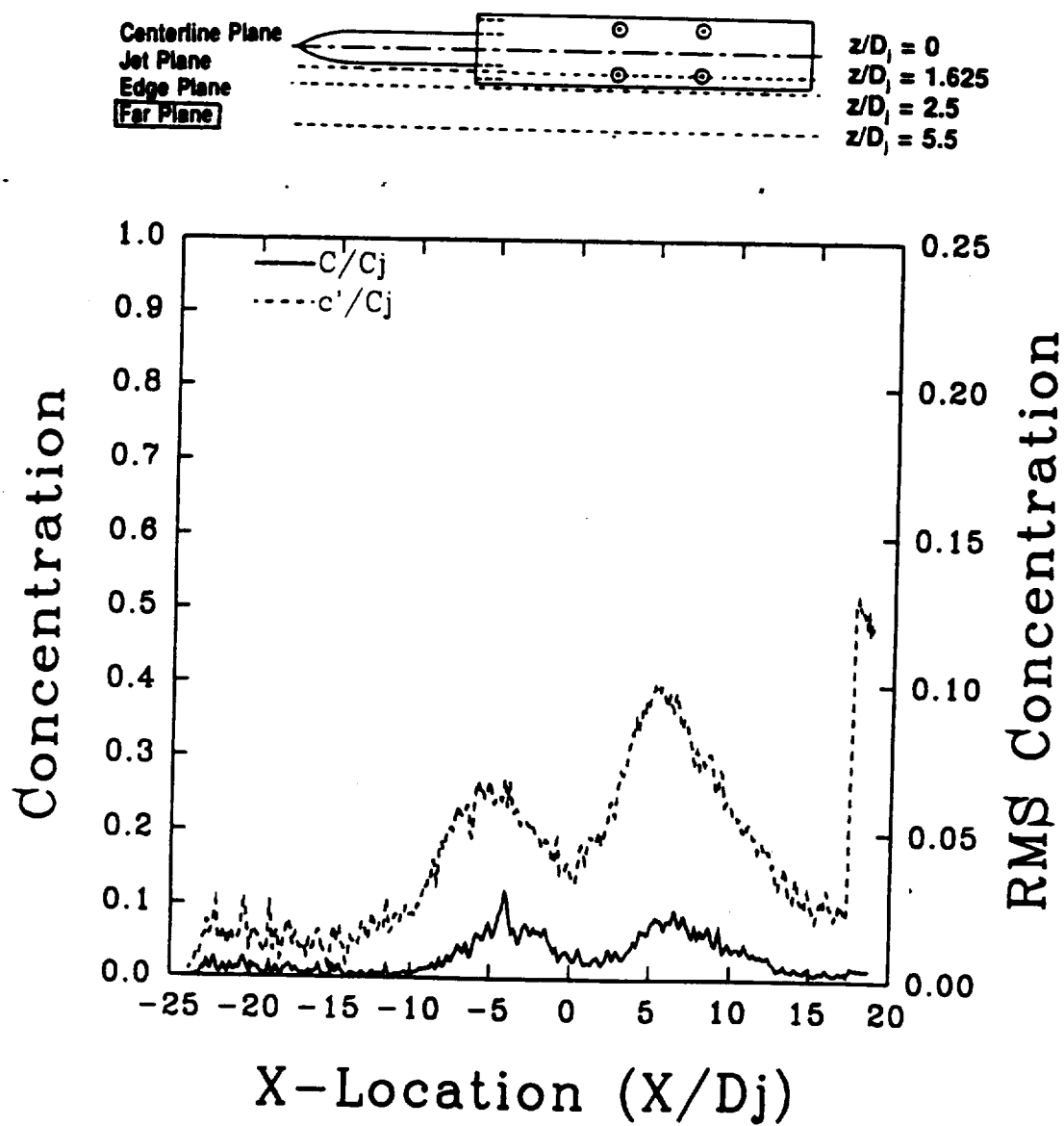


Figure 4.73: Mean and RMS Concentration Profiles at Far Plane: $z/D_j = 5.5$
 Laser Sheet at Mid Plane: $y/D_j = 2.0$, $H/D_j = 6$, $U/V_j = 0.09$

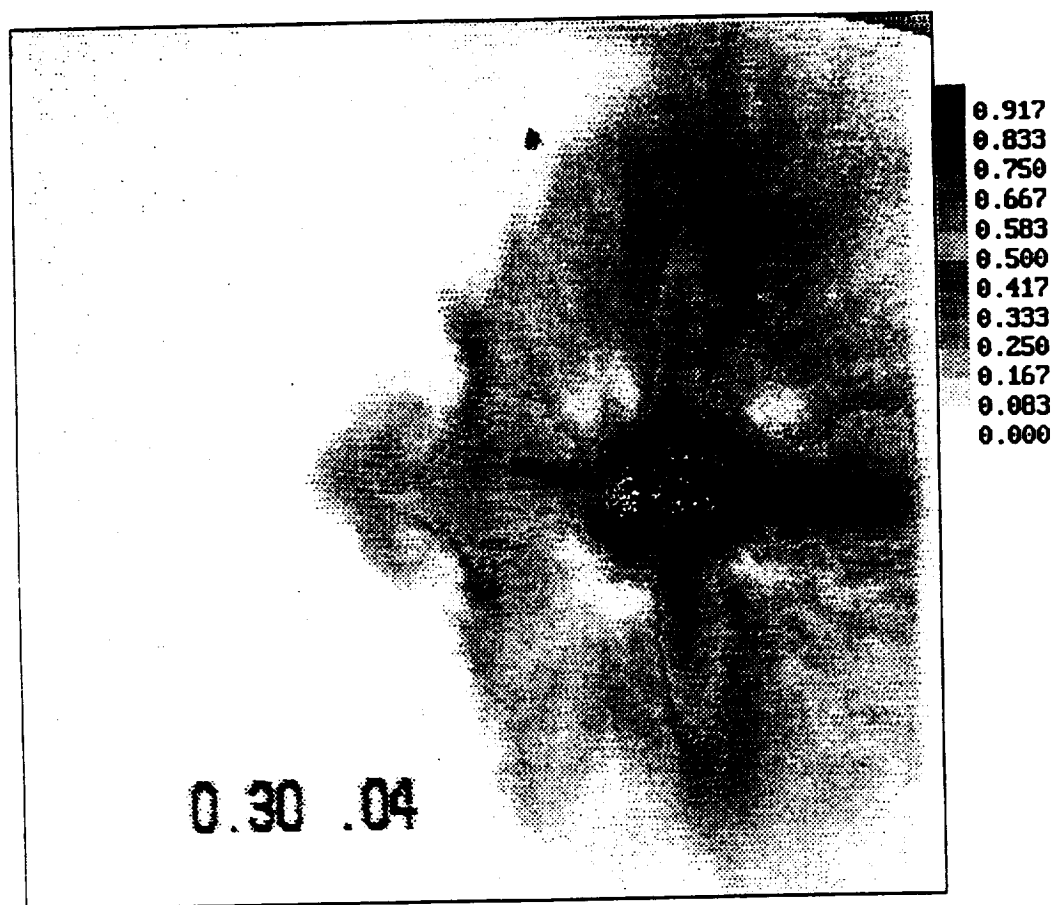


Figure 4.74: Single Frame Image of Smoke Concentration with suction
 $y/D_j = 0.6$, $H/D_j = 2$, $U/V_j = 0.04$

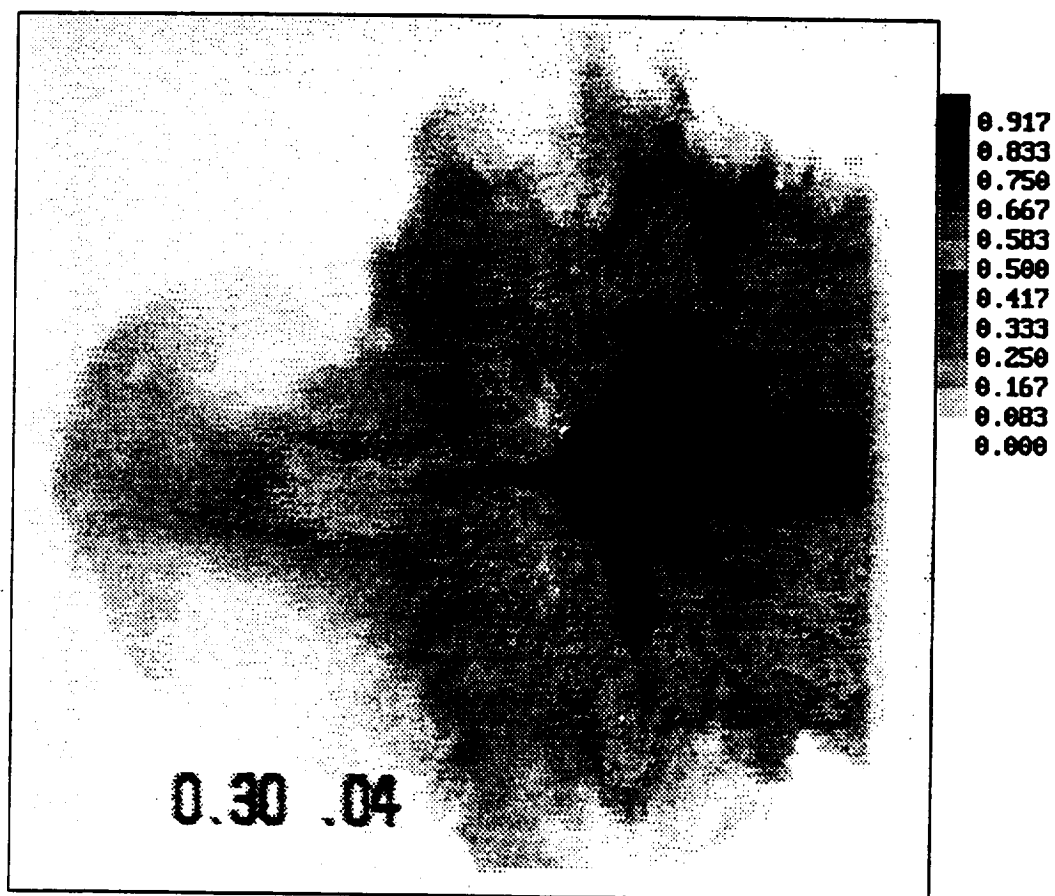


Figure 4.75: Single Frame Image of Smoke Concentration without suction
 $y/D_j = 0.6$, $H/D_j = 2$, $U/V_j = 0.04$

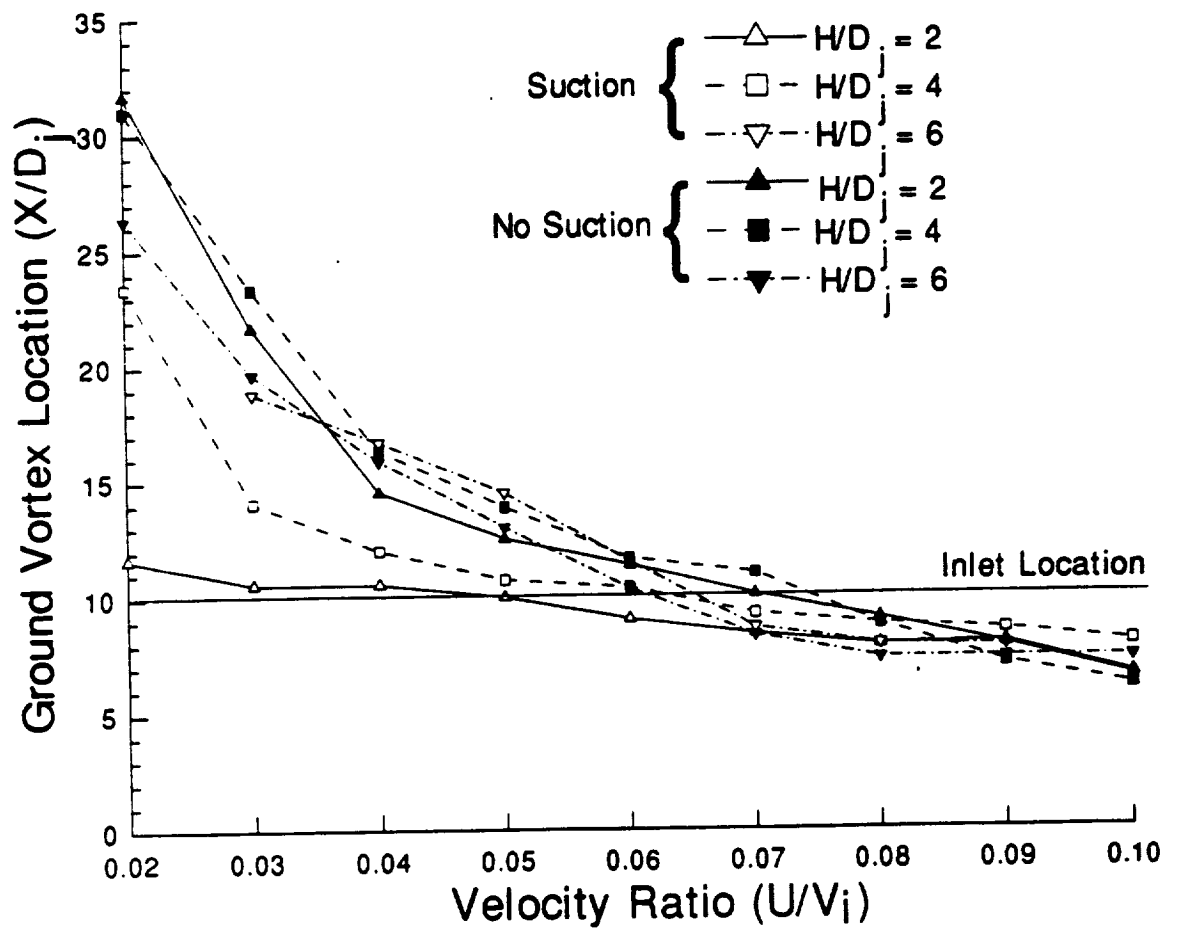


Figure 4.76: Ground Vortex Location Versus Velocity Ratio (U/V_i)
With and Without Suction

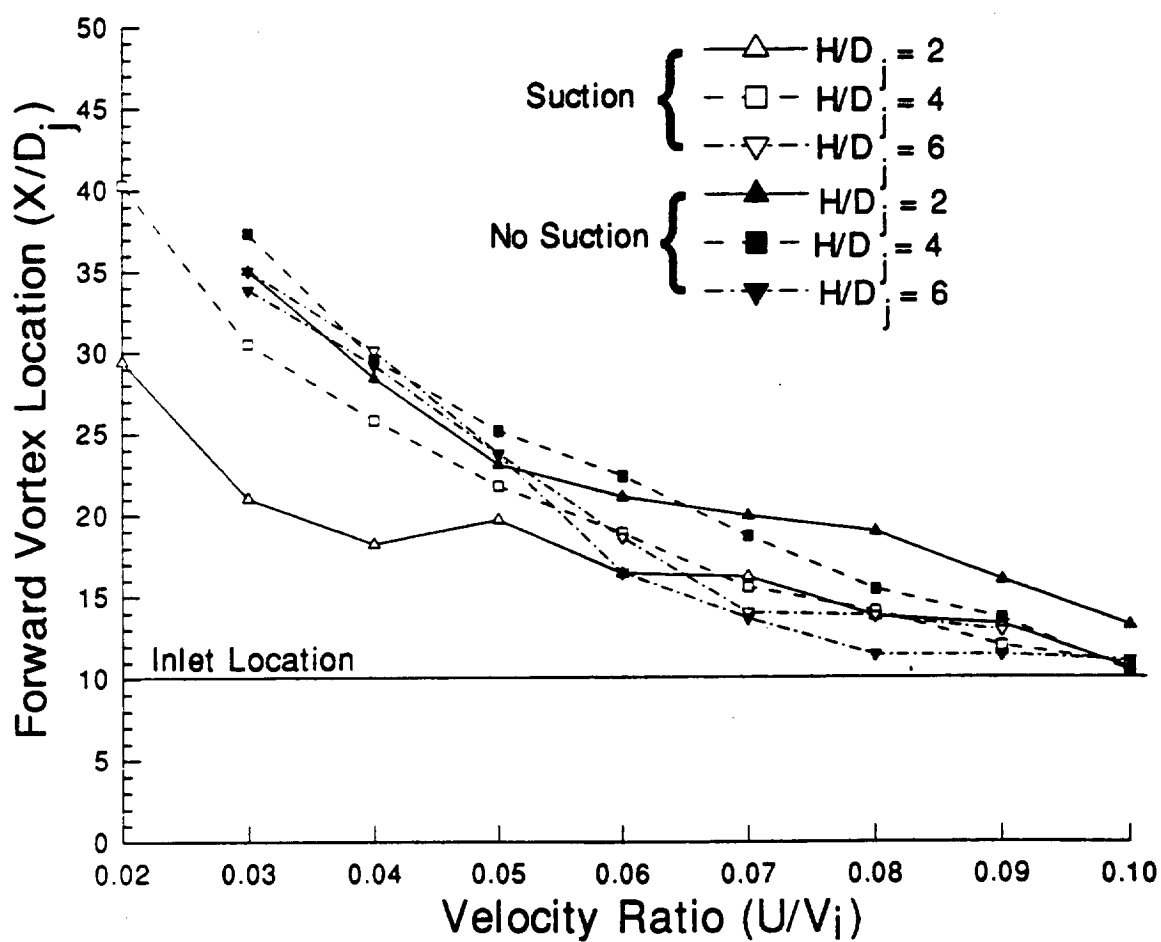


Figure 4.77: Forward Vortex Pair Location Versus Velocity Ratio (U/V_i)
With and Without Suction

5. COMPARISON OF NUMERICAL AND EXPERIMENTAL RESULTS

Comparisons of numerical temperature distribution done by Tafti and Vanka [52] and experimental concentration measurements with the same geometry and velocity ratios show a large number of similarities. In some cases, the normalized temperature distribution and experimental concentration are nearly the same. However, there are several differences in the flow structures between the numerical and experimental results. Several of these differences may be related to differences in flow conditions between the numerical model and experiment. The numerical model uses a jet velocity of 1000 feet per second, compared to 75 feet per second for the experiment. The numerical model also uses an absolute temperature of 1000 degrees Kelvin at the jet exit plane. The experiment is run at close to ambient temperature. However, most of the differences between the two flowfields may possibly be attributed to deficiencies in the kappa-epsilon turbulence model used in the numerical model, according to Tafti and Vanka [52]. Vortex flows appear to make up a large percentage of the structure in the flowfield, and may contribute to some of the differences, since large velocity gradients may occur in such structures.

In the numerical model, suction does not appear to have the same effect on the flowfield as in the experiment. Table 5.1 shows the location of the forward extent of the flow for both numerical and experimental data for four cases, courtesy of Tafti and Vanka [52]. Agreement is close for cases 1, 3, and 4, with suction on, but case 2, at a velocity ratio of 0.03 and a height of 2 jet diameters, shows a large difference between the experiment and numerical calculations with the suction on. With the suction off, the two flowfields agree much more closely.

ORIGINAL PAGE IS
OF POOR QUALITY

Presented next are images of both the numerical and experimental flowfields, for a model height of 4 jet diameters and velocity ratios of 0.09 and 0.03, at the ground, mid, and body planes. After each set of images, plots of normalized concentration and normalized temperature versus location relative to the forward pair of jets are presented for data through the model centerline, through the left side jet pair centerline, at the edge of the model 2.5 jet diameters from the model centerline, and 5.5 jet diameters from the model centerline. Also presented are plots of normalized concentration and temperature through the centerline of the forward and rear pairs of jets, and at a plane midway between the forward jet pair and the inlets.

5.1 Numerical and Experimental Comparisons at $U/V_j = 0.09$

In the next three sections, numerical and experimental results are compared at the ground, mid and body planes for a velocity ratio of 0.09 and a model height of four jet diameters.

5.1.1 Ground Plane Comparisons

Figures 5.1 and 5.2 show images of the flowfield near the ground plane for numerical temperature profiles and experimental concentration measurements respectively.

The velocity ratio is 0.09, and the model height is four jet diameters. Both flowfields are quite similar, with two main differences. The first difference is seen in the fountain region, where the numerical data show a sharp rise in temperature moving downstream, which appears in the experimental data as a peak in smoke concentration. The second difference occurs at the forward extent of the flow, where the structure corresponding to the forward vortex pair in the experimental data does not appear in the numerical data.

Plots of the numerical and experimental data through the centerline show the large similarity between the two flowfields, as shown in figure 5.3. The major difference between the two flowfields occurs in the fountain region. The experimental data shows

a sharp peak, with nearly equal concentration on either side, and the numerical data shows a sharp rise in temperature in the same region. These differences may be attributed to the turbulence model used in the numerical code, which controls the amount of mixing which occurs in the flowfield. Also displayed are data from a single frame of experimental concentration measurements, which shows some of the extent of flowfield unsteadiness.

Figure 5.4 shows a similar plot through the side jet centerline. Again, there are some differences in the fountain region. The main difference is seen in the area upstream of the forward pair of jets. In this region, a high experimental smoke concentration exists where the forward vortex pair is seen. The numerical data shows no peak in this region, and therefore does not show the existence of the forward vortex pair. Figure 5.5 shows numerical and experimental profiles at a plane at the edge of the model, 2.5 jet diameters from the model centerline. Again, both experimental and numerical measurements are similar, except in the fountain region and forward vortex pair region. At a plane 5.5 jet diameters from the model centerline, shown in figure 5.6, there are some differences between the two flowfields. However, the main structures are visible in both, and normalized temperature and smoke concentration values are nearly the same.

Across the forward pair of jets, in figure 5.7, the numerical temperature and experimental concentration profiles show a large number of similarities, except in a small region outside the jets. These differences may be attributed to differences between the numerical and experimental data in the structure of the wall jets. The numerical data may not be taking into account the increase in thickness of this structure as it propagates away from the jet region. At the rear pair of jets, in figure 5.8, the numerical data show much higher values outside the jets. This difference may be related to differences in the fountain region being propagated out into the outer flowfield in the wall jet. In the jet region itself, the numerical and experimental data agree quite well. Figure 5.9 shows

profiles of numerical and experimental data at a plane midway between the forward pair of jets and the inlet locations. The large differences between the two flows may be attributed to the existence of the forward vortex pair in the experimental data, which is not seen in the numerical temperature profile.

5.1.2 Comparisons at Mid Plane

Figures 5.10 and 5.11 show false color images of the flowfield for numerical temperature distribution and experimental smoke concentration at a plane midway between the ground and the model. The numerical data have a higher normalized temperature in the rear fountain region and along the centerline, and the experimental data show a much more distinct ground vortex, and more extensive flow. Aside from these differences, the two flowfields are quite similar.

Figure 5.12 shows experimental concentration and numerical temperature profiles along the model centerline. The two profiles, while slightly different, do show the same trends. The numerical profile generally has a higher normalized temperature than the experimental smoke concentration, especially downstream of the fountain region. The two profiles are the same in the fountain region itself. The experimental data extend about 5 jet diameters further upstream than the numerical data.

At the jet plane, shown in figure 5.13, the two flowfields again exhibit similar structures, but the size and scale of the flow structures is different between the numerical and experimental profiles. In the forward vortex pair region the normalized experimental smoke concentration profile shows a larger amplitude, and extends further upstream than the numerical temperature distribution. Unlike at the ground plane, the numerical data does show a structure which could be related to the forward vortex pair. In the fountain region, both the numerical and experimental data follow the same trend, but the experimental data shows a greater variation in changes in smoke concentration.

Figure 5.14 shows numerical temperature and experimental concentration profiles at the edge of the model, 2.5 jet diameters from the model centerline. The differences at this plane are much greater than in the inner flow region. The numerical data does not show the upstream peak which appears in the experimental data, and which corresponds to the ground vortex. The second ground vortex is seen in both the numerical and experimental data as the downstream peak. The peaks in the numerical and experimental data are much different, however.

At a plane 5.5 jet diameters from the model centerline, shown in figure 5.15, the ground vortex, associated with the forward peak, and the second ground vortex, associated with the downstream peak, are quite evident in the experimental smoke concentration. The numerical temperature distribution shows these two structures as much smaller and less extensive. This may be partially due to the turbulence model used in the numerical model, which may not account for the large amount of mixing between the ground vortices and the free stream. The grid size may also be a factor in the flowfield structures.

Experimental smoke concentration and numerical temperature profiles are similar across both the forward and rear pairs of jets, as seen in figures 5.16 and 5.17, respectively. Even outside the inner flow region, the experimental and numerical results are similar. At the plane midway between the inlets and forward jet pair, shown in figure 5.18, there are some differences between the numerical and experimental results. While both show similar central structure, the extent of the experimental results is much greater. This again may be attributed to the greater size of the forward vortex pair and ground vortex in the experimental data.

5.1.3 Model Body Plane Comparisons

Figures 5.19 and 5.20 show false color images of the flowfield for numerical temperature distribution and experimental smoke concentration through a plane near the

model body undersurface, at a velocity ratio of 0.09. Both flowfields appear quite similar, with the major difference being the existence of low smoke concentration in the region of the inlets in the experimental results. This is also seen in figure 5.21, a profile of experimental smoke concentration and numerical temperature distribution through the model centerline. The experimental smoke concentration does extend about 5 jet diameters forward of the numerical results, possibly due to the existence of the forward vortex pair, which was not seen in profiles at the ground and mid planes as well. The structure in the fountain region is also different for the two cases, but normalized temperature and smoke concentration are still close.

A comparison of profiles through the model jet centerline, seen in figure 5.22, shows good agreement again everywhere but in the forward region, where the forward vortex pair is located, and the fountain region, where numerical results show lower temperatures than the experimental results behind the forward jet. These differences may be due to greater mixing occurring in the experimental results, which the numerical results are not seeing. Figure 5.23 shows a plane at the model edge, 2.5 jet diameters from the model centerline, numerical results show a sharp rms peak upstream in the region corresponding to the ground vortex. In the experimental results, this region is much broader and lower in amplitude. The downstream peak in the numerical results is in better agreement with experimental results, but some of its structure is not seen in the experimental results. Numerical results also do not predict the high smoke concentration seen in the experimental results downstream of these two peaks. Most of the differences seen in figure 5.23 may be attributed to the unsteady nature of the flowfield in the experimental results. Figure 5.24 shows a plane 5.5 jet diameters from the model centerline. The numerical results do not show any peaks associated with the ground vortex and second ground vortex in this figure. Both are very prominent in the experimental results. This suggests the ground vortex and second ground vortex are much

larger in diameter than the numerical results predict, since these two structures were seen at the mid and ground planes in both the numerical and experimental results.

Numerical and experimental profiles across the forward jet pair, seen in figure 5.25, show good agreement, although experimental results show higher amplitudes in the fountain region. Outside the fountain region, the numerical results show some structure not seen in the experimental results. It appears that the numerical results do not predict the smooth tapering of flow around the jets, and instead expect to see lobes off to the sides, indicating that mixing in the normalized experimental smoke concentration is much more extensive than predicted by the numerical results. The extent of the flow side to side is the same for both numerical and experimental profiles. Figure 5.26, a profile at the rear jet pair, shows good agreement between numerical and experimental results, with both magnitudes and flow structures nearly the same. Agreement is also quite good at a plane between the inlets and forward jet pair, shown in figure 5.27, with both the extent and magnitude of the experimental results being accurately predicted by the numerical calculations.

5.2 Numerical and Experimental Comparisons at $U/V_j = 0.03$

The next set of figures shows numerical and experimental data comparisons for a velocity ratio of 0.03 and a model height of four jet diameters. False color images of the flowfield at the ground, mid, and body planes will be presented, along with several plots of numerical and experimental data at several planes in the flowfield.

5.2.1 Ground Plane Comparisons

False color images at the ground plane are shown in figures 5.28 and 5.29, of numerical and experimental results respectively. The two color images both have the same maximum concentration in the flowfield, giving a fairly accurate comparison between the two. It appears that the major difference between the two flowfields is in

the extent and magnitude of the temperature and smoke concentration in the flowfields. The numerical data show a larger extent of lower amplitude temperature distribution, whereas the experimental data show a much higher amplitude smoke concentration located in a region which is much less extensive than in the numerical results. While it appears that the forward extent of the two flows is nearly the same, the numerical results exhibit a high amplitude spike along the model centerline.

Figure 5.30 shows a plot of the numerical temperature distribution and experimental smoke concentration along the model centerline. The two flowfields are in disagreement in the fountain region, where a peak occurs in the experimental data, which is not seen in the numerical data. This is similar to that seen in figure 5.3, at a velocity ratio of 0.09. The forward extent of the two flows appears similar, although it is difficult to tell for the experimental data, since the smoke concentration merges with the background in this area. The normalized temperatures in the numerical data have a lower value than the experimental data in the region upstream of the jets. This is also seen in a profile through the jet centerline in figure 5.31, although there is a bulge in numerical concentration near the forward extent of the flow. The bulge in the numerical data may correspond to the forward vortex pair. However, this structure will be steady in the numerical data, rather than exhibiting the unsteadiness seen in the experimental data. Frame averaged figures of the experimental data, due to the unsteadiness in the flow, will not show a distinct forward vortex pair. The fountain shows the same differences between numerical and experimental results as figure 5.30.

Figure 5.32 shows a profile at the model edge, 2.5 jet diameters from the model centerline. The normalized temperature of the numerical results is almost uniformly lower than the experimental results, although both profiles exhibit the same flow structures. Outside the region near the model, differences between the two flowfields become more apparent. Figure 5.33 shows a profile of numerical and experimental results 5.5 jet

diameters from the model centerline. The small peak in the experimental results near -30 is the forward vortex pair, and is not seen in the numerical results. The numerical results also have a lower normalized temperature in large areas of the flowfield when compared to the experimental smoke concentration. The fountain structure is also visible as peaks in both the numerical and experimental results. The peak in numerical results is much sharper than in the experimental results. The lower normalized temperature in the numerical data may be offset by the further extent of the flowfield for the numerical data.

Profiles across the forward jets of numerical and experimental results are shown in figure 5.34. Agreement in the jet and fountain region is good. Outside of this area, the numerical results exhibit a sharper fall in normalized temperature than the experimental results, which show a nearly linear drop in smoke concentration. The extent of the numerical results to the sides is much greater, and is more apparent in figure 5.35, at the rear jet pair. The numerical results seem to predict a much broader extent to the flowfield than the experimental results show. This may in part be due to the size of the experimental flowfield. With a test section 30 inches wide, the experimental flowfield for this case extends to the edges of the test section. Another possibility is that the boundary layer in the numerical results is not thickening or mixing with the free stream as seen in the experimental data. At a plane midway between the inlets and forward jet pair, seen in figure 5.36, the numerical results again show a much broader extent, at the same time lower in magnitude than the experimental results.

5.2.2 Mid Plane Comparisons

Figures 5.37 and 5.38 show images of numerical and experimental results respectively at a plane midway between the ground and model for a velocity ratio of 0.03, and a model height of 4 jet diameters. False color images of both flowfields appear somewhat dissimilar. Visible in both are also dim, low amplitude structures in the forward region of the flow and far to the sides corresponding to the ground vortex and

part of the forward vortex pair. Figure 5.39 shows profiles along the model centerline. This profile is very similar to figure 5.30 for both the numerical and experimental results. The numerical results show a sharp cutoff at the forward extent of the flow, while the experimental smoke concentration shows only a gradual merging with the background. Other structures are also similar to figure 5.30. Figure 5.40 shows profiles of experimental smoke concentration and numerical temperature distribution through the model jet centerline. The two profiles are dissimilar, especially in the fountain region. In the fountain region, the numerical results underpredict the extent of mixing and recirculation. At this forward velocity ratio, an extensive recirculation zone exists between the jets and fountain, which as discussed above, consist of a pair of counter-rotating vortices. The numerical results apparently do not predict the extent to which these vortices mix and distribute flow in the inner flow region. Outside the inner flow region between the jets, many of the differences can be attributed to the unsteady nature of the flow. The single frame, shown in the dotted line in figure 5.117, shows some of the unsteadiness in the flow, which is not seen in numerical calculations. The extent of this unsteadiness is much greater at a velocity ratio of 0.03 than was seen at a velocity ratio of 0.09. This may contribute to the gradual decline in smoke concentration in the experimental results in the upstream region of the flow. These large differences are also seen in figure 5.41, at the edge of the model, 2.5 jet diameters from the model centerline. The numerical temperature distribution and experimental smoke concentration are much different. The single frame also shows some of the extent of the unsteadiness in this area of the flow. Figure 5.42 shows a numerical temperature distribution and smoke concentration profile at a plane 5.5 jet diameters from the model centerline. The two flows show similar structures, although the extent and magnitude of the experimental results is much greater than the numerical results. Also visible in the single frame data

is some structure in the forward region of the flow, associated with the ground vortex and forward vortex pair.

Figure 5.43 shows experimental and numerical results across the forward pair of jets. The two flows are comparable in the inner flow region. In the outer flow region, the experimental results show a much broader extent than the numerical results. At the rear pair of jets, seen in figure 5.44, the numerical results agree well with the experimental results, except for the two regions just outside the jets, where the numerical results show a peak. This is not seen in the experimental results. These two side peaks are also seen in results midway between the inlets and forward jets in the numerical results, as seen in figure 5.45. The experimental results do not show these structures, possibly because of unsteadiness and mixing in the experimental flowfield. Also not visible in the experimental results is the broad, low amplitude increase in temperature further from the model centerline.

5.2.3 Model Body Plane Comparisons

The numerical temperature distribution and experimental concentration measurements at a plane close to the model are similar. Figures 5.46 and 5.47, images of the numerical and experimental results respectively, show this. The numerical results do show a higher normalized temperature in the forward region of the flow, but the extent of the flow to the sides is not as great as the experimental results. The experimental smoke concentration shows a higher magnitude in the inner flow region between the jets.

Figure 5.48, profiles of numerical and experimental data along the model centerline, show some of these differences. these trends are also similar to those seen for the ground and mid plane centerline as well. The single frame profile in figure 5.122 shows some of the extent of the unsteadiness in the forward region of the flowfield. At a plane through the side jet centerline, seen in figure 5.49, the experimental data and

numerical data exhibit similar structures in the flowfield, especially in the region upstream of the forward pair of jets. The numerical data does show higher magnitudes than the experimental data both upstream and downstream of the jets. In the fountain region between the jets, the numerical data again does not show the extent to which recirculation mixes the flowfield.

At a plane near the edge of the model, 2.5 jet diameters from the model centerline, the numerical and experimental data show good agreement everywhere except in a region downstream of the jet locations. This is seen in figure 5.50. There is also some differences in magnitude of the flow from between the side jets. These differences may be caused by the same mechanisms which are seen in the inner flowfield. Other structures at this plane show very good agreement.

In figure 5.51, 5.5 jet diameters from the model centerline, the experimental results show a peak emerging from the inner flowfield, which is not seen in the numerical results. This is similar to that seen at a velocity ratio of 0.09, in figure 5.24. The main reason for these differences is again the size of the ground and forward vortex pairs, which appear to be smaller in the numerical data.

Figure 5.52 is a profile of numerical and experimental results across the forward jet pair centerline. The experimental results show a much broader central region than in the numerical data. the magnitude in the fountain region is also somewhat different, again possibly due to the model used for mixing in the numerical calculations. The two flows agree quite well at the rear pair of jets, seen in figure 5.53, if the two peaks just outside the jet peaks are smoothed into the center. This again can be attributed to an underprediction in the amount of mixing which is occurring in the flowfield. Figure 5.54 shows numerical and experimental results through a plane midway between the inlets and forward jet pair. The two flowfields are generally in agreement, although the numerical results show some structure far away from the model centerline.

5.3 Vertical Plane Numerical and Experimental Comparisons

Figures 5.55 through 5.86 show comparisons of images for numerical and experimental results, with the images oriented vertically. In all these figures, the flow is coming from the left, with the model above the ground plane. Figures 5.55 through 5.70 show vertical images along the x-axis at the model centerline, side jet centerline, model edge (2.5 jet diameters from the model centerline), and 5.5 jet diameters from the model centerline, for both numerical and experimental results at velocity ratios of 0.09 and 0.03, all at a model height of 4 jet diameters. Figures 5.71 through 5.86 show images along the z-axis, with images located across the forward pair of jets, the rear pair of jets, midway between the forward and rear pair of jets, and midway between the inlets and forward pair of jets, for both numerical and experimental results, at velocity ratios of 0.09 and 0.03, all at a model height of 4 jet diameters.

5.3.1 Numerical and Experimental Comparisons for $U/V_j = 0.09$

This first sequence shows comparisons of numerical and experimental results at a velocity ratio of 0.09, along the x-axis of the model. Figures 5.55 and 5.56 show images of the flowfield at the centerline for numerical and experimental results respectively. Taking into account the different scales and orientation of the two figures, the two flowfields are quite similar. Major differences are only seen in the fountain region, where the fountain in the numerical results remains vertical, compared to the downstream tilt to the fountain in the experimental results. Other differences are seen in the forward region of the flow, where the free stream appears to penetrate and mix much further downstream in the experimental data.

At the side jet centerline, shown in figures 5.57 and 5.58 for numerical and experimental data respectively, the two flowfields show some differences, although the structures in each of the flowfields is nearly the same. Major differences are seen in the forward area of the flow, where the numerical results show higher temperatures near the

model undersurface, and the experimental results show portions of the ground vortex and forward vortex pair near the ground plane. Other differences appear in the fountain region, which is vertically oriented in the numerical results, and pushed over by the free stream in the experimental results. These differences may account for the greater mixing in the experimental results in the fountain region, as noted above.

Figures 5.59 and 5.60 show images at the model edge, 2.5 jet diameters from the model centerline. Again, there are differences in the forward region of the flowfield, which shows higher temperatures near the model in the numerical data, and higher smoke concentration near the ground plane in the vicinity of the ground vortex and forward vortex pair, at the ground plane. The other structures seen in the experimental and numerical results are very similar in shape, although the amplitudes are different. The formation of a second ground vortex associated with the downstream pair of jets is apparent in both figures.

Figures 5.61 and 5.62 show numerical and experimental images respectively, at a plane 5.5 jet diameters from the model centerline. In the experimental data, both the ground vortex and second downstream ground vortex are visible, and quite distinct. These two features appear much smaller in the numerical results, even taking into account the scale of the two images. Part of this may be due to the differences seen in the forward area of the flowfield in the previous two pairs of figures.

5.3.2 Numerical and Experimental Comparisons at $U/V_j = 0.03$

The next set of eight figures shows the same vertical planes shown in figures 5.55 through 5.62 for numerical and experimental results at a velocity ratio of 0.03. Some of the same trends seen at a velocity ratio of 0.09 are seen in these figures.

Figures 5.63 and 5.64 show false color images of numerical and experimental results at the model centerline, for a velocity ratio of 0.03. Both these flowfields show

similar extents and similar structures, although the experimental data show higher concentrations in the fountain region, especially at the model undersurface.

Figures 5.65 and 5.66 show images of numerical and experimental data through the side jet centerline. Both flowfields contain similar structures. The fountain in the experimental results is less distinct, and suggesting more mixing is occurring in this region in the experimental results, especially closer to the model undersurface. The wall jet and flow along the model undersurface forward of the upstream jet also appear to be larger and more developed than seen in the numerical results. The numerical data also show a much broader flow along the model undersurface, and a much less distinct wall jet.

At the edge of the model, 2.5 jet diameters from the model centerline, the differences between the numerical and experimental results become distinct. Figures 5.67 and 5.68 show images of the flowfield for numerical and experimental data respectively. Visible in the experimental results is the wall jet, the ground vortex, and the counter-rotating vortex pair between the fountain and jets. Almost none of these structures is visible in the numerical temperature image, although some of the structures may be related.

At a plane 5.5 jet diameters from the centerline, the numerical and experimental results do show some of the same structures, as seen in figures 5.69 and 5.70 respectively. The size and extent of the structures is somewhat different, with the ground vortex and second ground vortex, as well as the wall jet, much more distinct and visible in the experimental results. These differences may possibly be related to differences between the numerical and experimental results in the inner flow region influencing the flowfield in this area. Since these flowfield structures are different in the inner flowfield, they will be different in the outer area as well.

5.3.3 Numerical and Experimental Comparisons Along Z-Axis

The next sequence of figures shows false color images of numerical and experimental data for velocity ratios of 0.09 and 0.03 along the z-axis, across the model and normal to the free stream flow. The images are located at the forward jet pair centerline, rear jet pair centerline, midway between the forward and rear jet pairs, and midway between the inlets and forward jet pairs. At high velocity ratios, no flow in the numerical data reached the inlets, so these planes are not shown.

For a velocity ratio of 0.09, the numerical and experimental results agree well at the forward jets, aft jets, and midway between the forward and aft jets, as seen in figures 5.71 through 5.76. There are no clear differences between the two flowfields for these planes. At the plane midway between the inlets and forward jet pair, the two flowfields are quite dissimilar. Figures 5.77 and 5.78 show numerical and experimental data respectively for this plane. Most of the flow in the numerical data appears near the model undersurface, rather than at the ground plane, as seen in the experimental data. The experimental data is much more extensive than the numerical data as well. This extensive region in the experimental data is due to the forward vortex pair and ground vortex, which are both located in this area. As seen in the previous sequence of figures along the model, the numerical model does not predict these features well.

At a velocity ratio of 0.03, false color images across the forward and rear pairs of jets, as well as the model centerline, show large similarities in the structure and extent of the flowfield features seen in the numerical and experimental data. Figures 5.79 through 5.84 show the flowfield for numerical and experimental data for these planes. These images show a much thicker wall jet in the experimental data, as well as a more extensive mid plane. Most of the other flow features are similar, however.

At the plane midway between the inlets and forward jet pair, seen in figures 5.85 and 5.86 for numerical and experimental results, the two flowfields also appear similar,

the major difference again being in the wall jet thickness and intensity. The 127 frame averaged experimental flowfield also does not distinctly show the vortex features on the underside of the model, seen in the numerical data. These vortices could be present in the experimental data. They may also have propagated from out between the forward pair of jets, acting similar to the side jet pair's counter-rotating vortex pair. Unsteadiness in this vortex pair in the experimental results may have smeared this vortex pair, making it difficult to see in the time-averaged images.

Table 5.1: Extent of Recirculating Hot Gas Zone Upstream of Forward Lift Jets

Case	U/V_j	H/D_j	Numerical Results [52]	Experimental Results	
				Suction On	Suction Off
1	0.03	4.0	35	31	38
2	0.03	2.0	46	22	35
3	0.09	4.0	10	12	14
4	0.09	2.0	12.5	14	17

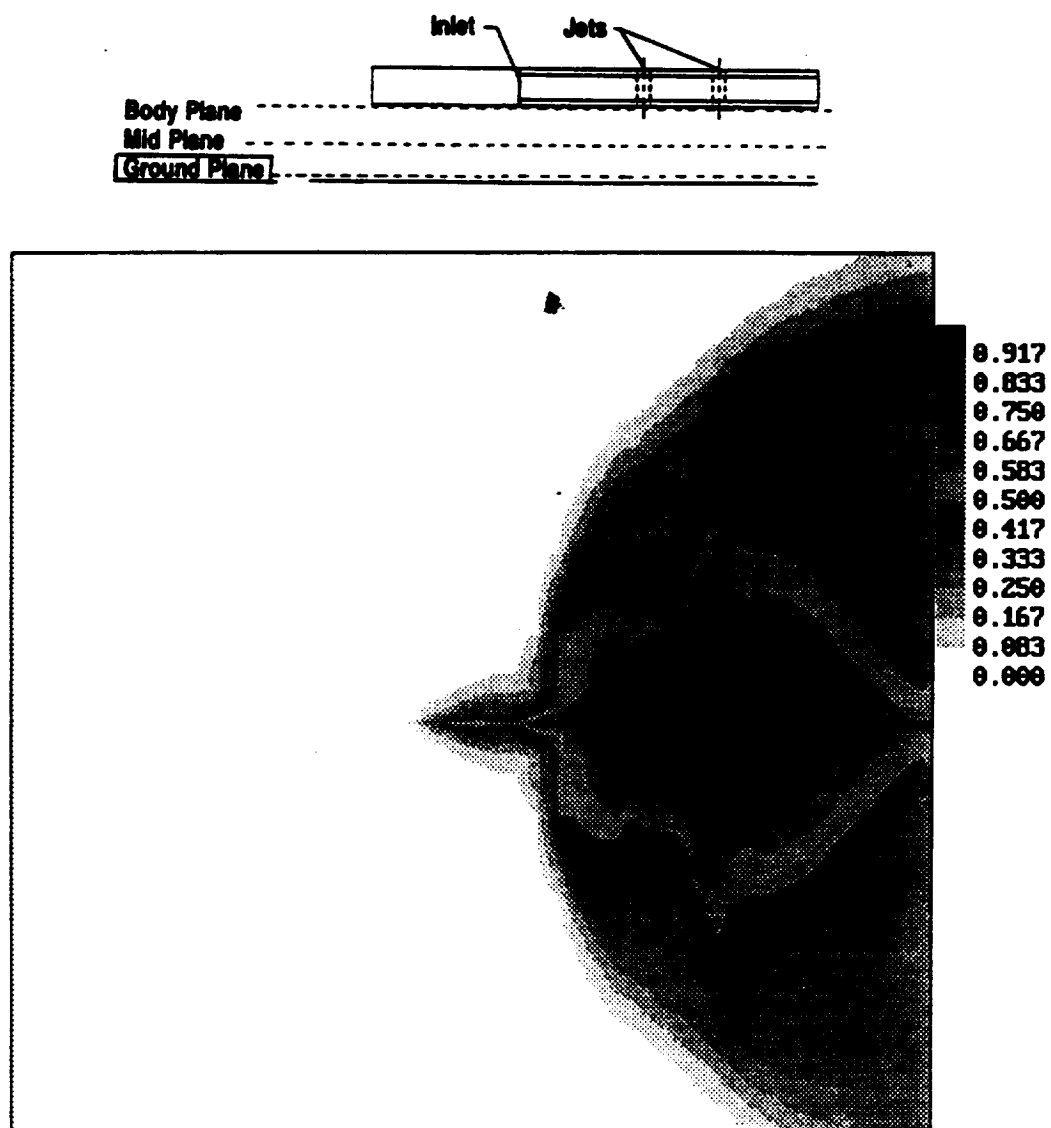


Figure 5.1: Numerical Temperature Profile at Ground Plane: $y/D_j = 0.0$
 $H/D_j = 4$, $U/V_j = 0.09$

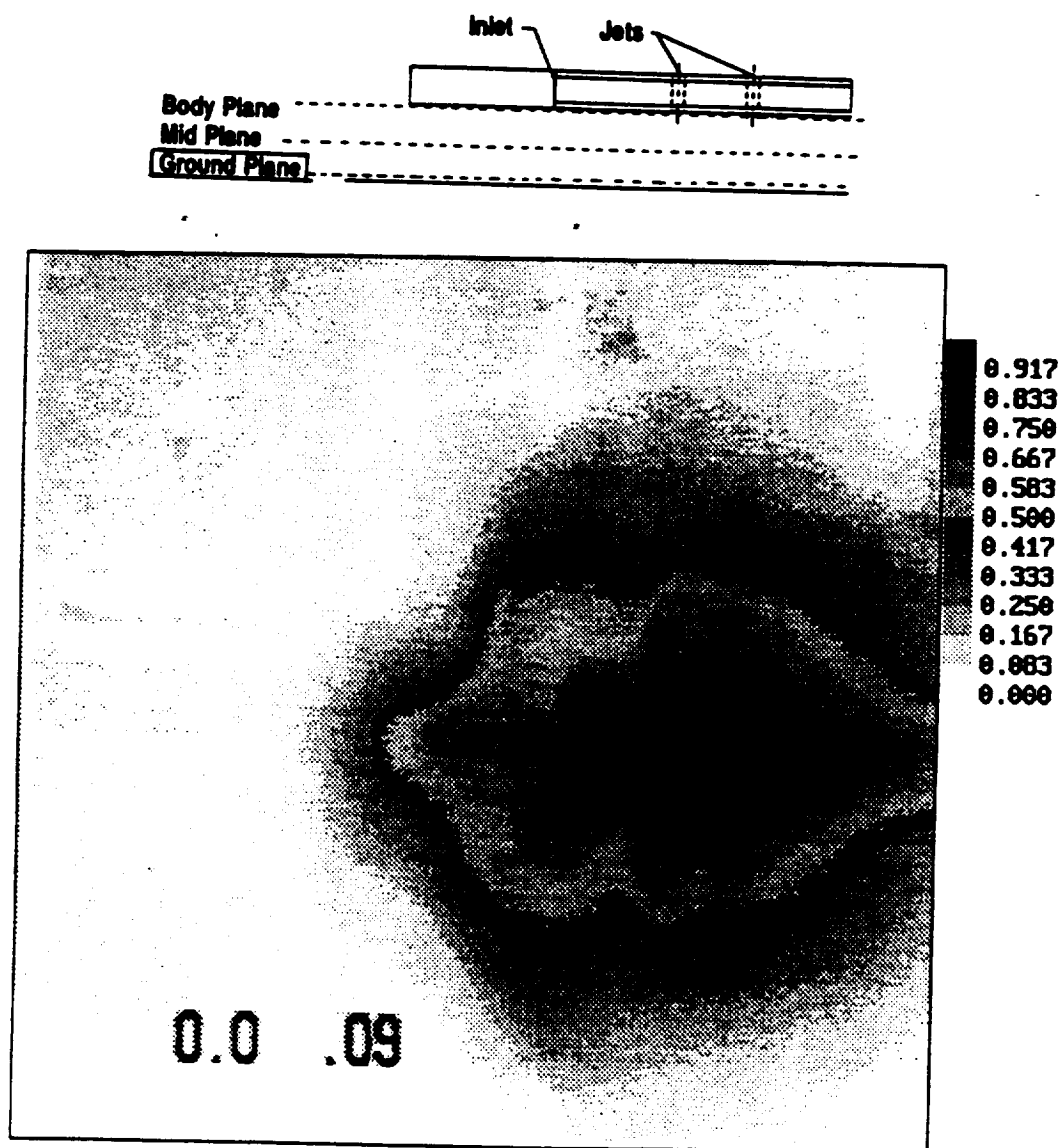


Figure 5.2: Experimental Smoke Concentration Profile at Ground Plane: $y/D_j = 0.0$
 $H/D_j = 4$, $U/V_j = 0.09$

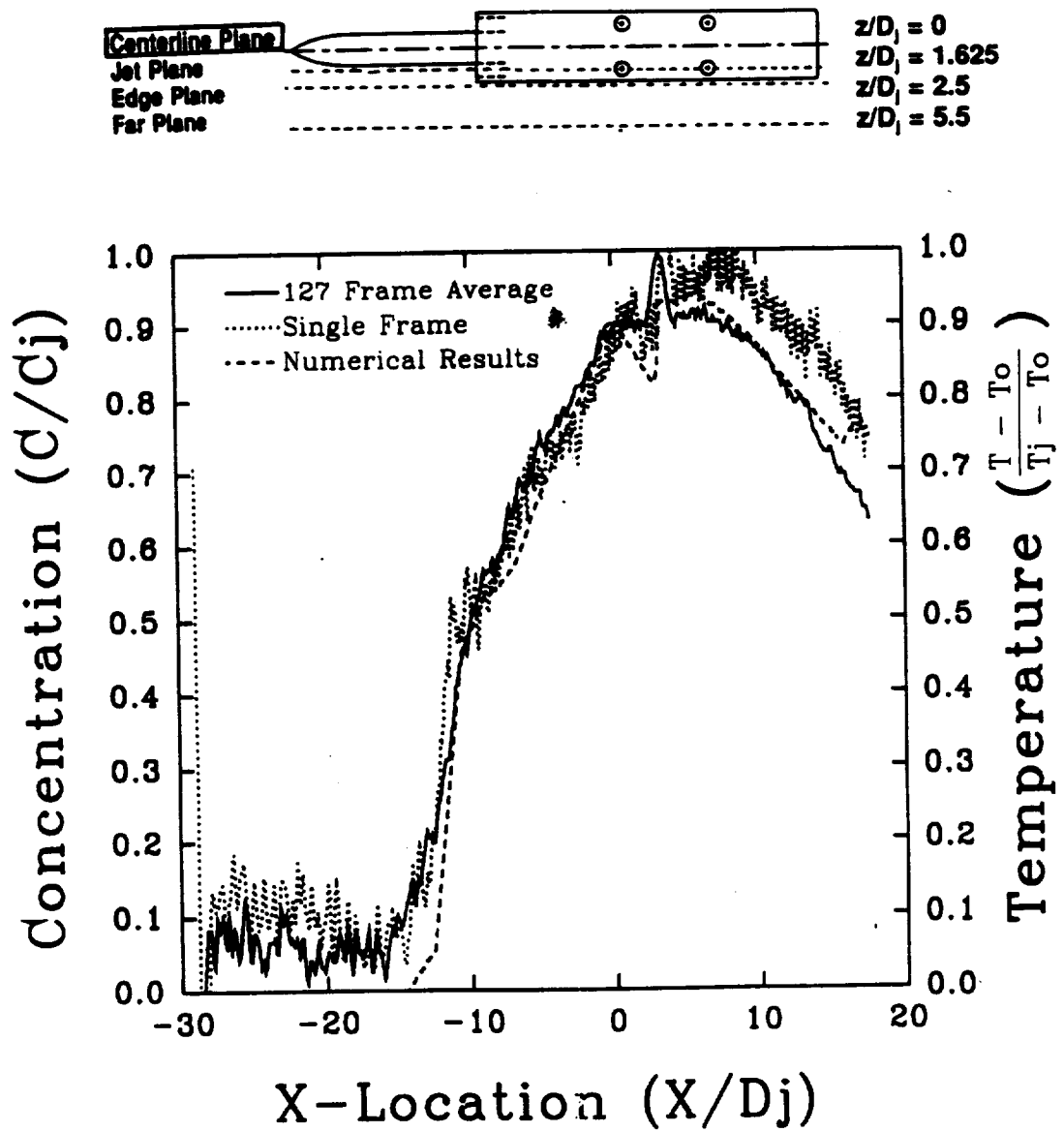


Figure 5.3: Numerical and Experimental Results Along Model Centerline: $z/D_j = 0$
 $y/D_j = 0.0$, $H/D_j = 4$, $U/V_j = 0.09$

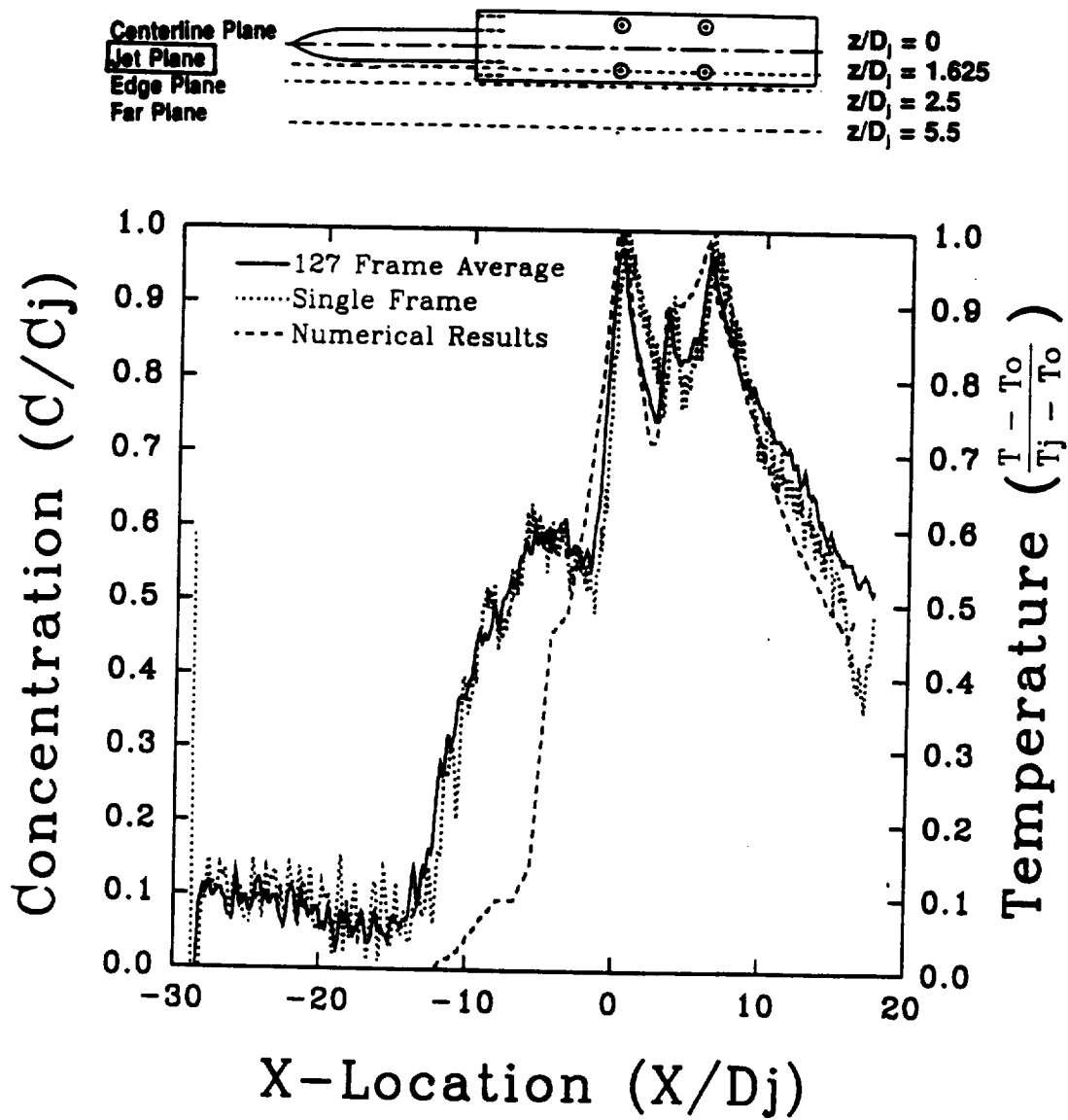


Figure 5.4: Numerical and Experimental Results At Side Jet Centerline: $z/D_j = 1.625$
 $y/D_j = 0.0$, $H/D_j = 4$, $U/V_j = 0.09$

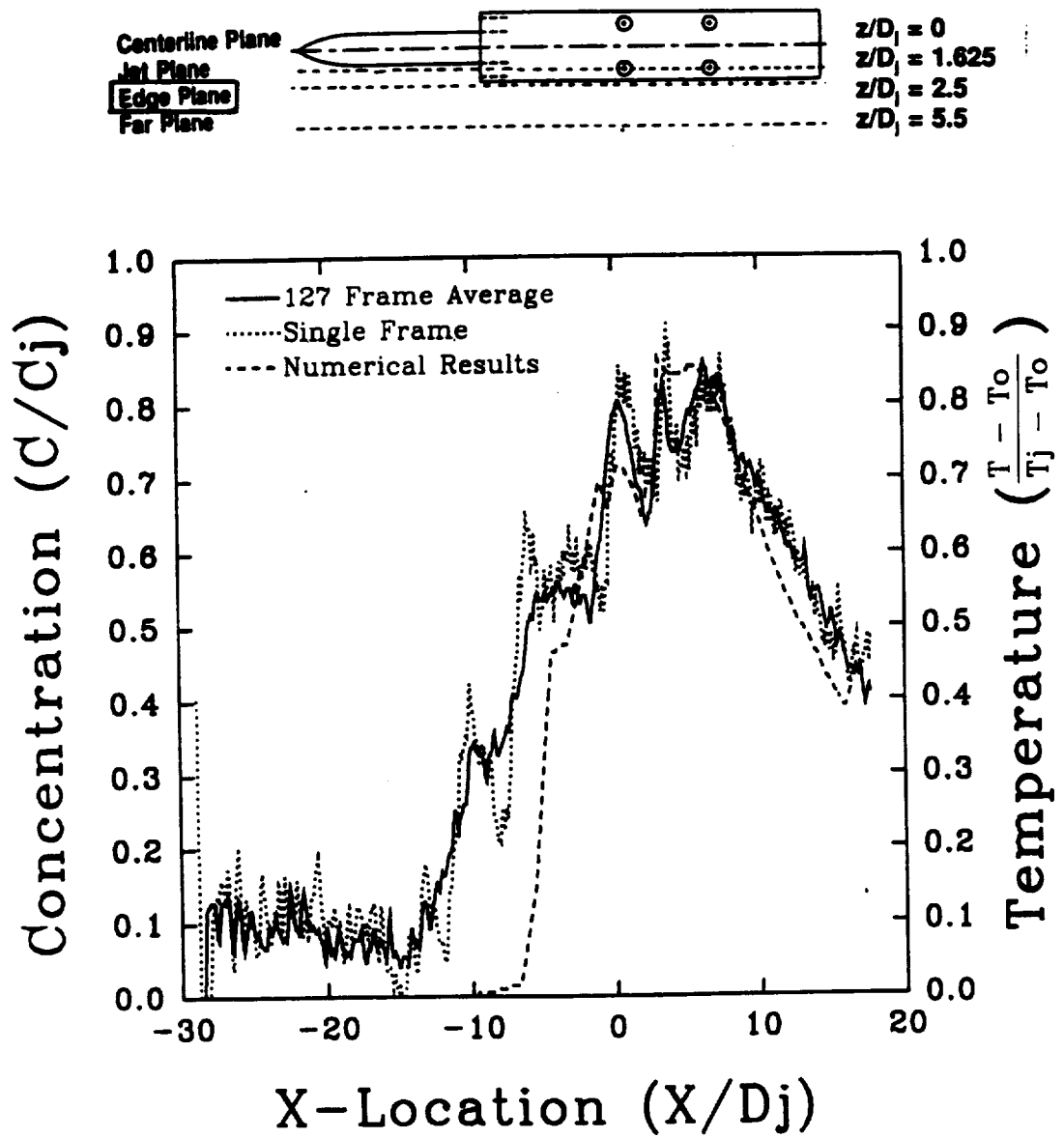


Figure 5.5: Numerical and Experimental Results Along Model Edge: $z/D_j = 2.5$
 $y/D_j = 0.0$, $H/D_j = 4$, $U/V_j = 0.09$

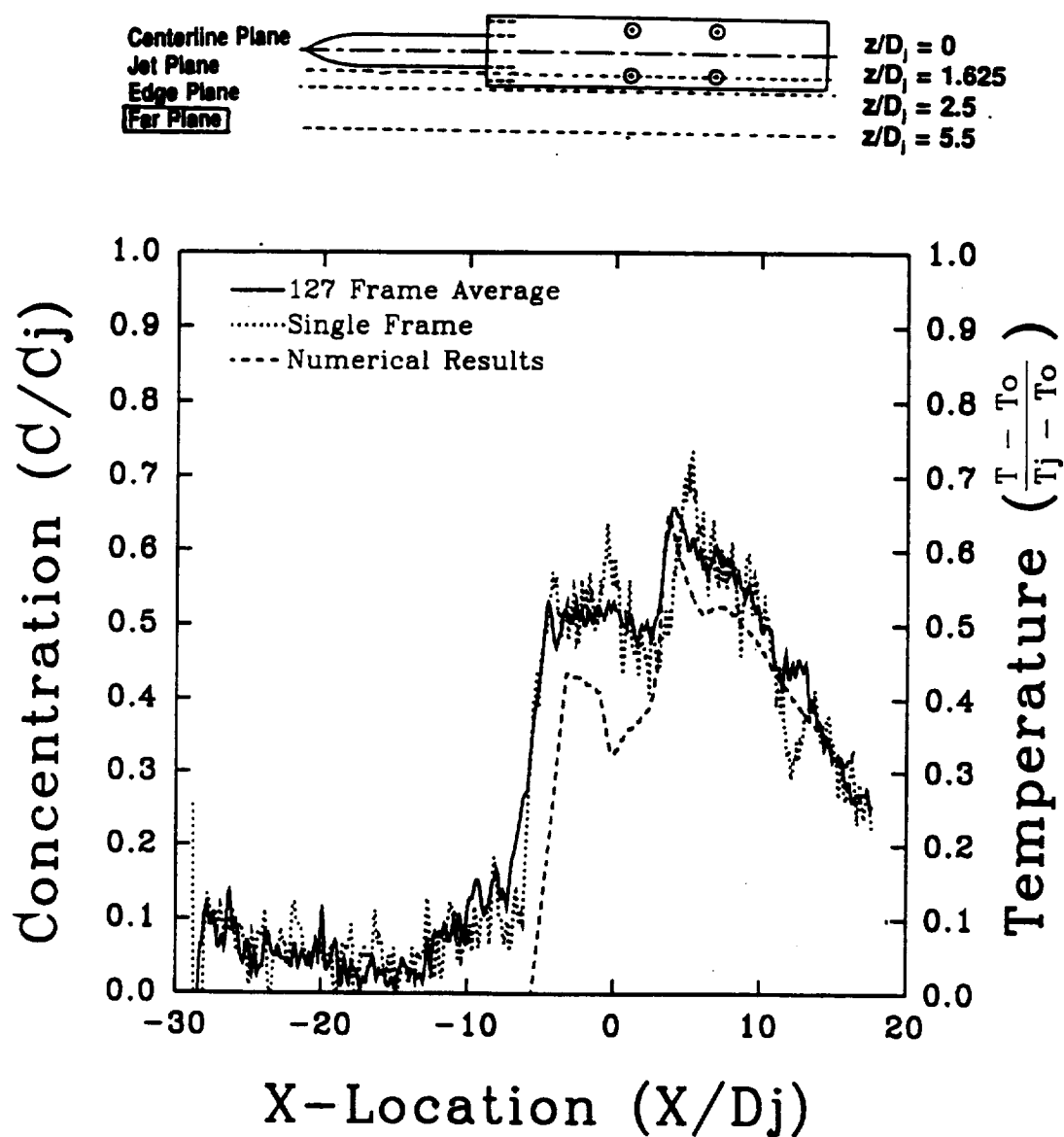


Figure 5.6: Numerical and Experimental Results at $z/D_j = 5.5$
 $y/D_j = 0.0$, $H/D_j = 4$, $U/V_j = 0.09$

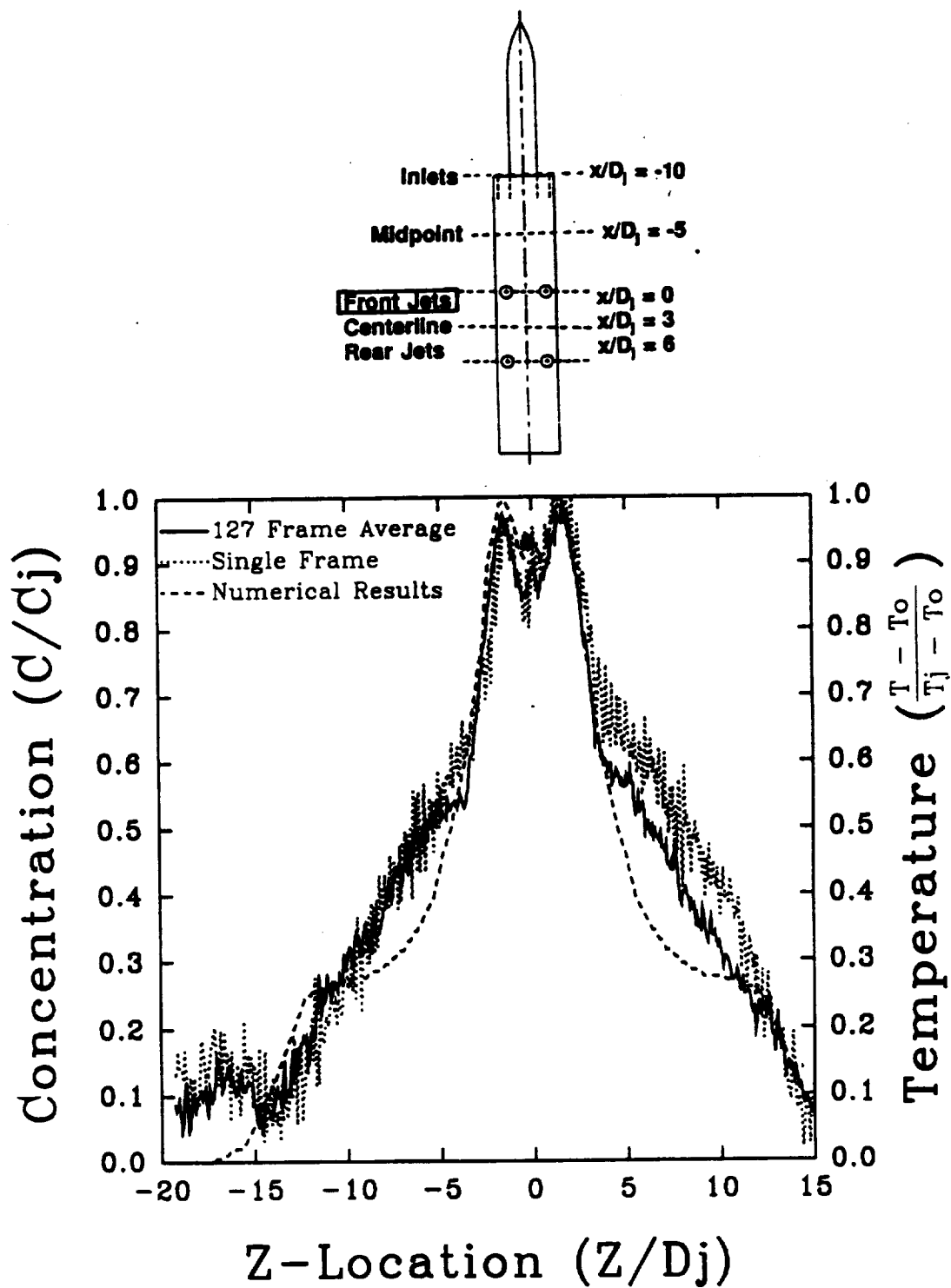


Figure 5.7: Numerical and Experimental Results Across Front Jet Pair: $x/D_j = 0$
 $y/D_j = 0.0$, $H/D_j = 4$, $U/V_j = 0.09$

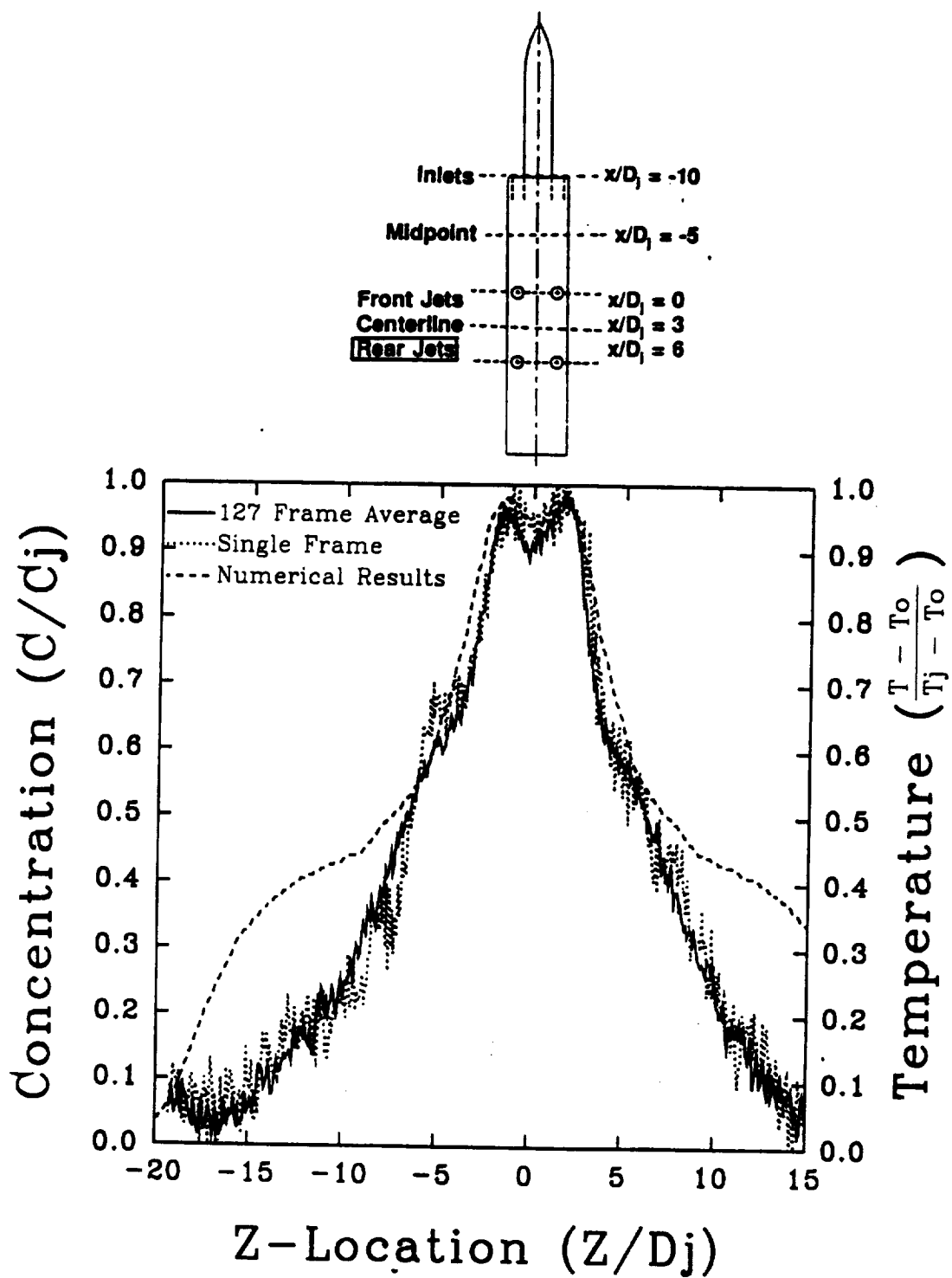


Figure 5.8: Numerical and Experimental Results Across Rear Jet Pair: $x/D_j = 6$
 $y/D_j = 0.0$, $H/D_j = 4$, $U/V_j = 0.09$

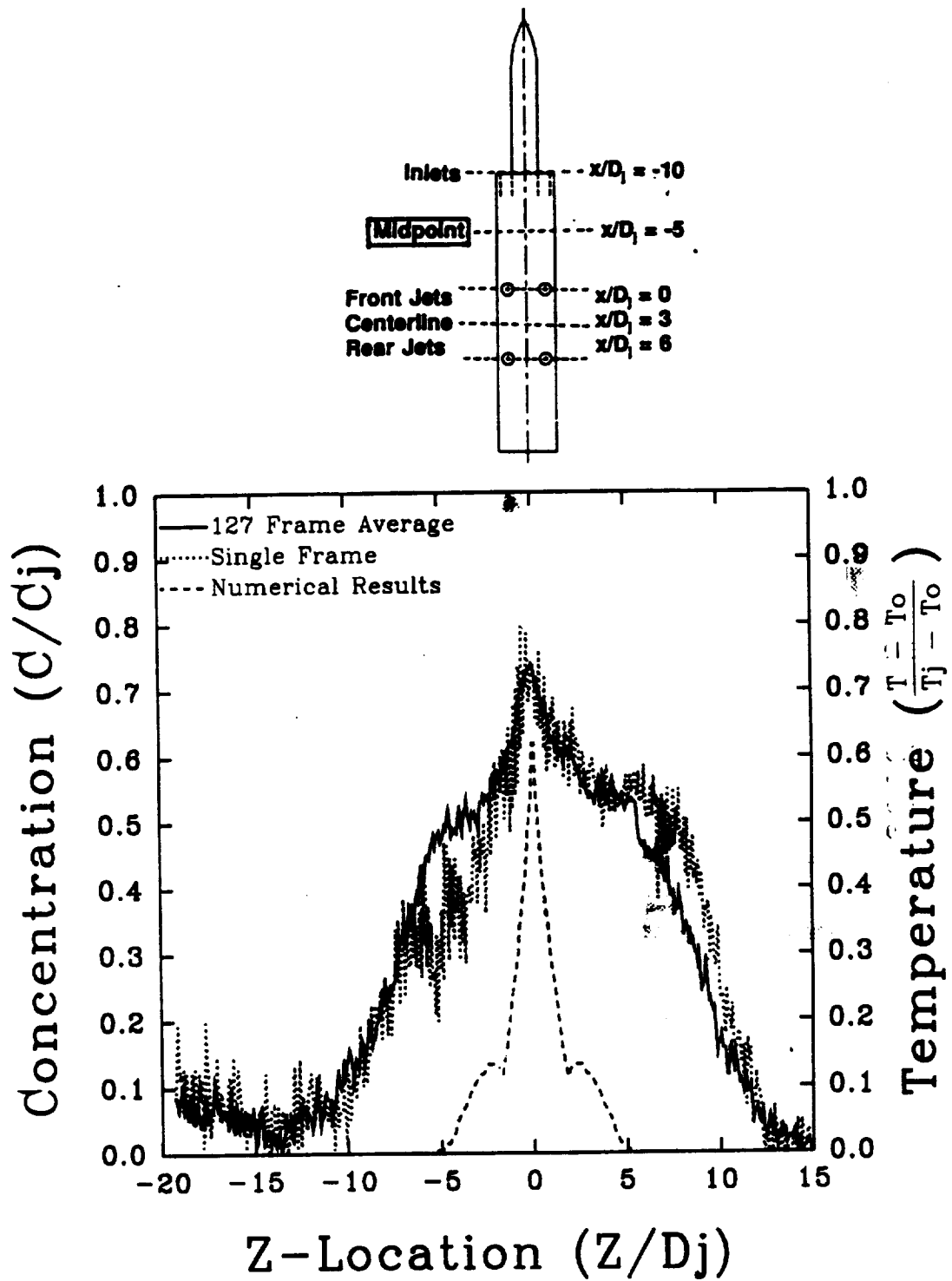


Figure 5.9: Numerical and Experimental Results Between Inlets and Front Jets:
 $z/D_j = -5$, $y/D_j = 0.0$, $H/D_j = 4$, $U/V_j = 0.09$

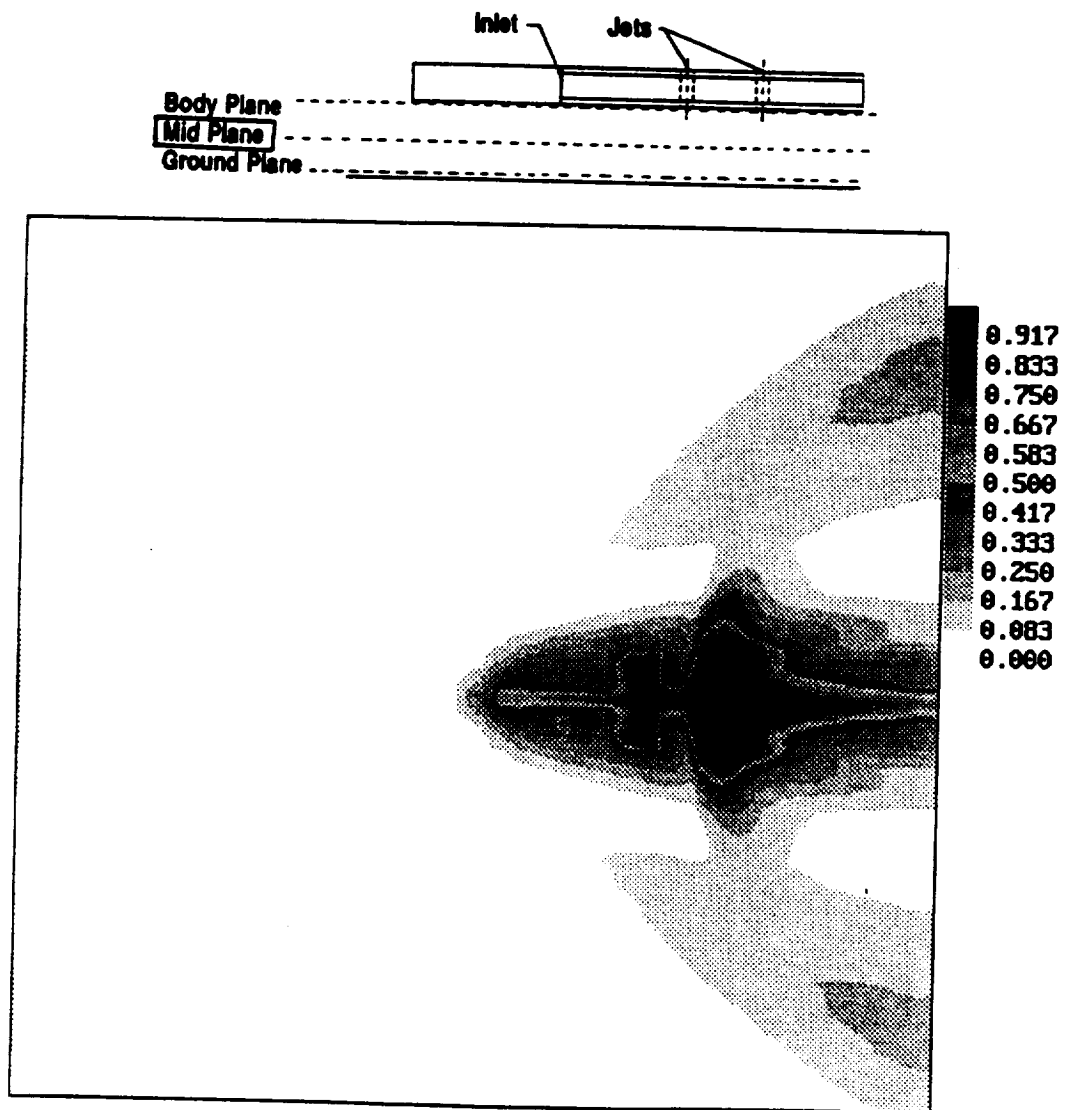


Figure 5.10: Numerical Temperature Profile at Mid Plane: $y/D_j = 2.0$
 $H/D_j = 4$, $U/V_j = 0.09$

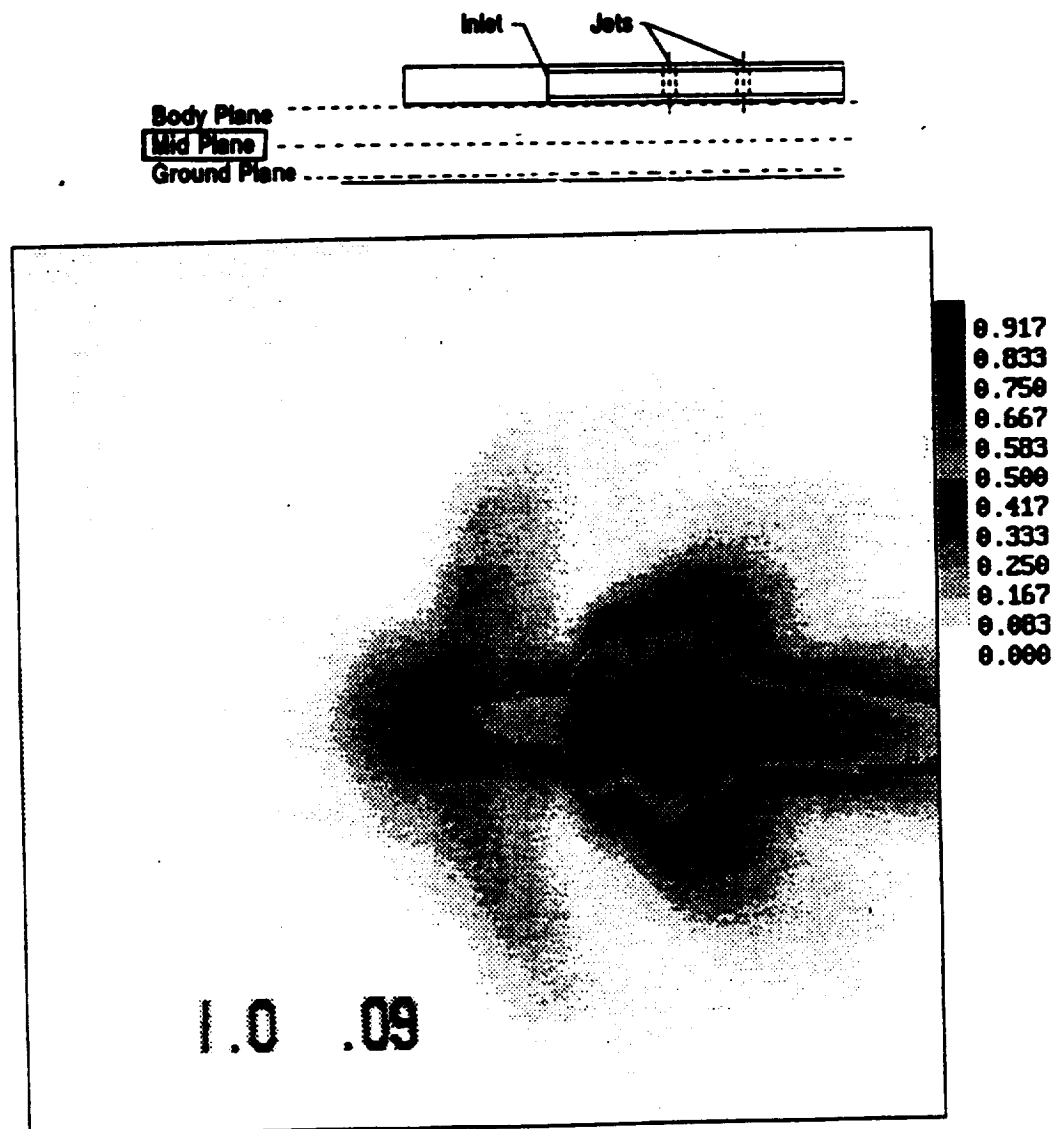


Figure 5.11: Experimental Smoke Concentration Profile at Mid Plane: $y/D_j = 2.0$
 $H/D_j = 4$, $U/V_j = 0.09$

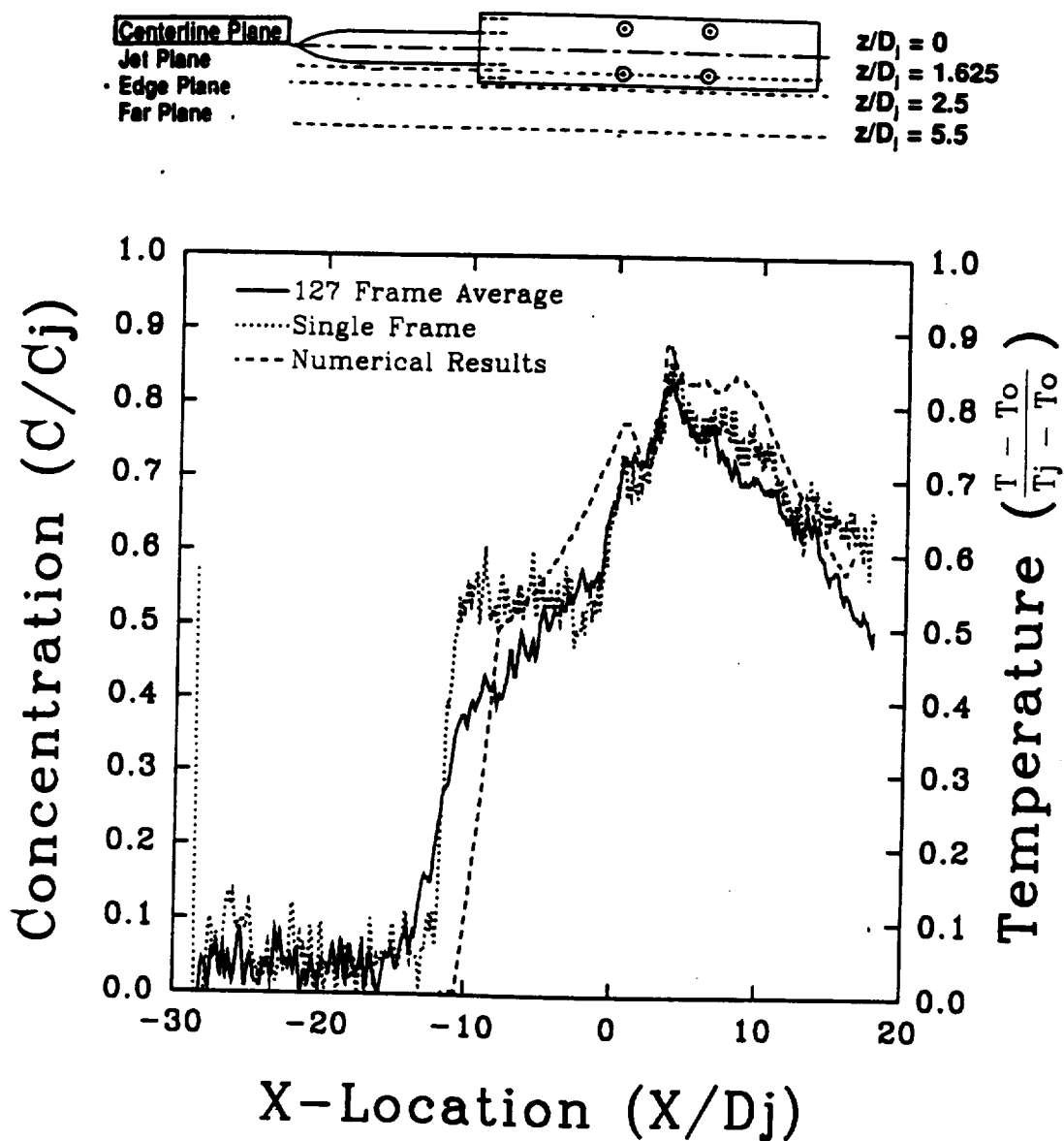


Figure 5.12: Numerical and Experimental Results Along Model Centerline: $z/D_j = 0$
 $y/D_j = 2.0$, $H/D_j = 4$, $U/V_j = 0.09$

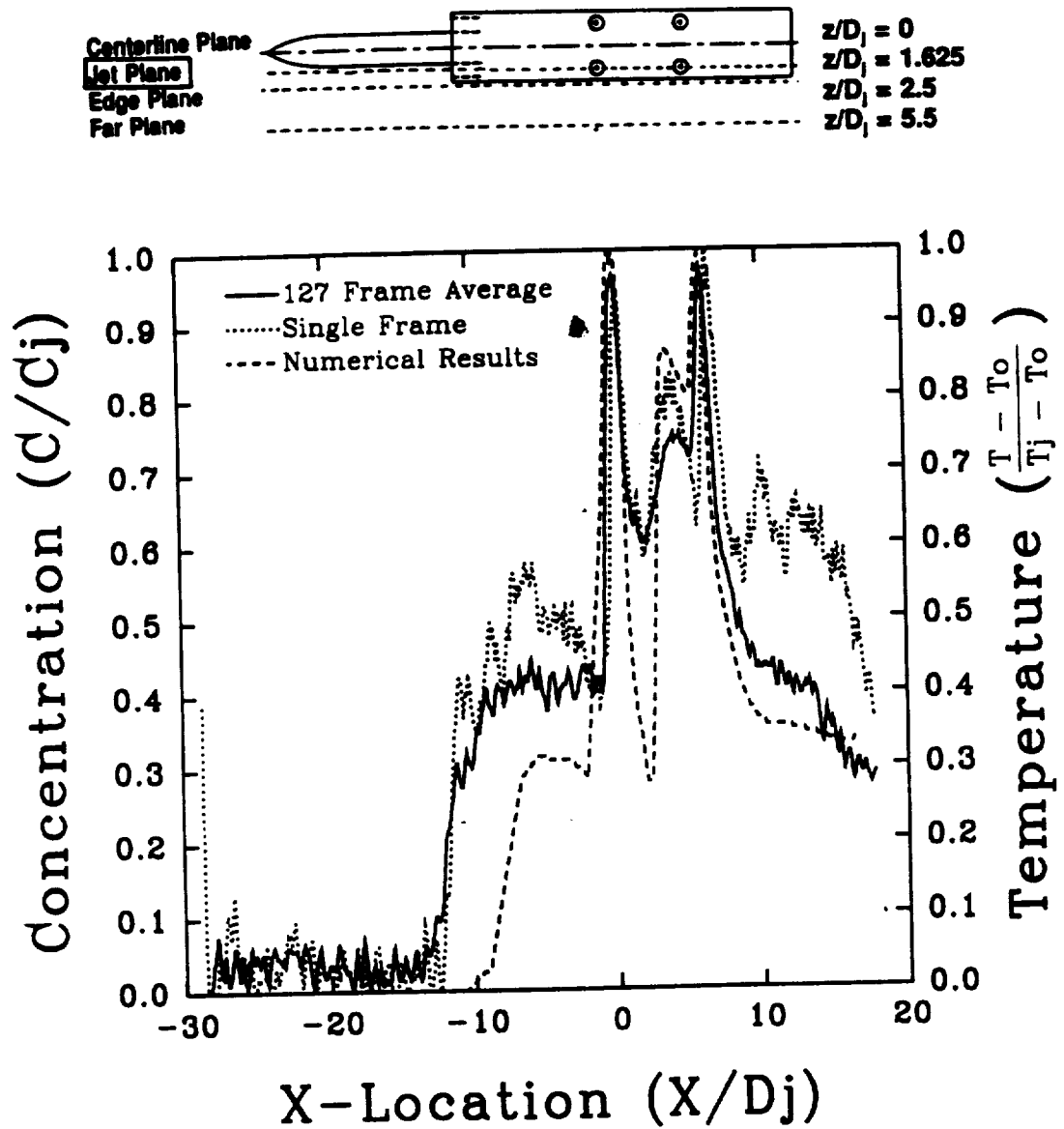


Figure 5.13: Numerical and Experimental Results At Side Jet Centerline: $z/D_j = 1.625$
 $y/D_j = 2.0$, $H/D_j = 4$, $U/V_j = 0.09$

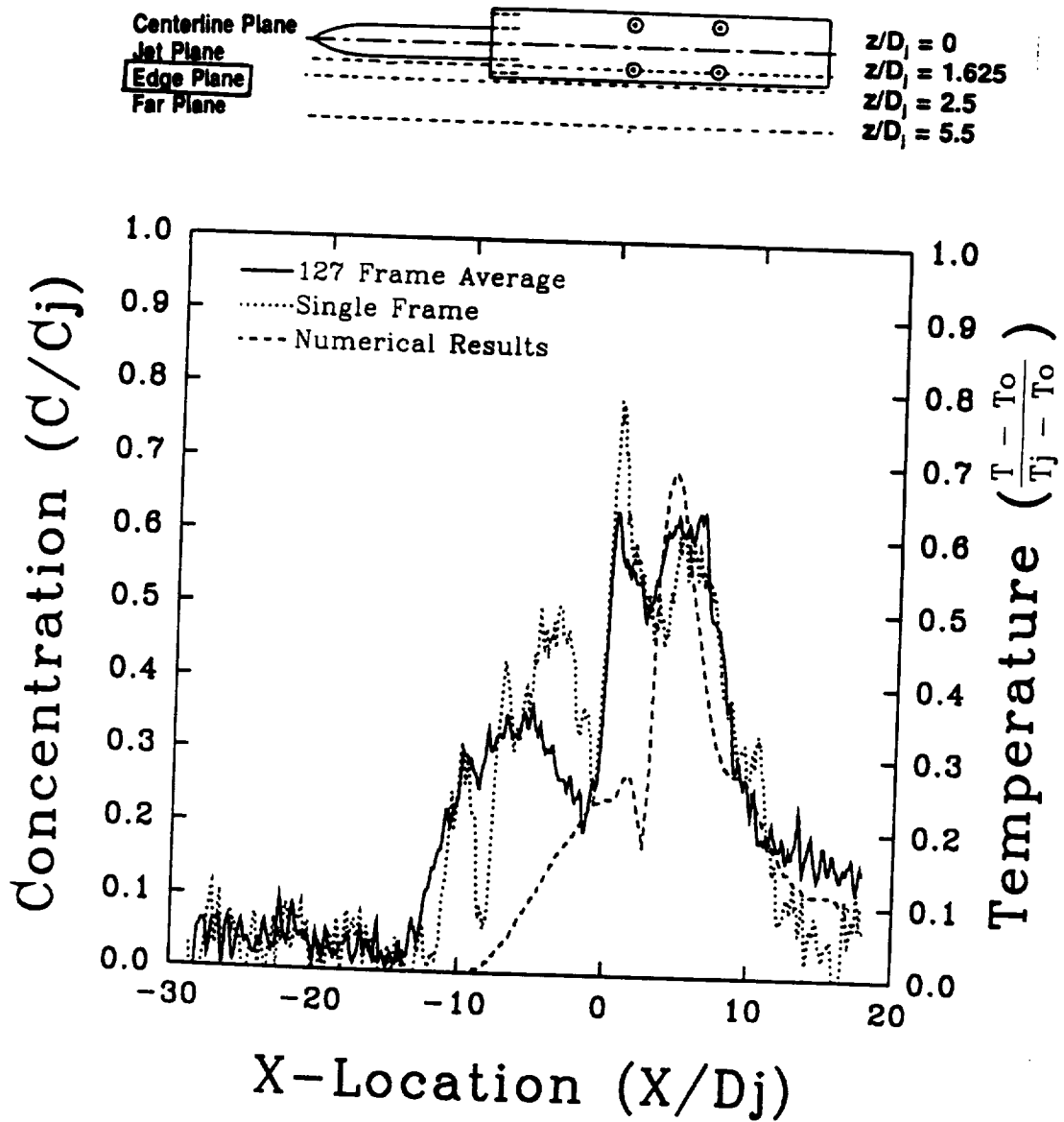


Figure 5.14: Numerical and Experimental Results Along Model Edge: $z/D_j = 2.5$
 $y/D_j = 2.0$, $H/D_j = 4$, $U/V_j = 0.09$

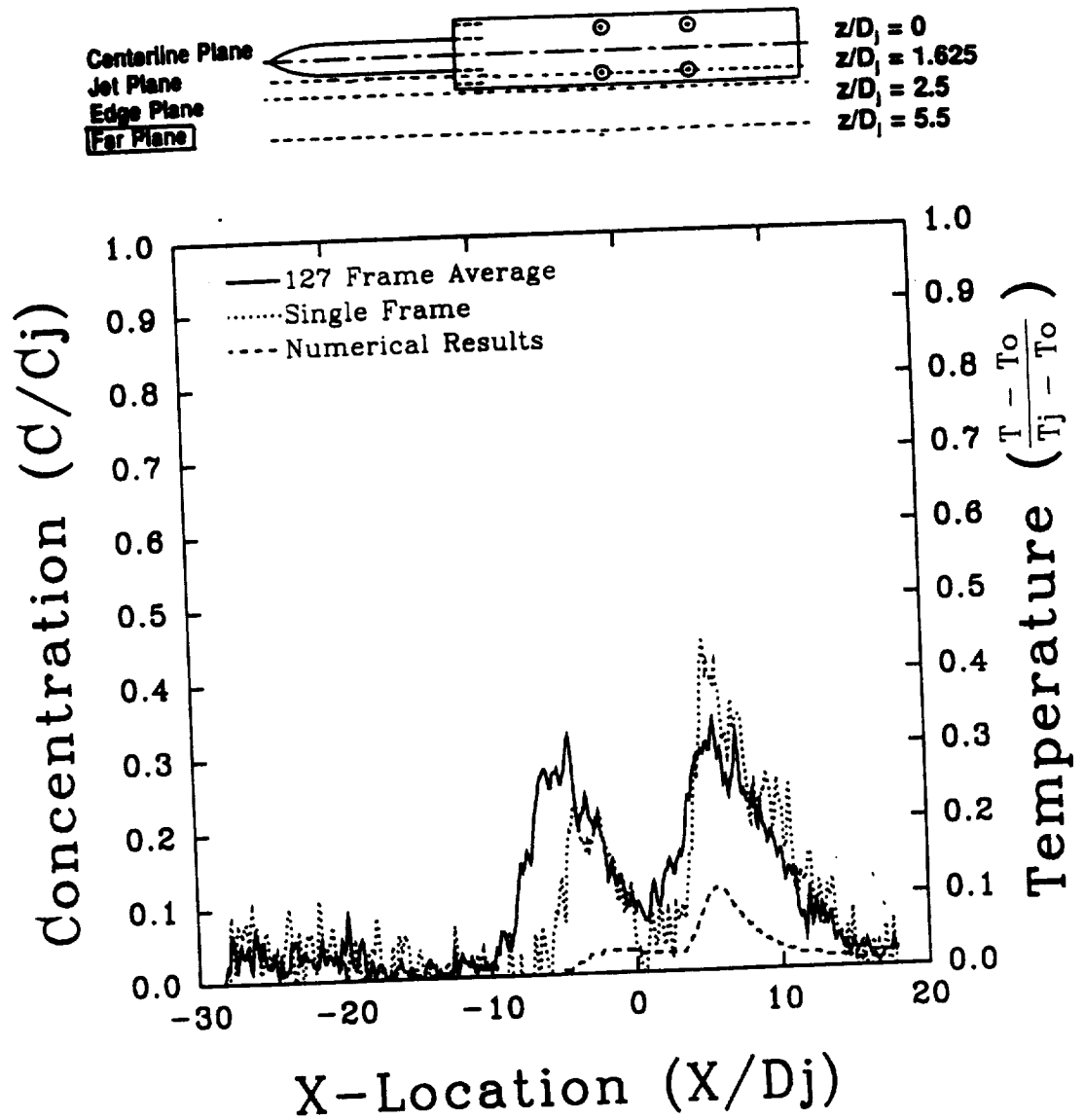


Figure 5.15: Numerical and Experimental Results at $z/D_j = 5.5$
 $y/D_j = 2.0$, $H/D_j = 4$, $U/V_j = 0.09$

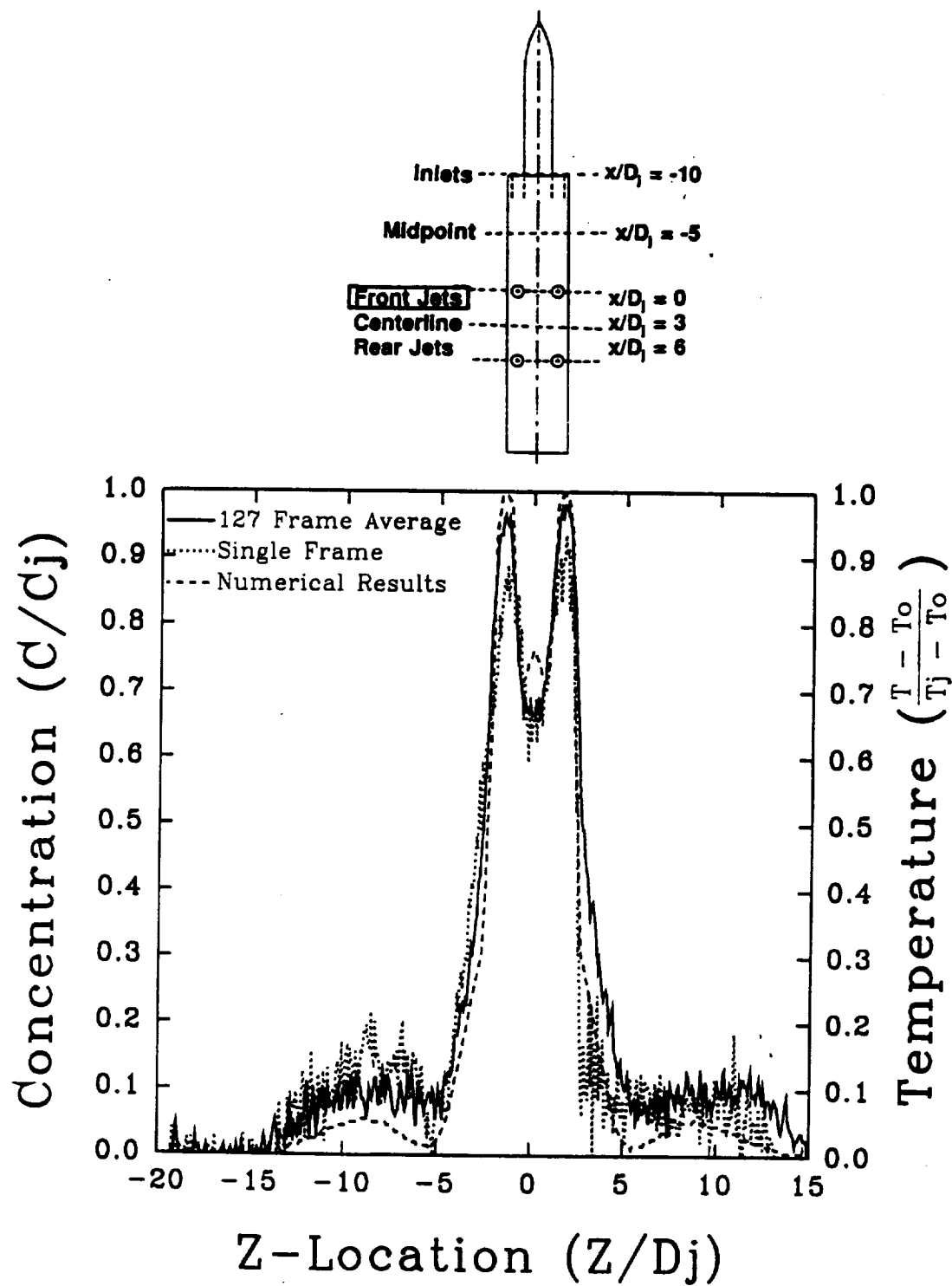


Figure 5.16: Numerical and Experimental Results Across Front Jet Pair: $x/D_j = 0$
 $y/D_j = 2.0$, $H/D_j = 4$, $U/V_j = 0.09$

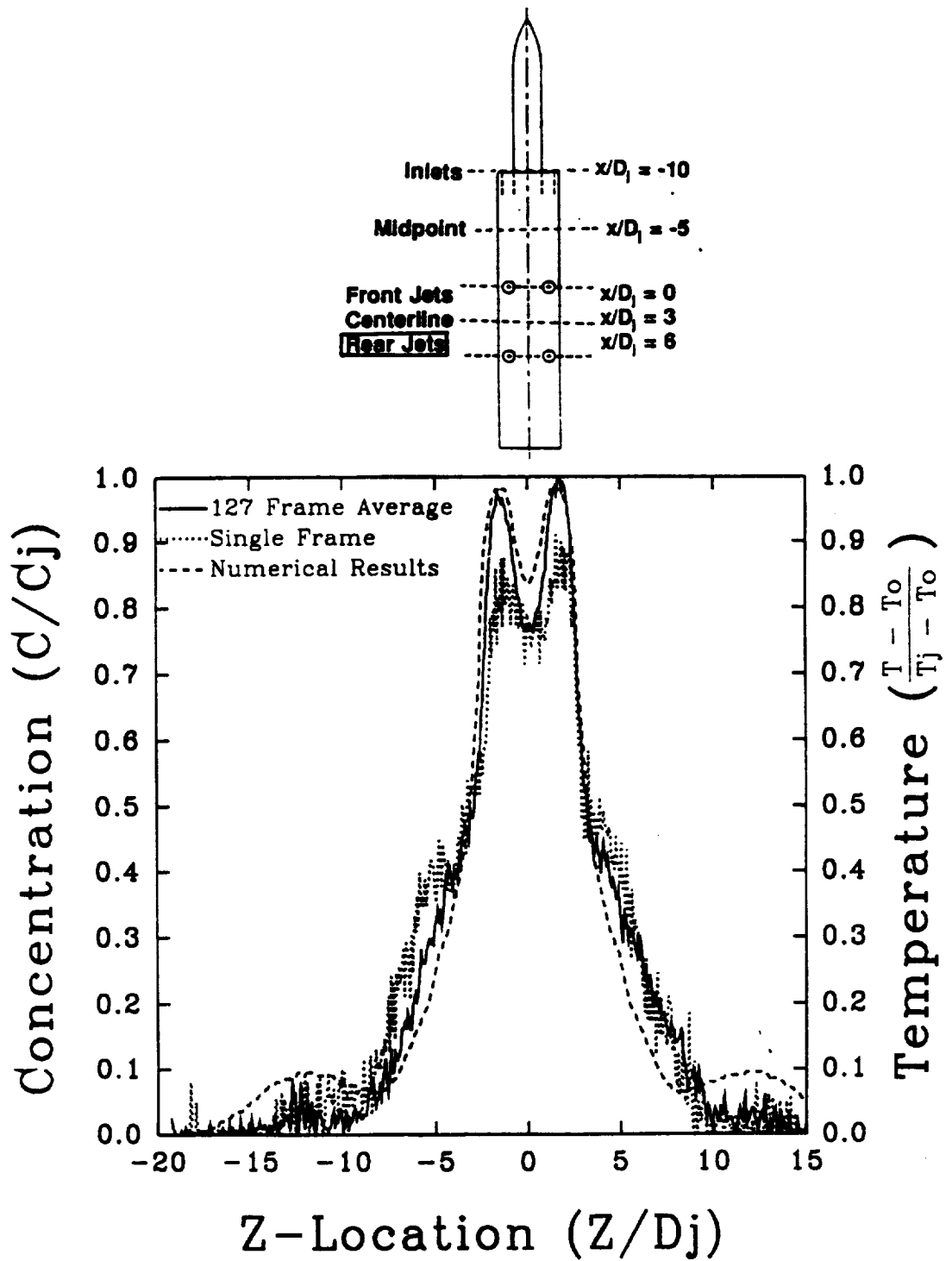


Figure 5.17: Numerical and Experimental Results Across Rear Jet Pair: $x/D_j = 6$
 $y/D_j = 2.0$, $H/D_j = 4$, $U/V_j = 0.09$

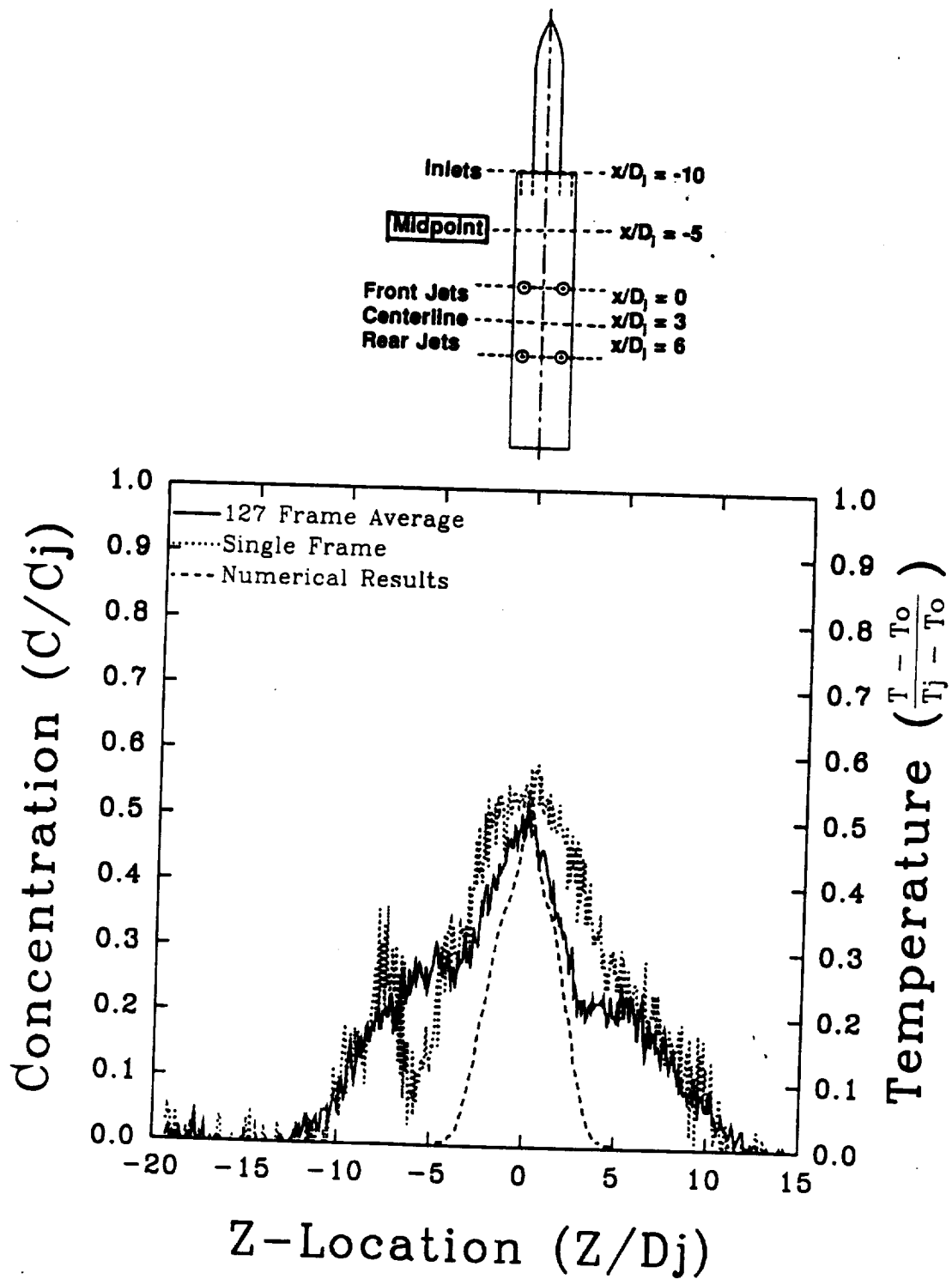


Figure 5.18: Numerical and Experimental Results Between Inlets and Front Jets
 $z/D_j = -5$, $y/D_j = 2.0$, $H/D_j = 4$, $U/V_j = 0.09$

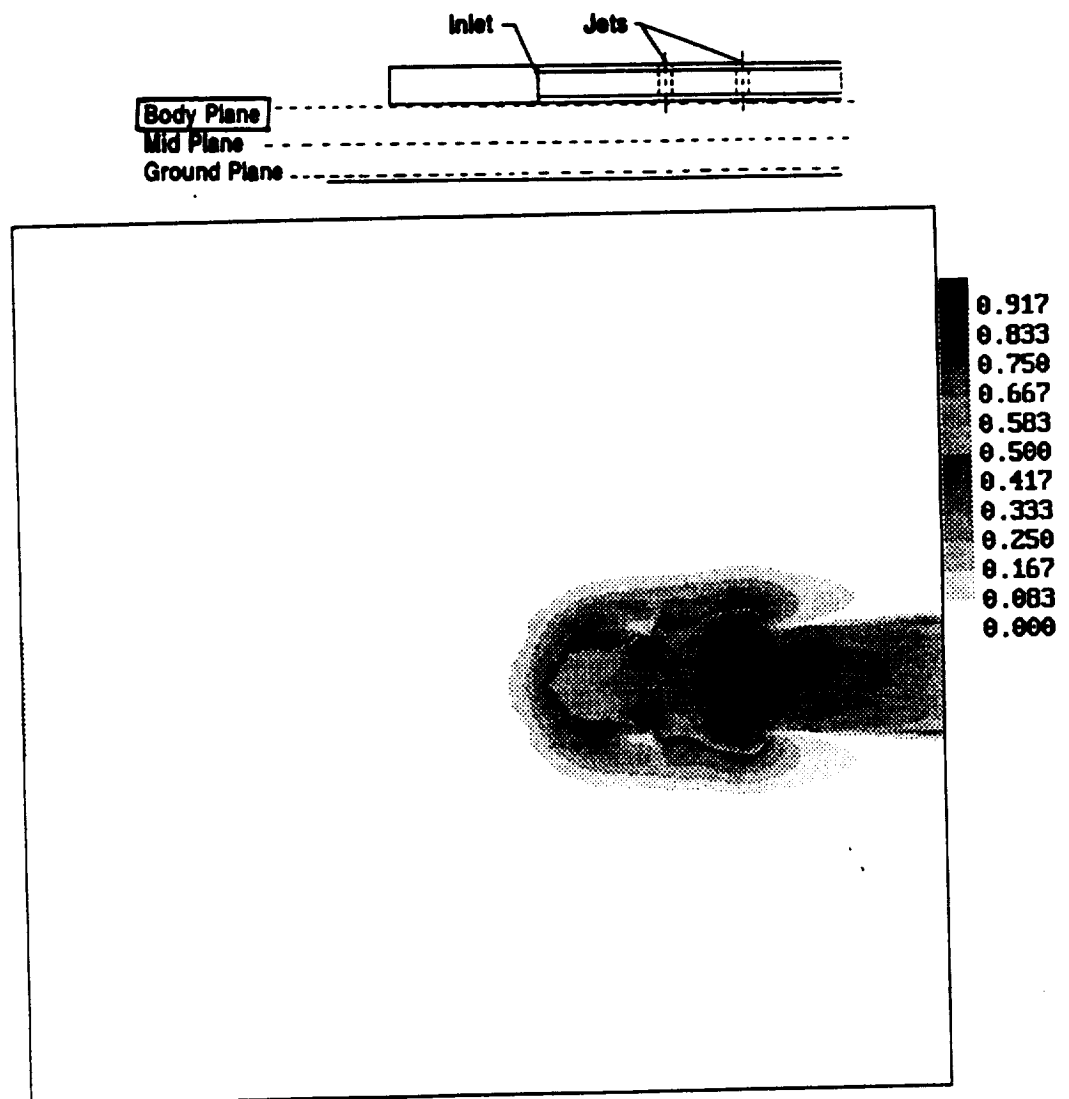


Figure 5.19: Numerical Temperature Profile at Model Body Plane: $y/D_j = 3.6$
 $H/D_j = 4$, $U/V_j = 0.09$

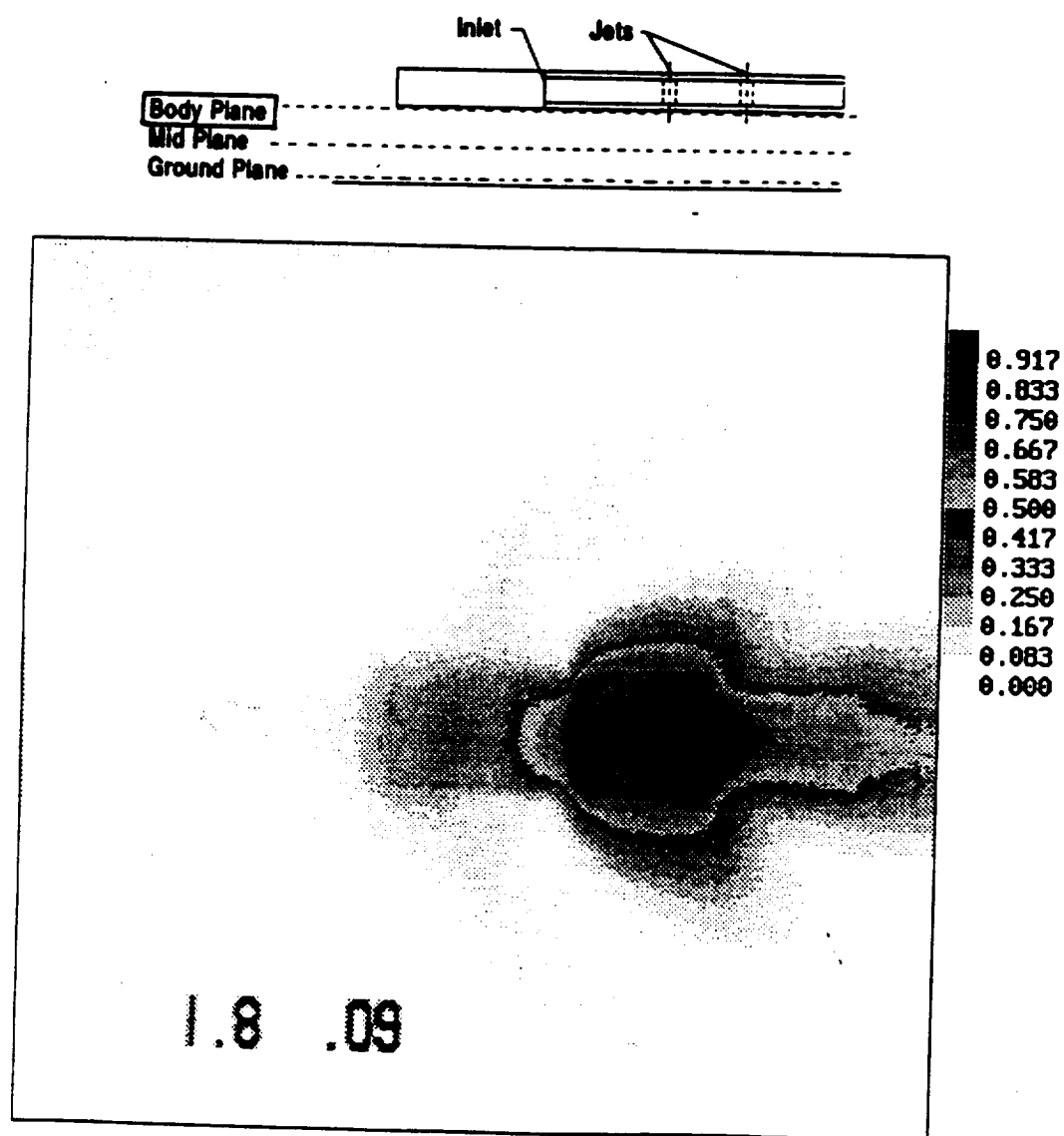


Figure 5.20: Experimental Smoke Concentration Profile at Model Body Plane: $y/D_j = 3.6$
 $H/D_j = 4$, $U/V_j = 0.09$

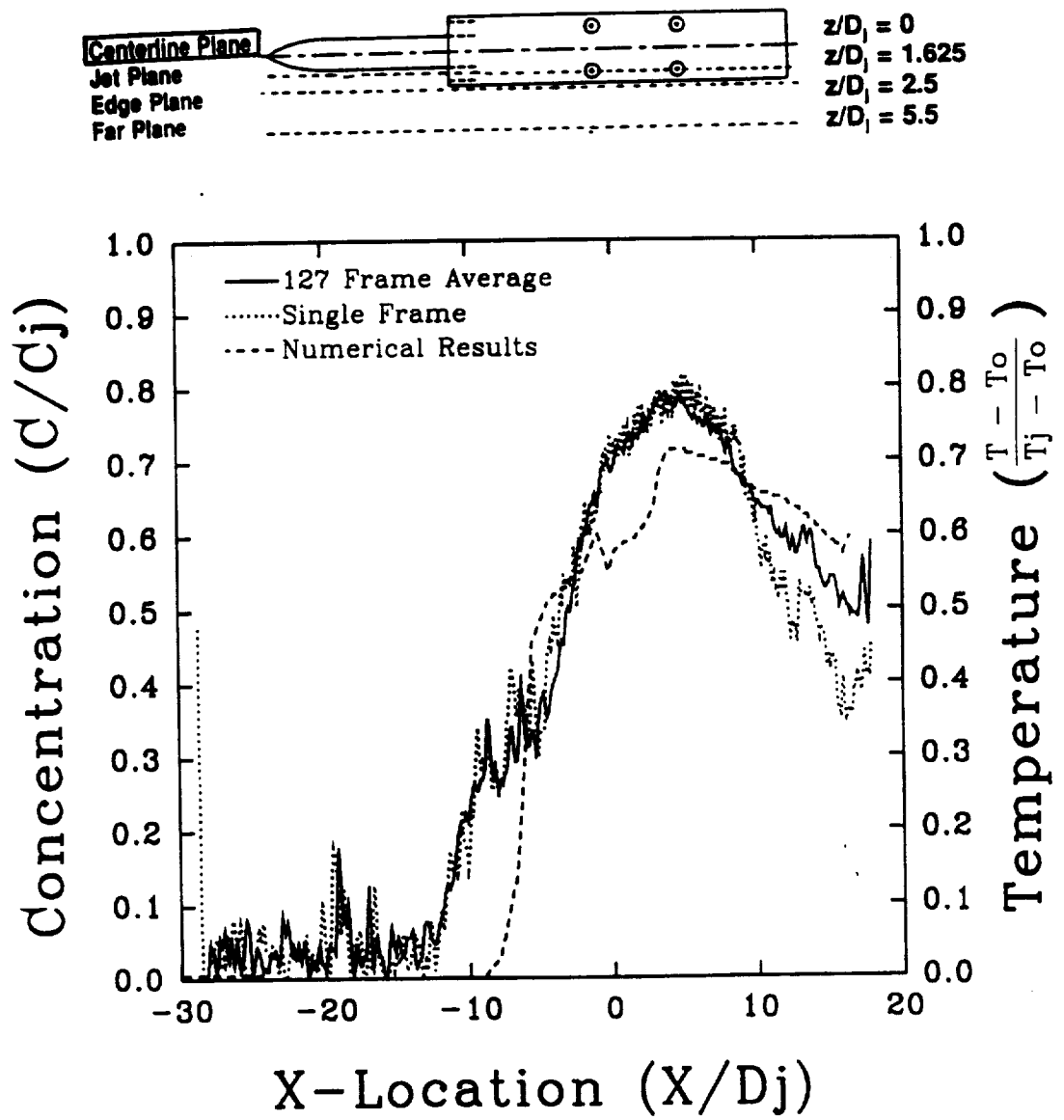


Figure 5.21: Numerical and Experimental Results Along Model Centerline: $z/D_j = 0$
 $y/D_j = 3.6$, $H/D_j = 4$, $U/V_j = 0.09$

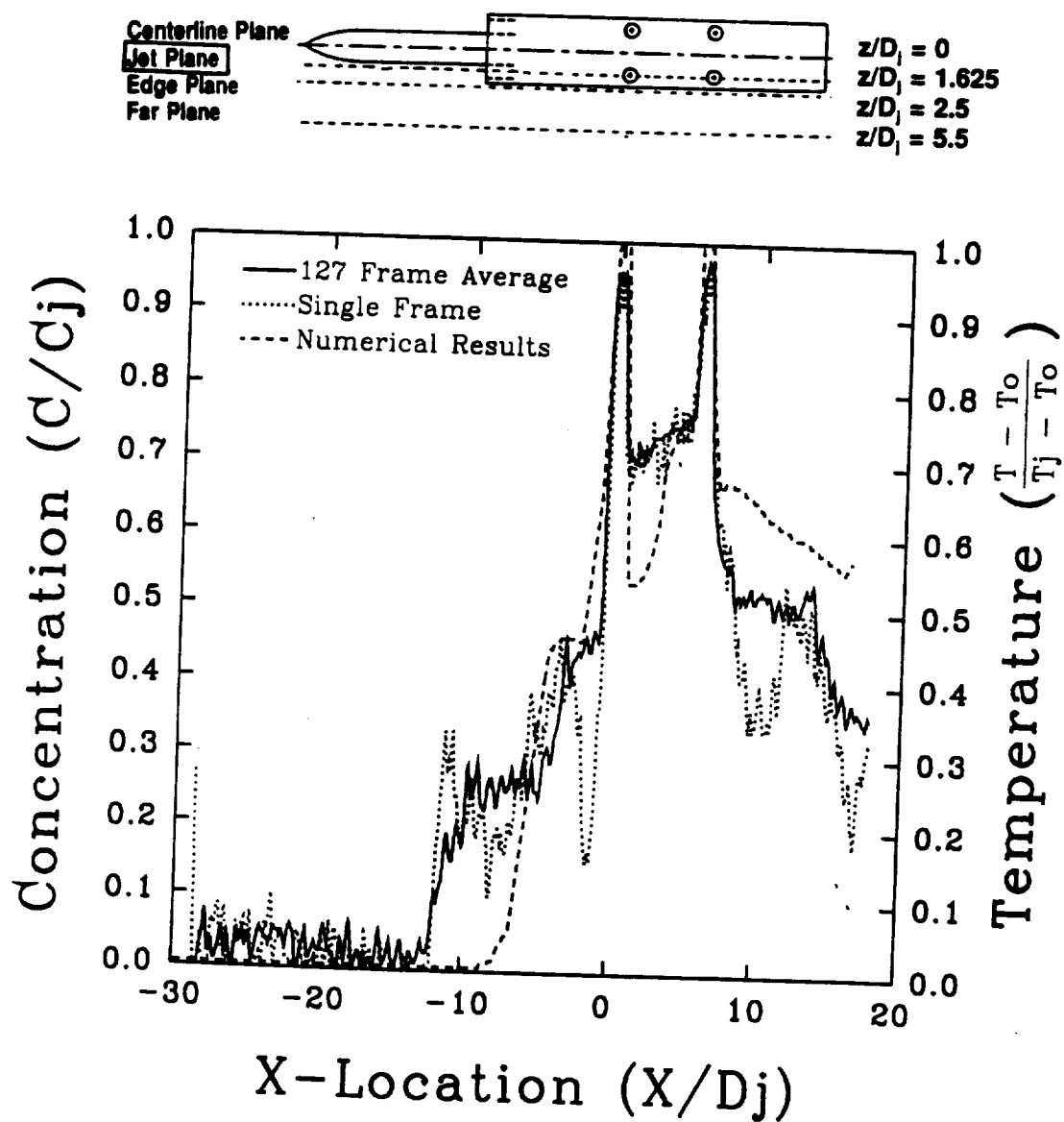


Figure 5.22: Numerical and Experimental Results At Side Jet Centerline: $z/D_j = 1.625$
 $y/D_j = 3.6$, $H/D_j = 4$, $U/V_j = 0.09$

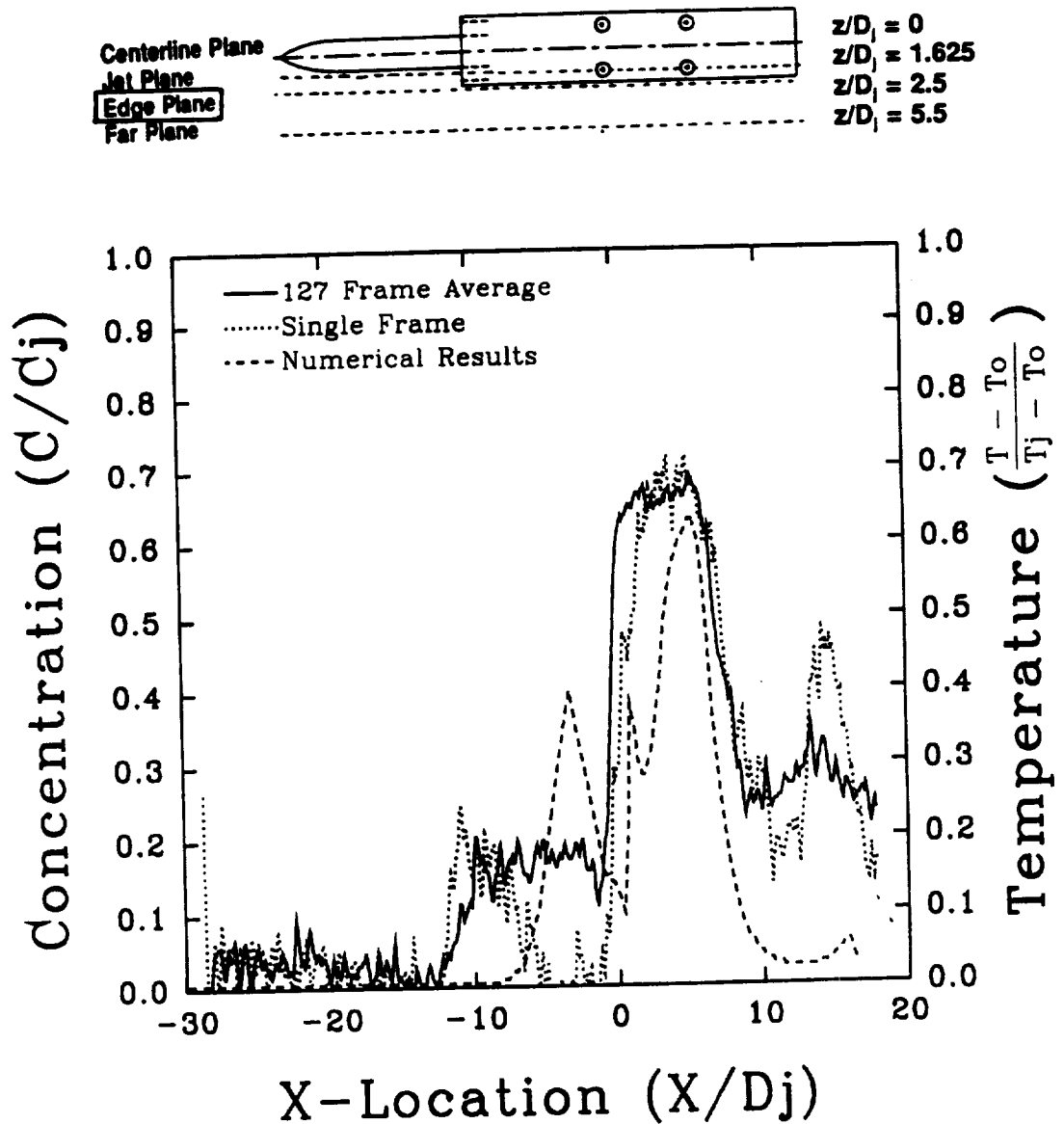


Figure 5.23: Numerical and Experimental Results Along Model Edge: $z/D_j = 2.5$
 $y/D_j = 3.6$, $H/D_j = 4$, $U/V_j = 0.09$

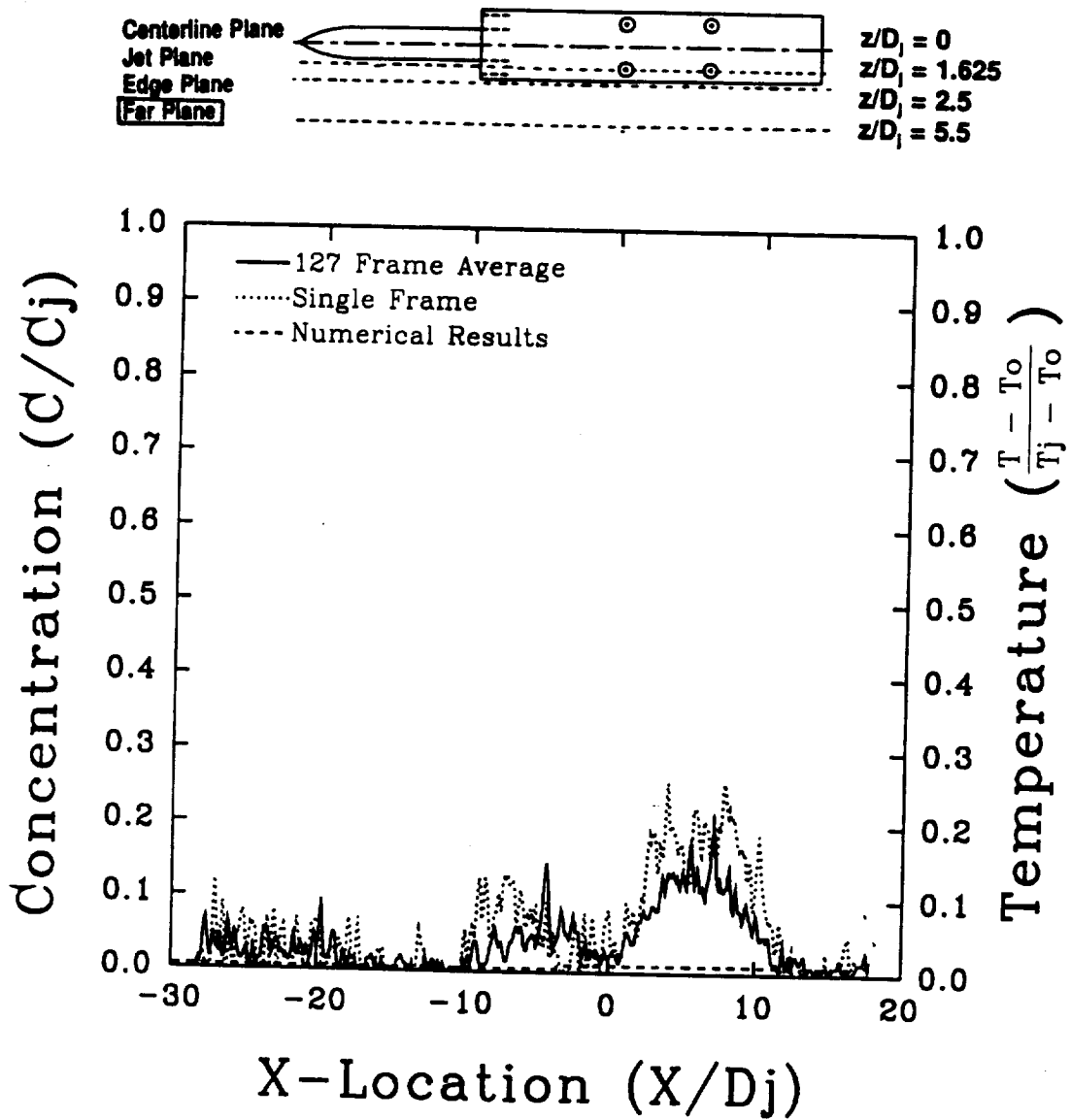


Figure 5.24: Numerical and Experimental Results at $z/D_j = 5.5$
 $y/D_j = 3.6$, $H/D_j = 4$, $U/V_j = 0.09$

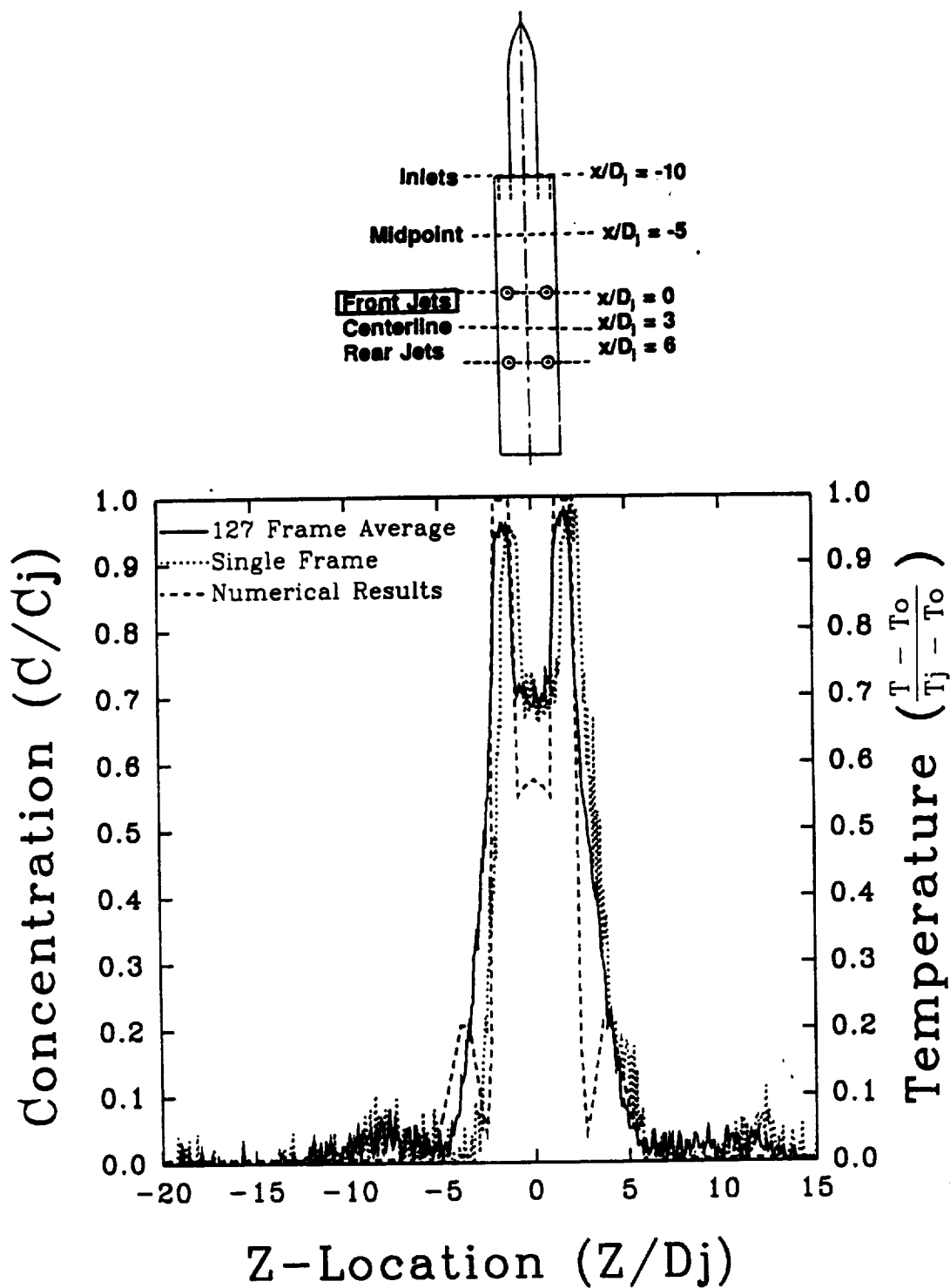


Figure 5.25: Numerical and Experimental Results Across Front Jet Pair: $x/D_j = 0$
 $y/D_j = 3.6$, $H/D_j = 4$, $U/V_j = 0.09$

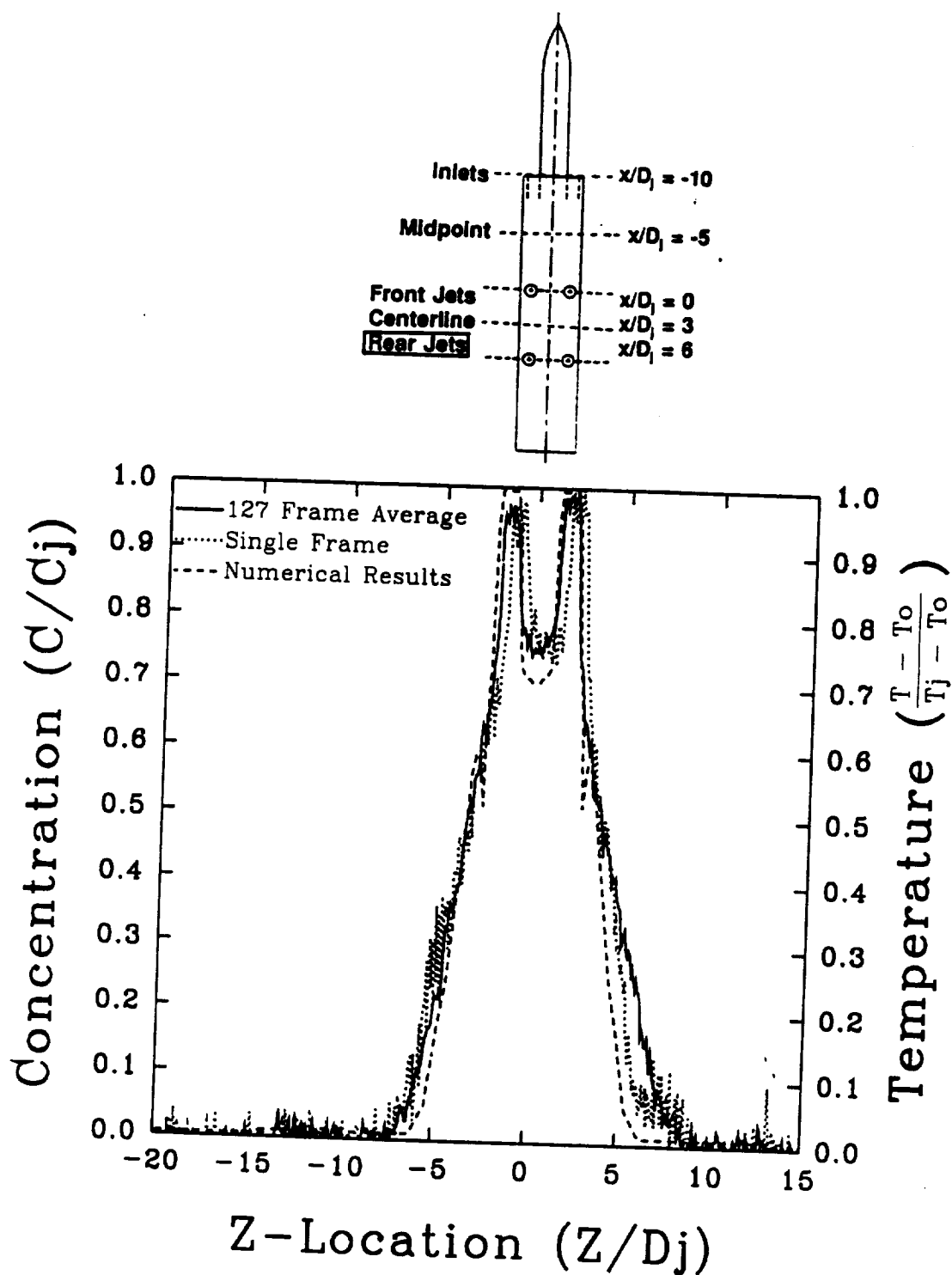


Figure 5.26: Numerical and Experimental Results Across Rear Jet Pair: $x/D_j = 6$
 $y/D_j = 3.6$, $H/D_j = 4$, $U/V_j = 0.09$

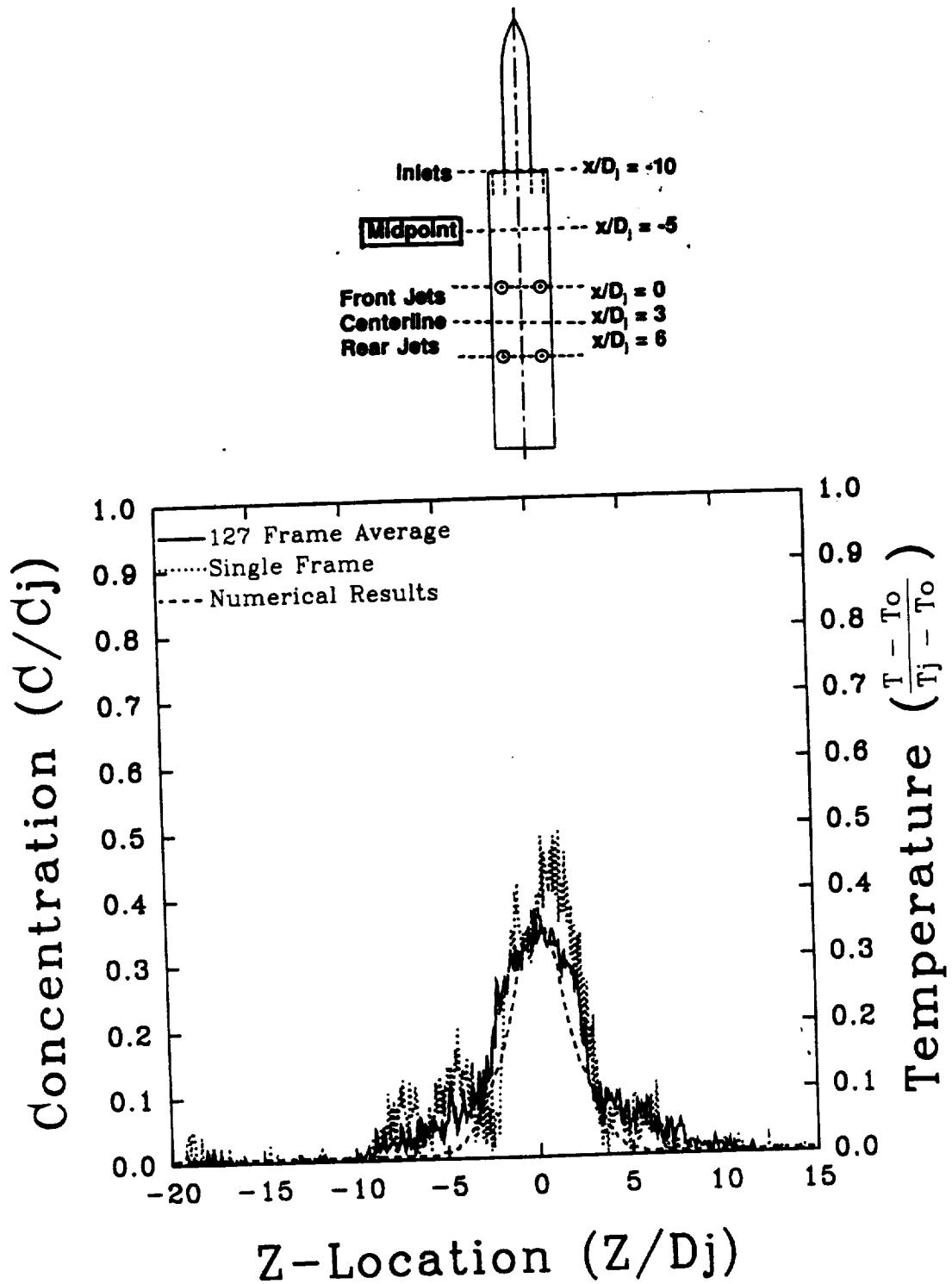


Figure 5.27: Numerical and Experimental Results Between Inlets and Front Jets
 $z/D_j = -5$, $y/D_j = 3.6$, $H/D_j = 4$, $U/V_j = 0.09$

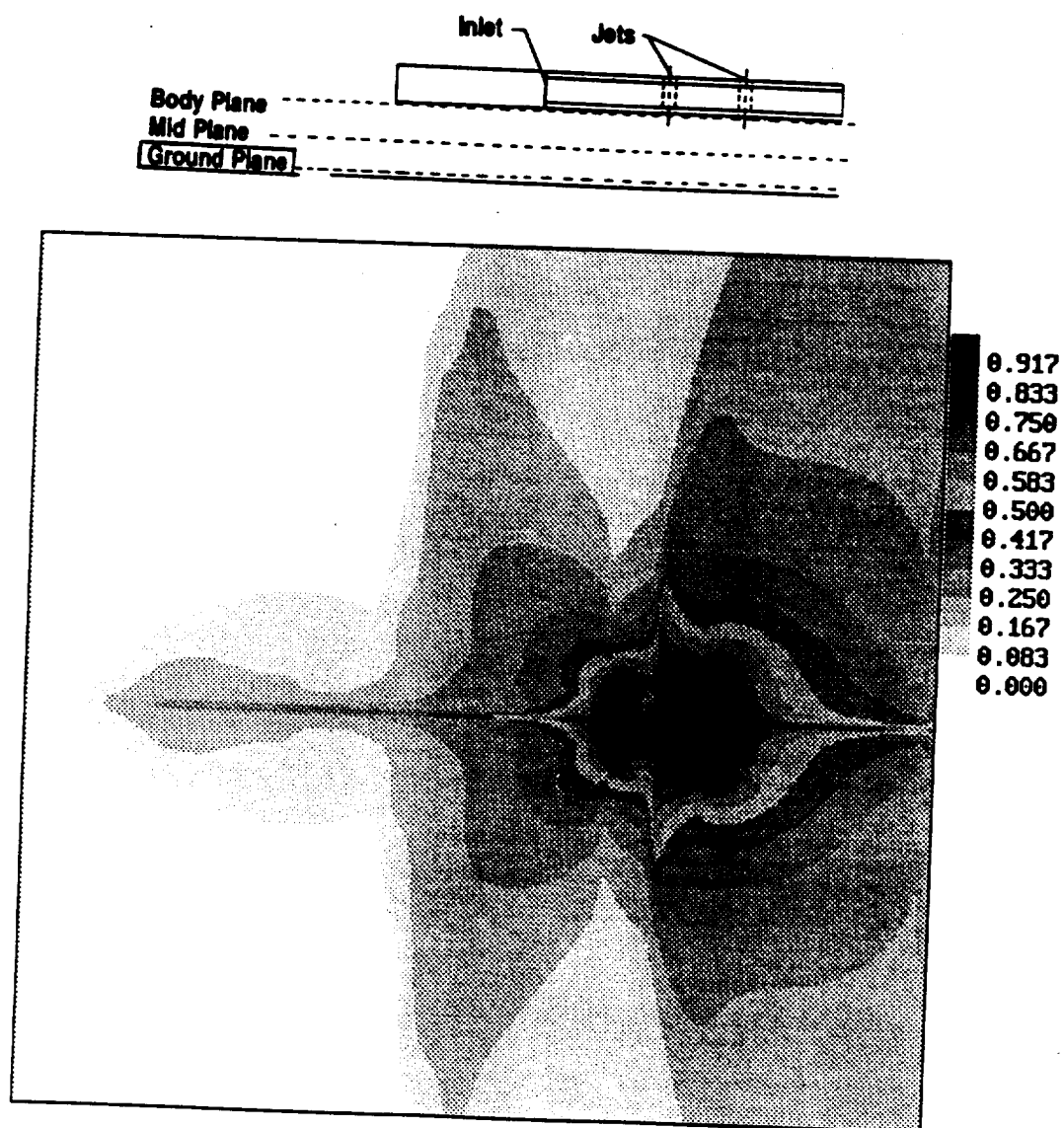


Figure 5.28: Numerical Temperature Profile at Ground Plane: $y/D_j = 0.0$
 $H/D_j = 4$, $U/V_j = 0.03$

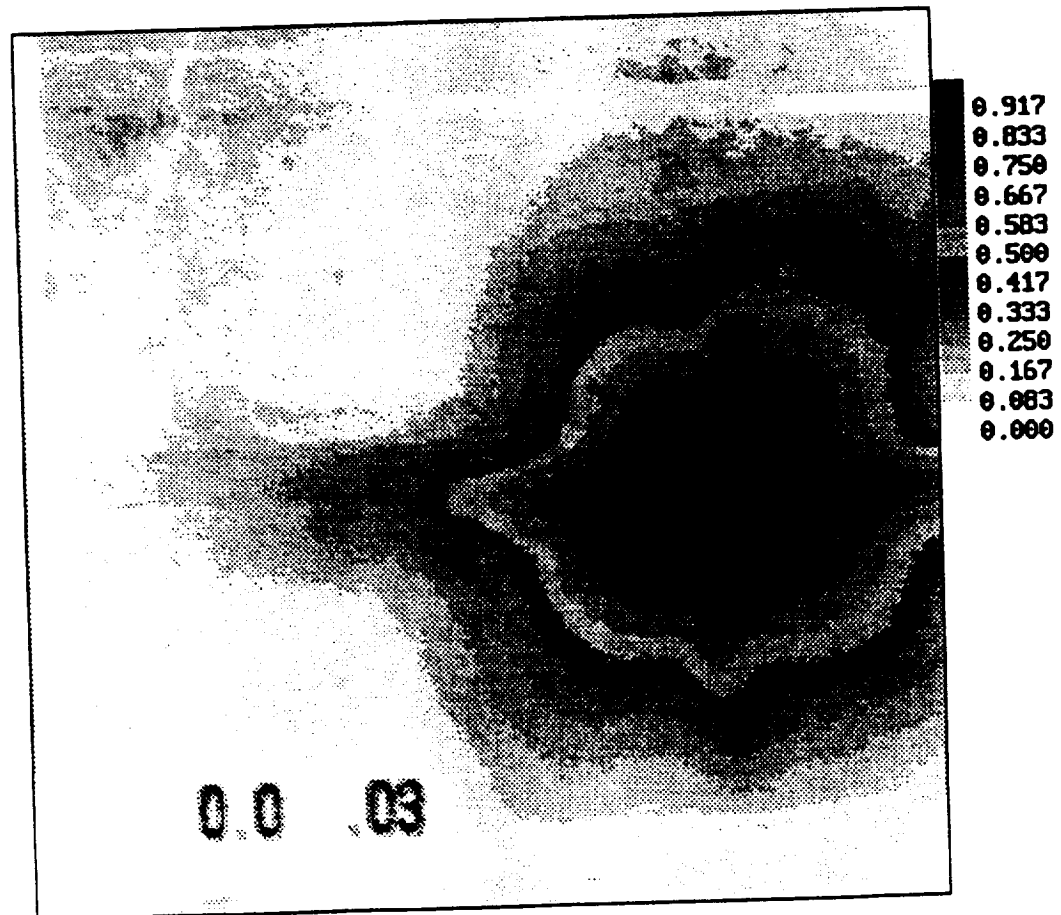
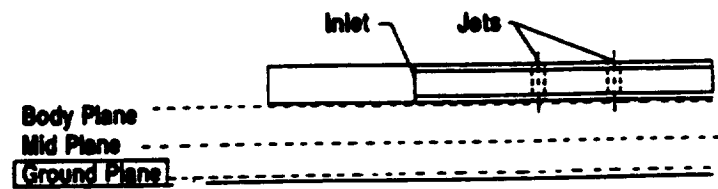


Figure 5.29: Experimental Smoke Concentration Profile at Ground Plane: $y/D_j = 0.0$
 $H/D_j = 4$, $U/V_j = 0.03$

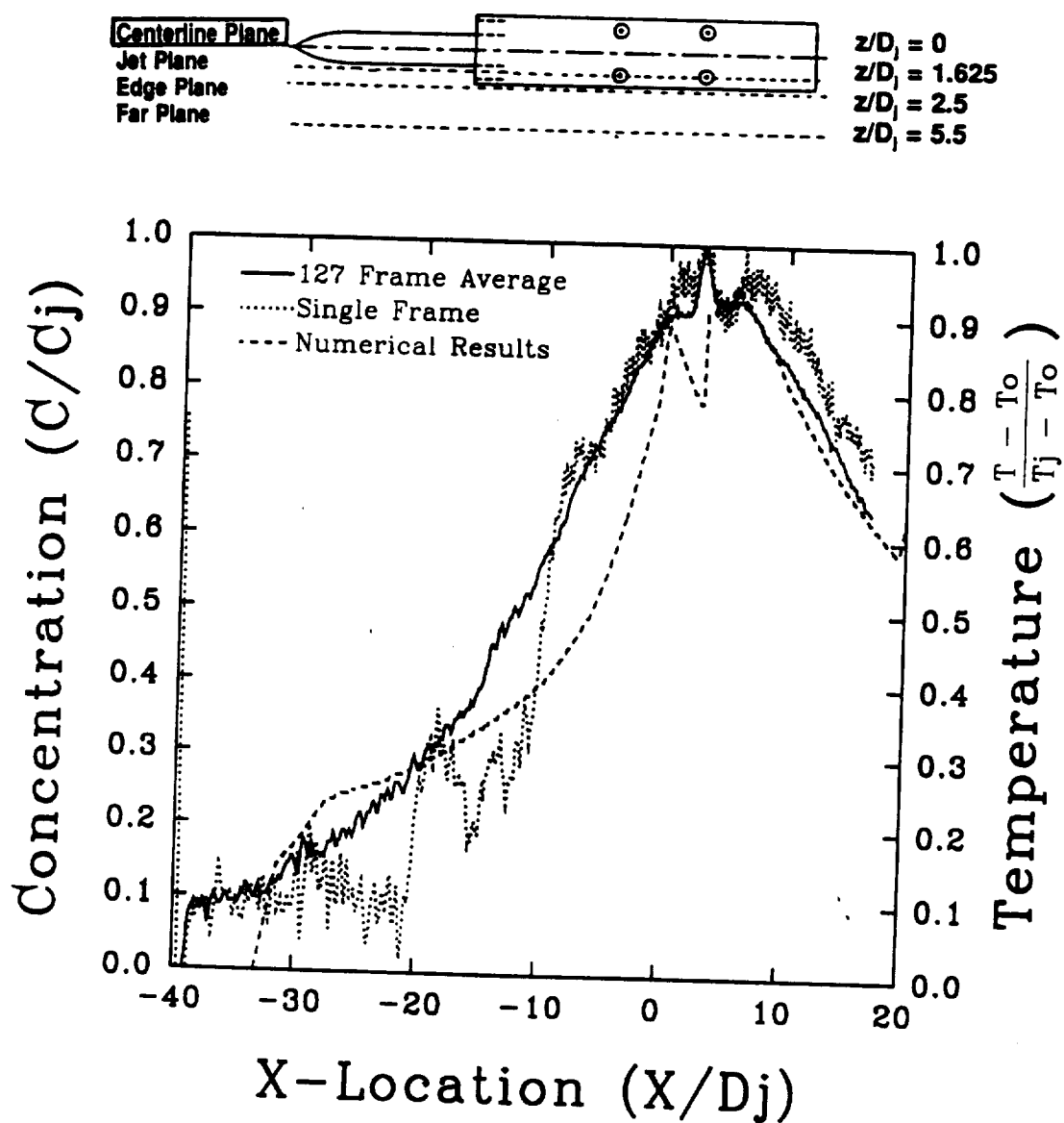


Figure 5.30: Numerical and Experimental Results Along Model Centerline: $z/D_j = 0$
 $y/D_j = 0.0$, $H/D_j = 4$, $U/V_j = 0.03$

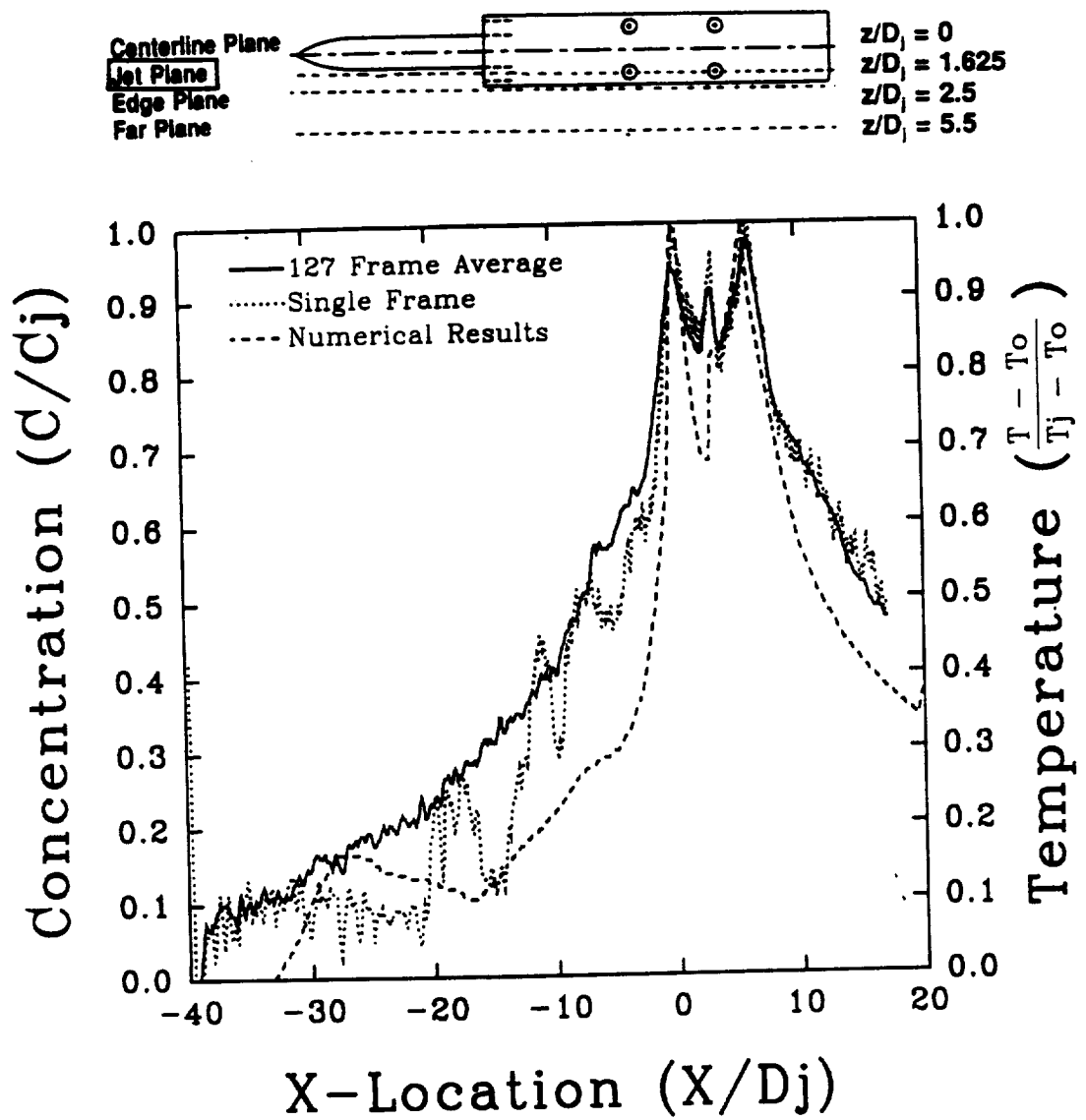


Figure 5.31: Numerical and Experimental Results At Side Jet Centerline
 $z/D_j = 1.625$, $y/D_j = 0.0$, $H/D_j = 4$, $U/V_j = 0.03$

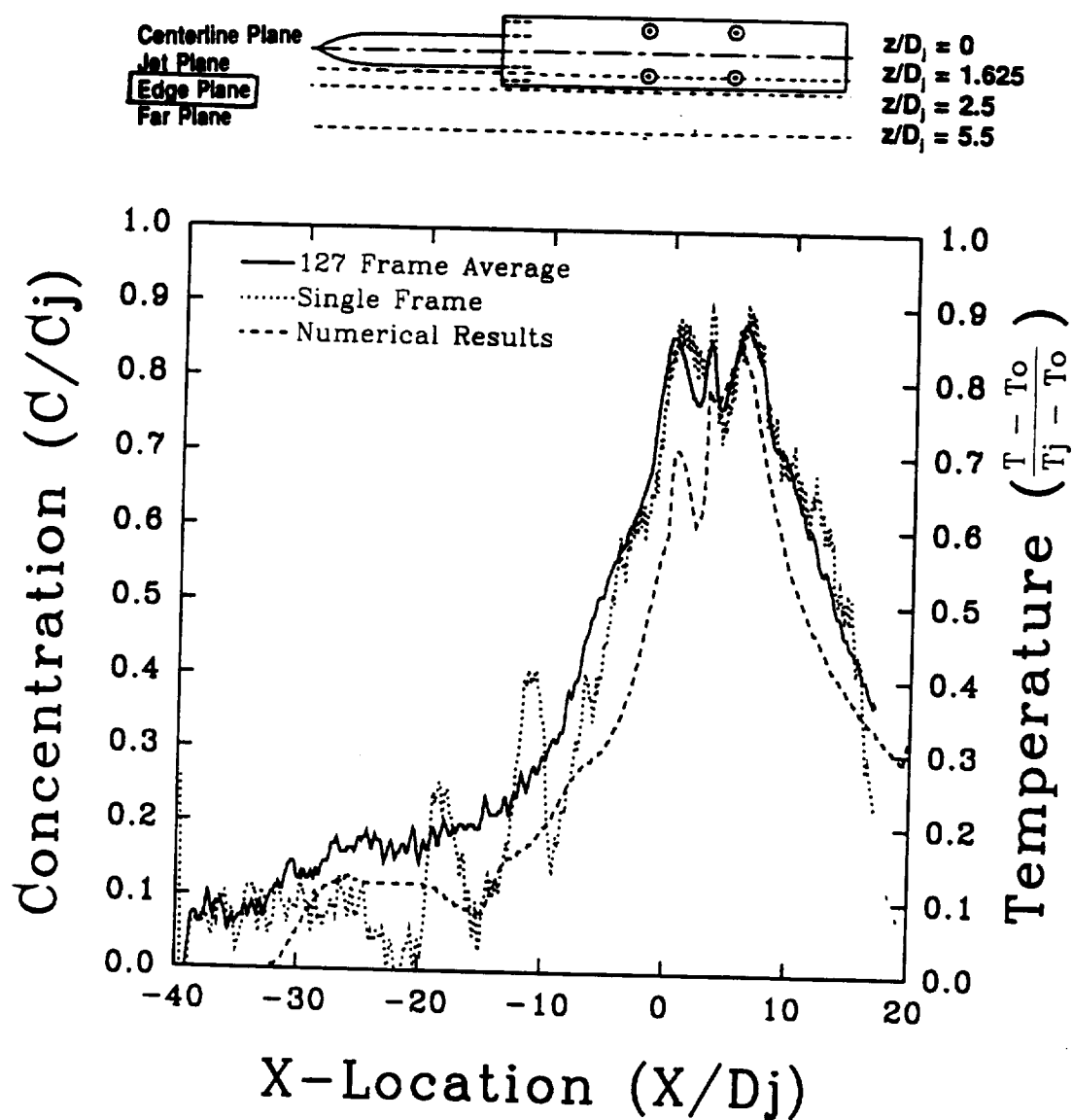


Figure 5.32: Numerical and Experimental Results Along Model Edge: $z/D_j = 2.5$
 $y/D_j = 0.0$, $H/D_j = 4$, $U/V_j = 0.03$

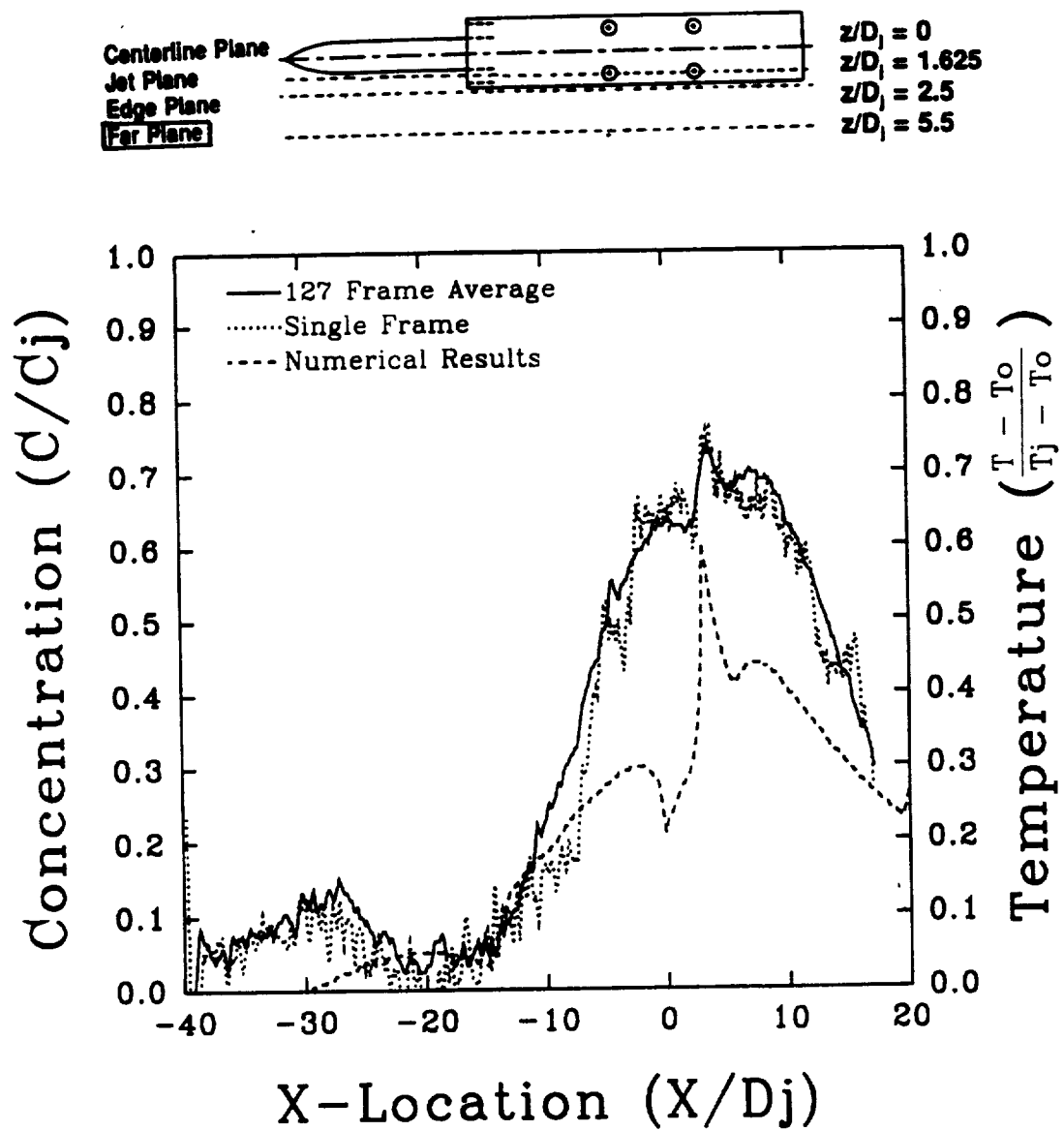


Figure 5.33: Numerical and Experimental Results at $z/D_j = 5.5$
 $y/D_j = 0.0$, $H/D_j = 4$, $U/V_j = 0.03$

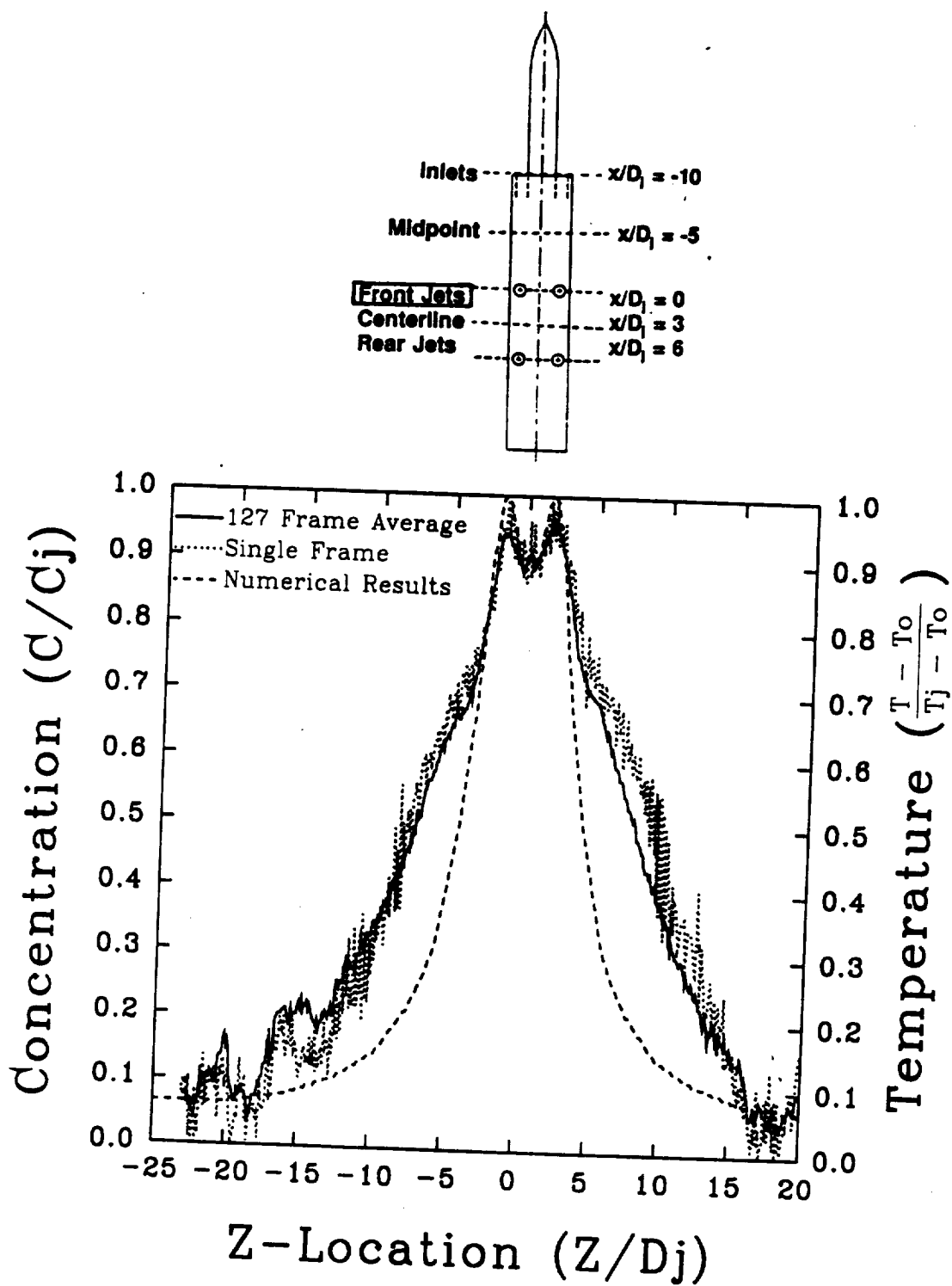


Figure 5.34: Numerical and Experimental Results Across Front Jet Pair: $x/D_j = 0$
 $y/D_j = 0.0$, $H/D_j = 4$, $U/V_j = 0.03$

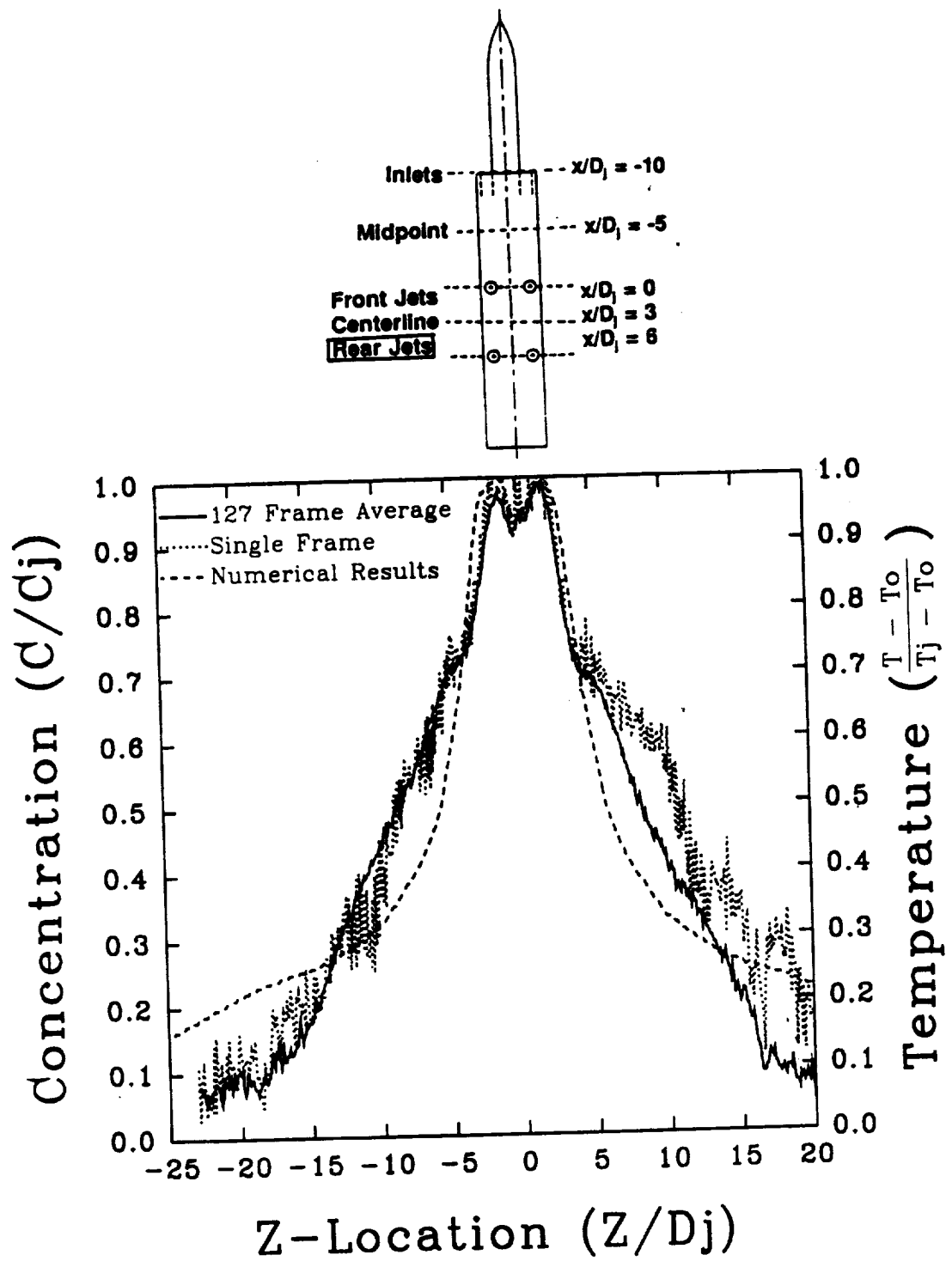


Figure 5.35: Numerical and Experimental Results Across Rear Jet Pair: $x/D_j = 6$
 $y/D_j = 0.0$, $H/D_j = 4$, $U/V_j = 0.03$

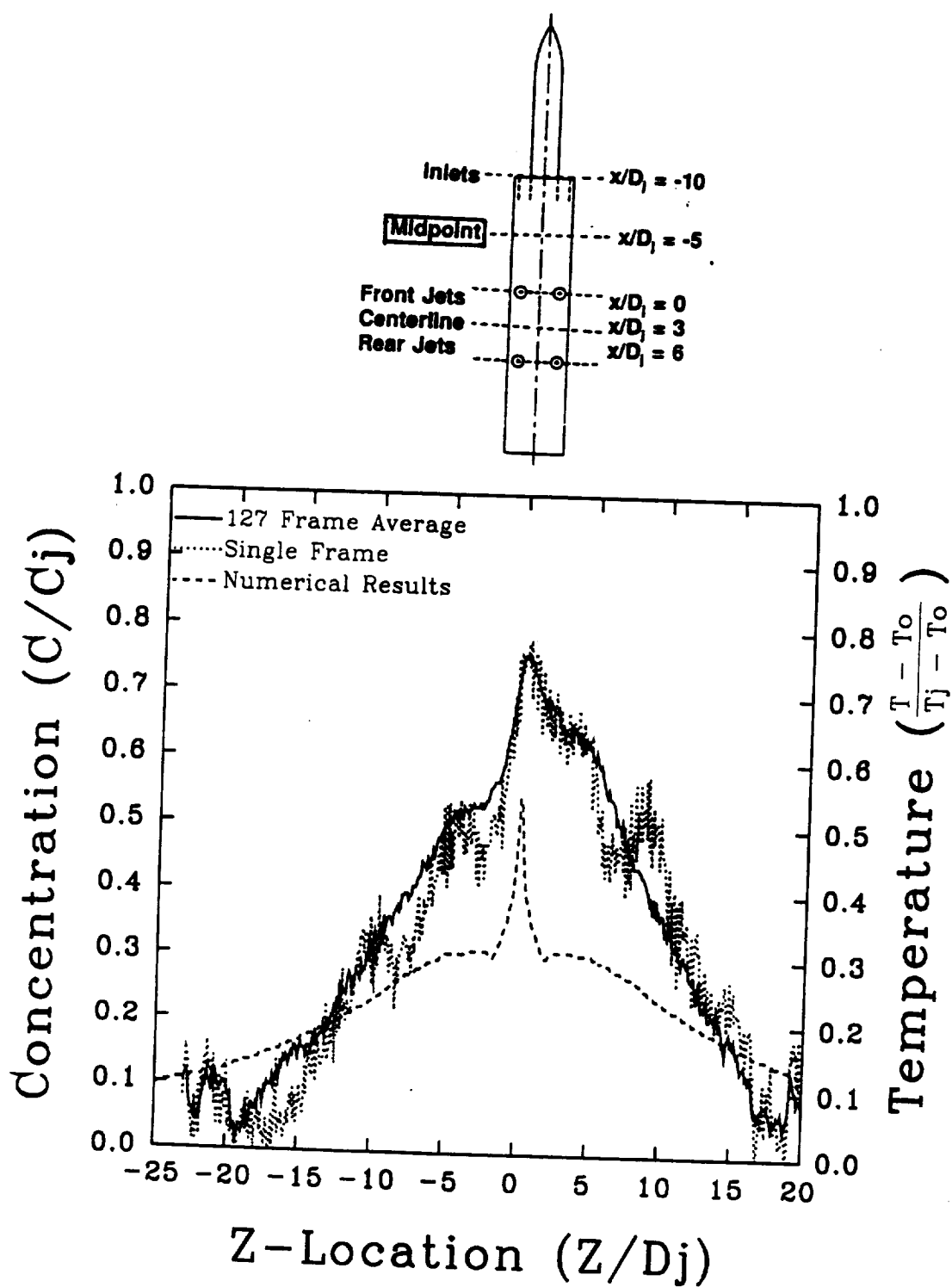


Figure 5.36: Numerical and Experimental Results Between Inlets and Front Jets
 $z/D_j = -5$, $y/D_j = 0.0$, $H/D_j = 4$, $U/V_j = 0.03$

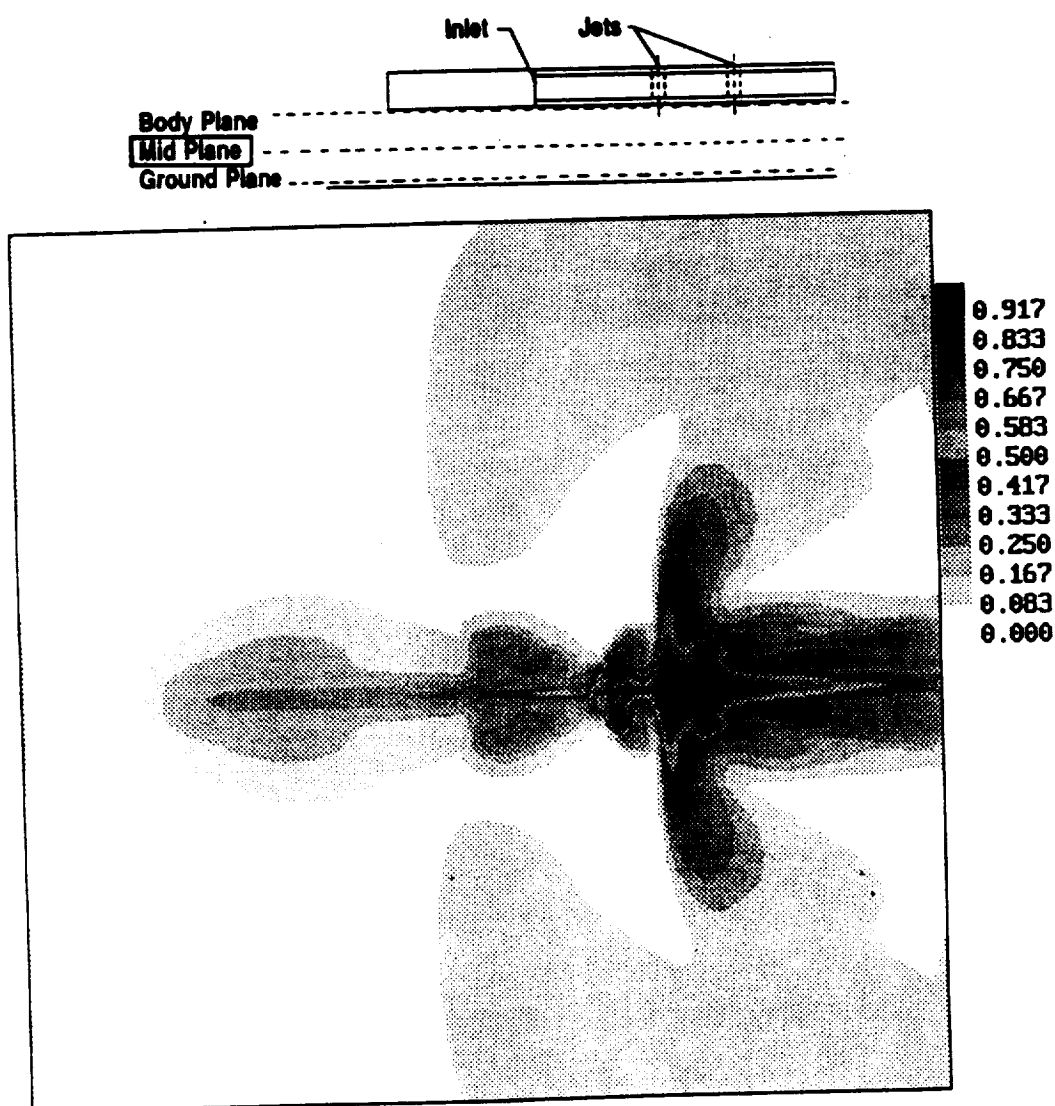


Figure 5.37: Numerical Temperature Profile at Mid Plane: $y/D_j = 2.0$
 $H/D_j = 4$, $U/V_j = 0.03$

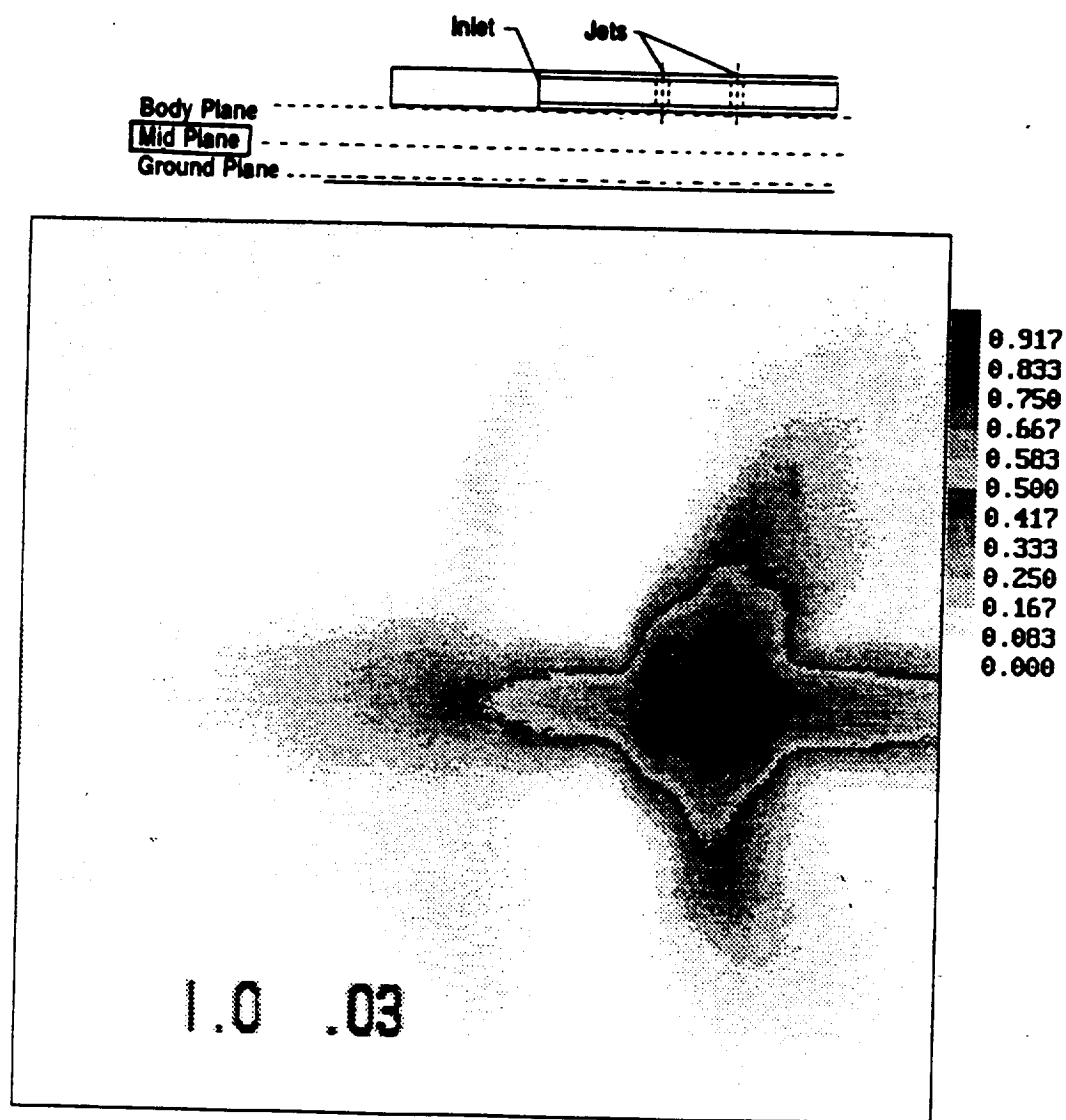


Figure 5.38: Experimental Smoke Concentration Profile at Mid Plane: $y/D_j = 2.0$
 $H/D_j = 4$, $U/V_j = 0.03$

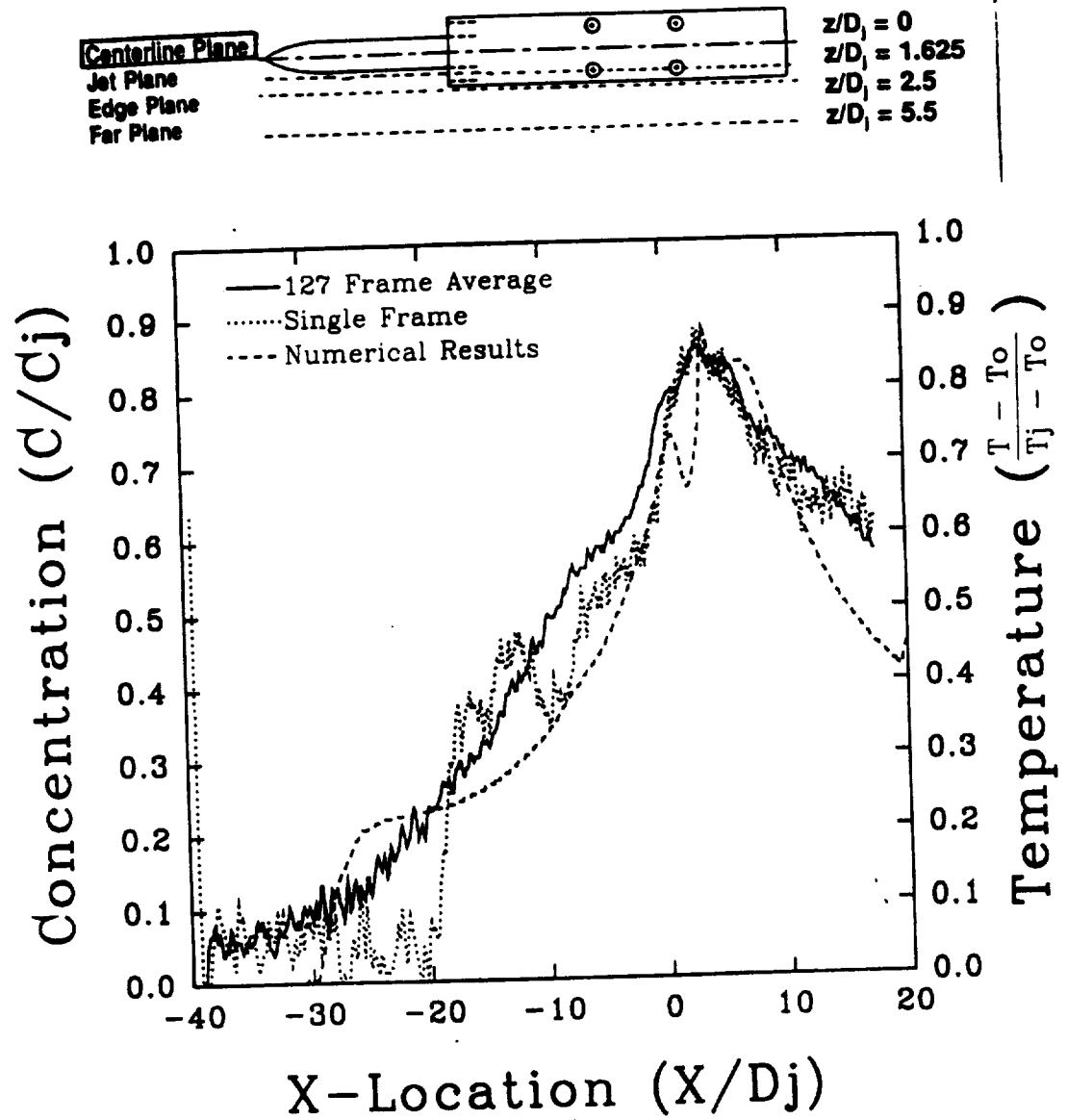


Figure 5.39: Numerical and Experimental Results Along Model Centerline: $z/D_j = 0$
 $y/D_j = 2.0$, $H/D_j = 4$, $U/V_j = 0.03$

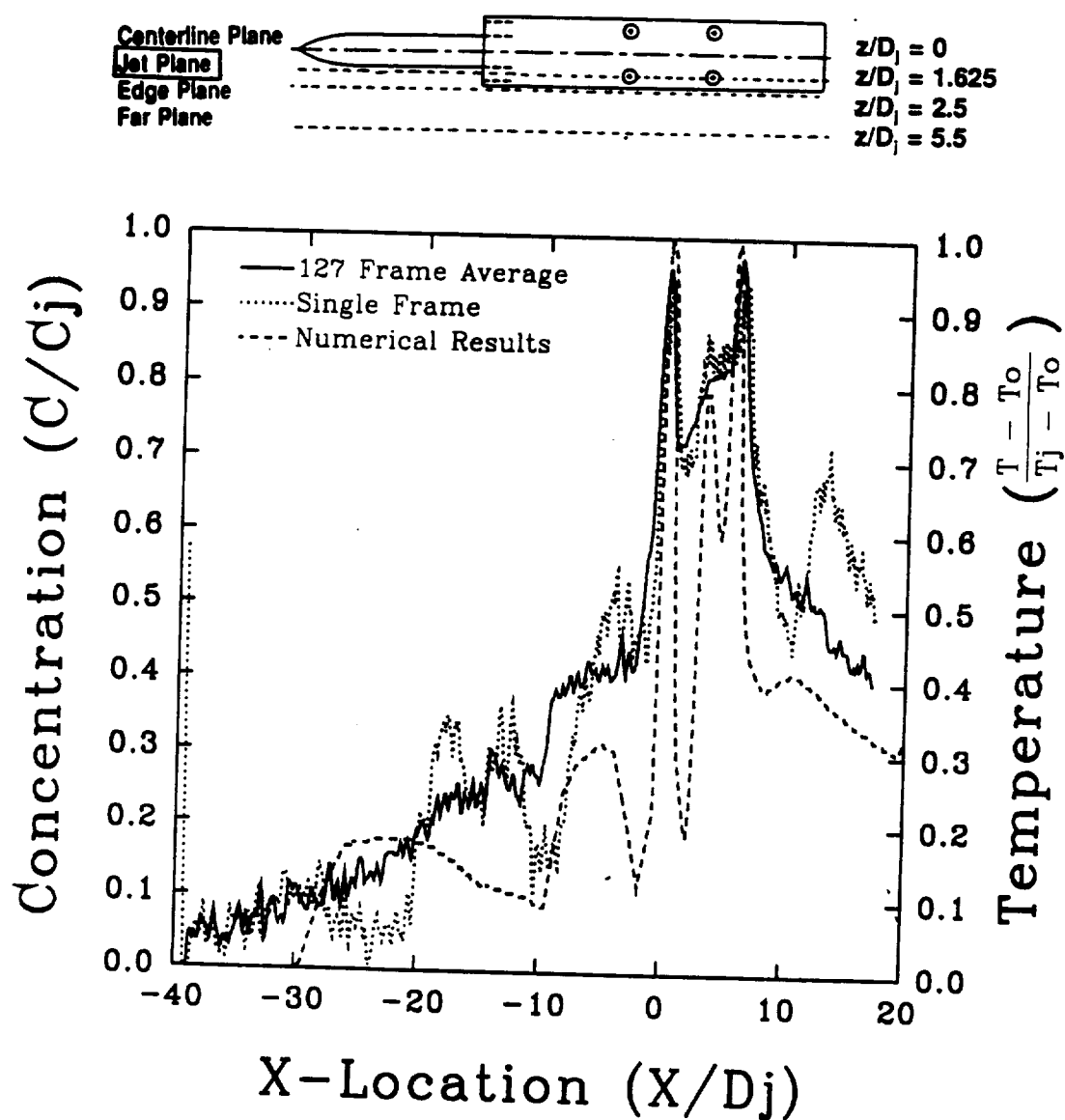


Figure 5.40: Numerical and Experimental Results At Side Jet Centerline
 $z/D_j = 1.625$, $y/D_j = 2.0$, $H/D_j = 4$, $U/V_j = 0.03$

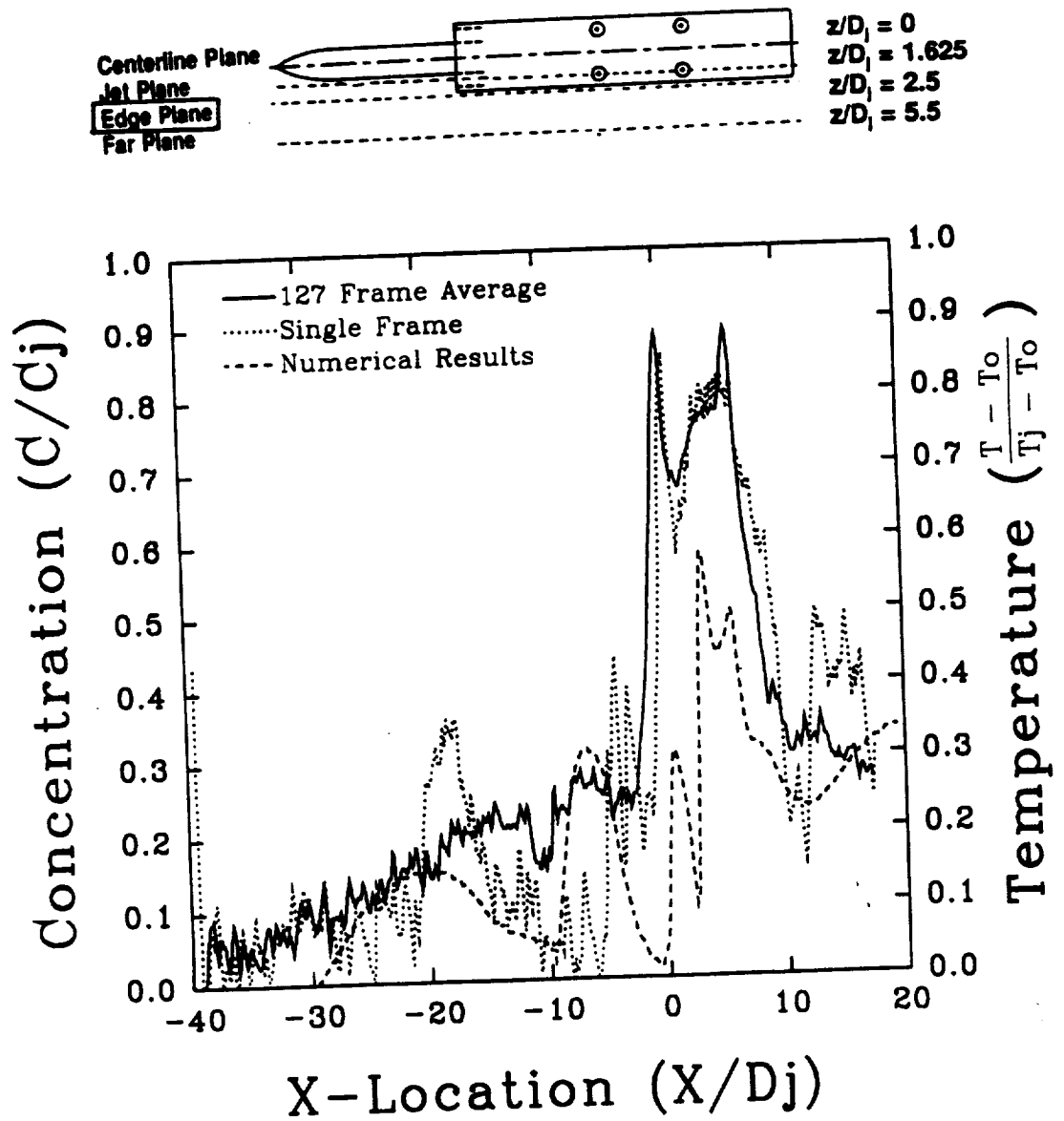


Figure 5.41: Numerical and Experimental Results Along Model Edge: $z/D_j = 2.5$
 $y/D_j = 2.0$, $H/D_j = 4$, $U/V_j = 0.03$

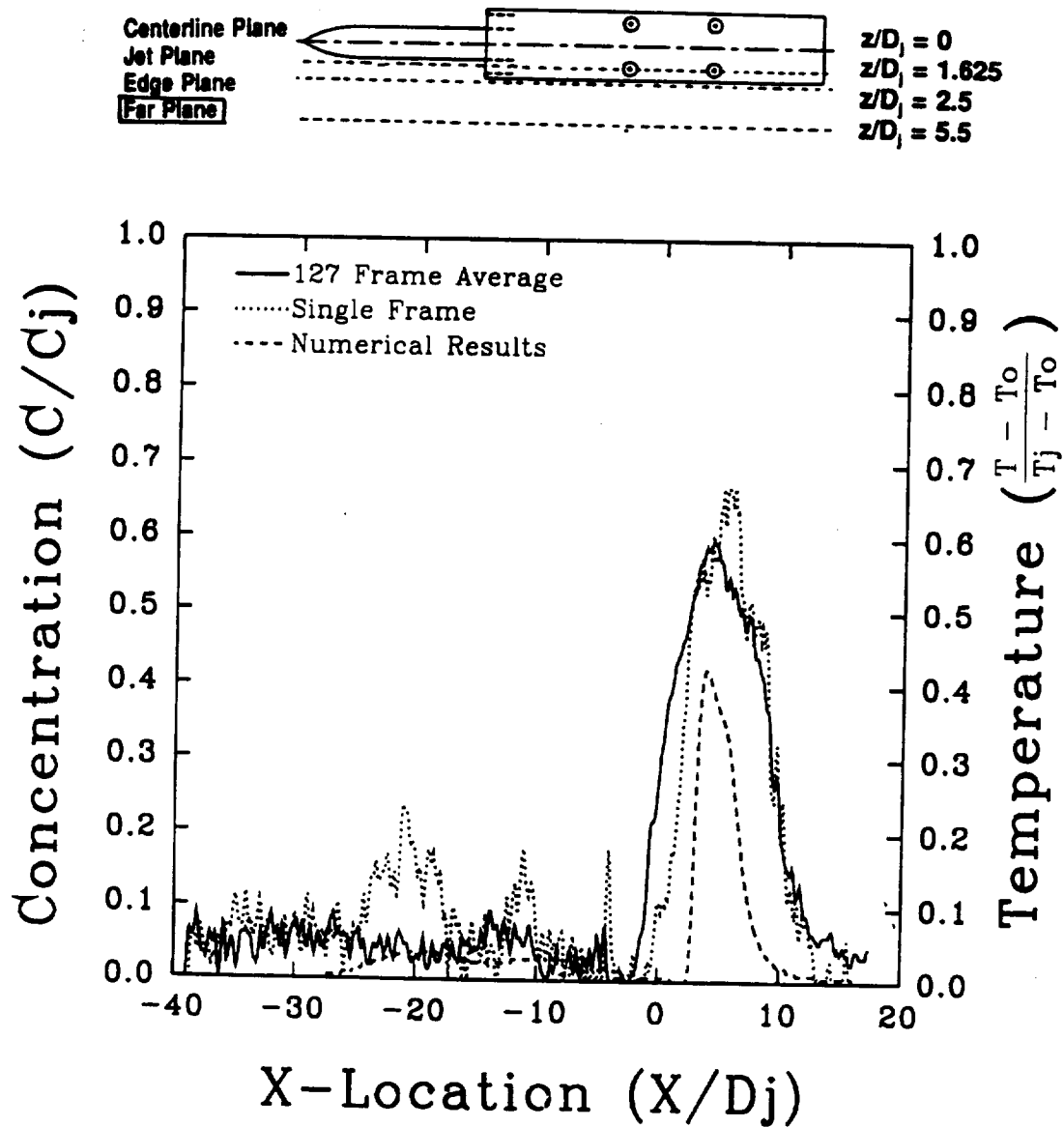


Figure 5.42: Numerical and Experimental Results at $z/D_j = 5.5$
 $y/D_j = 2.0$, $H/D_j = 4$, $U/V_j = 0.03$

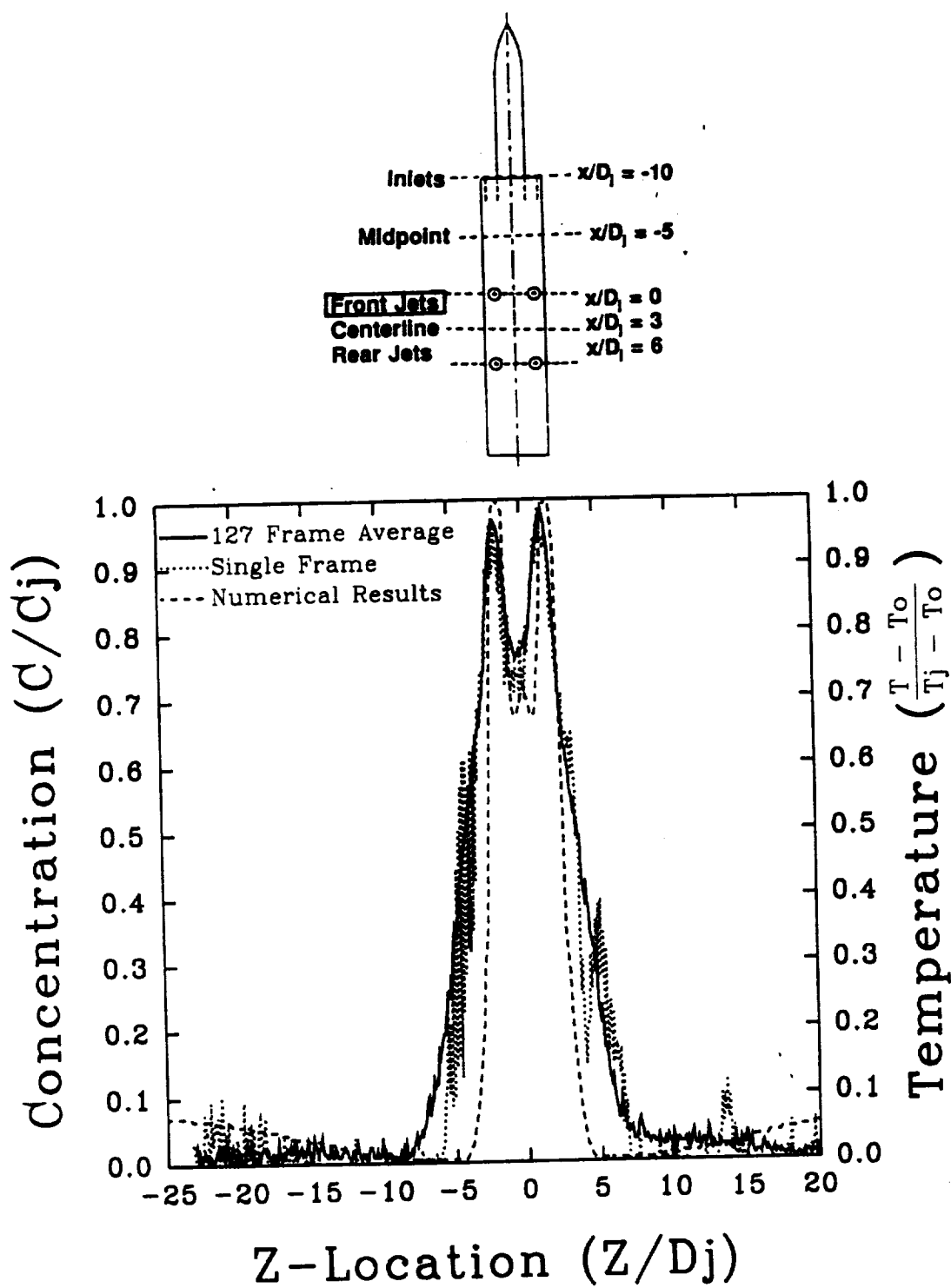


Figure 5.43: Numerical and Experimental Results Across Front Jet Pair: $x/D_j = 0$
 $y/D_j = 2.0$, $H/D_j = 4$, $U/V_j = 0.03$

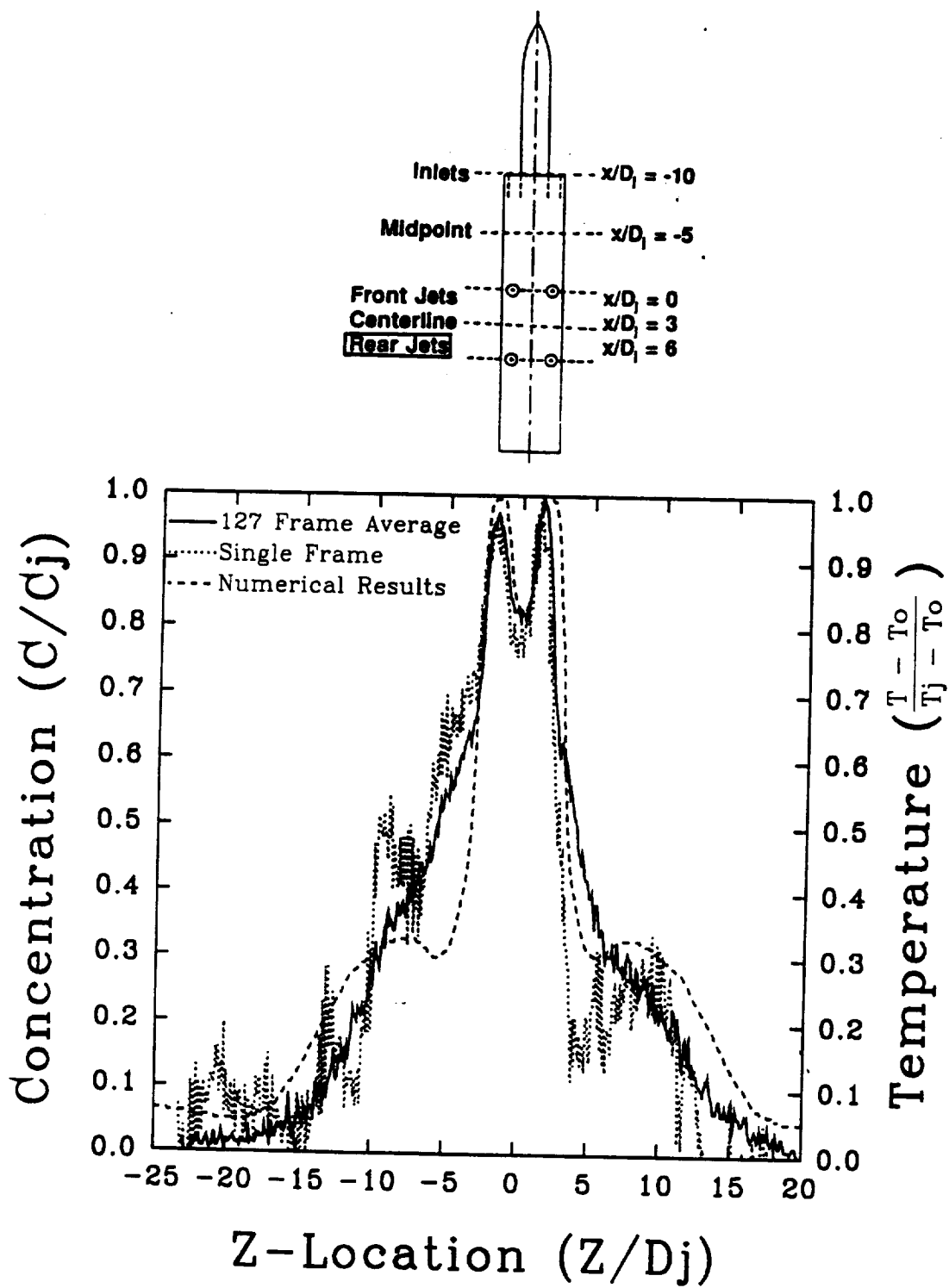


Figure 5.44: Numerical and Experimental Results Across Rear Jet Pair: $x/D_j = 6$
 $y/D_j = 2.0$, $H/D_j = 4$, $U/V_j = 0.03$

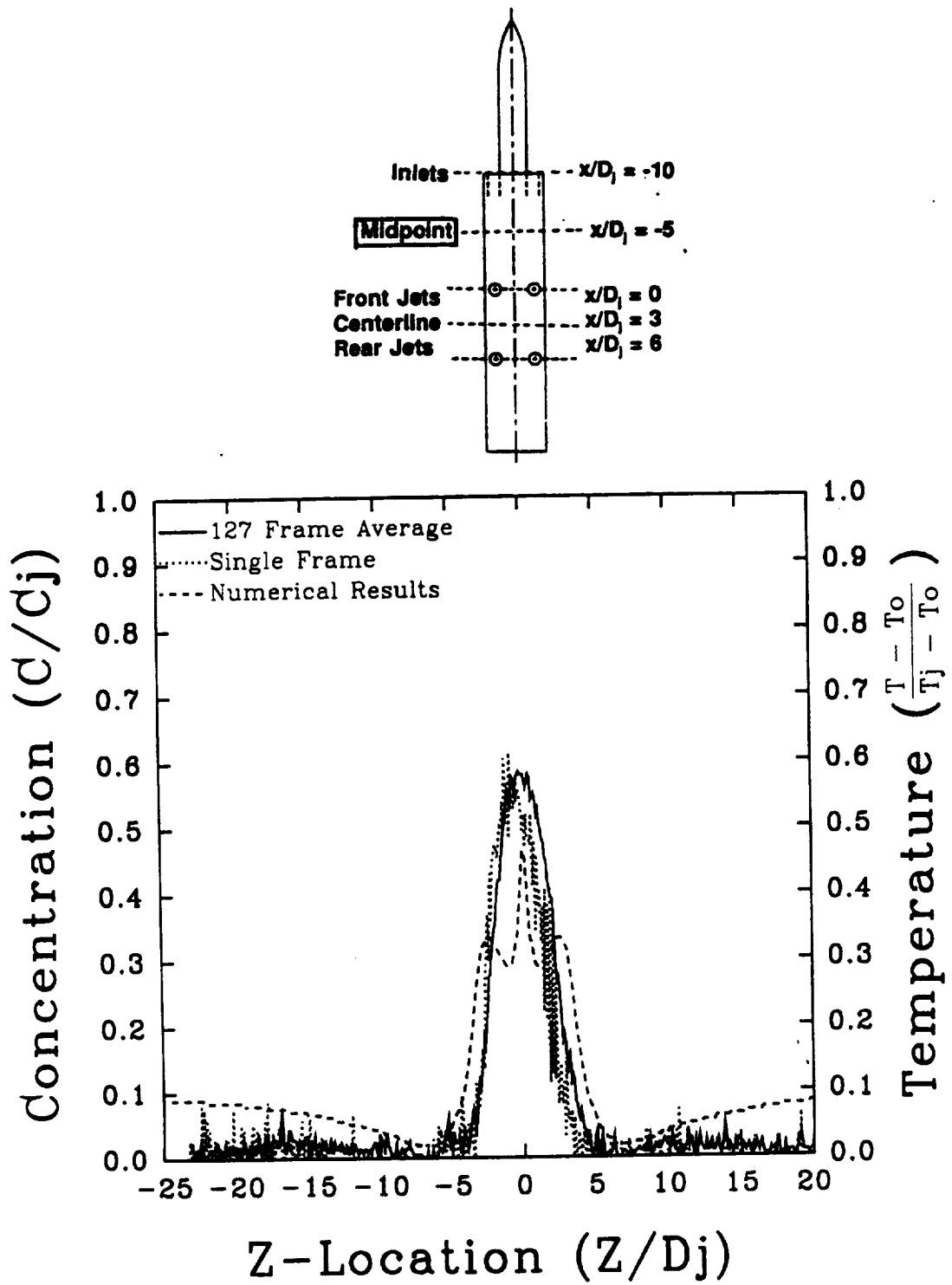


Figure 5.45: Numerical and Experimental Results Between Inlets and Front Jets
 $z/D_j = -5$, $y/D_j = 2.0$, $H/D_j = 4$, $U/V_j = 0.03$

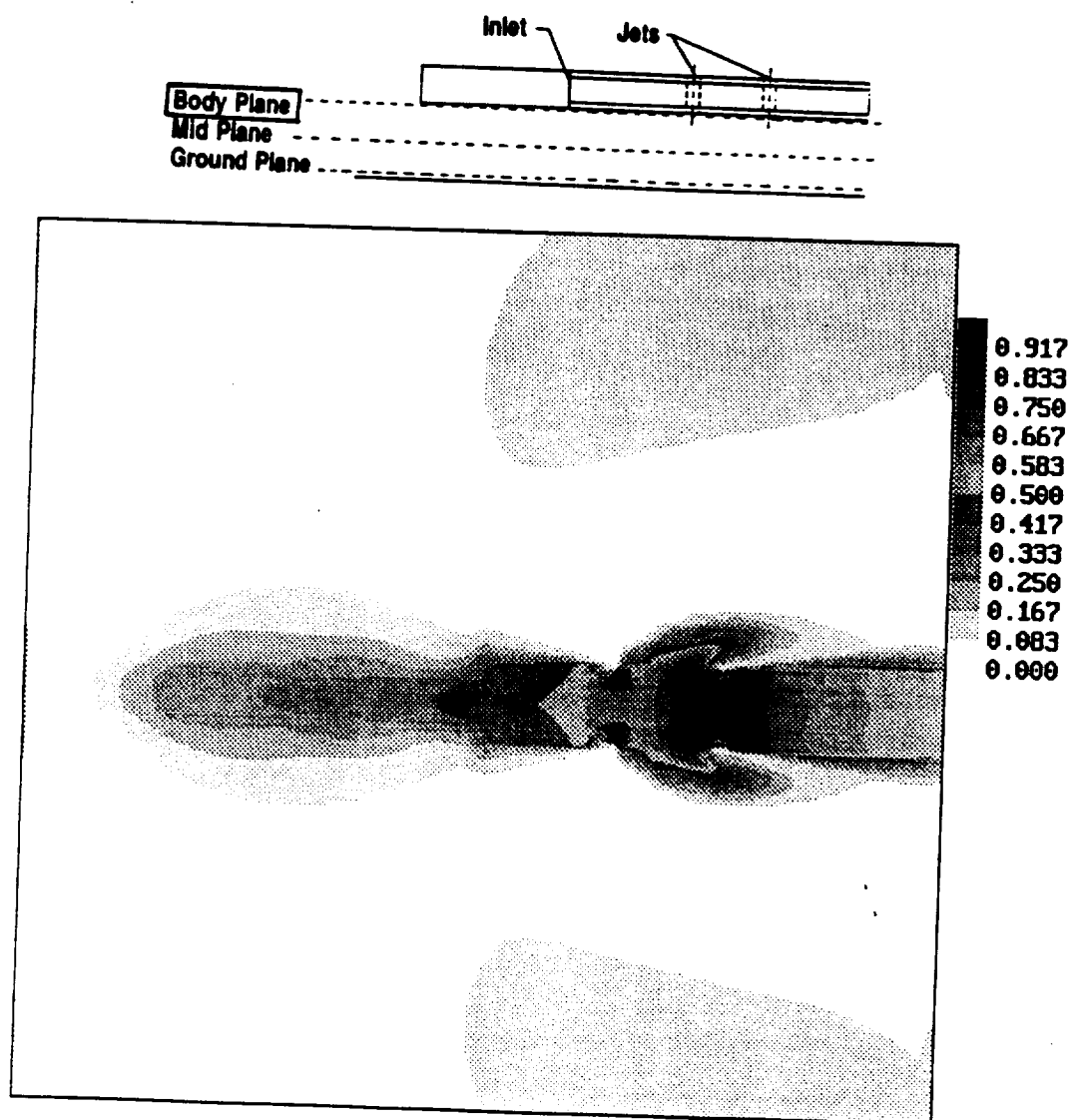


Figure 5.46: Numerical Temperature Profile at Model Body Plane: $y/D_j = 3.6$
 $H/D_j = 4$, $U/V_j = 0.03$

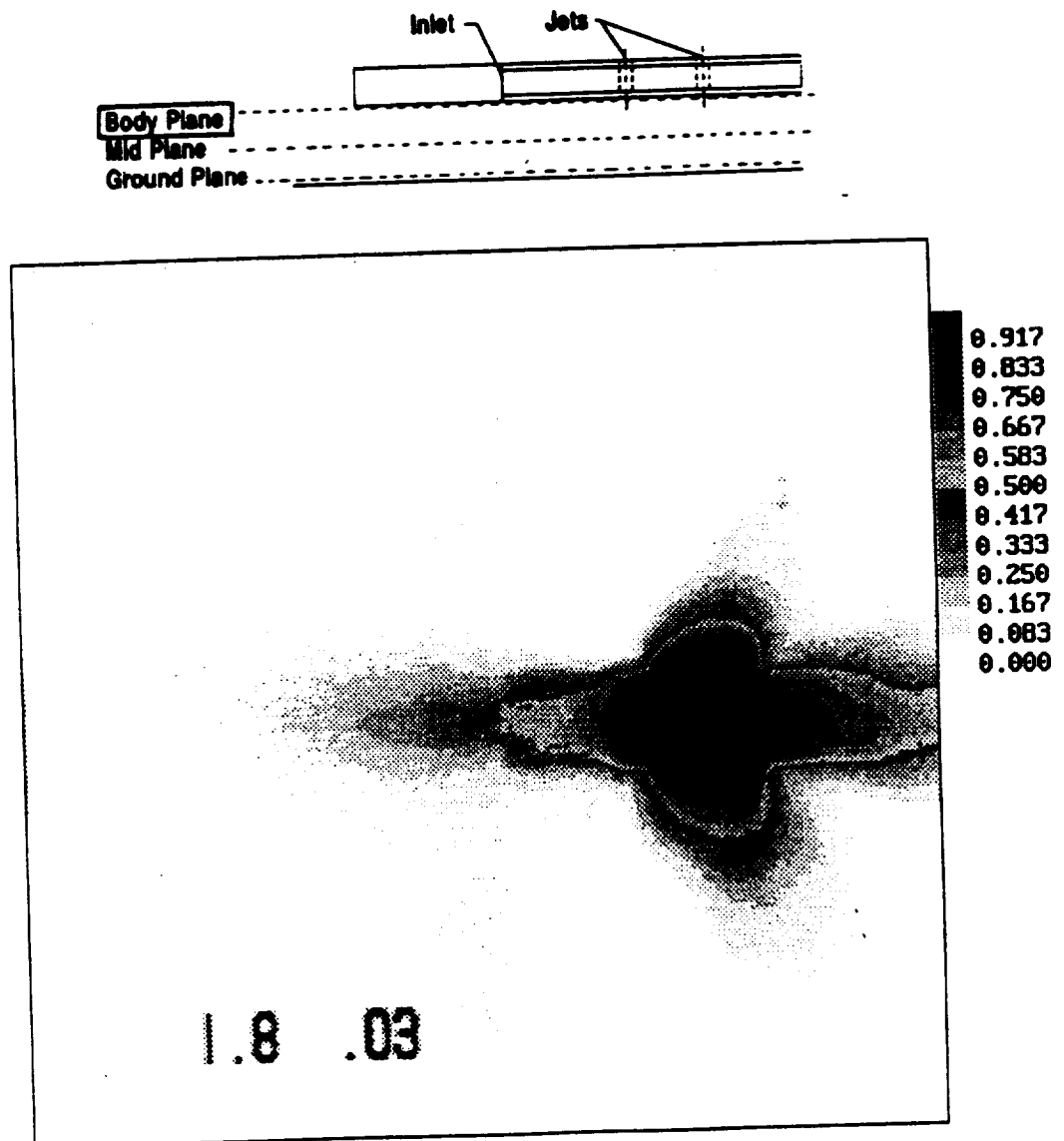


Figure 5.47: Experimental Smoke Concentration Profile at Model Body Plane
 $y/D_j = 3.6$, $H/D_j = 4$, $U/V_j = 0.03$

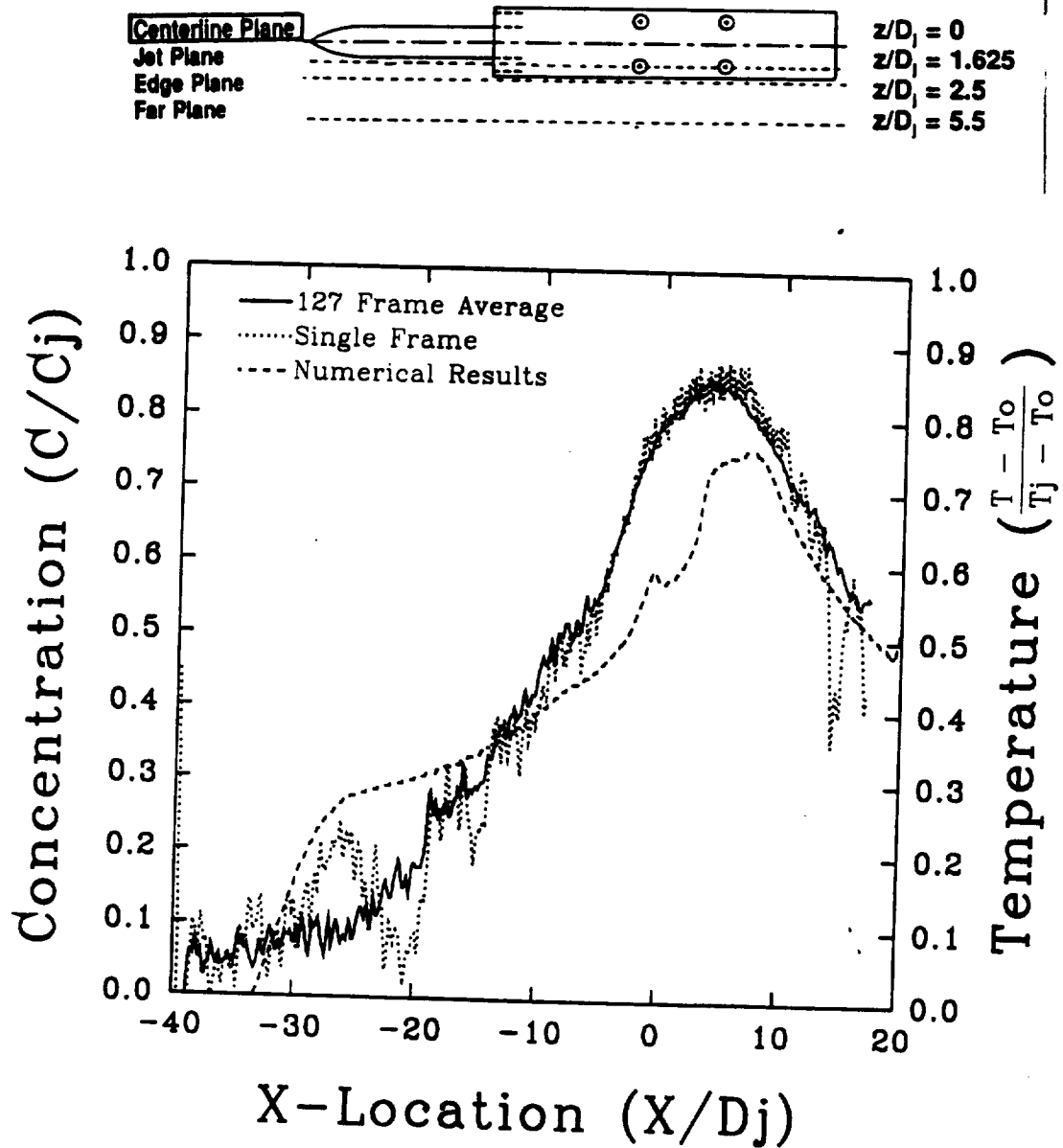


Figure 5.48: Numerical and Experimental Results Along Model Centerline: $z/D_j = 0$
 $y/D_j = 3.6$, $H/D_j = 4$, $U/V_j = 0.03$

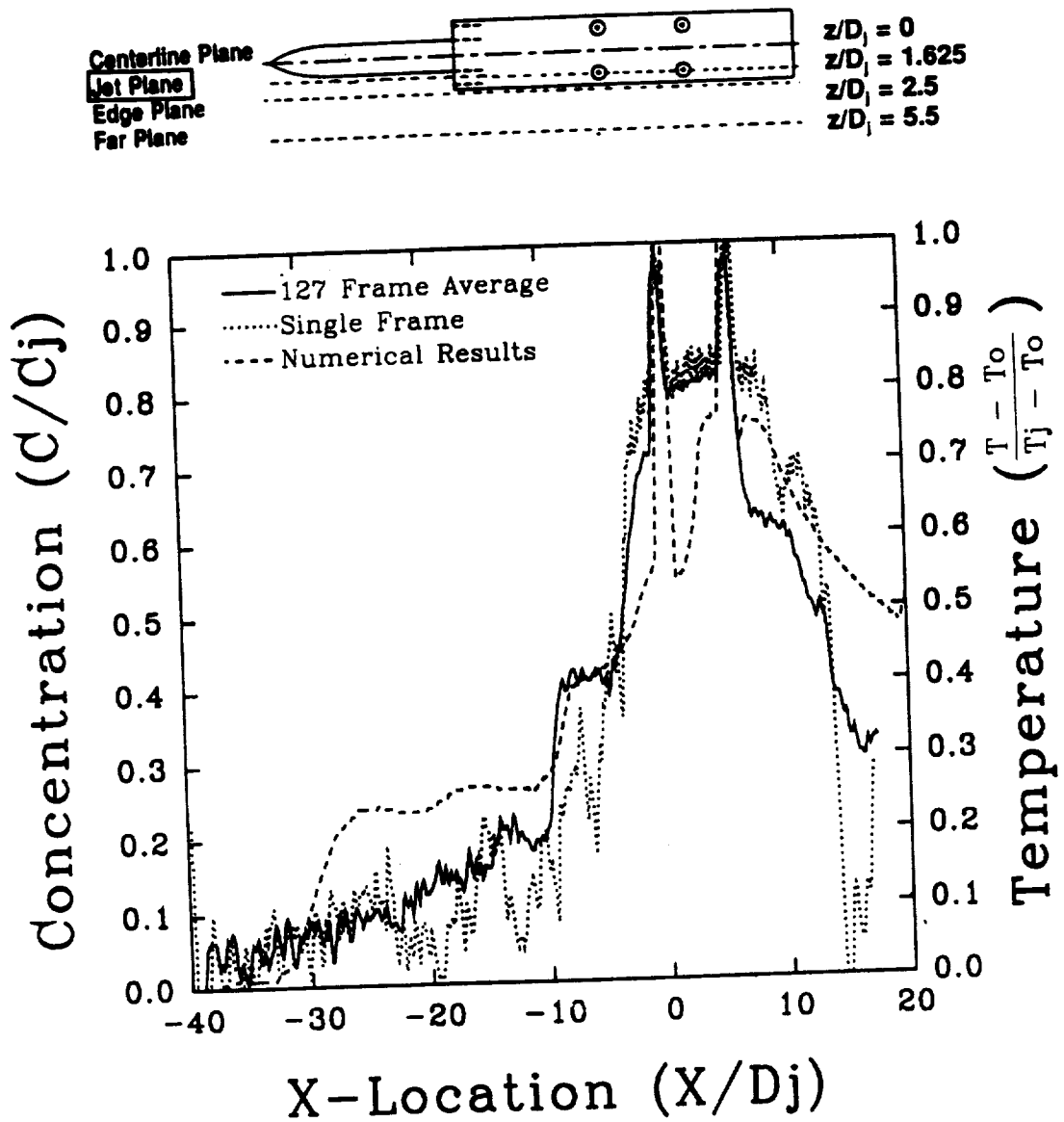


Figure 5.49: Numerical and Experimental Results At Side Jet Centerline
 $z/D_j = 1.625$, $y/D_j = 3.6$, $H/D_j = 4$, $U/V_j = 0.03$

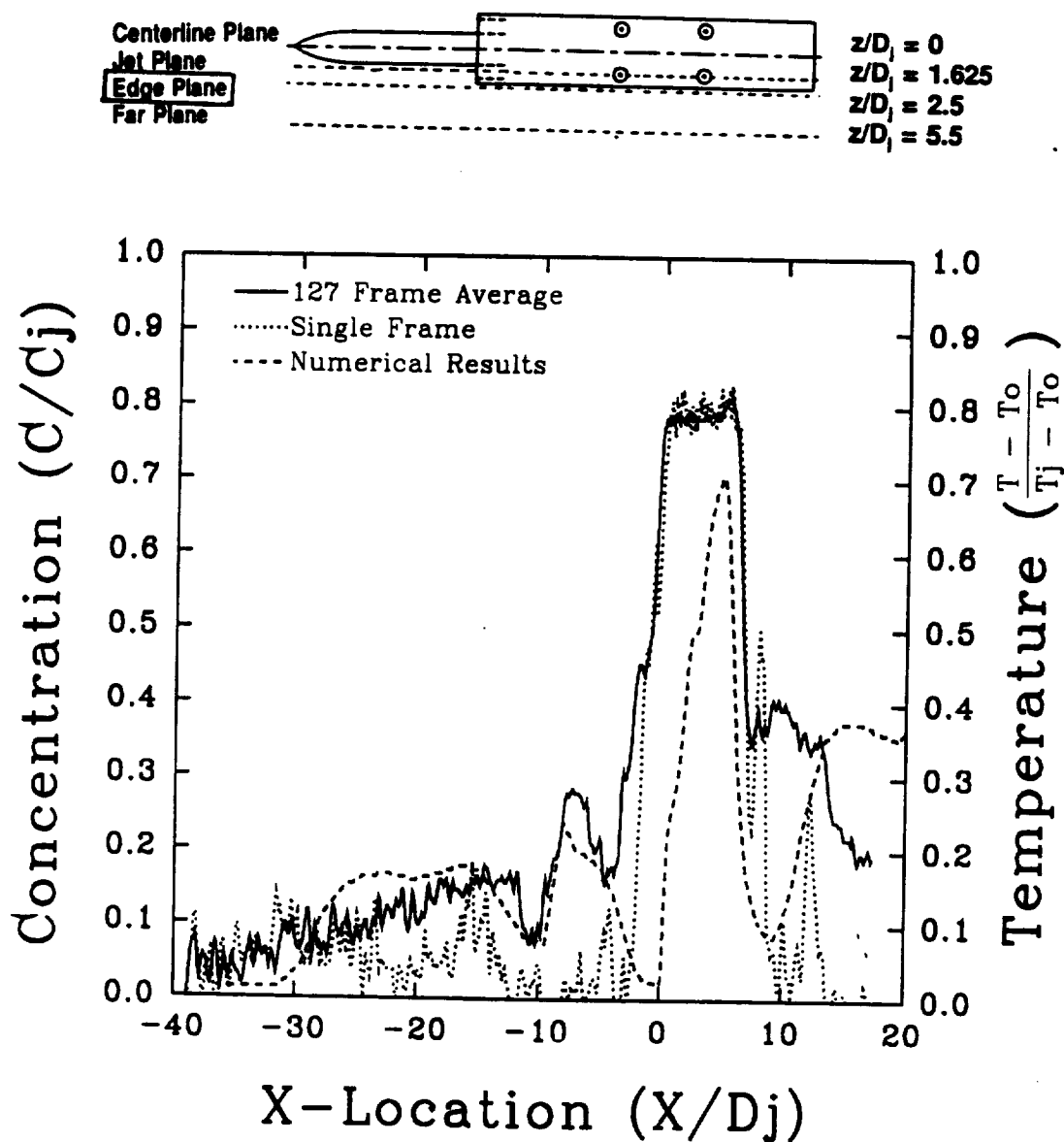


Figure 5.50: Numerical and Experimental Results Along Model Edge: $z/D_j = 2.5$
 $y/D_j = 3.6$, $H/D_j = 4$, $U/V_j = 0.03$

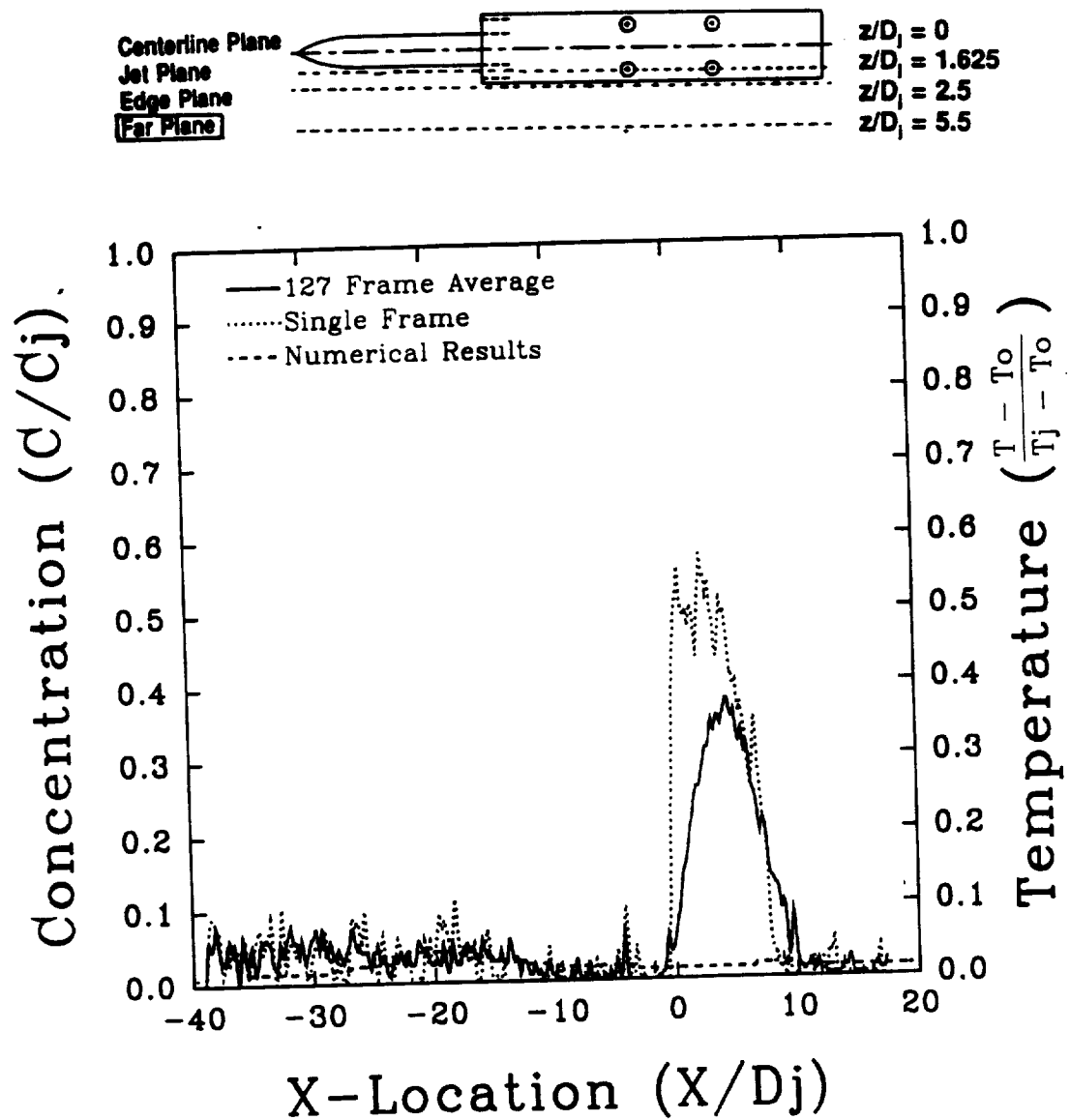


Figure 5.51: Numerical and Experimental Results at $z/D_j = 5.5$
 $y/D_j = 3.6$, $H/D_j = 4$, $U/V_j = 0.03$

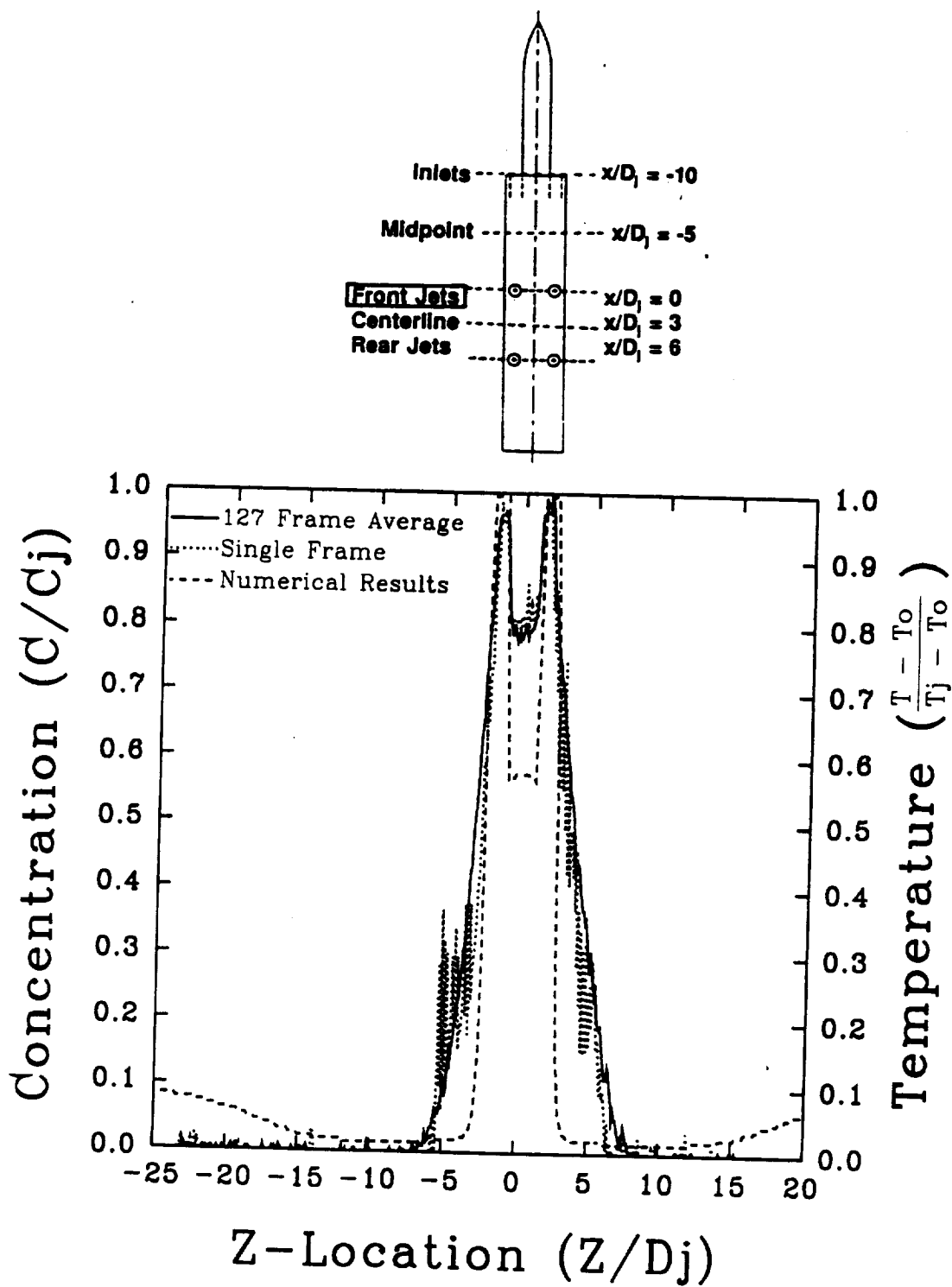


Figure 5.52: Numerical and Experimental Results Across Front Jet Pair: $x/D_j = 0$
 $y/D_j = 3.6$, $H/D_j = 4$, $U/V_j = 0.03$

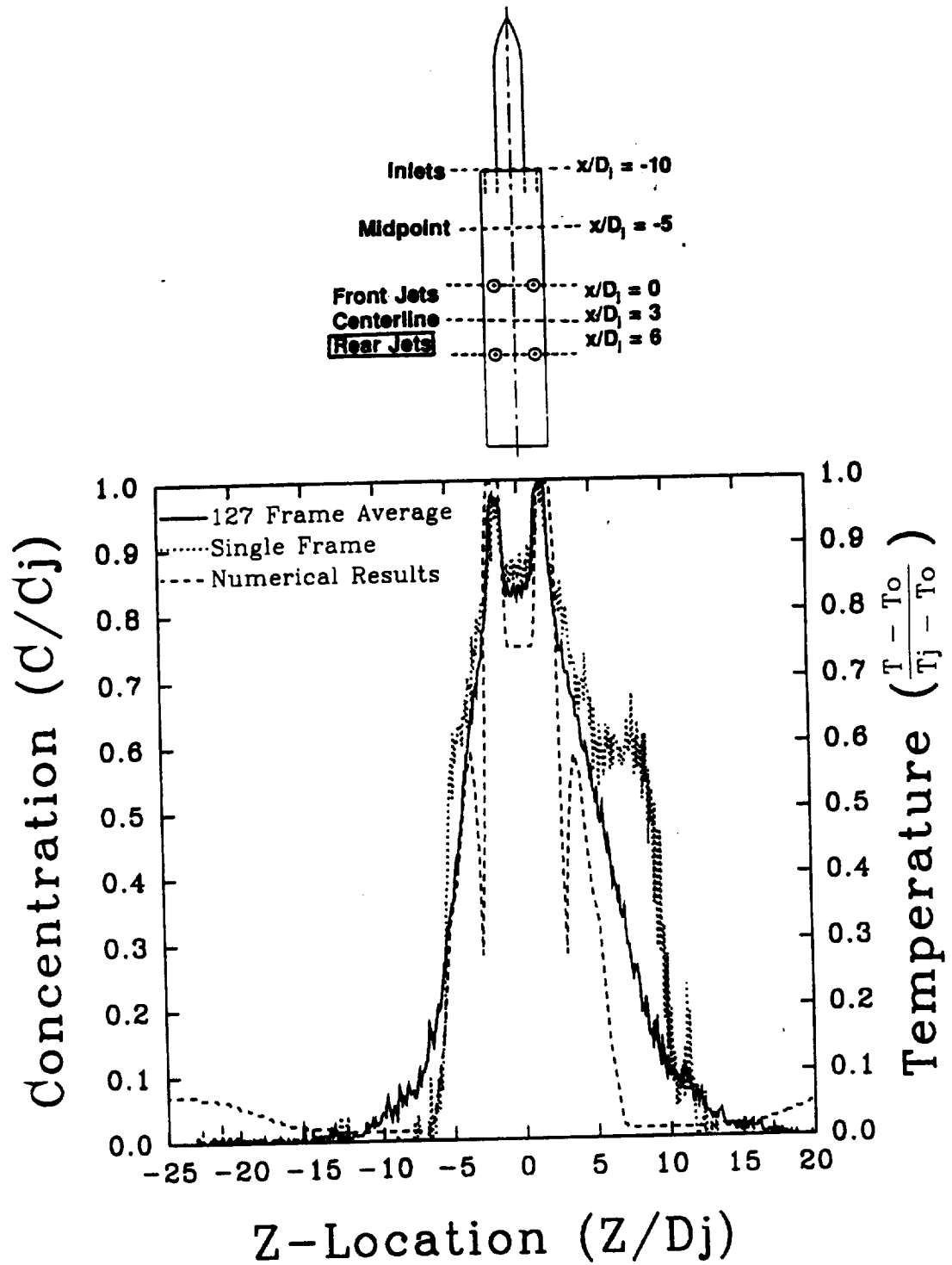


Figure 5.53: Numerical and Experimental Results Across Rear Jet Pair: $x/D_j = 6$
 $y/D_j = 3.6$, $H/D_j = 4$, $U/V_j = 0.03$

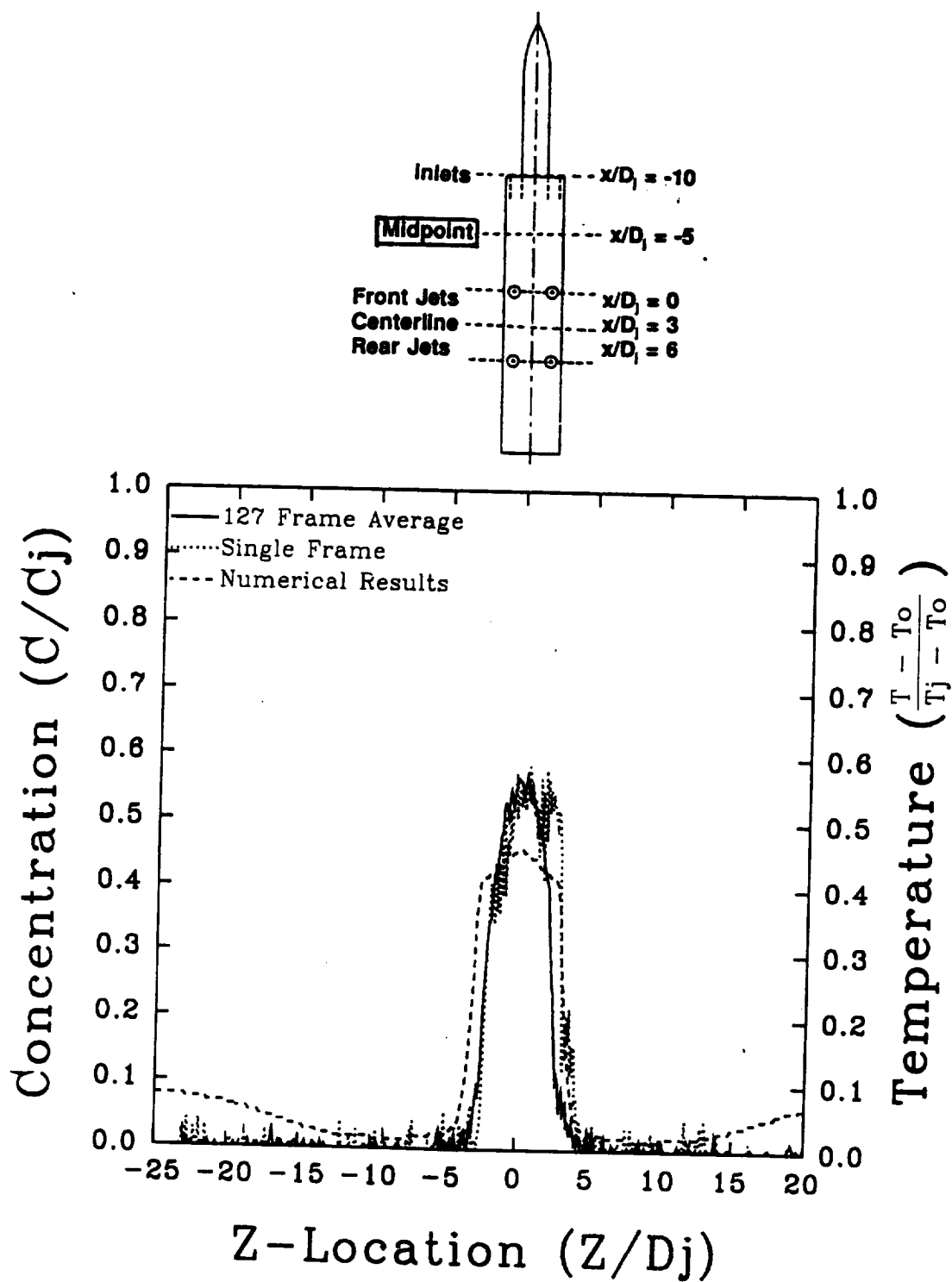


Figure 5.54: Numerical and Experimental Results Between Inlets and Front Jets
 $z/D_j = -5$, $y/D_j = 3.6$, $H/D_j = 4$, $U/V_j = 0.03$

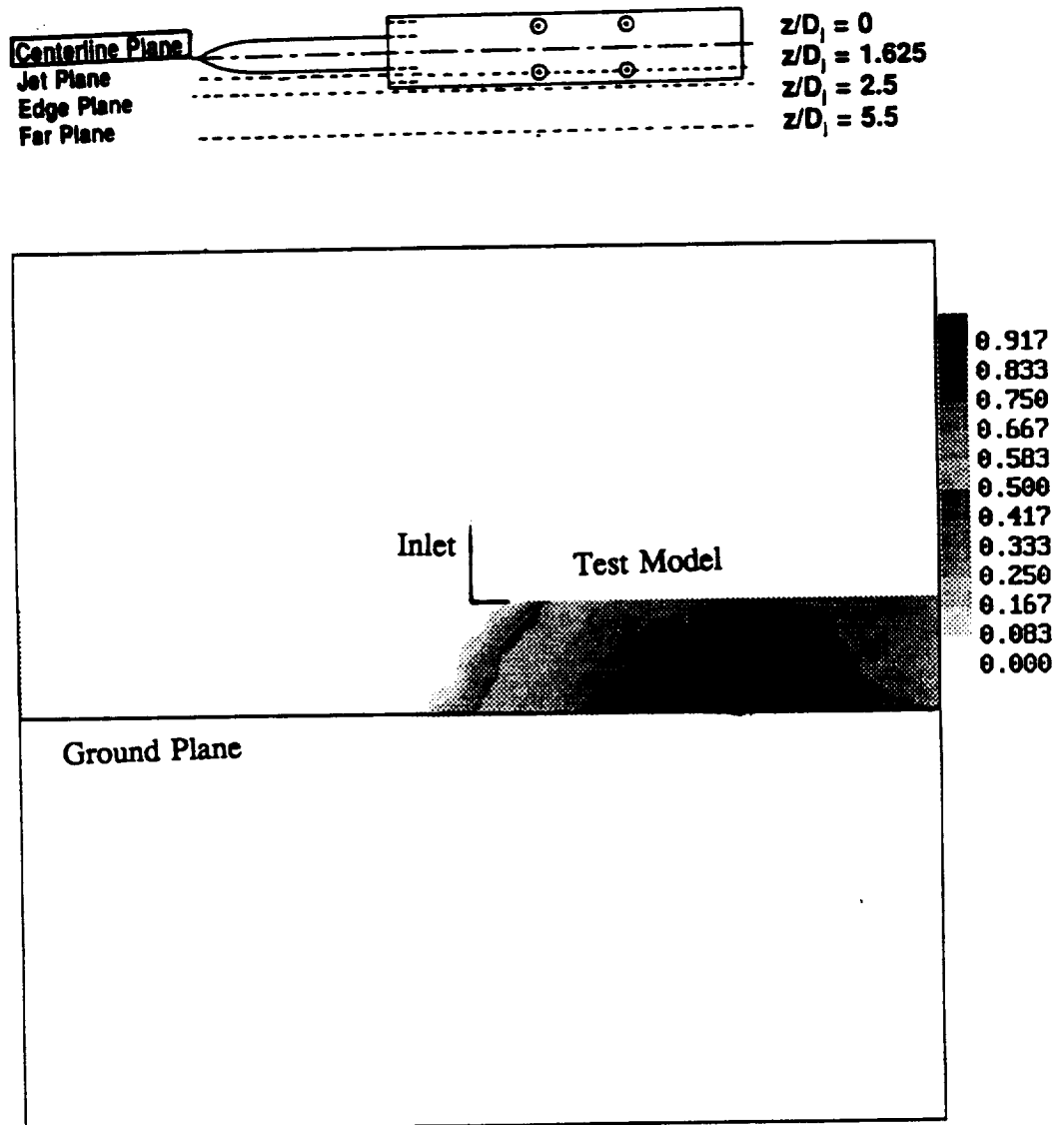


Figure 5.55: Numerical Temperature Distribution Along Model Centerline
 $z/D_j = 0.0$, $H/D_j = 4$, $U/V_j = 0.09$

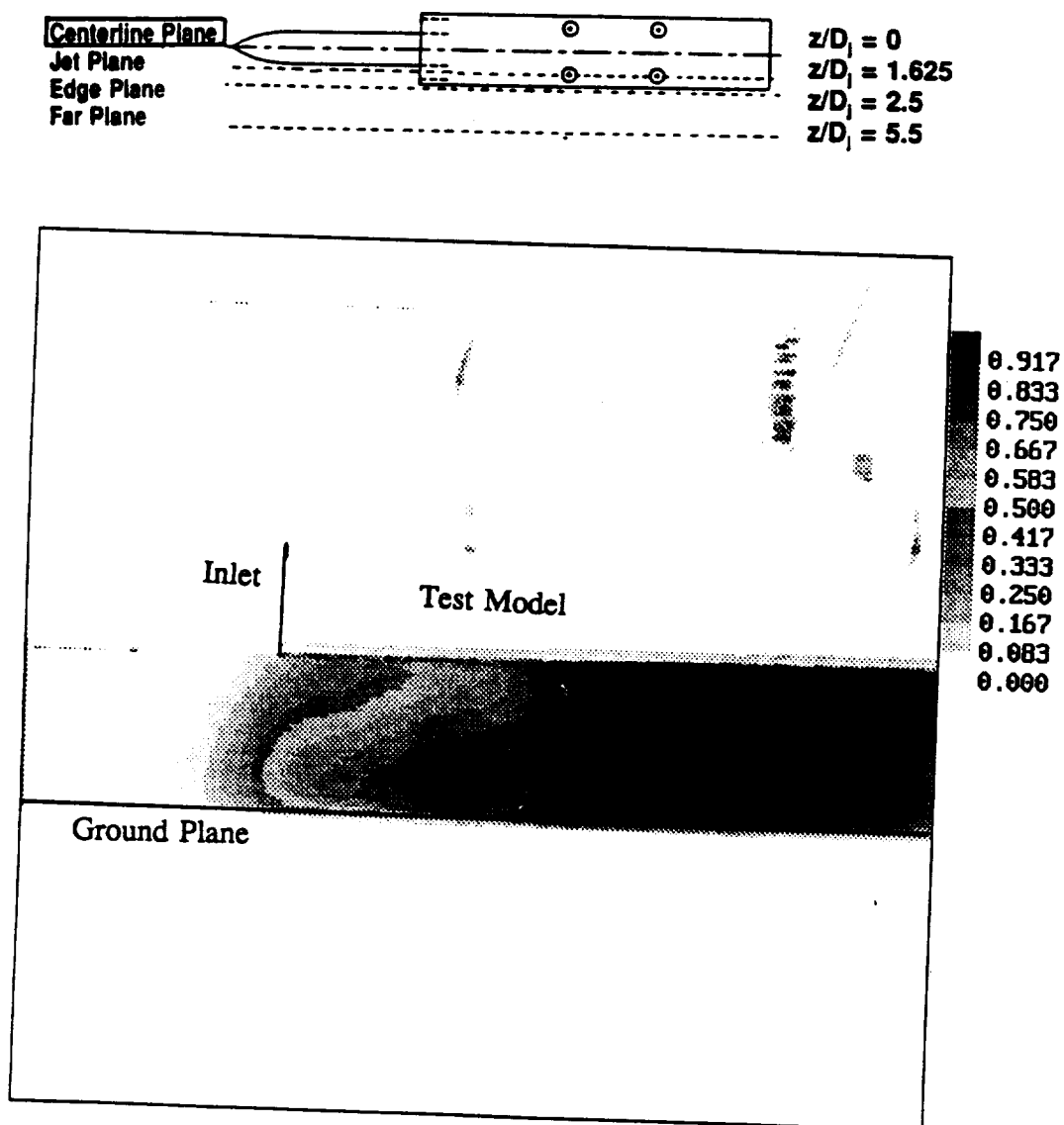


Figure 5.56: Experimental Smoke Concentration Along Model Centerline
 $z/D_j = 0.0$, $H/D_j = 4$, $U/V_j = 0.09$

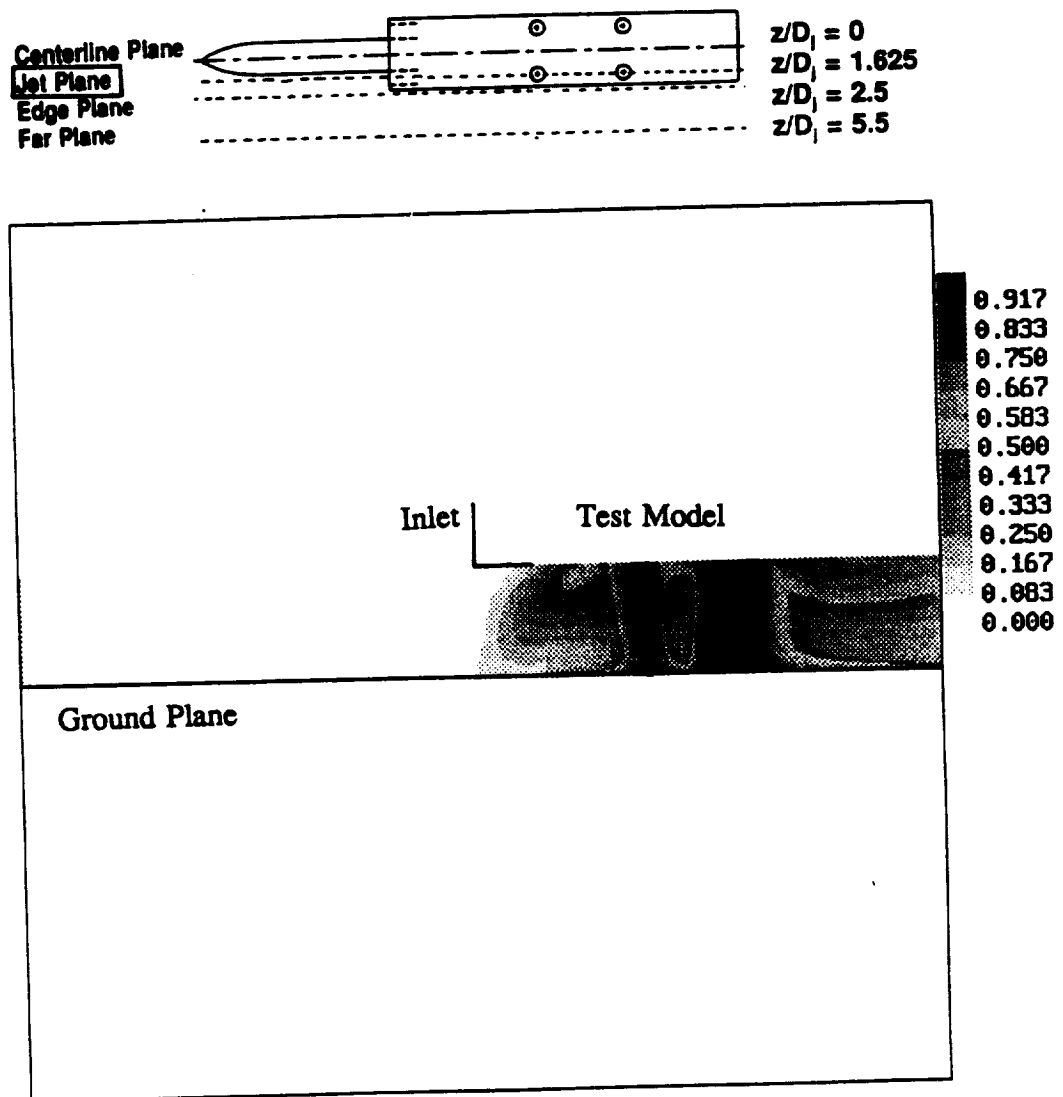


Figure 5.57: Numerical Temperature Distribution Along Side Jet Centerline
 $z/D_j = 1.625$, $H/D_j = 4$, $U/V_j = 0.09$

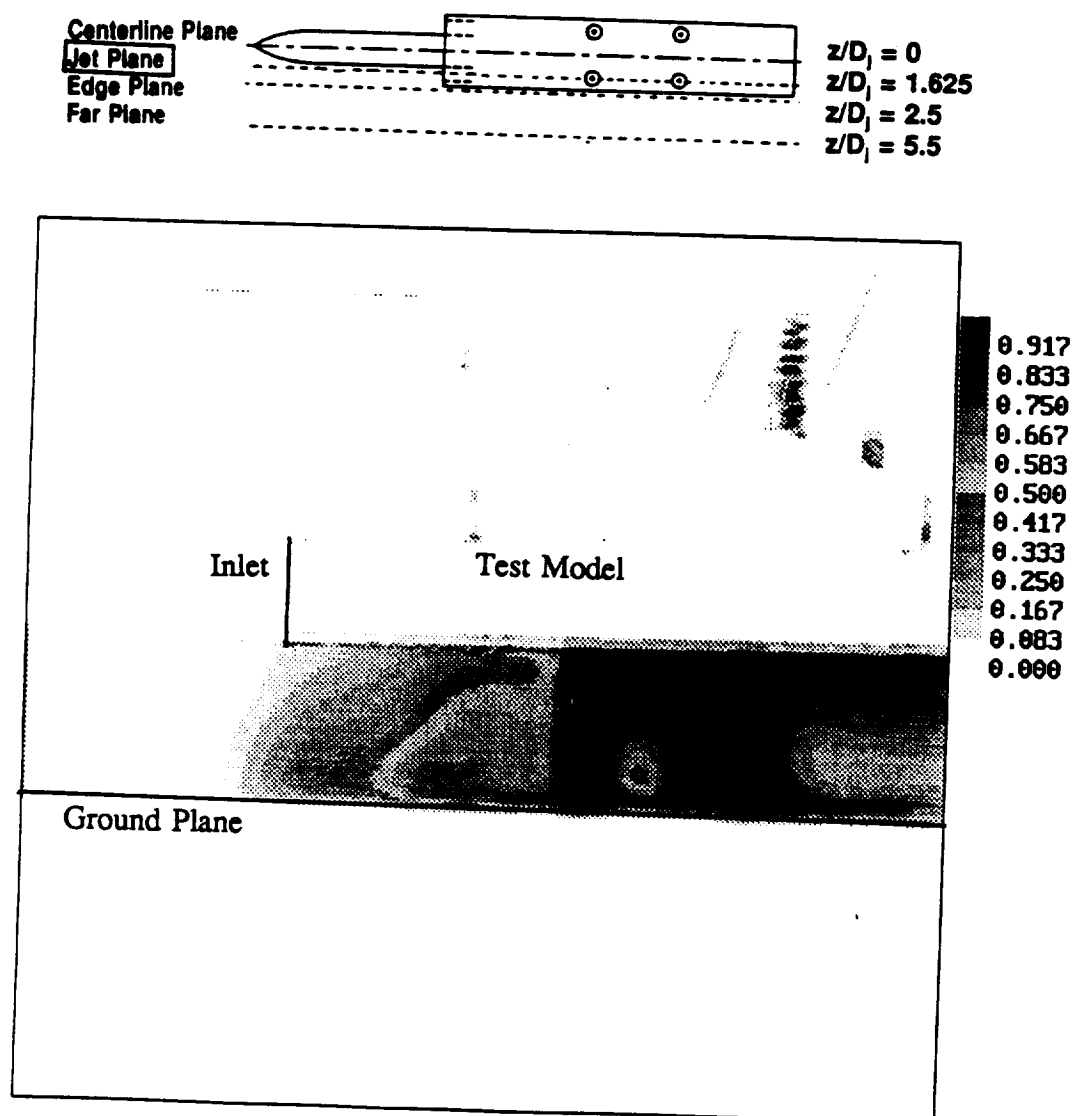


Figure 5.58: Experimental Smoke Concentration Along Side Jet Centerlines
 $z/D_j = 1.625$, $H/D_j = 4$, $U/V_j = 0.09$

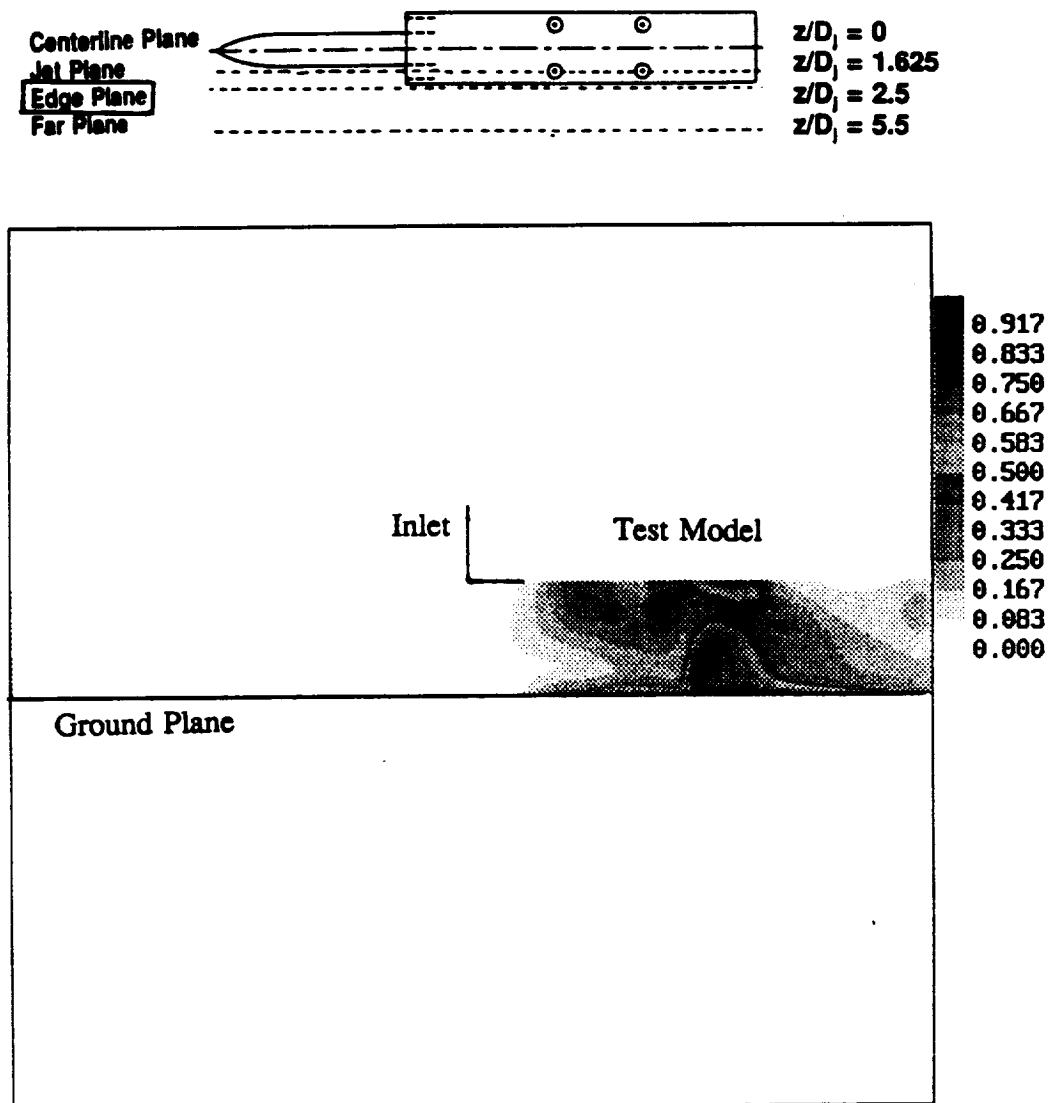


Figure 5.59: Numerical Temperature Distribution Along Model Edge
 $z/D_j = 2.5$, $H/D_j = 4$, $U/V_j = 0.09$

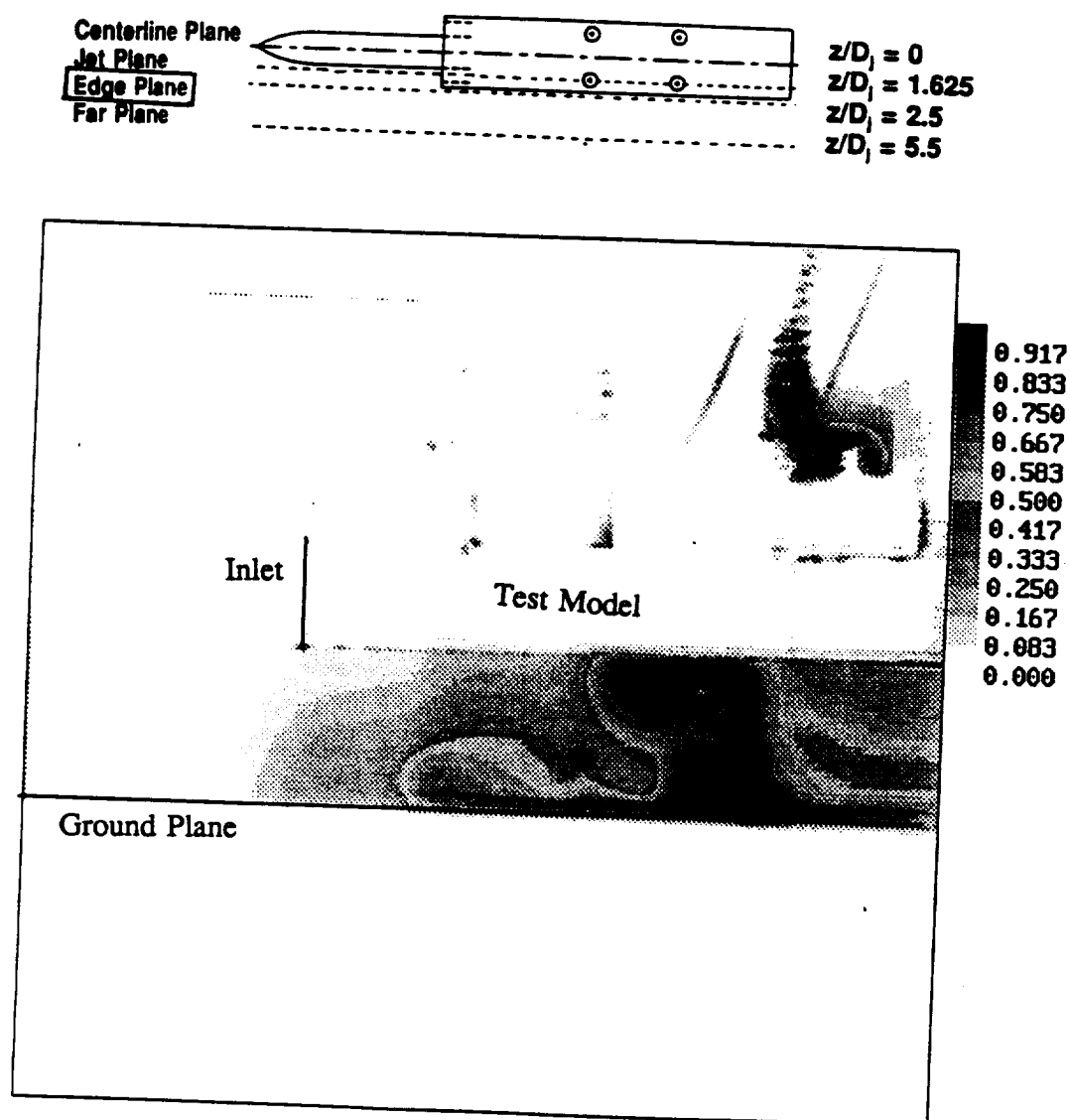


Figure 5.60: Experimental Smoke Concentration Along Model Edge
 $z/D_j = 2.5$, $H/D_j = 4$, $U/V_j = 0.09$

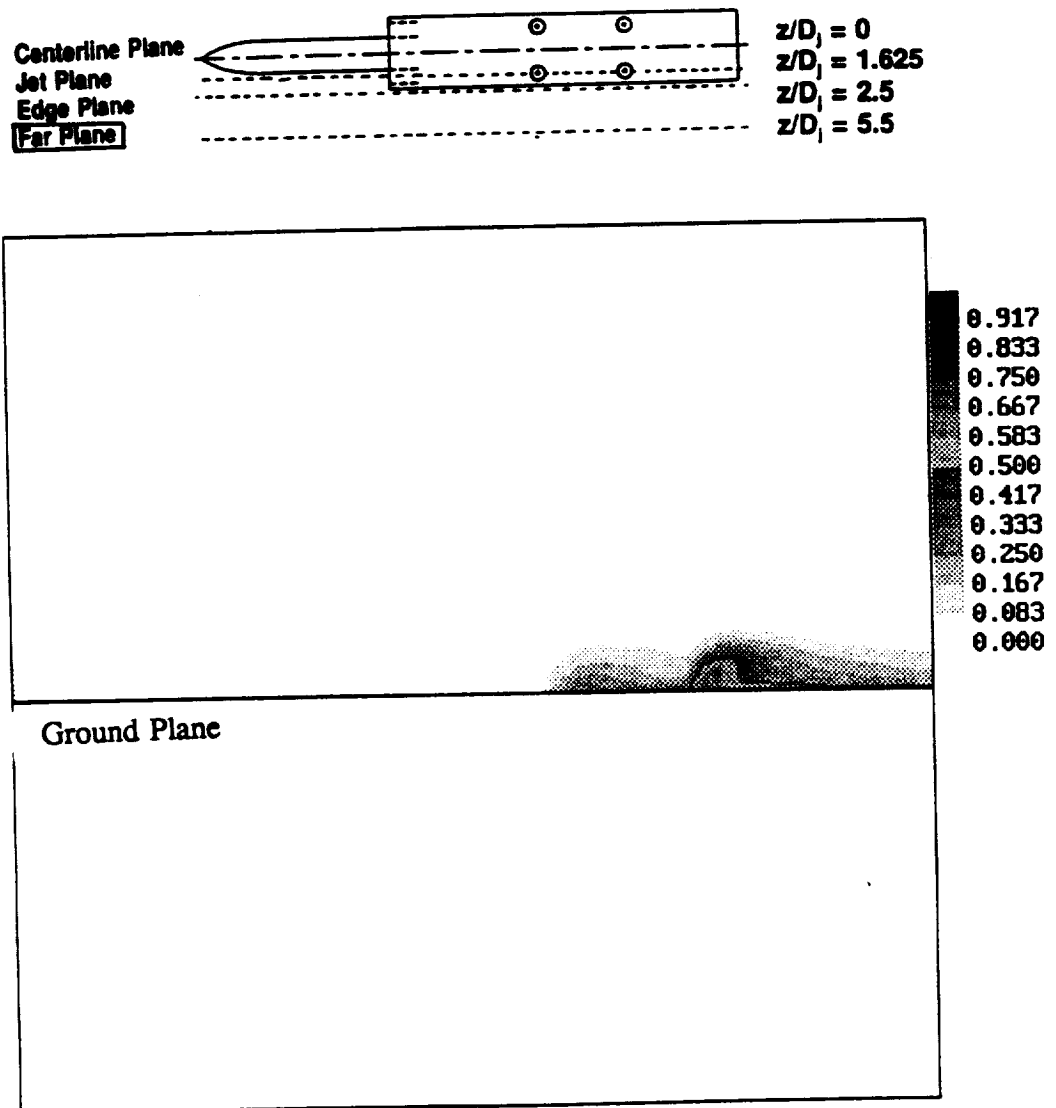


Figure 5.61: Numerical Temperature Distribution Along $z/D_j = 5.5$
 $H/D_j = 4$, $U/V_j = 0.09$

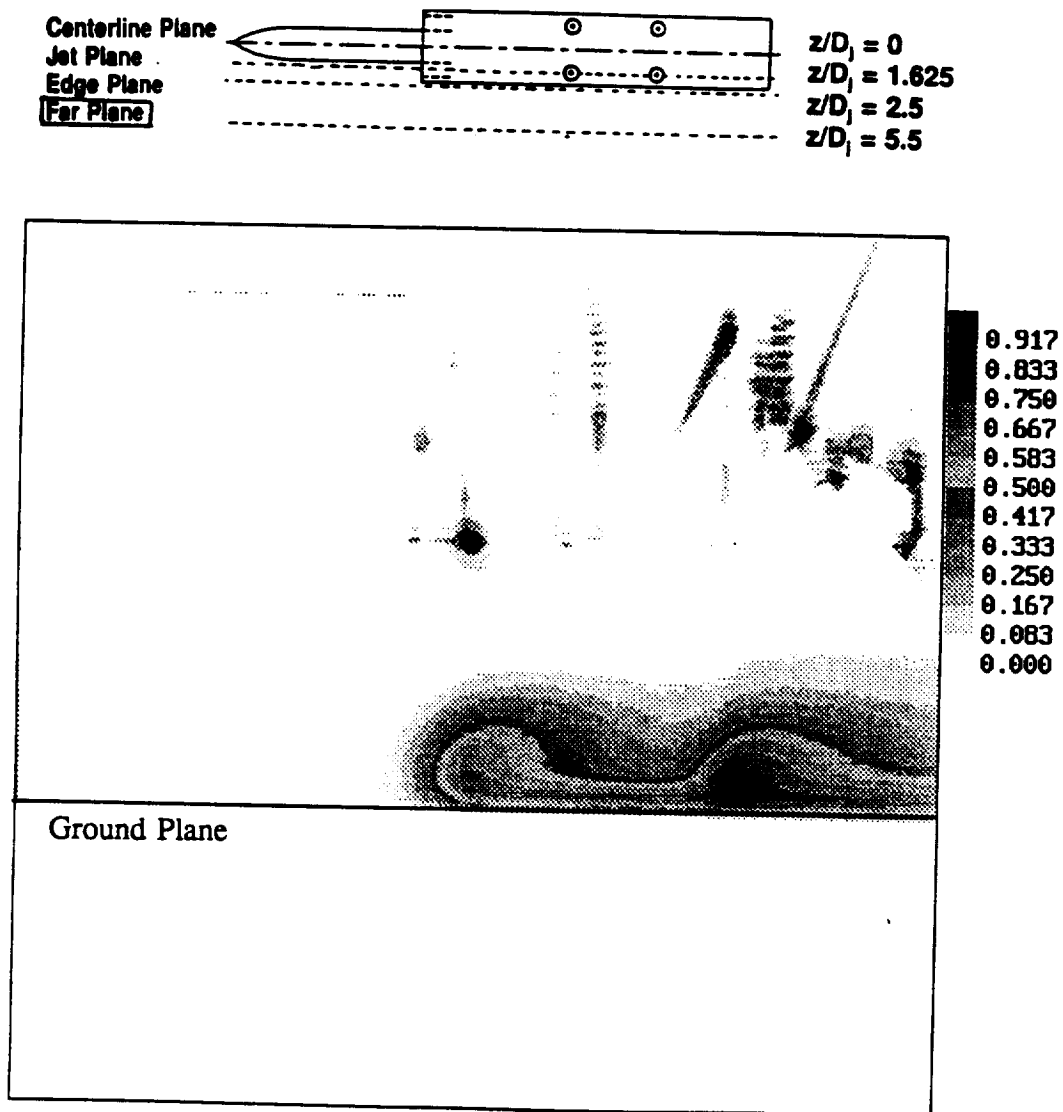


Figure 5.62: Experimental Smoke Concentration Along $z/D_j = 5.5$
 $H/D_j = 4$, $U/V_j = 0.09$

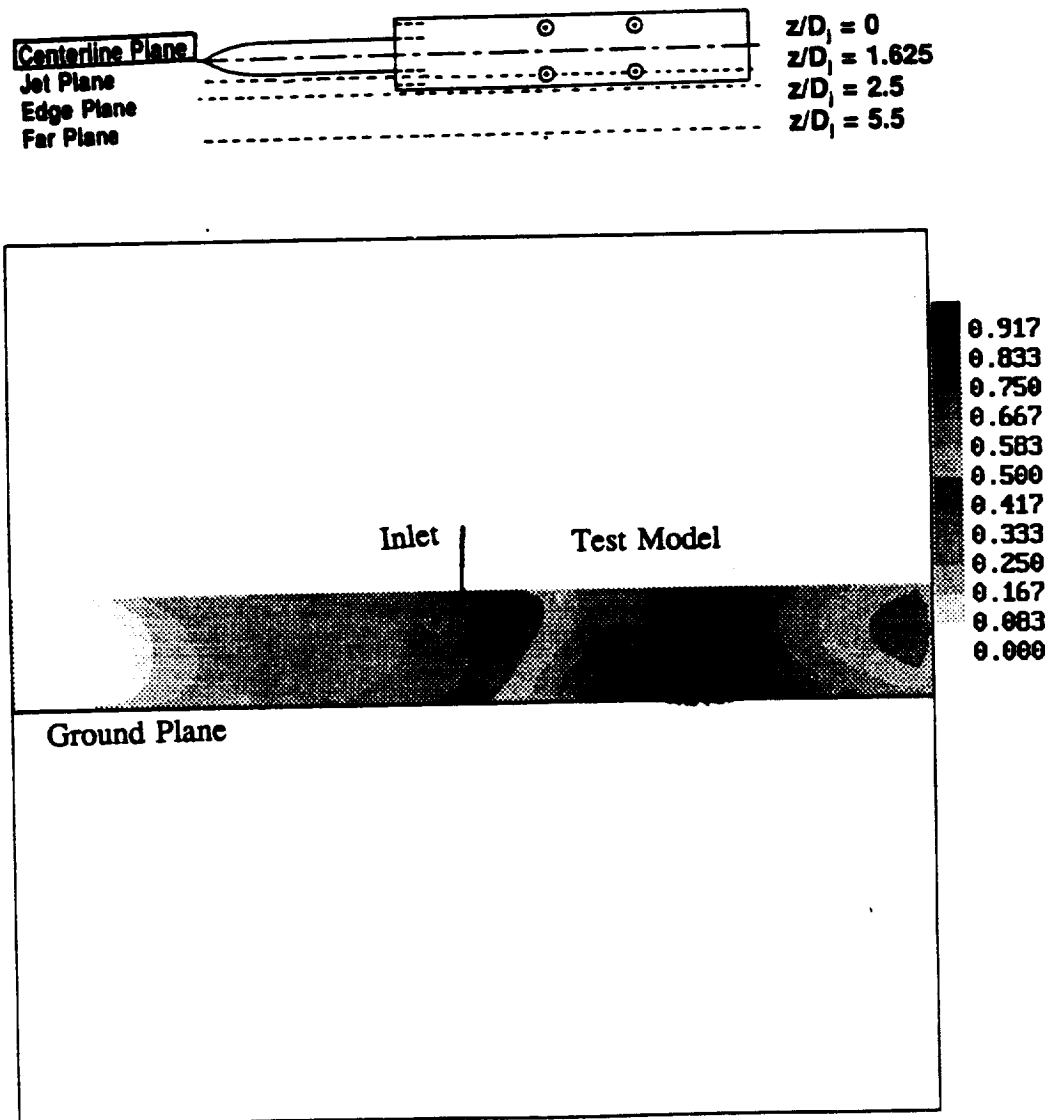


Figure 5.63: Numerical Temperature Distribution Along Model Centerline
 $z/D_j = 0.0$, $H/D_j = 4$, $U/V_j = 0.03$

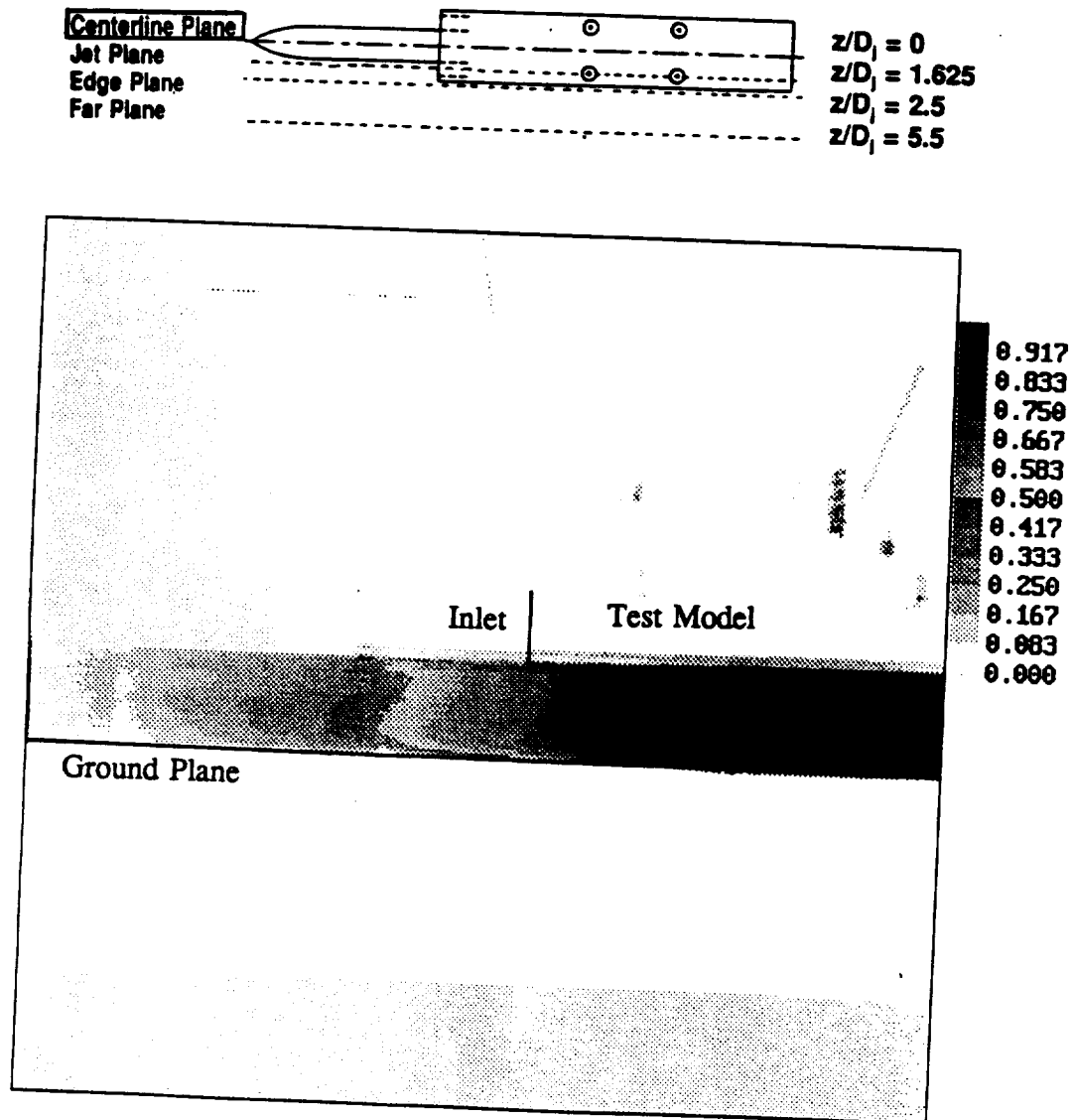


Figure 5.64: Experimental Smoke Concentration Along Model Centerline
 $z/D_j = 0.0$, $H/D_j = 4$, $U/V_j = 0.03$

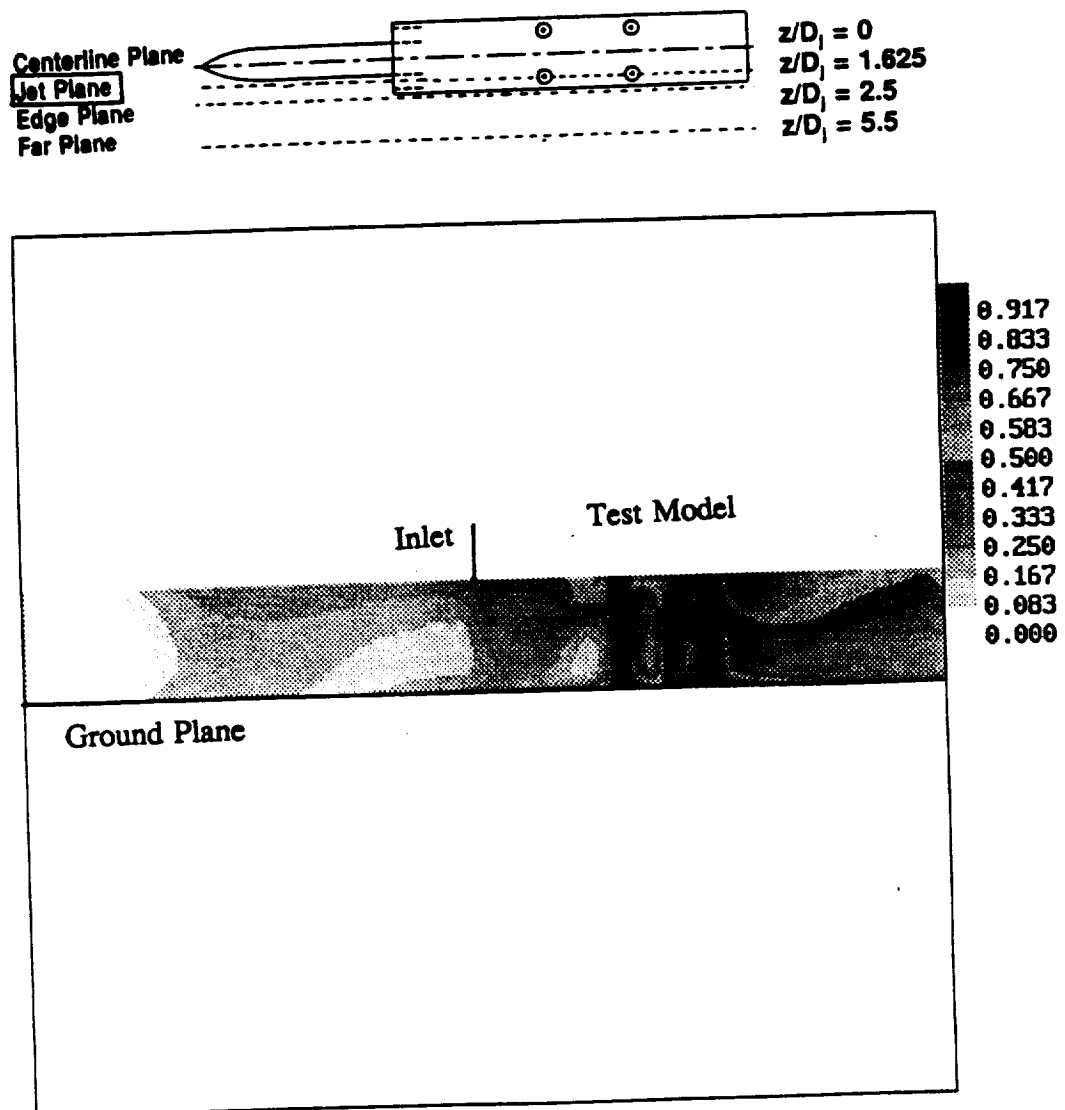


Figure 5.65: Numerical Temperature Distribution Along Side Jet Centerline
 $z/D_j = 1.625$, $H/D_j = 4$, $U/V_j = 0.03$

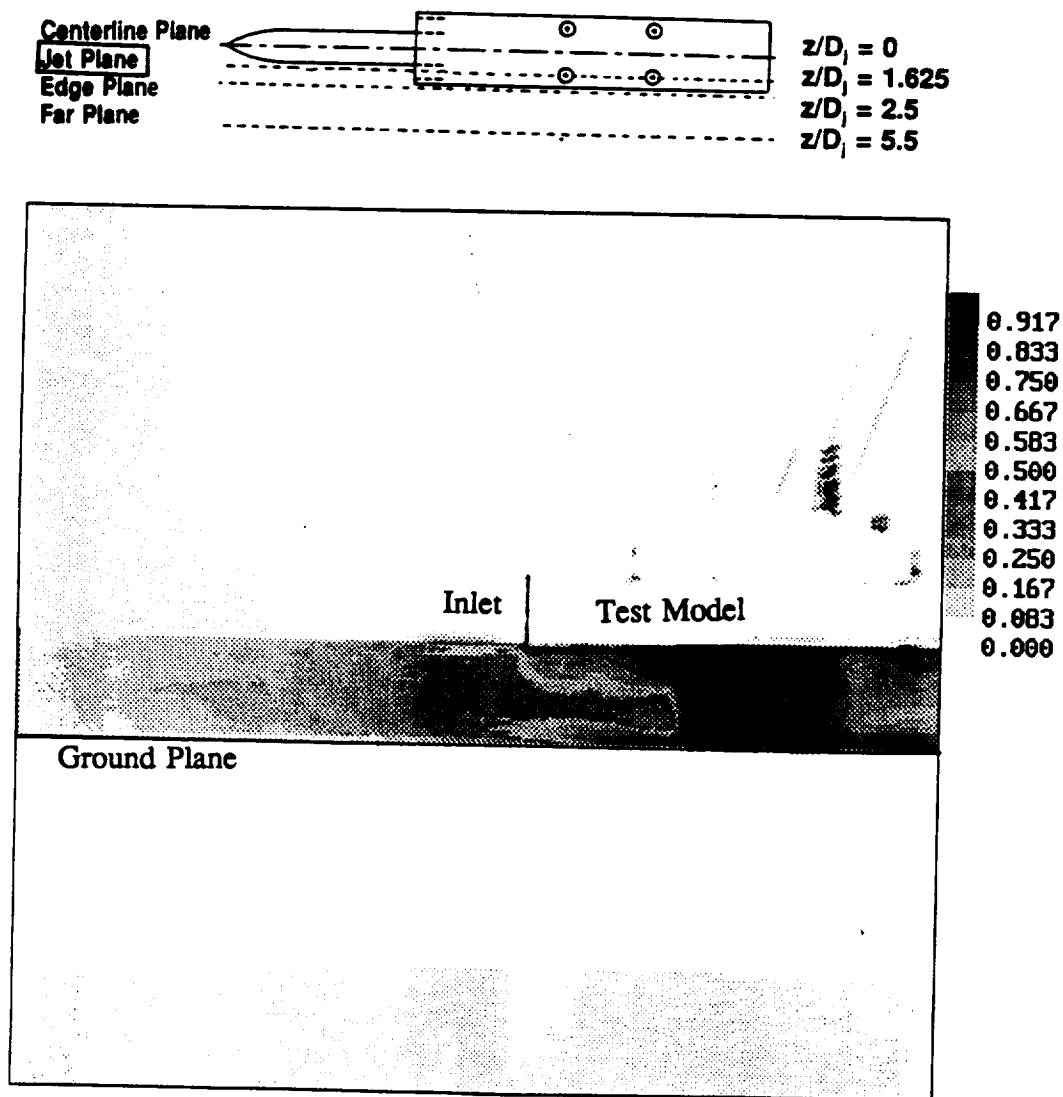


Figure 5.66: Experimental Smoke Concentration Along Side Jet Centerlines
 $z/D_j = 1.625$, $H/D_j = 4$, $U/V_j = 0.03$

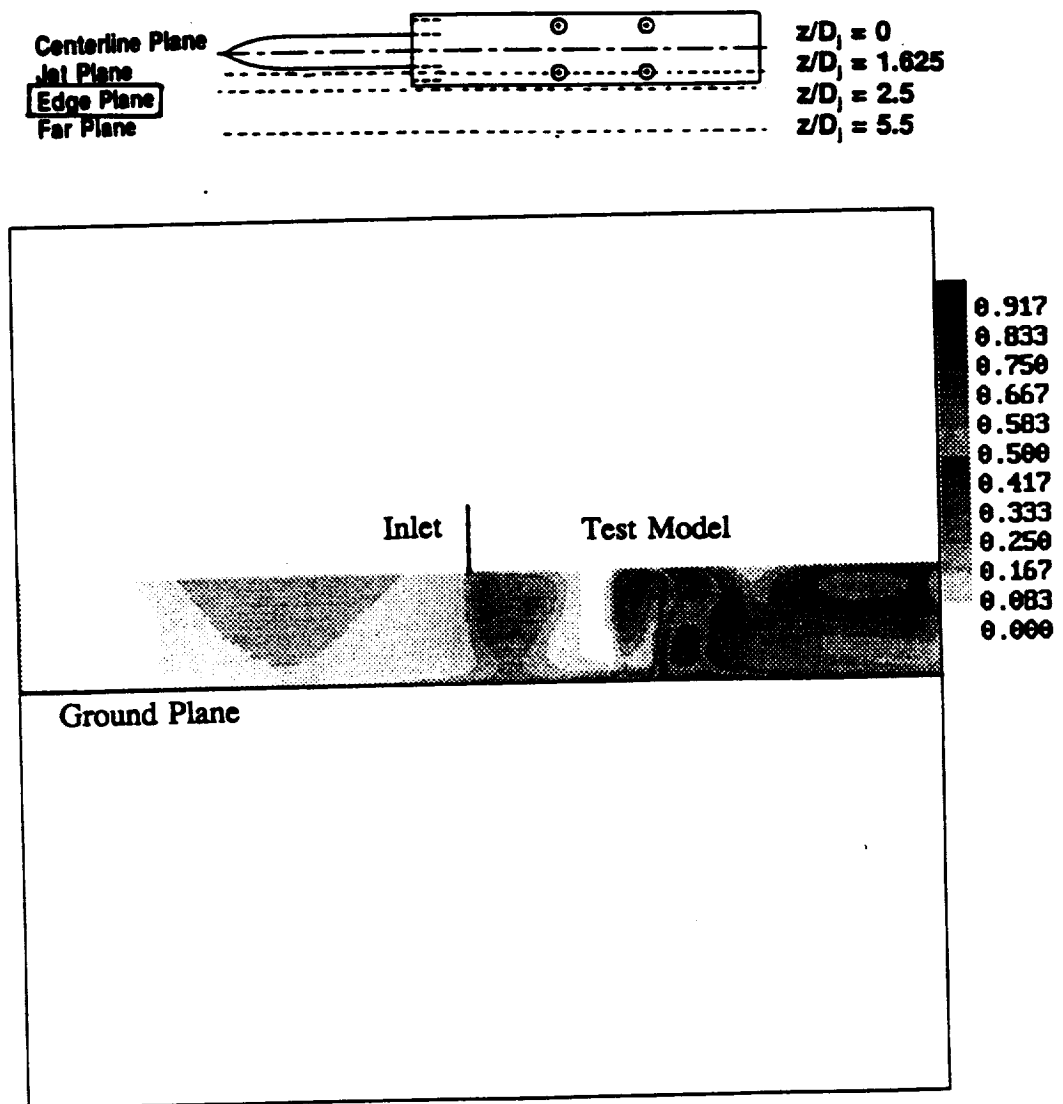


Figure 5.67: Numerical Temperature Distribution Along Model Edge
 $z/D_j = 2.5$, $H/D_j = 4$, $U/V_j = 0.03$

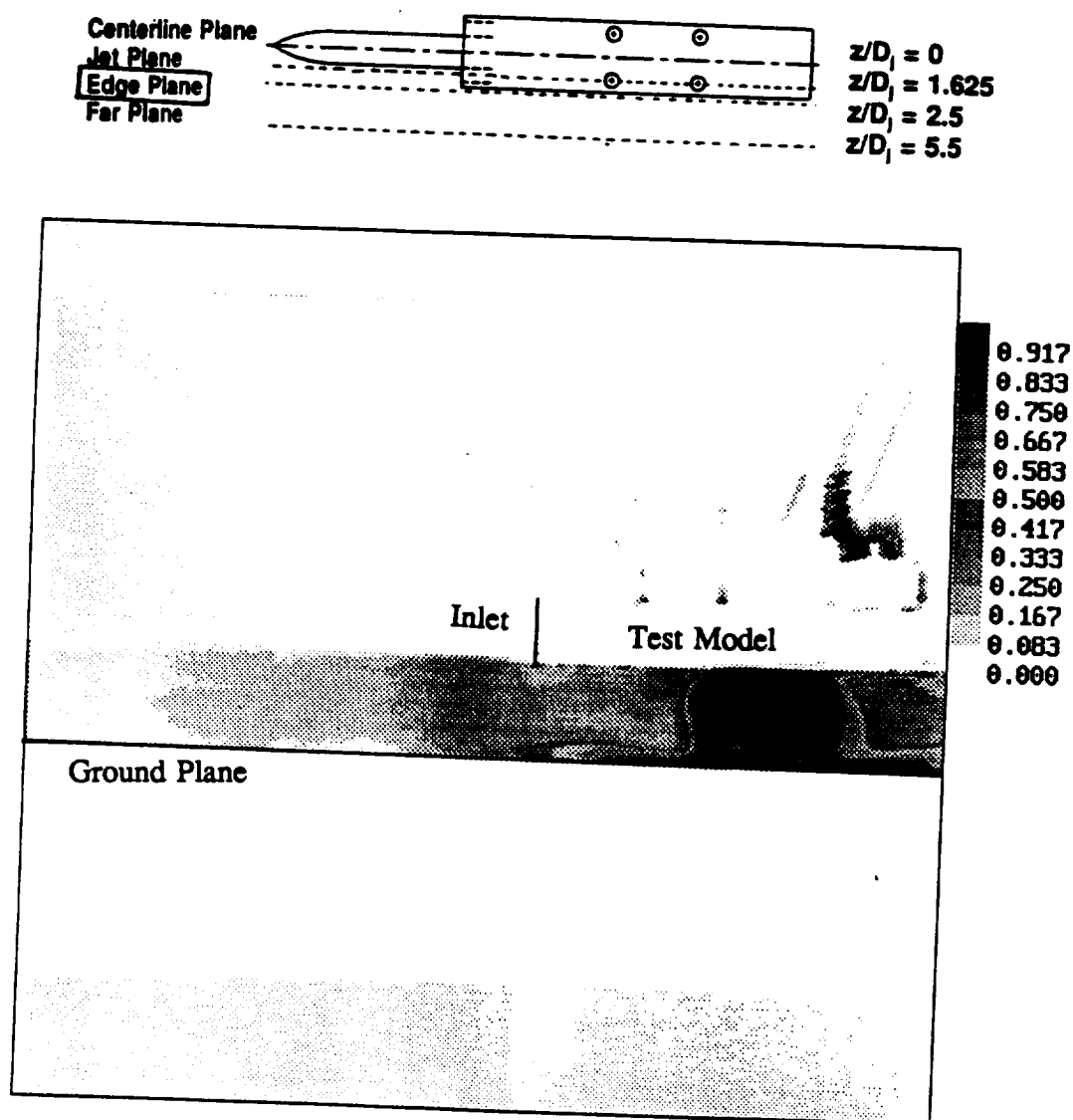


Figure 5.68: Experimental Smoke Concentration Along Model Edge
 $z/D_j = 2.5$, $H/D_j = 4$, $U/V_j = 0.03$

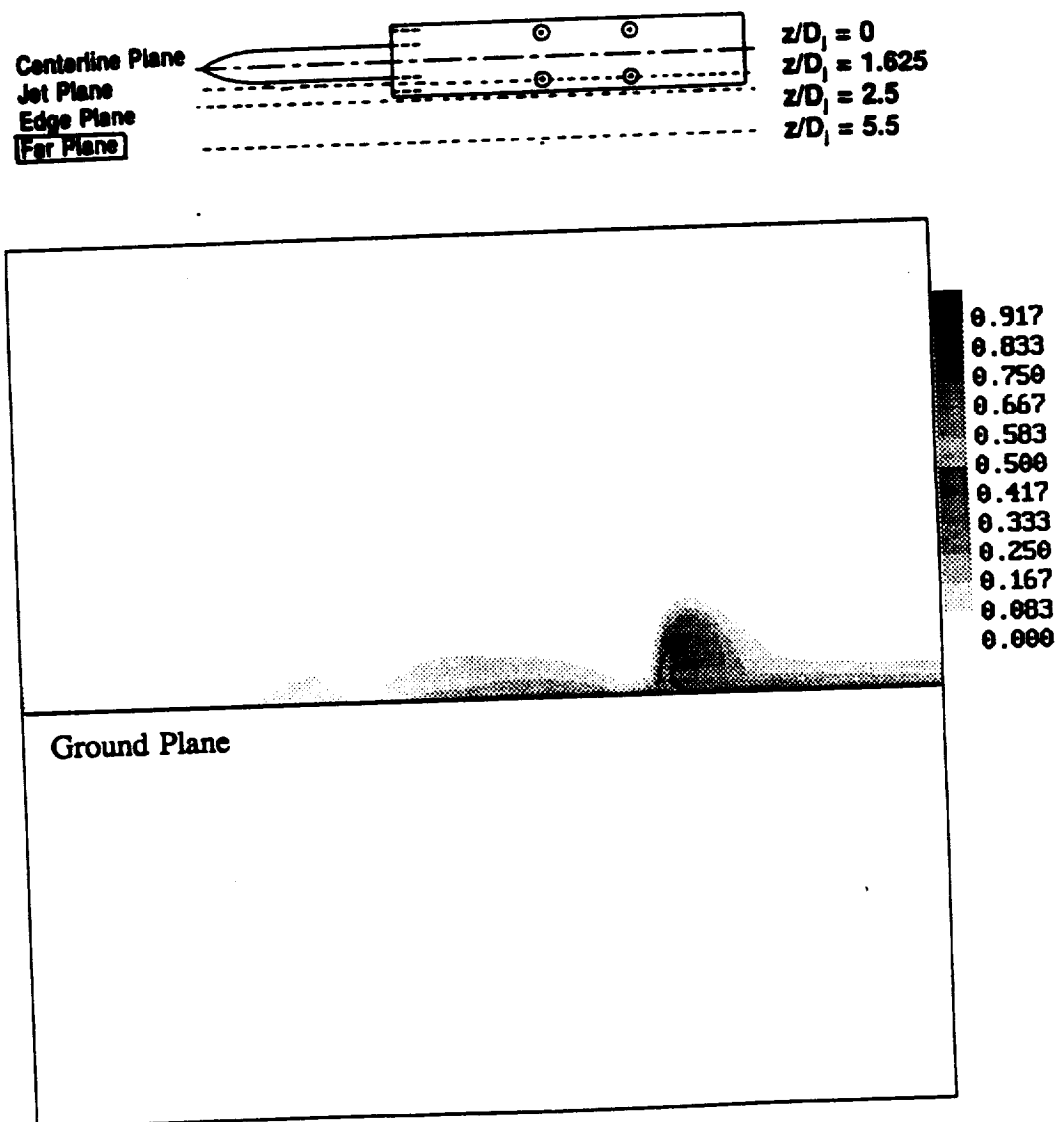


Figure 5.69: Numerical Temperature Distribution Along $z/D_j = 5.5$
 $H/D_j = 4$, $U/V_j = 0.03$

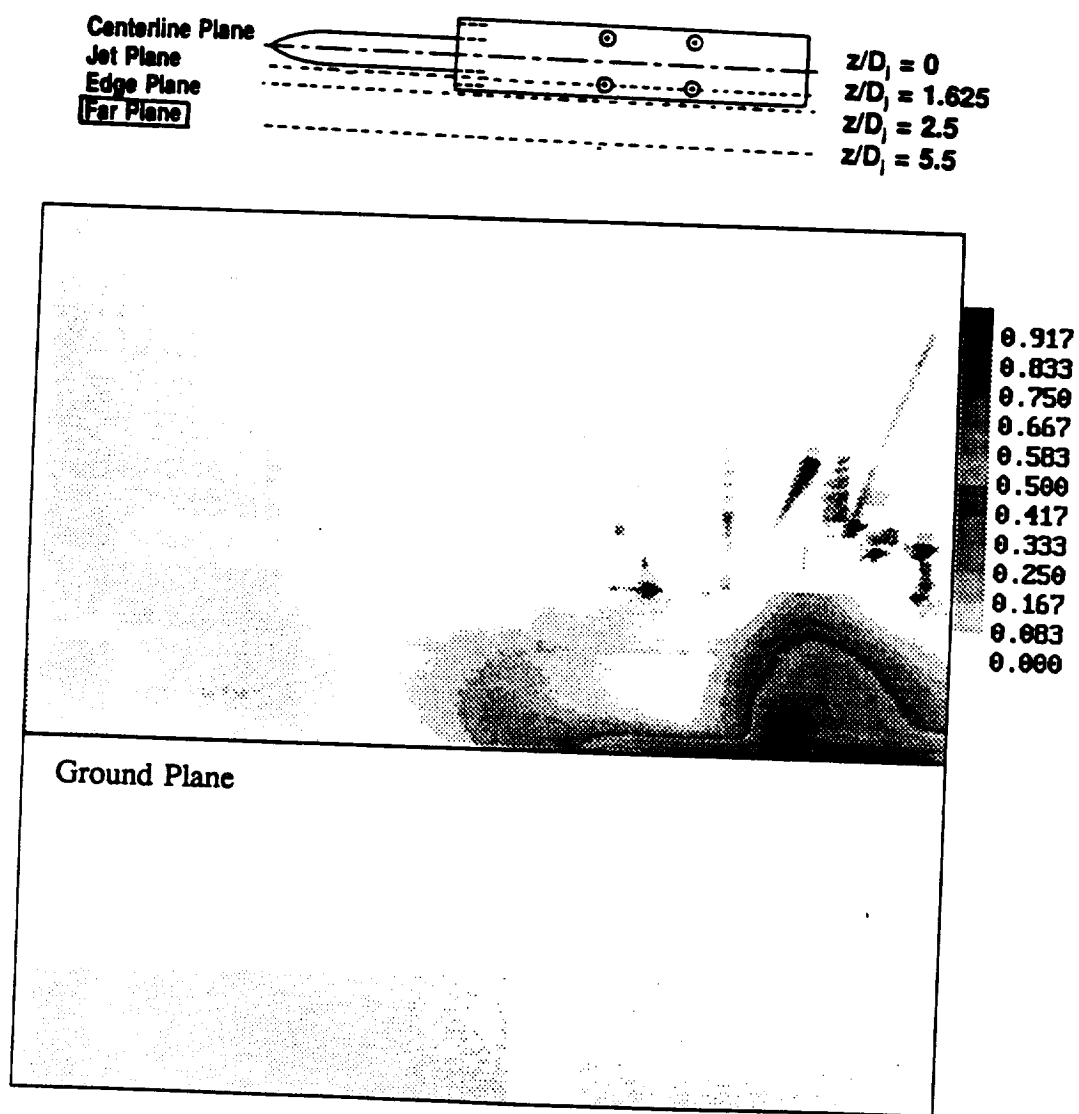


Figure 5.70: Experimental Smoke Concentration Along $z/D_j = 5.5$
 $H/D_j = 4$, $U/V_j = 0.03$

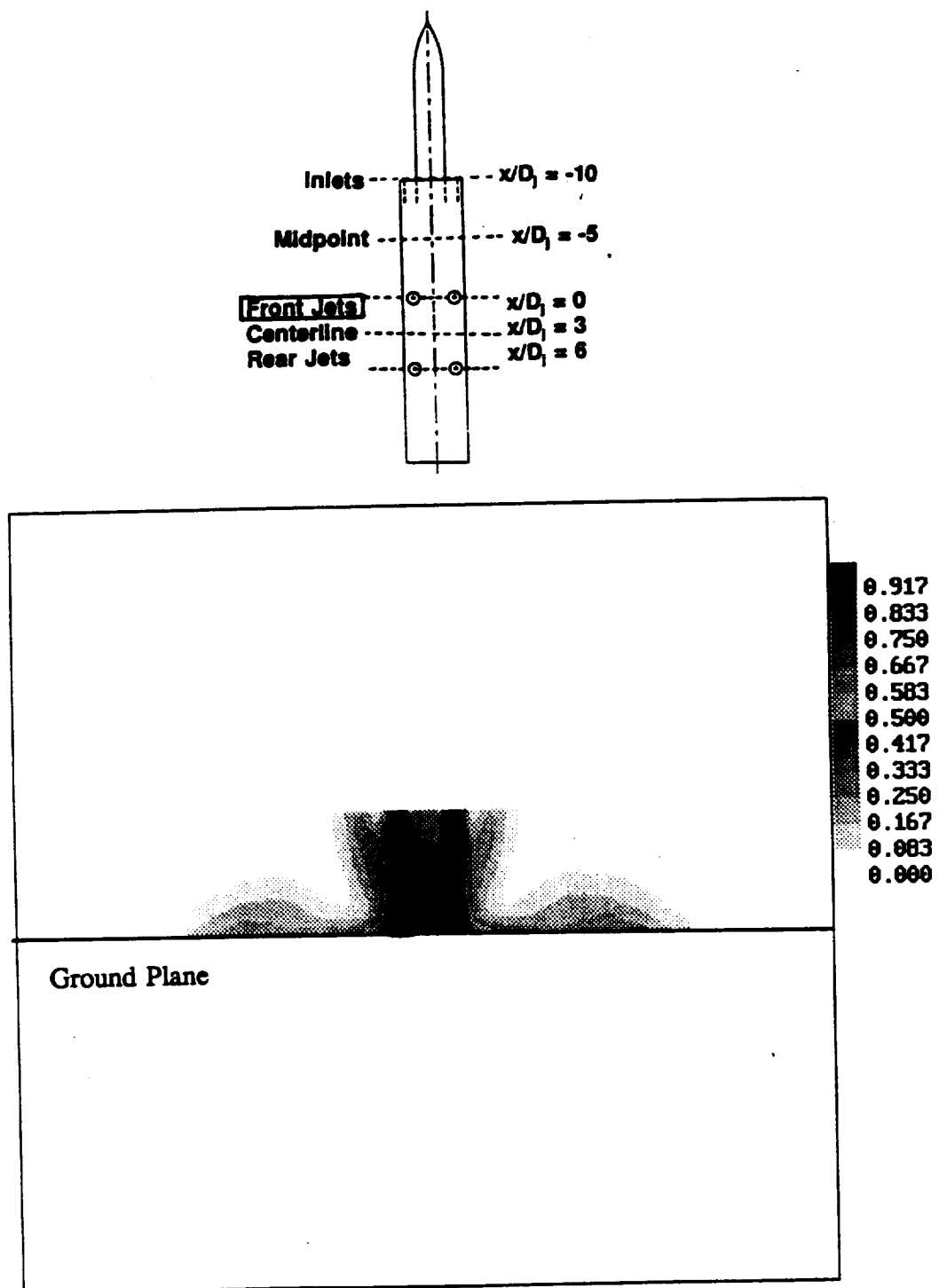


Figure 5.71: Numerical Temperature Distribution Across Front Jets
 $x/D_j = 0.0$, $H/D_j = 4$, $U/V_j = 0.09$

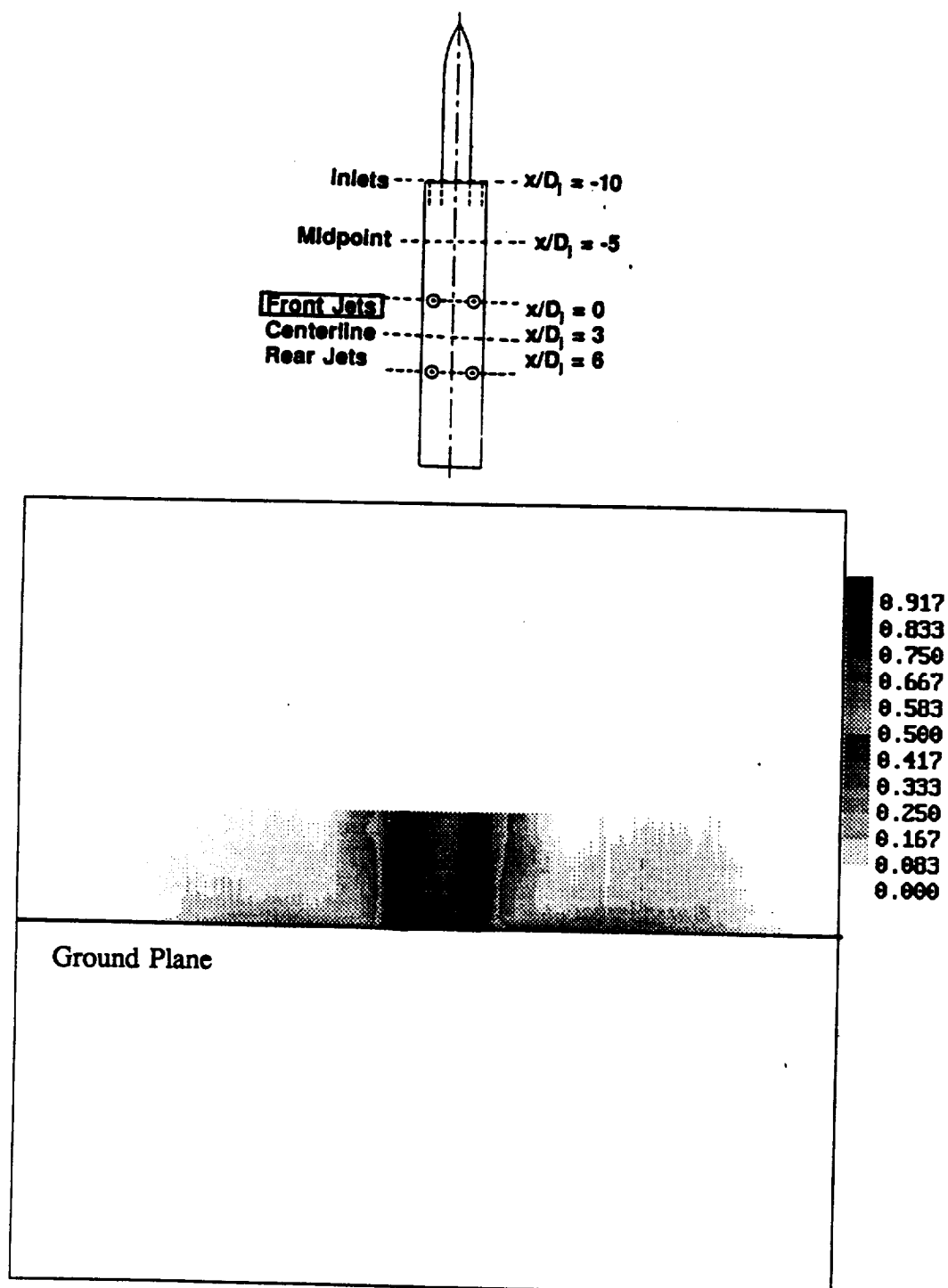


Figure 5.72: Experimental Smoke Concentration Across Front Jets
 $x/D_j = 0.0$, $H/D_j = 4$, $U/V_j = 0.09$

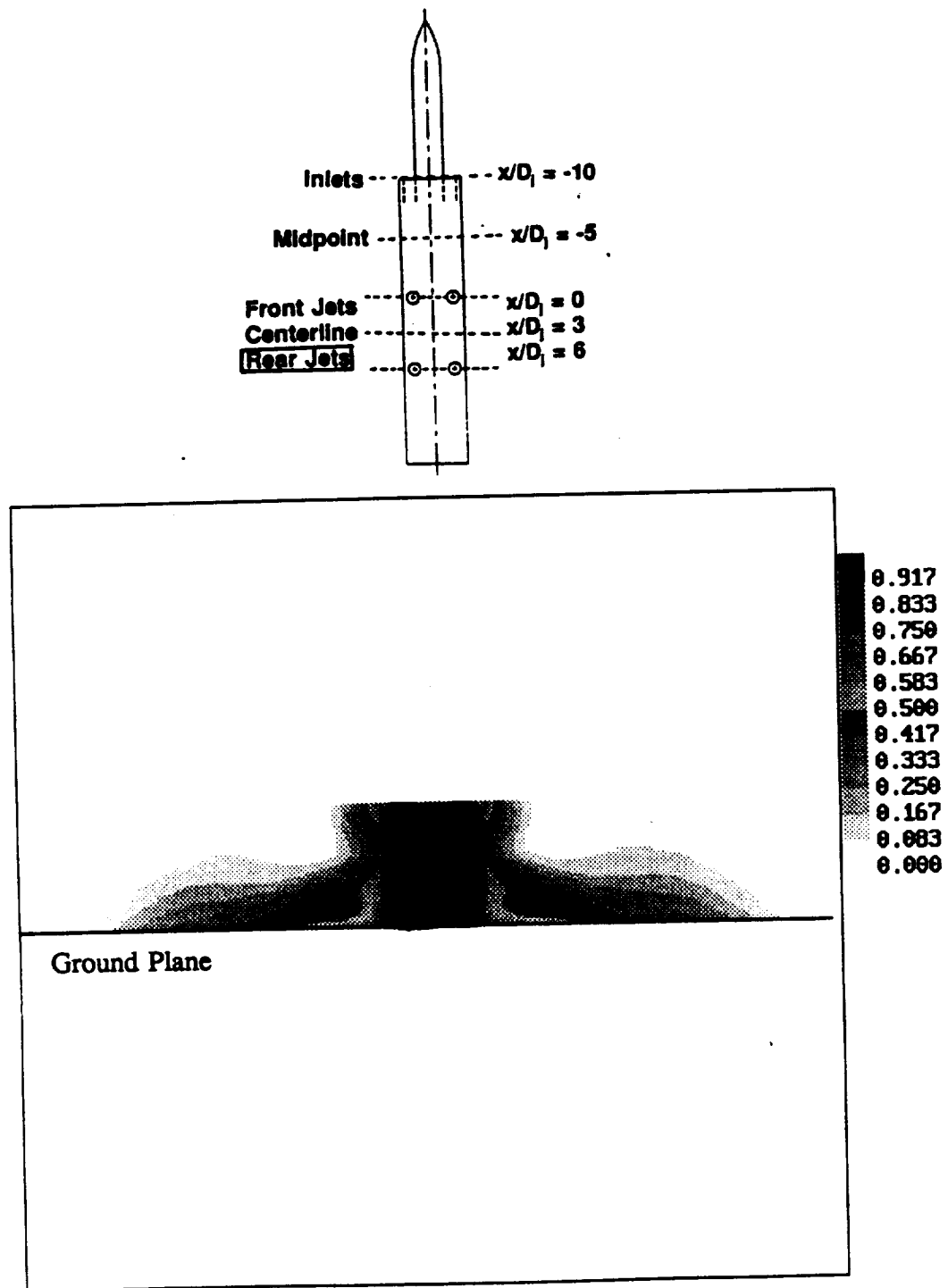


Figure 5.73: Numerical Temperature Distribution Across Rear Jets
 $x/D_j = 6.0$, $H/D_j = 4$, $U/V_j = 0.09$

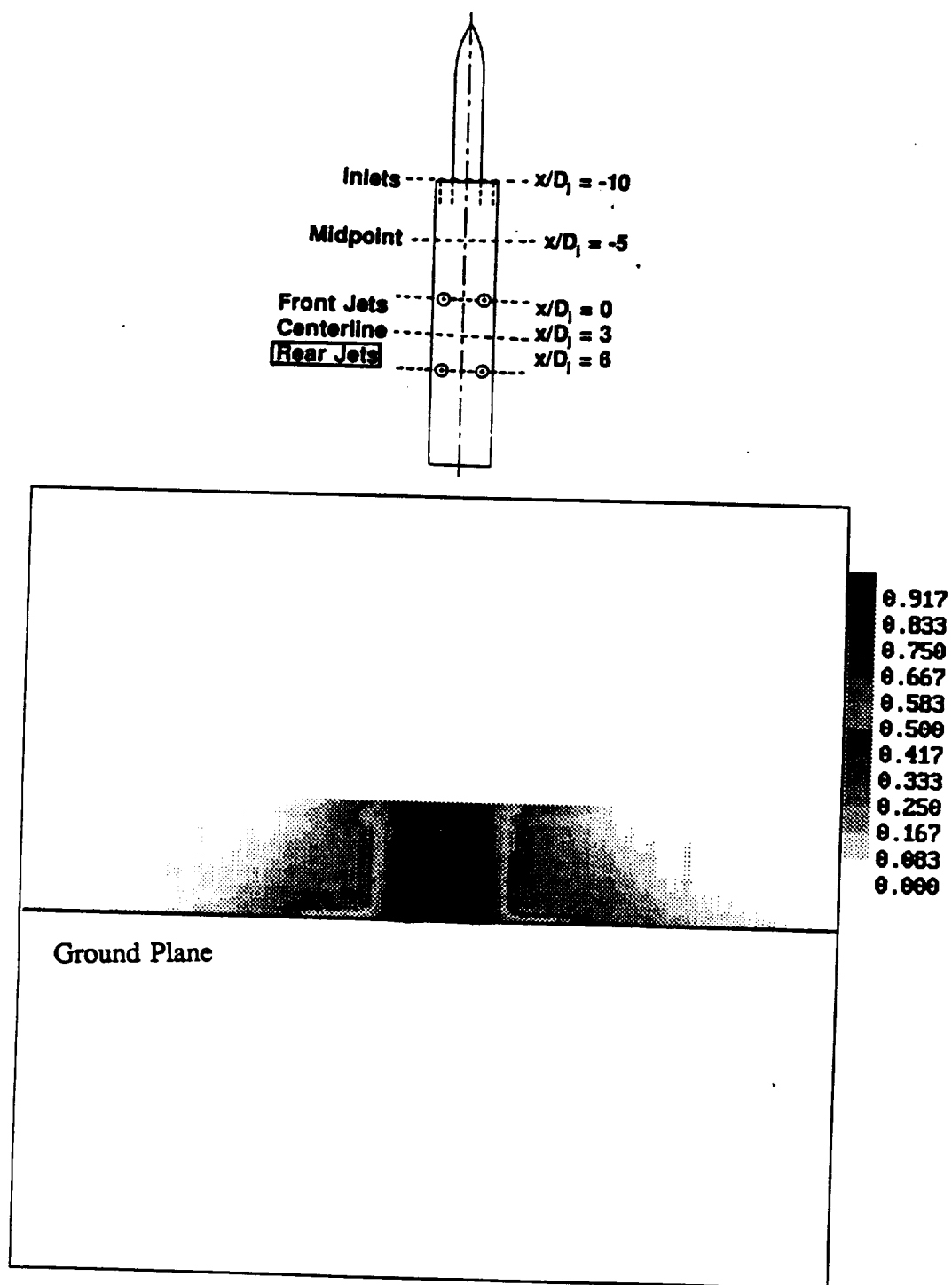


Figure 5.74: Experimental Smoke Concentration Across Rear Jets
 $x/D_j = 6.0$, $H/D_j = 4$, $U/V_j = 0.09$

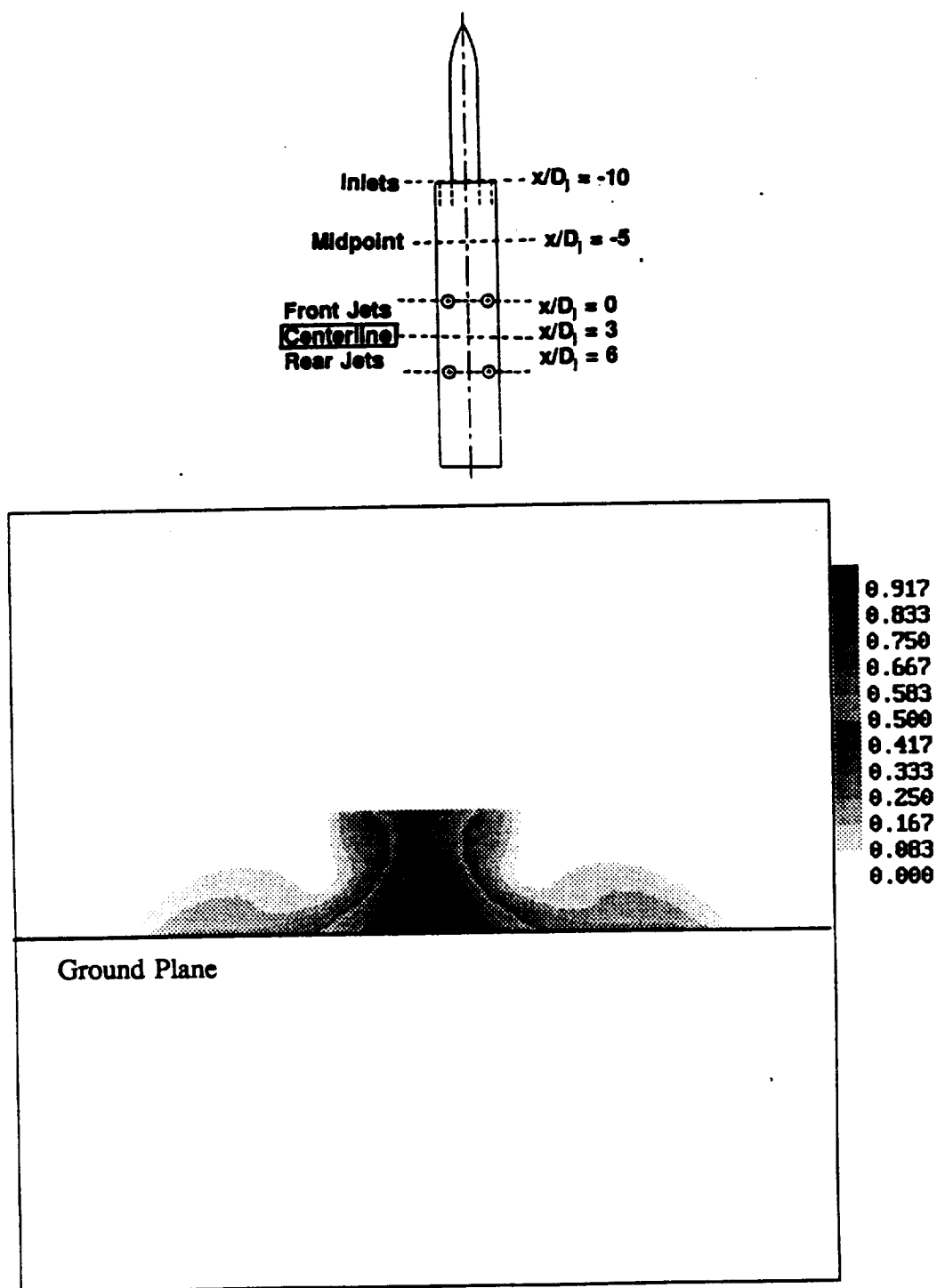


Figure 5.75: Numerical Temperature Distribution Between Front and Rear Jets
 $x/D_j = 3.0$, $H/D_j = 4$, $U/V_j = 0.09$

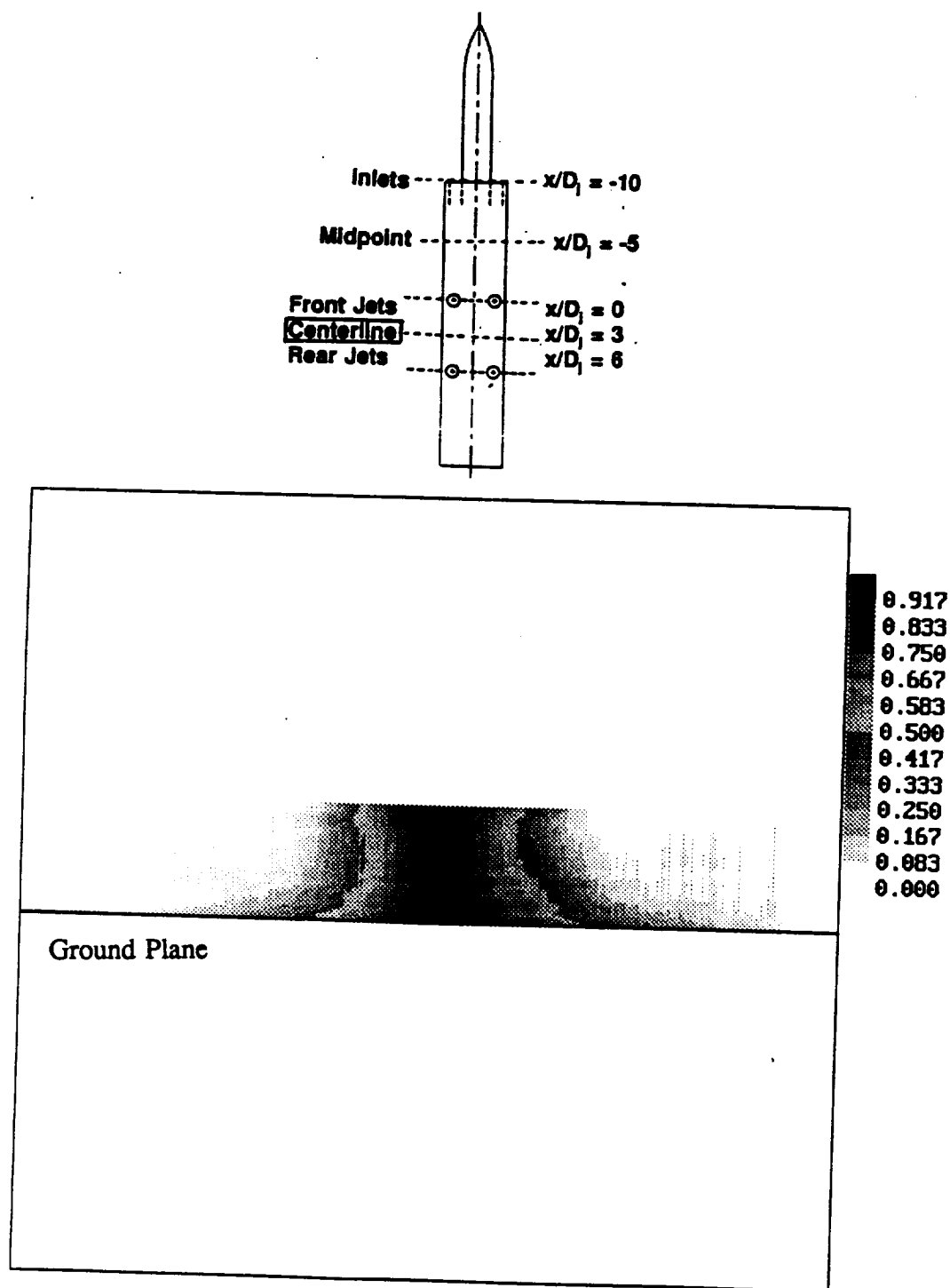


Figure 5.76: Experimental Smoke Concentration Between Front and Rear Jets
 $x/D_j = 3.0$, $H/D_j = 4$, $U/V_j = 0.09$

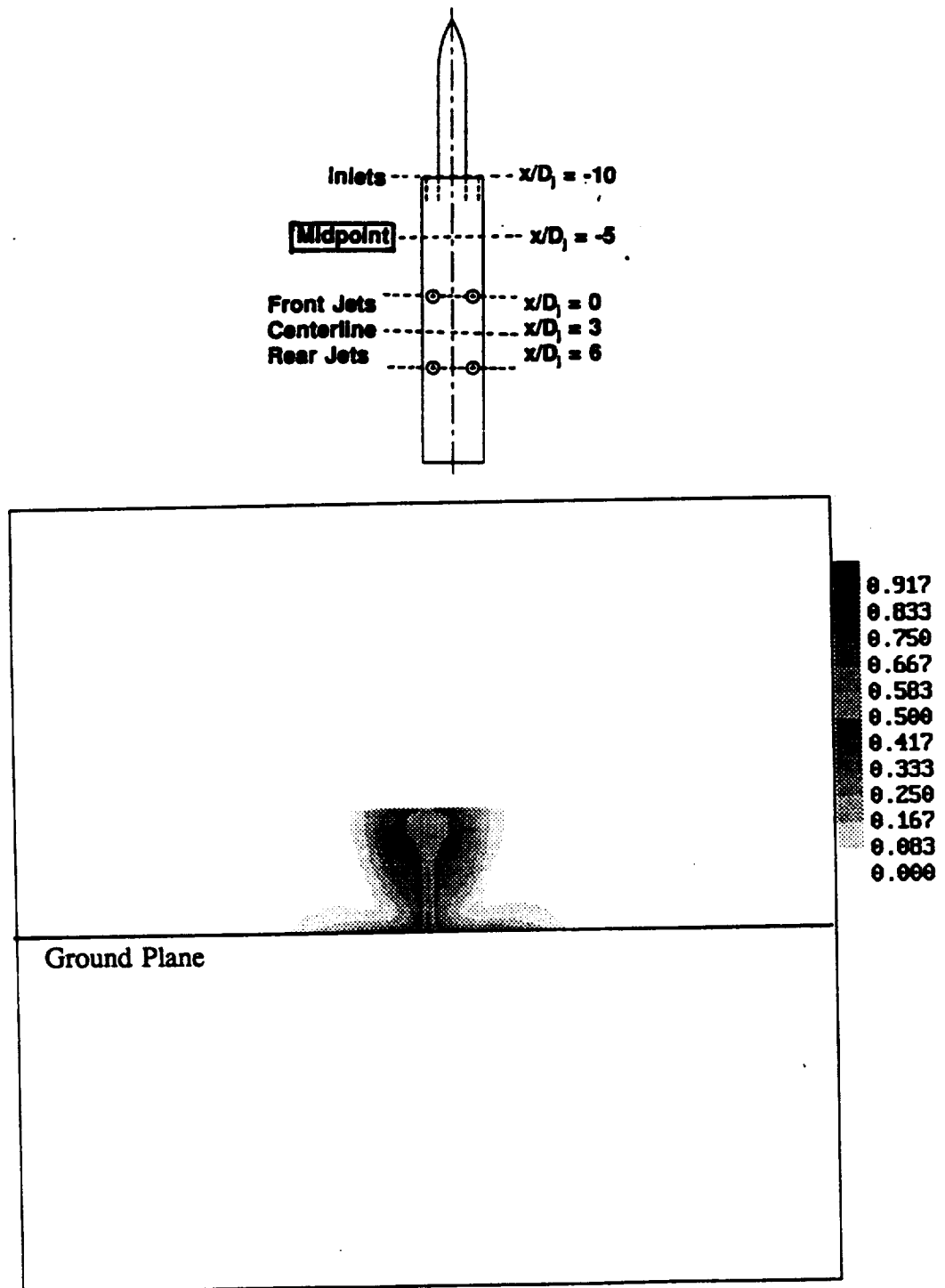


Figure 5.77: Numerical Temperature Distribution Between Inlets and Front Jets
 $x/D_j = -5.0$, $H/D_j = 4$, $U/V_j = 0.09$

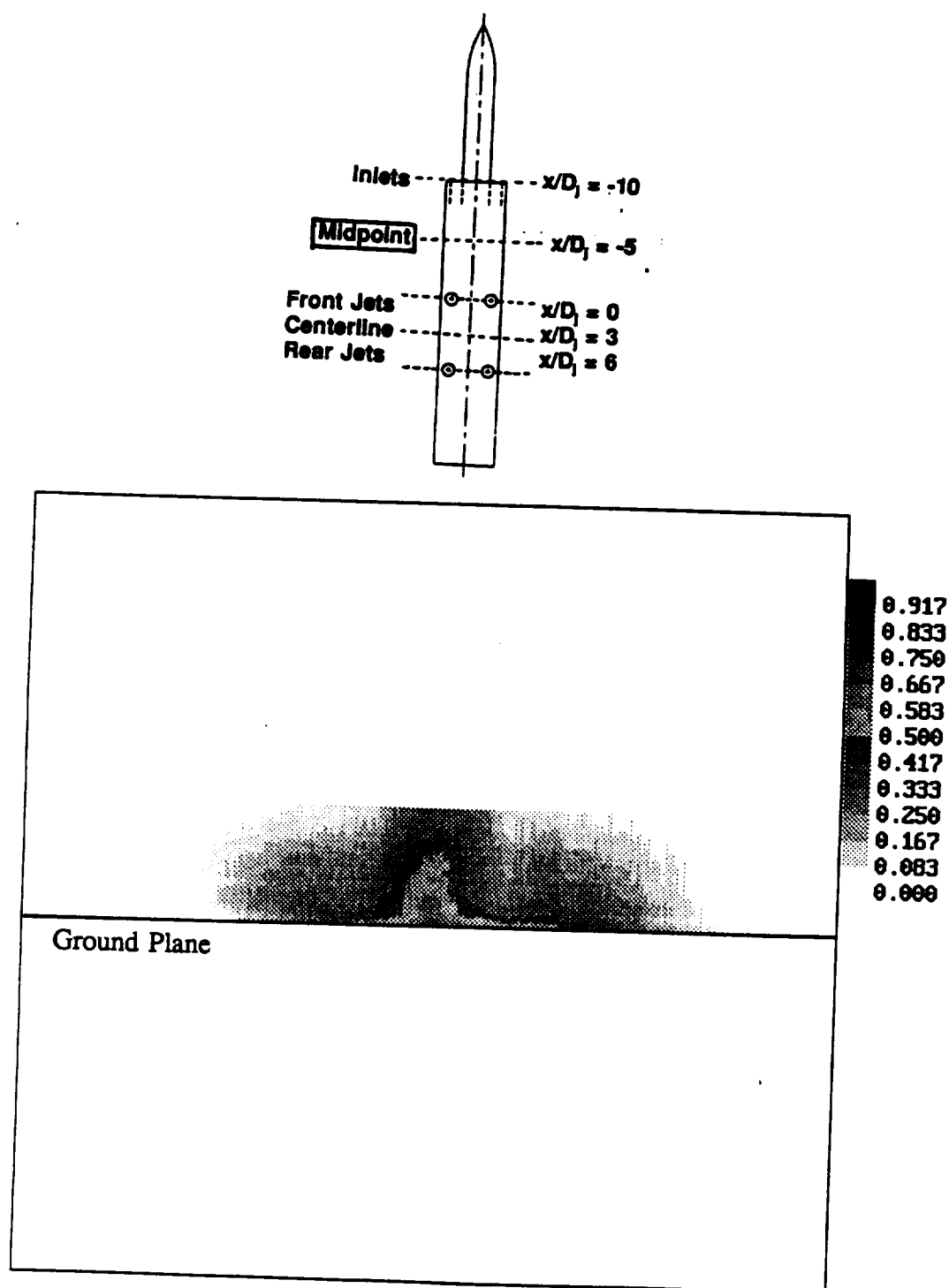


Figure 5.78: Experimental Smoke Concentration Between Inlets and Front Jets
 $x/D_j = -5.0$, $H/D_j = 4$, $U/V_j = 0.09$

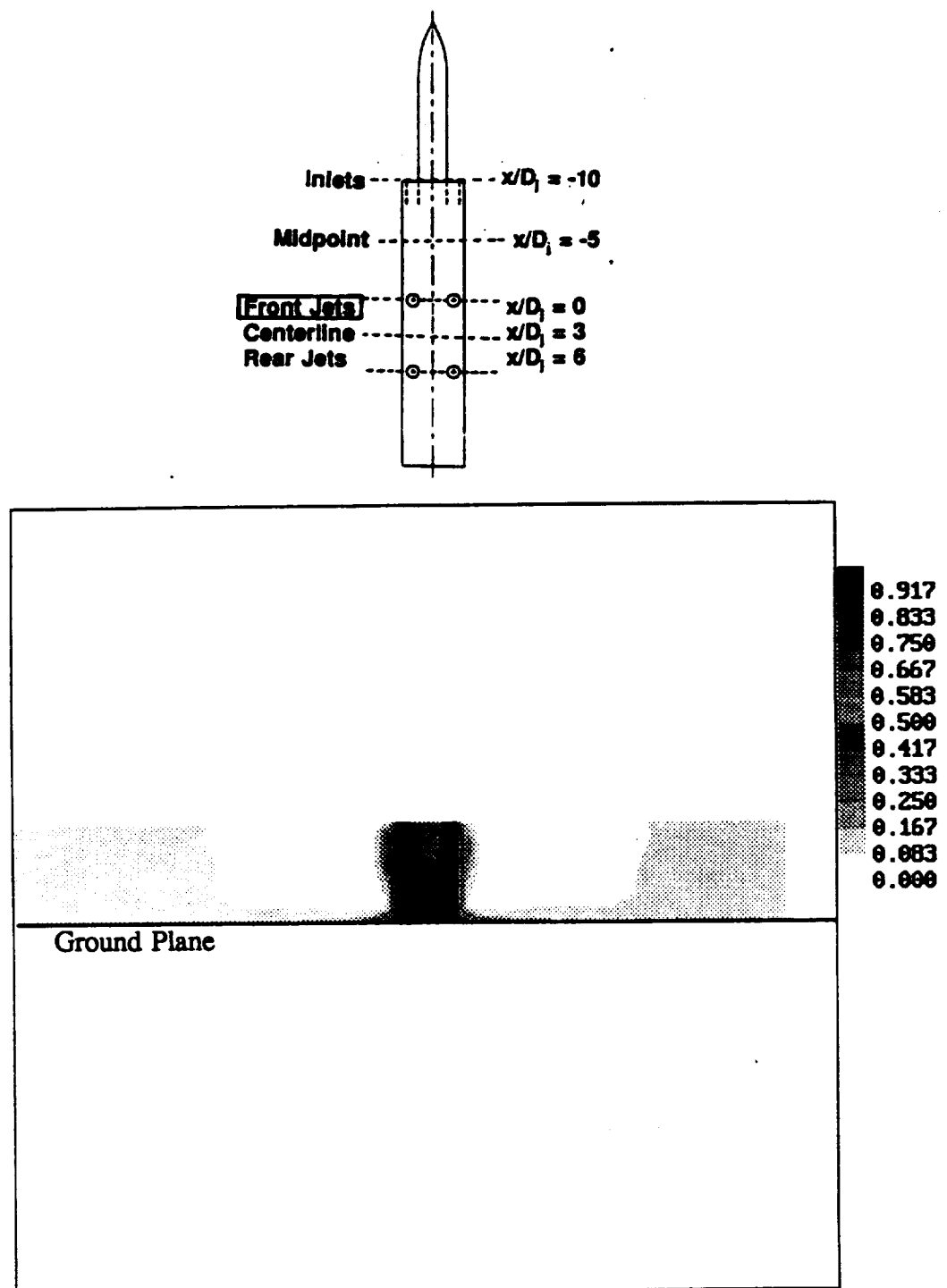


Figure 5.79: Numerical Temperature Distribution Across Front Jets
 $x/D_j = 0.0$, $H/D_j = 4$, $U/V_j = 0.03$

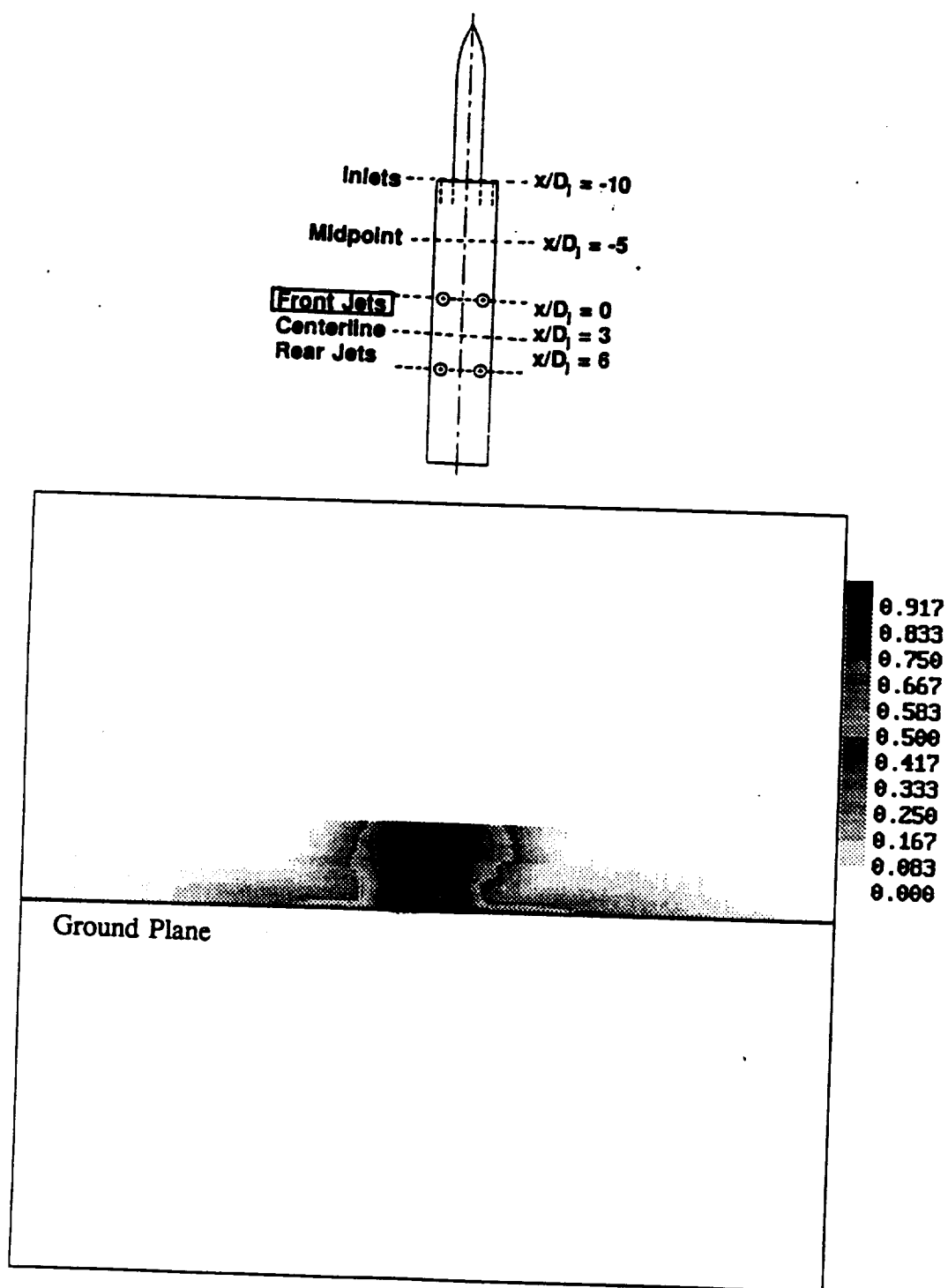


Figure 5.80: Experimental Smoke Concentration Across Front Jets
 $x/D_j = 0.0$, $H/D_j = 4$, $U/V_j = 0.03$

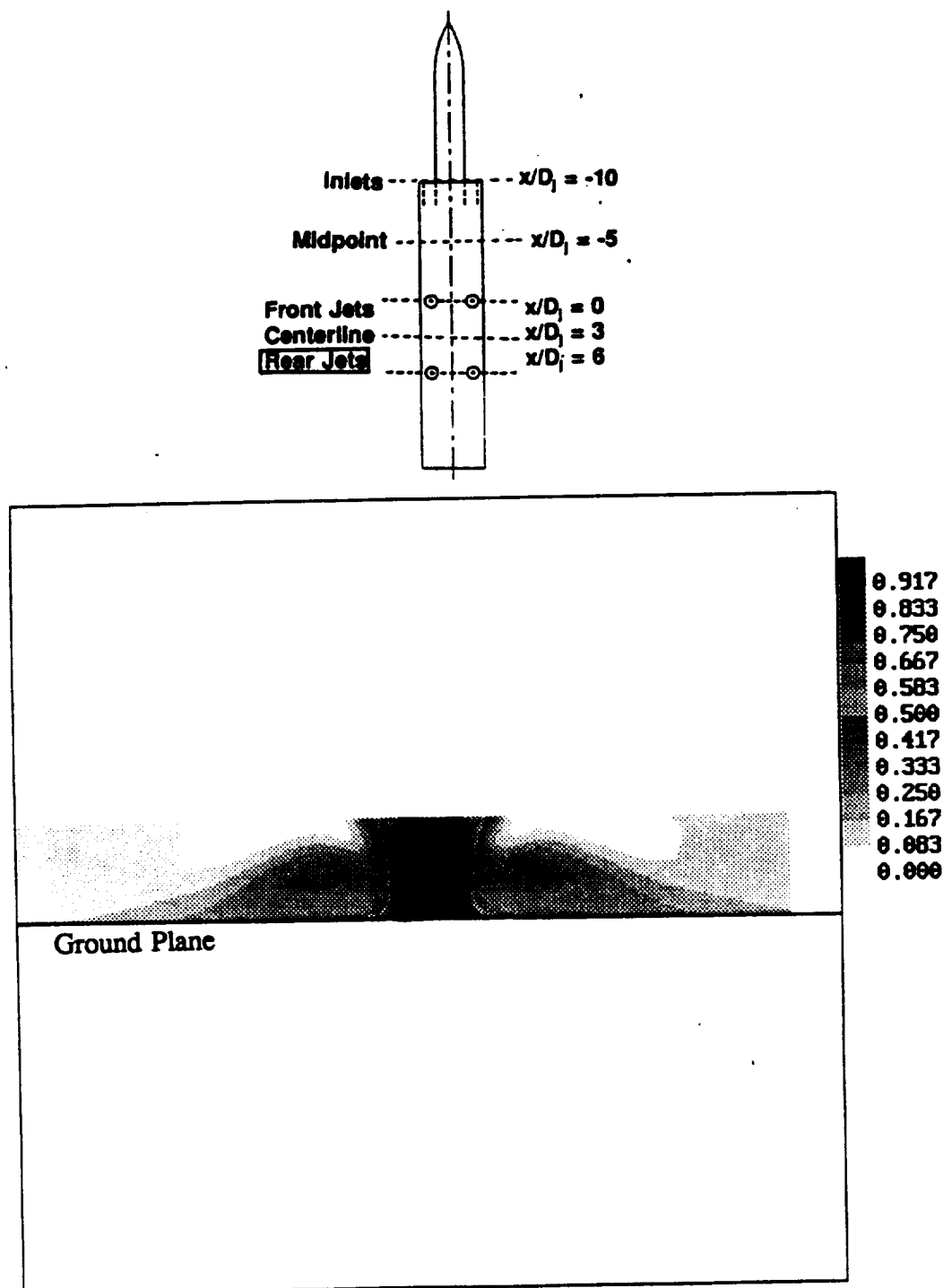


Figure 5.81: Numerical Temperature Distribution Across Rear Jets
 $x/D_j = 6.0$, $H/D_j = 4$, $U/V_j = 0.03$

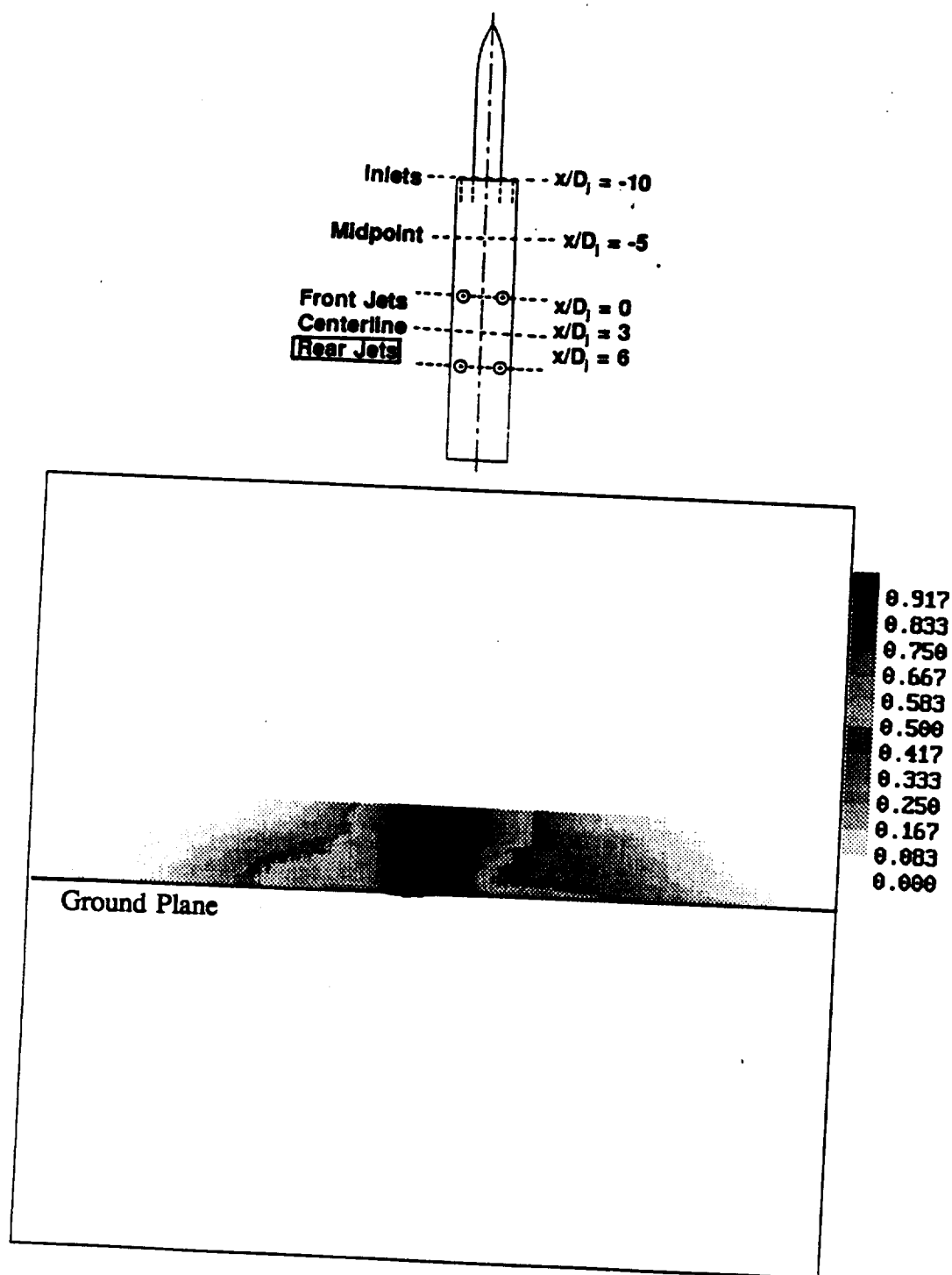


Figure 5.82: Experimental Smoke Concentration Across Rear Jets
 $x/D_j = 6.0$, $H/D_j = 4$, $U/V_j = 0.03$

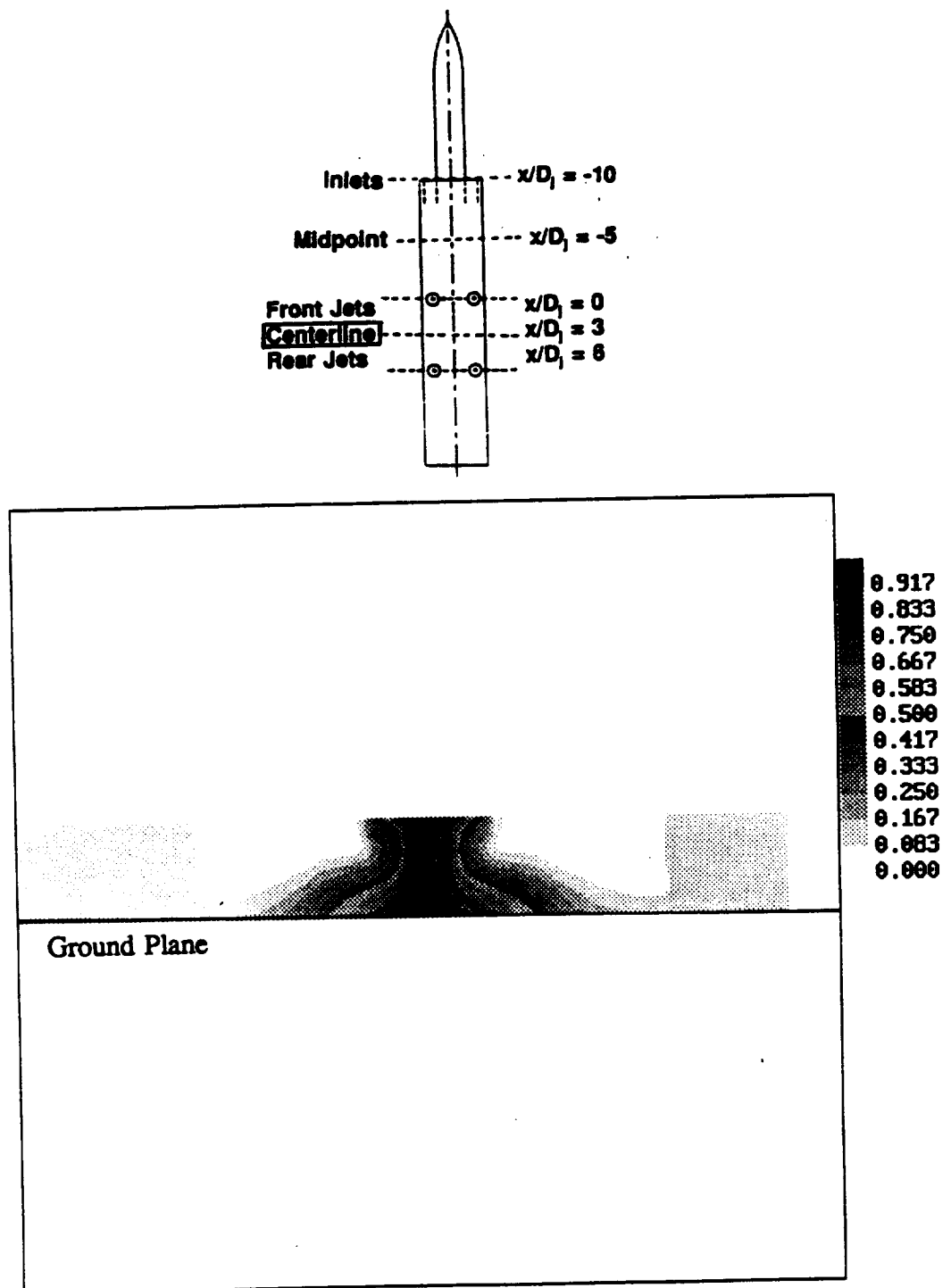


Figure 5.83: Numerical Temperature Distribution Between Front and Rear Jets
 $x/D_j = 3.0$, $H/D_j = 4$, $U/V_j = 0.03$

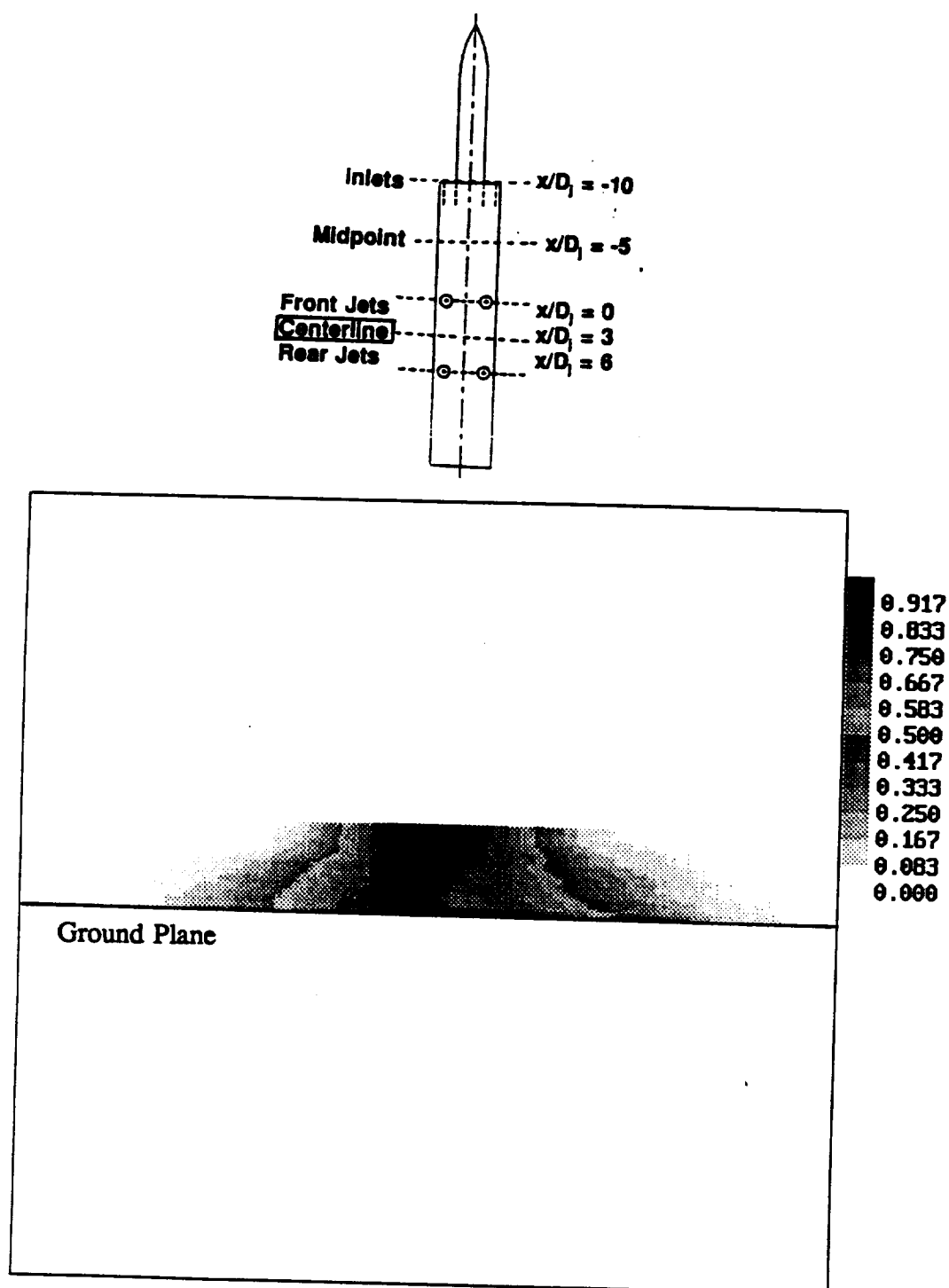


Figure 5.84: Experimental Smoke Concentration Between Front and Rear Jets
 $x/D_j = 3.0$, $H/D_j = 4$, $U/V_j = 0.03$

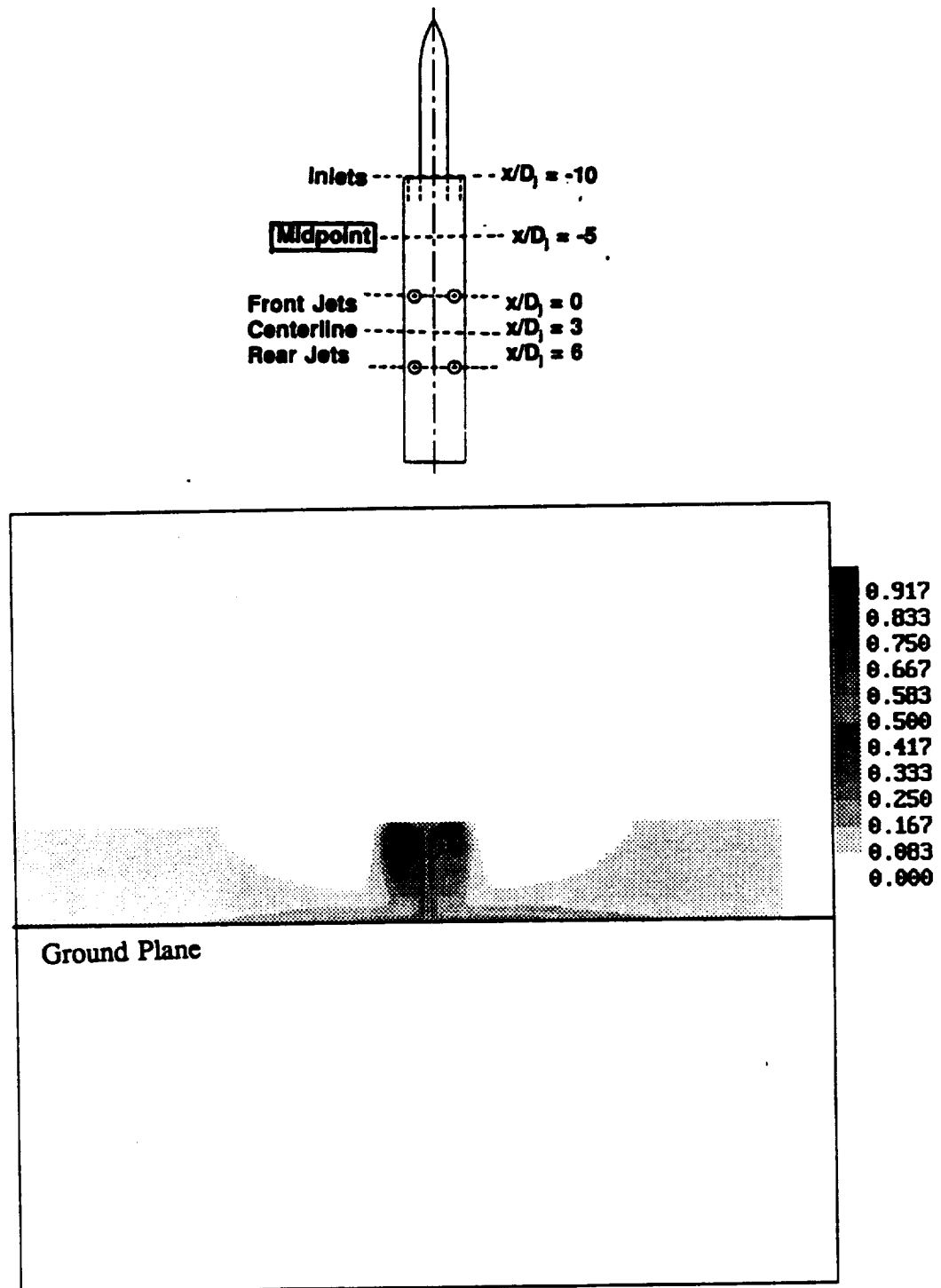


Figure 5.85: Numerical Temperature Distribution Between Inlets and Front Jets
 $x/D_j = -5.0$, $H/D_j = 4$, $U/V_j = 0.03$

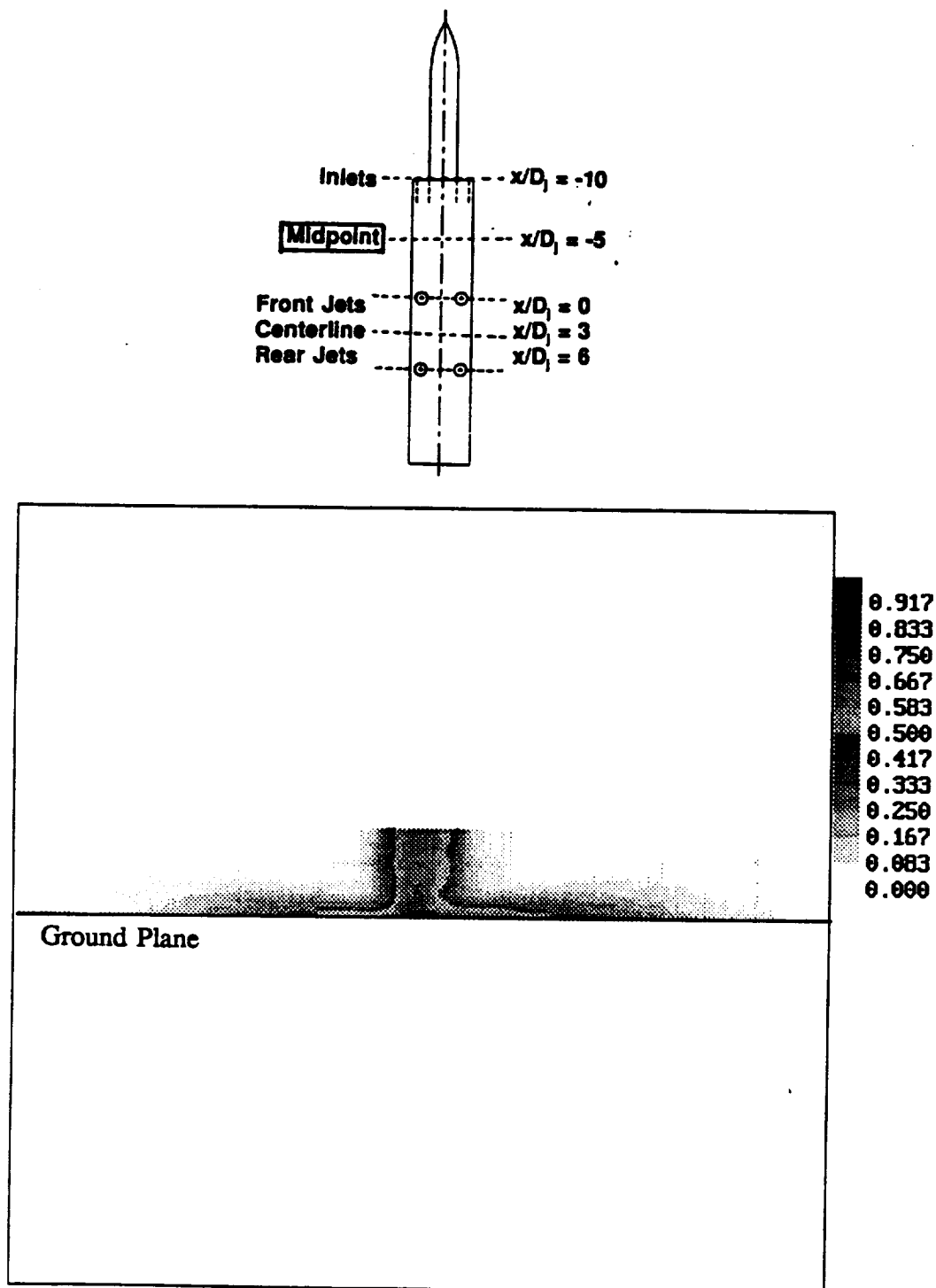


Figure 5.86: Experimental Smoke Concentration Between Inlets and Front Jets
 $x/D_j = -5.0$, $H/D_j = 4$, $U/V_j = 0.03$

6. CONCLUSIONS

Experimental investigations of the hot gas environment around a four jet, two inlet V/STOL model configuration have shown a number of flow features which may contribute to hot gas ingestion. Marker nephelometry using smoke particles illuminated by a laser sheet has also provided large amounts of data for comparison with numerical temperature profiles of the same model configuration.

The marker nephelometry technique used in this experiment has proven successful in providing both qualitative and quantitative information about smoke concentration in a complex flowfield. Data at both short time intervals and time-averaged data were obtained using this technique. Smoke concentration measurements of both turbulent and steady flows could then be examined. Measurements of root-mean-square concentration were also possible, although only giving information on large-scale unsteadiness for this experiment.

Qualitative measurements of smoke concentration in the flowfield show the existence of a number of flow features. The flowfield itself, and the individual flow features, are unsteady to some degree. Several features noted by earlier researchers were seen, including the ground vortex and a vortex pair between the fountain and jets at low forward velocities. Several other features have not been documented before. The forward vortex pair, located in the stagnation area of flow from the fountain and the free stream flow, is quite prominent, and appears to be oriented normal to the ground plane. This structure could be responsible for some far field hot gas ingestion. A second ground

vortex, associated with the rear pair of jets, is also apparent in most of the cases tested in this experiment.

The location of both the ground vortex and forward vortex pair depend upon both the velocity ratio and model height. At high velocity ratios, the distance between the forward pair of jets and the ground vortex and forward vortex pair locations appear to be independent of test model height. Inlet suction also does not appear to influence the location of the ground vortex and forward vortex pair at these high velocity ratios. At low velocity ratios, the distance between the forward pair of jets and the ground vortex and forward vortex pair locations appear to increase with increasing height. Inlet suction plays an important role at low velocity ratios, greatly influencing the location of the ground vortex and forward vortex pair. In some instances, the ground vortex is very near the inlet. Without inlet suction, the ground vortex and forward vortex pair are essentially independent of model height.

Comparisons of experimental smoke concentration and numerical temperature data show a large number of similarities. This provides confirmation that smoke concentration and temperature distribution can be considered analogous to one another, as long as convection is the primary means of transport in the flowfield.

There are some differences between the experimental smoke concentration measurements and numerical temperature distribution. Most of these differences can be related to specific flowfield features. The forward vortex does not appear as prominently in the numerical results. The ground vortex in the numerical results is also much smaller than that seen in the experimental results. Inlet suction does not appear to influence the numerical flowfield to the great degree seen in the experimental smoke concentration at low model heights and forward velocity ratios. Numerical and experimental results also are different in the fountain region as well.

Most of the differences between the numerical temperature distribution and experimental smoke concentration can be attributed to inadequacies in mixing in the numerical flowfield. Numerical results using the κ - ϵ turbulence model appear to underpredict the degree of unsteadiness and mixing in this complex flowfield.

Further research is necessary with improved data acquisition and processing hardware before accurate measurements of the actual unsteadiness in the flowfield is possible. Creating a model using jets with choked flow would also be necessary in order to model more realistic aircraft configurations. In addition, one, two, and three jet configurations also need to be studied in order to determine characteristics of the basic flow features such as the ground vortex and forward vortex pair. Of particular interest is the minimum configuration necessary to create the forward vortex pair.

This experiment has shown, for a simple four jet, two inlet V/STOL configuration, that smoke concentration measurements of the flowfield can be used to predict some of the characteristic flow features around STOVL and V/STOL aircraft relatively easily. In addition, this technique of marker nephelometry allows quantitative measurements of smoke concentration, providing large amounts of data for comparison with numerical calculations. Using this experimental technique in conjunction with numerical methods, it should be relatively easy to test V/STOL and STOVL aircraft concepts with some degree of confidence in the results. This will allow many more design concepts to be tested, and facilitate the design of future V/STOL and STOVL aircraft.

LIST OF REFERENCES

LIST OF REFERENCES

1. Agarwal, Ramesh K., "Recent Advances in Prediction Methods for Jet-Induced Effects on V/STOL Aircraft," Recent Advances in Aerodynamics, Edited by Anjaneyulu Krothapalli and Charles A. Smith, Springer-Verlag, New York, NY, 1986.
2. Agarwal, R. K., and Bower, W. W., "Navier-Stokes Computations of Turbulent Compressible Two-Dimensional Impinging Jet Flowfields," AIAA Journal, Vol. 20, No. 5, May 1982., pp. 577-584.
3. Agarwal, Ramesh K., and Deese, Jerry E., "Euler Solutions for Airfoil/Jet/Ground-Interaction Flowfields," Journal of Aircraft, Vol. 23, No. 5, May 1986, pp. 376-381.
4. Aoyagi, Kiyoshi, and Snyder, Phillip K., "Experimental Investigation of a Jet Inclined to a Subsonic Crossflow," December, 1981, AIAA Paper No. 81-2610.
5. Aulehla, P., and Kissel, G. K., "Experience with High Performance V/STOL Fighter Projects at MBB," AIAA/NASA Ames VSTOL Conference, Palo Alto, California, December 1981, AIAA Paper No. 81-2614.
6. Barata, J., Durao, D., and McGuirk, J., "Numerical Study of Single Impinging Jets Through a Crossflow," 27th Aerospace Sciences Meeting, Reno, Nevada, January, 1989, AIAA Paper No. 89-0449.
7. Barrack, Jerry P., and Kirk, Jerry V., "Low-Speed Characteristics of High-Performance Lift-Engine V/STOL Aircraft," Aeronautics and Space Engineering and Manufacturing Meeting, Los Angeles, California, October, 1968, SAE Paper No. 680644.
8. Balint, J. L., Ayrault, M., and Scon, J. P., "Quantitative Investigation of the Velocity and Concentration Fields of Turbulent Flows Combining Visualization and Image Processing," Flow Visualization III, Proceedings of the Third International Symposium on Flow Visualization, Sept., 1983, Univ. of Michigan, Ann Arbor, Michigan, Edited by W. J. Yang, Hemisphere Publishing Corp., Washington, D. C.
9. Becker, H. A., "Mixing, Concentration Fluctuations and Marker Nephelometry," Studies in Convection, Volume 2: Theory, Measurement, and Application, Edited by B. E. Launder, Academic Press, New York, NY, 1977.
10. Borleteau, J. P., "Concentration Measurement with Digital Image Processing," ICIASF '83 Record, pp. 37-42, St. Louis, France, September 1983.

11. Bower, W., Saripalli, K., and Agarwal, R., "A Summary of Jet-Impingement Studies at McDonnell Douglas Research Labs," AIAA/NASA Ames VSTOL Conference, Palo Alto, California, December, 1981, AIAA Paper No. 81-2613.
12. Brandt, A., "Hydrodynamic Flowfield Imaging," Flow Visualization III, Proceedings of the Third International Symposium on Flow Visualization, Sept., 1983, Univ. of Michigan, Ann Arbor, Michigan, Edited by W. J. Yang, Hemisphere Publishing Corp., Washington, D. C.
13. Brennan, M. J., "V/STOL Developments in Hawker Siddeley Aviation Limited," 12th Anglo-American Aeronautical Conference, Calgary, Canada, July, 1971, Canadian Aeronautics and Space Institute Paper No. 72/18.
14. Chawla, K., Van Dalsem, W. R., and Rao, K. V., "Simulation and Analysis of a Delta Planform with Multiple Jets in Ground Effect," 28th Aerospace Sciences Meeting, Reno, Nevada, January 1990, AIAA Paper No. 90-0299.
15. Childs, R. E., and Nixon, D., "Simulation of Impinging Turbulent Jets," AIAA 23rd Aerospace Sciences Meeting, Reno, Nevada, January, 1985, AIAA Paper No. 85-0047.
16. Childs, E., and Patel, B., "Turbulence Model Performance in V/STOL Flow Field Simulation," AIAA/SAE/ASME/ASEE 26th Joint Propulsion Conference, Orlando, Florida, July, 1990, AIAA Paper No. 90-2248.
17. Colin, F. E., and Olivari, D., "The Impingement of a Circular Jet Normal to a Flat Surface With and Without Crossflow," European Research Office, United States Army Replort No. AD-688953, January 1969.
18. Donaldson, Coleman Dup., and Snedeker, Richard S., "A Study of Free Jet Impingement. Part 1. Mean Properties of Free and Impinging Jets," Journal of Fluid Mechanics, Vol. 45, Part 2, pp. 281-319, 1971.
19. Donaldson, Coleman Dup., Snedeker, Richard S., and Margolis, David P., "A Study of Free Jet Impingement. Part 2. Free Jet Turbulence Structure and Impingement Heat Transfer," Journal of Fluid Mechanics, Vol. 45, Part 3, pp. 477-512, 1971.
20. Dwenger, Richard, "Laser Doppler Velocimeter Measurements and Laser Sheet Imaging in an Annular Combustor Model," M. S. Thesis, Purdue University, May 1990.
21. Elliott, D. W., Hoskins, P. D., Miller, R. F., and Simmons, J. R., "A Remote Tip-Driven Fan Powered Supersonic Fighter Concept," AIAA/ASME/SAE/ASEE 26th Joint Propulsion Conference, Orlando, Florida, July, 1990, AIAA Paper No. 90-2415.
22. Farbridge, J. E., and Smith, Ronald C., "The Transonic Multi-Foil Augmentor-Wing," AIAA/NASA Ames V/STOL Conference, Palo Alto, California, June, 1977, AIAA Paper No. 77-606.

23. Fearn, Richard L., "Progress Towards a Model to Describe Jet/Aerodynamic-Surface Interference Effects," Recent Advances in Aerodynamics, Edited by Anjaneyulu Krothapalli and Charles A. Smith, Springer-Verlag, New York, NY, 1986.
24. Gittner, U., Hoffert, F., and Lotz, M., "Interaction Between Airframe-Powerplant Integration and Hot Gas Ingestion for Jet Lift V/STOL Transport Aircraft," Agard Conference Proceeding 27: Integration of Propulsion Systems in Airframes, September 1967.
25. Hall, Gordon R., and Rogers, Kenneth H., "Recirculation Effects Produced by a Pair of Heated Jets Impinging on a Ground Plane," NASA CR-1307, Northrop Corporation, September, 1969.
26. Hammond, Alexander D., and McLemore, H. Clyde, "Hot-Gas Ingestion and Jet Interference Effects for Jet V/STOL Aircraft," Agard Conference Proceeding 27: Integration of Propulsion Systems in Airframes, September 1967.
27. Hoad, Danny R., "Techniques and Problems Associated With Wind-Tunnel Testing of Multi-Fan VTOL Aircraft Models," Presented at the Navy Workshop on Prediction Methods for Jet V/STOL Propulsion Aerodynamics, Washington, D. C., July, 1975.
28. Johns, Albert L., "Hot Gas Ingestion Testing of an Advanced STOVL Concept in the NASA Lewis 9- by 15-Foot Low Speed Wind Tunnel With Flow Visualization," AIAA/ASME/SAE/ASEE 24th Joint Propulsion Conference, Boston, Massachusetts, July 1988, AIAA Paper No. 88-3025.
29. Kotansky, Donald R., "Multiple Jet Impingement Flowfields," Recent Advances in Aerodynamics, Edited by Anjaneyulu Krothapalli and Charles A. Smith, Springer-Verlag, New York, NY, 1986.
30. Kotansky, D. R., and Bower, W. W., "A Basic Study of the VTOL Ground Effect Problem for Planar Flow," AIAA/NASA Ames V/STOL Conference, Palo Alto, California, June, 1977, AIAA Paper No. 77-614.
31. Kotansky, Donald R., Durando, Norbert A., Bristow, Dean R., and Saunders, Philip W., "Multi Jet Induce Forces and Moments on VTOL Aircraft Hovering In and Out of Ground Effect," McDonnell Aircraft Co., Report No. NADC-77-229-30, April 1977.
32. Kotansky, D. R., and Glaze, L. W., "Impingement of Rectangular Jets on a Ground Plane," AIAA Journal, Vol. 20, No. 5, May 1982, pp. 585-586.
33. Kuhn, Richard E., "The Induced Aerodynamics of Jet and Fan Powered V/STOL Aircraft," Recent Advances in Aerodynamics, Edited by Anjaneyulu Krothapalli and Charles A. Smith, Springer-Verlag, New York, NY, 1986.
34. Kuhn, Richard E., and Eshleemann, James, "Ground Effects on V/STOL and STOL Aircraft--A Survey," Aircraft Design Systems and Operations Meeting, San Diego, California, November 1984, AIAA Paper No. 84-2530.

35. Lockwood, Vernard E., Turner, Thomas R., and Riebe, John M., "Wind-Tunnel Investigation of Jet-Augmented Flaps on a Rectangular Wing to High Momentum Coefficients", NACA TN-3865, December 1956.
36. Lord, P. A., "Development and Usage of a Small-Scale V/STOL Ground Effects Simulator," AIAA/AHS/ASME Aircraft Design Systems and Operations Meeting, Colorado Springs, Colorado, October, 1985, AIAA Paper No. 85-4037.
37. MacLean, R., Sullivan, J. P., and Murthy, S. N. B., "Hot Gas Environment Around STOVL Aircraft in Ground Proximity, Part I: Experimental Study," AIAA/SAE/ASME/ASME 26th Joint Propulsion Conference, Orlando, Florida, July 1990, AIAA Paper No. 90-2269.
38. Mineck, Raymond E., "Comparison of Theoretical and Experimental Interference Effects on a Jet VTOL Airplane Model," Presented at the Navy Workshop on Prediction Methods for Jet V/STOL Propulsion Aerodynamics, Washington, D. C., July 1975.
39. Morgan, Douglas C., "Concentration Measurements in a Cold Flow Model Annular Combustor Using Laser Induced Fluorescence," M. S. Thesis, Purdue University, August 1988.
40. Mueller, Thomas J., "Recent Developments in Smoke Flow Visualization," Flow Visualization III, Proceedings of the Third International Symposium on Flow Visualization, Sept., 1983, Univ. of Michigan, Ann Arbor, Michigan, Edited by W. J. Yang, Hemisphere Publishing Corp., Washington, D. C.
41. Nasseir, Nagy S., "Chapter 13: Impinging Jets," Encyclopedia of Fluid Mechanics, pp.349-366, Gulf Publishing, 1986.
42. Nasseir, N. S., and U. Peled, "The Pressure Field Generated by Jet-Jet Impingement," AIAA 10th Aeroacoustics Conference, Seattle, WA, July 1986, AIAA Paper No. 86-1951.
43. Patankar, Suhas V., Numerical Heat Transfer and Fluid Flow, Hemisphere Publishing Corp., Washington, D. C., 1980.
44. Saripalli, K. R., "Laser Doppler Velocimeter Measurements in a 3-D Impinging Twin-Jet Fountain Flow," Aircraft Design Systems and Operations Meeting, Colorado Springs, Colorado, October, 1985, AIAA Paper No. 85-4036.
45. Schwantes, E., "The Recirculation Flow Pattern of a VTOL Lift Engine," NASA TT F-14,912, June 1973.
46. Seal, Michael Damian II, "An Experimental Study of Swirling Flows as Applied to Annular Combustors," M. S. Thesis, Purdue University, May 1988.
47. Shayesteh, M. V., Shapaka, I. M. M. A., and P. Bradshaw, "Turbulence Structure of a Three Dimensional Impinging Jet in a Cross Stream," AIAA 23rd Aerospace Sciences Meeting, Reno, Nevada, January, 1985, AIAA Paper No. 85-0044.

48. Sherrieb, H. E., "Ground Effects Testing of Two-, Three-, and Four-Jet Configurations," Journal of Aircraft, Vol. 16, No. 6, June 1979, pp. 393-397.
49. Siclari, M. J., Migdal, D., Luzzi, T. W., Barche, J., and Palcza, J. L., "Development of Theoretical Models for Jet-Induced Effects on V/STOL Aircraft," Journal of Aircraft, Vol. 13, No. 12, December 1976, pp. 938-244.
50. Stewart, V., and Kemmerly, G., "Characteristics of the Ground Vortex Formed by a Jet Moving Over a Fixed Ground Plane," 27th Aerospace Sciences Meeting, Reno, Nevada, January 1989, AIAA Paper No. 89-0650.
51. Stewart, V. R., and Kuhn, R. E., "A Method for Estimating the Propulsion Induced Aerodynamic Characteristics of STOL Aircraft in Ground Effect," Report No. NADC 80226-60, August 1983.
52. Tafti, D., and Vanka, S. P., "Hot Gas Environment Around STOVL Aircraft in Ground Proximity, Part II: Numerical Study," AIAA/SAE/ASME/ASEE 26th Joint Propulsion Conference, Orlando, Florida, July 1990, AIAA Paper No. 90-2270.
53. VanOverbeke, Thomas J., and Holdeman, James D., "A Numerical Study of the Hot Gas Environment Around a STOVL Aircraft in Ground Proximity," AIAA/ASME/SAE/ASEE 24th Joint Propulsion Conference, Boston, Massachusetts, July 1988, AIAA Paper No. 88-2882.
54. Veret, C., "Flow Visualization by Light Sheet," Flow Visualization III, Proceedings of the Third International Symposium on Flow Visualization, Sept., 1983, Univ. of Michigan, Ann Arbor, Michigan, Edited by W. J. Yang, Hemisphere Publishing Corp., Washington, D. C.
55. Waesche, J. E., and Migdal, D., "High-Performance Jet V/STOL Development," Journal of Aircraft, Vol 14, No. 2, February 1977, pp. 97-103.
56. Weber, Henry A. "VTOL Recirculation and Impingement Model Testing," Presented at the AIAA/SAE Ninth Propulsion Conference, Las Vegas, Nevada, November, 1973, AIAA Paper No. 73-1183.
57. Winston, Matthew M., "Propulsion-Induced Aerodynamic Interference Effects on Jet Lift VTOL Aircraft," Presented at the Navy Workshop on Prediction Methods for Jet V/STOL Propulsion Aerodynamics, Washington, D. C., July 1975.
58. Wohllebe, F. A., and Siclari, M. J., "Fountain and Upwash Flowfields of Multijet Arrangements," Journal of Aircraft, Vol. 15, No. 8, August 1978, pp. 468-473.

APPENDIX

APPENDIX

The technique of marker nephelometry used in this experiment employs a cylindrical lens to create a laser sheet. Laser sheets created by cylindrical lenses have a gaussian distribution in intensity. Correcting for the gaussian beam distribution in intensity of the laser sheet created by a cylindrical lens is necessary in order to get an accurate measurement of smoke concentration in the flowfield. Without accounting for this gaussian beam distribution, smoke concentration at the edges of the laser sheet will appear much less. This section presents results of the calibration of a narrow laser sheet, as well as light curves of the wider laser sheet actually used in the experiment.

Three methods were used to measure the intensity of the laser sheet across the test section. The first method used an enclosed area filled with a uniform concentration of smoke, through which the laser sheet was directed. A blower in the enclosed area, and outside the laser sheet, assured that smoke was well mixed in the test volume, and of uniform concentration. Without the blower, small air currents in the test volume concentrated smoke particles in certain areas, leading to a non-uniform smoke distribution.

The next method used comparisons between a single 127 frame average with the laser sheet at the centerline, and a merged image consisting of 127 frame averages of the flowfield with the laser sheet centerline to the right edge, center, and left edge of the test section. The laser sheet intensity profile measured using the first method was used to correct the central 127 frame average. It was then compared to the merged image. Further corrections to the laser sheet intensity profile were then employed to match the central 127 frame average and merged image.

Figure A.1 shows profiles through the front jet pair centerline of the merged image, the image with the laser sheet at the center of the test section, and the image with the laser sheet to the side of the test section. The three files were merged by using shape functions of the form

$$\cos \pi(z - C_L)/120$$

with $0 < z < 480$; $-240 < (z - C_L) < 240$;

where:

C_L = Laser Sheet Centerline

z = pixel location in z -direction

The laser sheet centerlines were located at $z=0$, $z=240$, and $z=480$ for each of the three images. The shape function for each of the three respective images was multiplied by the values in the image, based on the pixel location in the z -direction (across the flow). All three images were then added together to create a single image. This merged image was then compared to the central image, corrected for gaussian beam distribution based on the intensity curve from the first calibration method. The results of this are shown in figure A.2. As can be seen, the corrected image does not agree at the edges with the merged image, although it is an improvement over the central, uncorrected image. Figure A.3 shows a much better correction, based on an intensity curve developed by trial and error from the one used in figure A.2.

The third method used a reflecting rod, which was placed in the test section, and viewed with the video camera. A direct measure of intensity was then possible.

Figure A.4 shows the results of the three laser sheet intensity curves. The narrowest of the three uses the reflecting rod to generate the intensity curve. The widest curve was generated using the first method, using a uniform smoke distribution. It appears that as the smoke concentration in the flowfield increases, that the laser sheet intensity distribution broadens.

A possible reason for this broadening involves the scattering of laser light off the smoke particles in the flowfield. Smoke particles scatter light from the laser sheet, generally using forward- and backward-scattering mechanisms. Some of the laser sheet light is scattered off to the sides, in regions where there is low laser sheet intensity. Some of this scattered light is then reflected into the camera. As the smoke particle density increases, more particles are available to scatter light to the sides, and more particles at the sides are available to reflect light into the camera. This scattering mechanism also decreases the laser sheet intensity along the centerline of the test section, as shown in figure A.5. The laser is located downstream in the positive x-direction. The laser sheet is artificially broadened by light scattering off smoke particles, and makes the laser sheet intensity distribution dependent on the smoke concentration in the flowfield. Since the laser sheet intensity curve depends on the amount of smoke in the flowfield, it is impossible to correct smoke concentration measurements for the gaussian beam distribution at the edges of the laser sheet. Therefore, concentration measurements will only be accurate in the central, high intensity portion of the laser sheet.

Figure A.6 shows the light intensity across the laser sheet used for this experiment. Only the central portion of the gaussian laser sheet is used. Results for the first and third calibration methods show a nearly uniform laser sheet intensity across the test section. The large scatter in the direct reflection method is due to the roughness of the rod, but does show a nearly uniform intensity distribution. The falloff at one end is caused by camera misalignment. Since the laser sheet is of nearly uniform distribution across the test section, no corrections in laser sheet intensity are necessary.

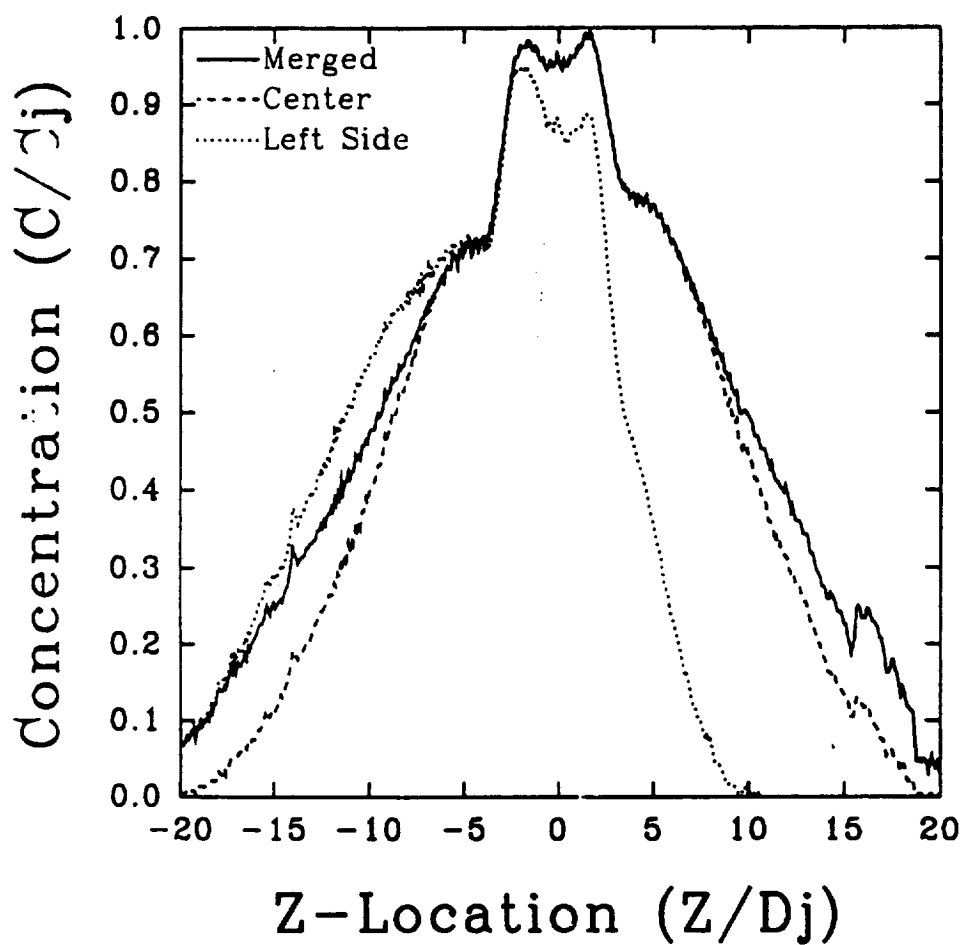


Figure A.1: Left, Central, and Merged Image Profiles Across Front Jet Centerline
Laser Sheet at Ground Plane, $H/D_j = 4$, $U/V_j = 0.09$

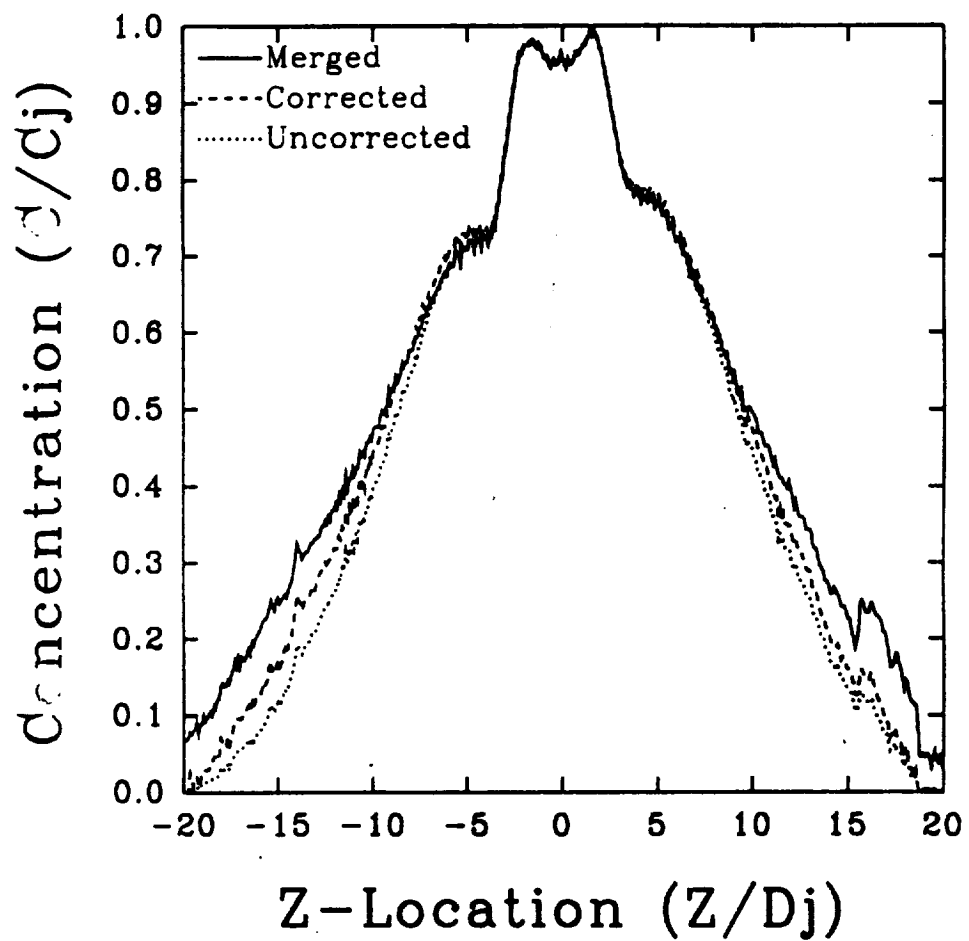


Figure A.2: Merged, Corrected, and Uncorrected Image Profiles At Front Jet Centerline
Laser Sheet at Ground Plane, $H/D_j = 4$, $U/V_j = 0.09$

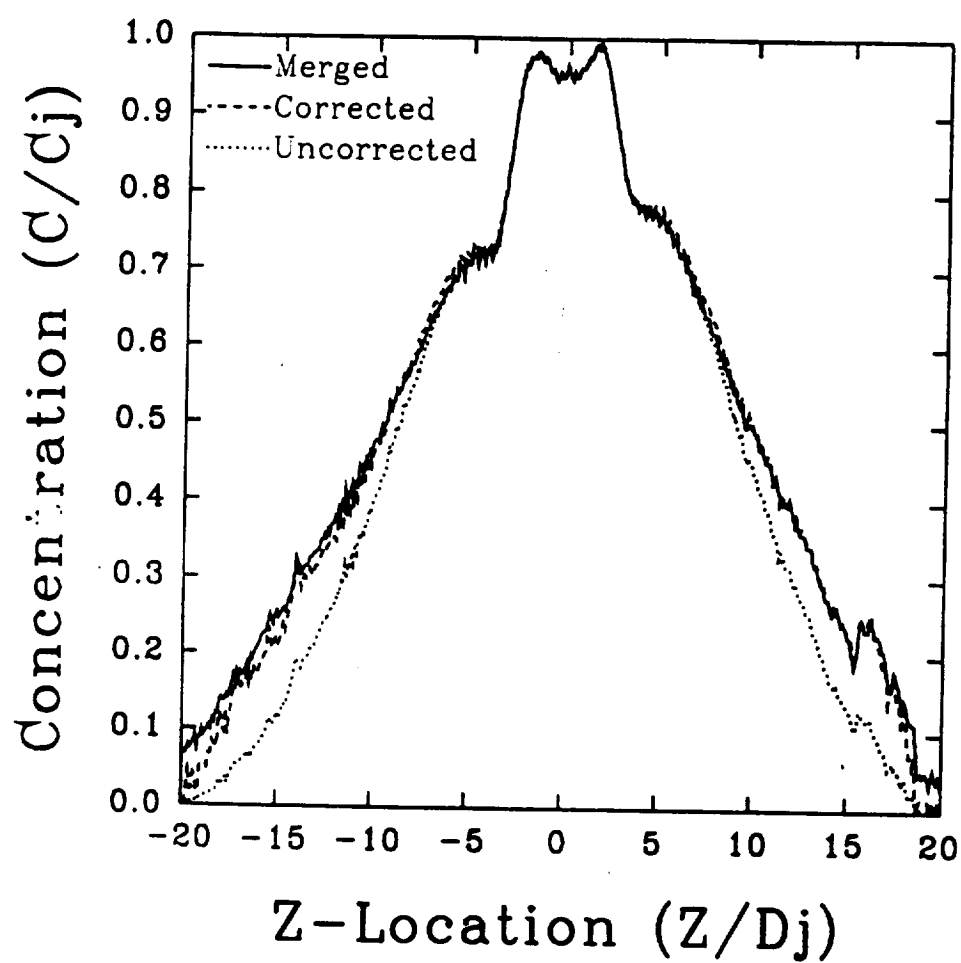


Figure A.3: Merged, Best Fit, and Uncorrected Image Profiles At Front Jet Centerline
Laser Sheet at Ground Plane, $H/D_j = 4$, $U/V_j = 0.09$

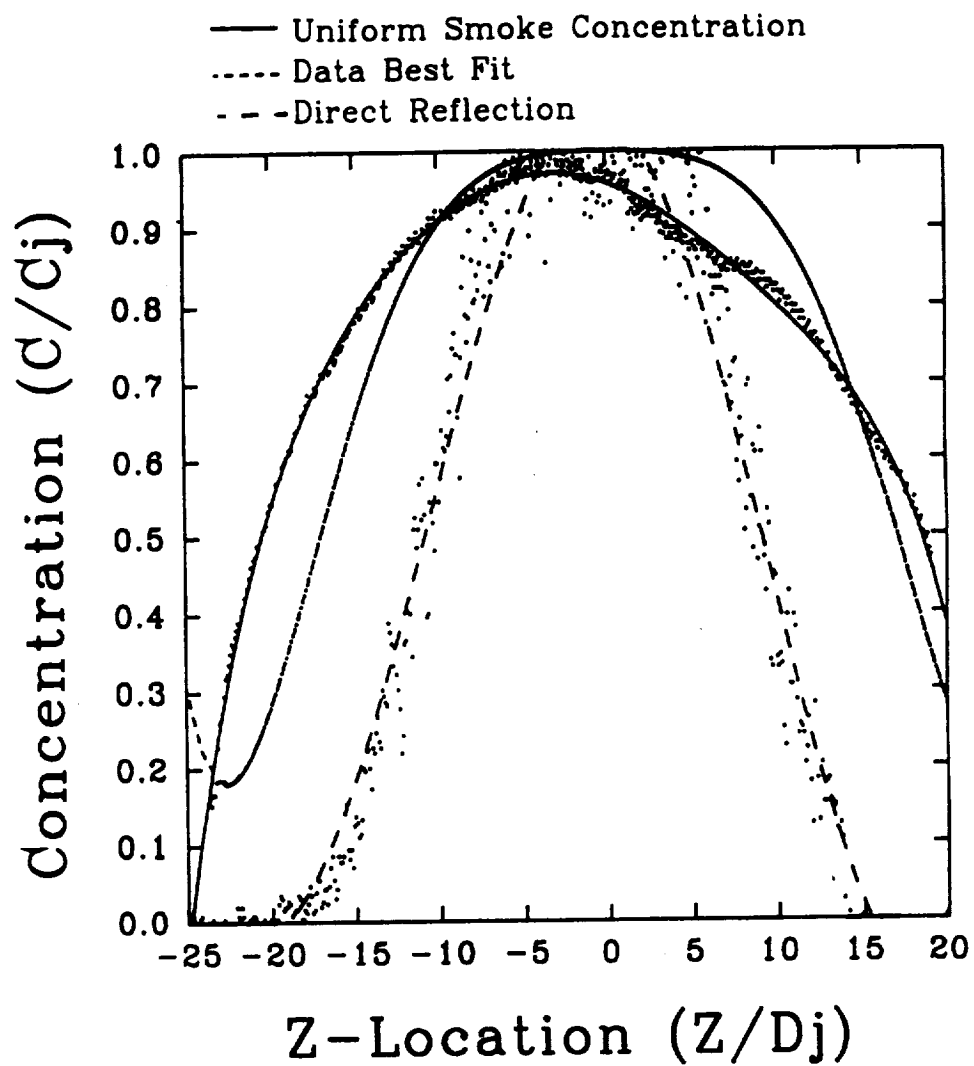


Figure A.4: Narrow Laser Sheet Intensity Curves

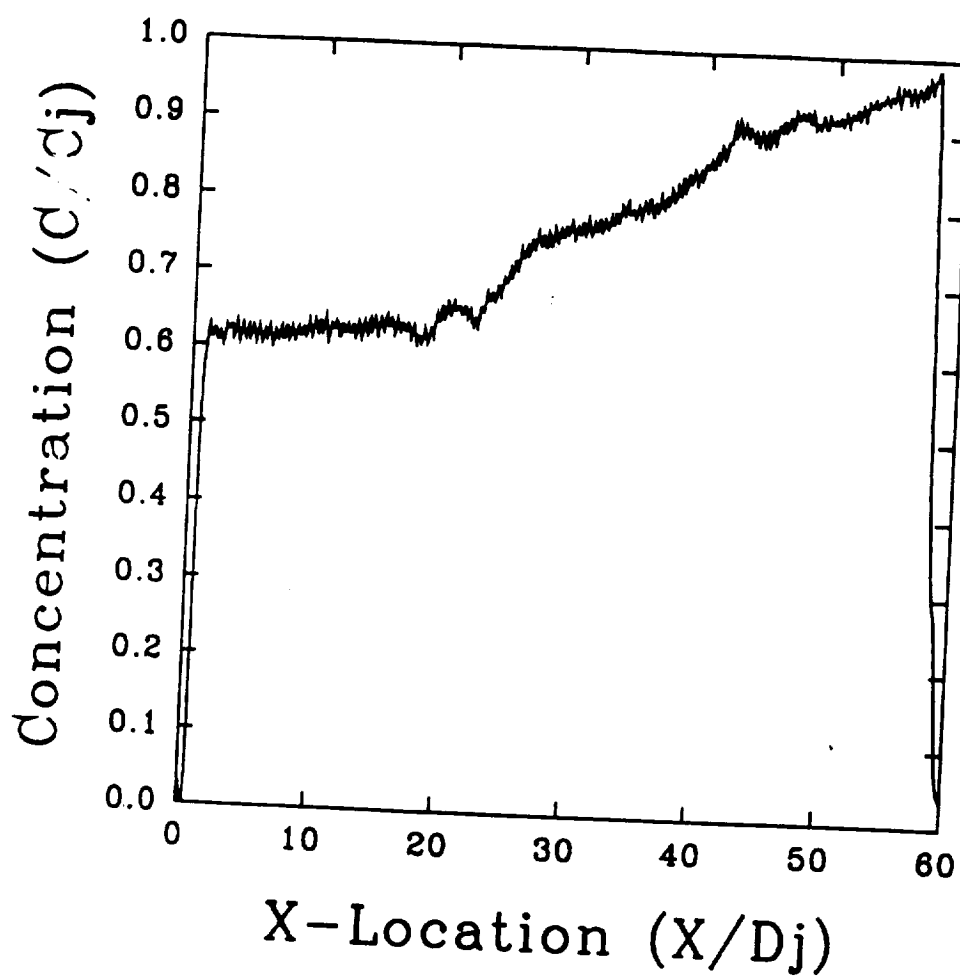


Figure A.5: Decrease in Laser Sheet Intensity Along X-Axis

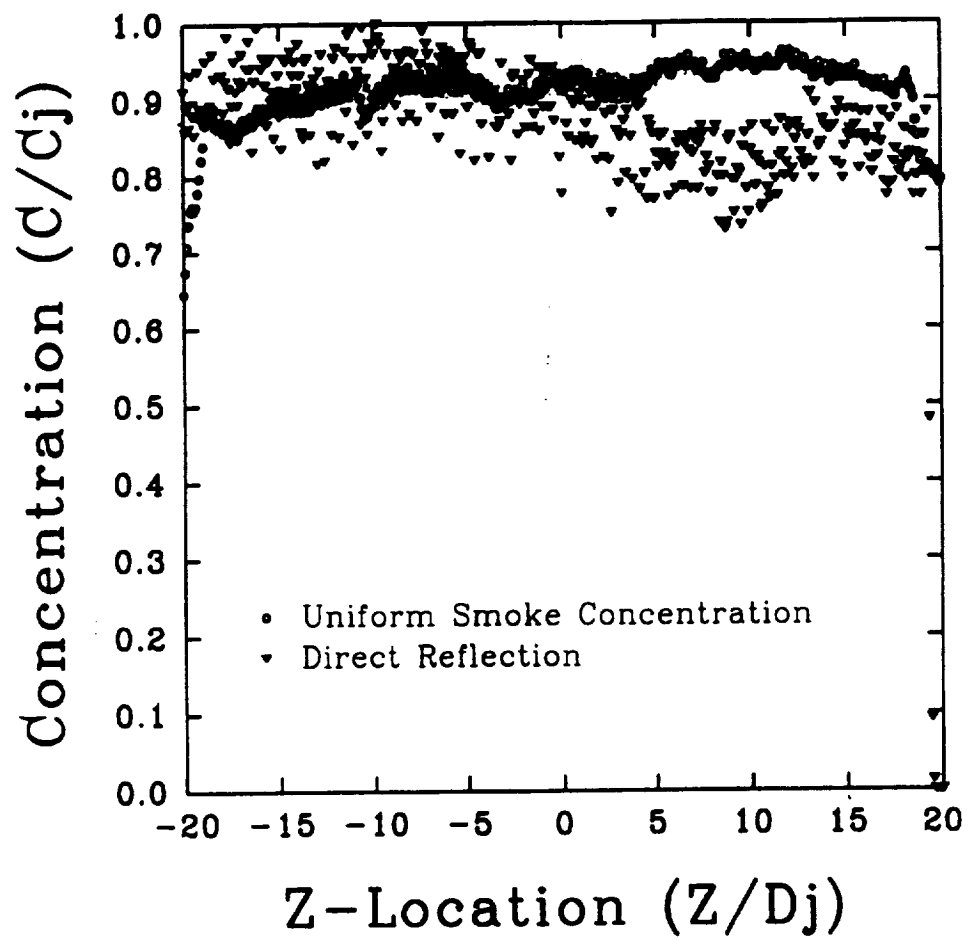


Figure A.6: Light Intensity Across Wide Laser Sheet

Report Documentation Page

1. Report No. NASA CR -187091		2. Government Accession No.		3. Recipient's Catalog No.	
4. Title and Subtitle The Flowfield Around a STOVL Aircraft Model in Ground Effect				5. Report Date May 1991	
				6. Performing Organization Code	
7. Author(s) Roderick J. MacLean				8. Performing Organization Report No. None	
				10. Work Unit No. 505-68-71	
9. Performing Organization Name and Address Purdue University School of Aeronautics and Astronautics West Lafayette, Indiana 47907				11. Contract or Grant No. NAG3-943	
				13. Type of Report and Period Covered Contractor Report Final	
12. Sponsoring Agency Name and Address National Aeronautics and Space Administration Lewis Research Center Cleveland, Ohio 44135 - 3191				14. Sponsoring Agency Code	
15. Supplementary Notes Project Manger, James D. Holdeman, Internal Fluid Mechanics Division, NASA Lewis Research Center, (216) 433-5846. This report was submitted as a dissertation in partial fulfillment of the requirements for the degree of Master of Science in Aeronautics and Astronautics to Purdue University, West Lafayette, Indiana in December 1990.					
16. Abstract An experimental investigation was conducted to determine the causes of hot gas ingestion of engine inlets in STOVL and V/STOL aircraft in ground effect. Marker nephelometry was used to establish the interactions between the jets, forward velocity, and ground for a typical aircraft model configuration. The aircraft test model consisted of a two inlet configuration with four low subsonic velocity jets impacting vertically on a flat plate. The vertical distance between the plate and model under-surface was adjustable, and a wind tunnel provided forward air velocities from 0 to 0.1 times the jet velocity to simulate landing into a wind. Single frame pictures of the smoke concentration distribution in the flowfield revealed several vortical features in the interaction region, which were affected variously by the distance between the ground plane and model, the forward wind velocity, and the inlet suction. Some of these vortical features, such as the ground vortex, have been seen before in experiments using single jets. Other vortical features in the flowfield, such as the forward vortex pair, have not been seen before. Frame-averaged experimental smoke concentration profiles compared favorably with numerical time-averaged predictions of temperature distribution carried out at the University of Illinois. However, such predictions did not seem to reveal some aspects of the vortical flow features which should affect instantaneous distortion into the engine inlet.					
17. Key Words (Suggested by Author(s)) Short take off aircraft; Vertical flight; Ground effect (aerodynamics); High temperature gases; Digestion (engines); Cross flow; Jet impingement; MIE scattering				18. Distribution Statement Unclassified - Unlimited Subject Category 07	
19. Security Classif. (of the report) Unclassified		20. Security Classif. (of this page) Unclassified		21. No. of pages 267	
				22. Price* A12	

